Modelling atmospheric CO_2 levels during the Phanerozoic: testing the main carbon sources and sinks as climate forcings over different timescales

Chloé Markussen Marcilly

Thesis submitted for the degree of Philosophiae Doctor

The Centre for Earth Evolution and Dynamics

Department of Geosciences

Faculty of Mathematics and Natural Sciences

University of Oslo, Norway

Series of dissertations submitted to the
Faculty of Mathematics and Natural Sciences, University of Oslo
No. 2576

ISSN 1501-7710

Print production: Graphics Center, University of Oslo.

Principal supervisor:

Trond H. Torsvik

Centre for Earth Evolution and Dynamics (CEED), University of Oslo, 0315 Oslo, Norway

School of Geosciences, University of Witwatersrand, Johannesburg 2050, South Africa

Subsidiary supervisors:

Thea Hatlen. Heimdal

Centre for Earth Evolution and Dynamics (CEED), University of Oslo, 0315 Oslo, Norway

Morgan T. Jones

Centre for Earth Evolution and Dynamics (CEED), University of Oslo, 0315 Oslo, Norway

Henrik H. Svensen

Centre for Earth Evolution and Dynamics (CEED), University of Oslo, 0315 Oslo, Norway

Main international collaborators:

Dana Royer

Department of Earth and Environmental Sciences, Wesleyan University, Middletown, Connecticut 06459, USA

Yves Goddéris

Géosciences-Environnement Toulouse, CNRS-Université Paul Sabatier, Toulouse, France

Funding:

This work was funded by the Research Council of Norway through its Centres of Excellence funding scheme, project number 223272 (CEED). I also acknowledge the support from the MatNat Faculty at the University of Oslo.

Preface

This doctoral thesis titled "Modelling atmospheric CO_2 levels during the Phanerozoic: testing the main carbon sources and sinks as climate forcings over different timescales" has been submitted to the Department of Geoscience at the University of Oslo (UiO) in accordance with the requirements for the degree of Philosophiae Doctor (Ph.D.). The work was conducted under the supervision of main supervisor **Trond H. Torsvik** and co-supervisor **Thea Hatlen Heimdal, Morgan T. Jones,** and **Henrik H. Svensen** at the Centre for Earth Evolution and Dynamics (CEED). The work presented in this thesis is supported by the Research Council of Norway through its Centres of Excellence funding scheme, project number 223272 (CEED).

This thesis consists of an introduction to the project, a theoretical background, three scientific papers published in international journals, and possible further directions for each of the research topics. The main results from the research have also been presented to the scientific community during several conferences, both as a poster and oral presentations. Paper 1 explores the influence of changing paleogeography and degassing forcings on CO_2 levels throughout the Phanerozoic using GEOCARBSULFvolc. Paper 2 investigates the reliability of flooding maps in assessing global sea levels. Paper 3 focuses on the Ordovician and Early Silurian and the role of paleogeography and degassing in the global cooling over the period.

Acknowledgments

Writing this Ph.D. has been an intensive learning period, both in the scientific arena and on a personal level. It would not have been possible without the support and guidance from many people on different levels.

First and foremost, I wish to thank my supervisors, **Trond H. Torsvik, Thea Hatlen Heimdal, Morgan T. Jones, and Henrik H. Svensen**, for guiding me through this project. I want to thank in particular **Trond** for giving me this opportunity and opening the door to the paleogeography and carbon modelling world. Thank you for all the support, availability, patience, and knowledge provided through those three years, even remotely during the corona outbreak. I could not have done this Ph.D. without your excellent guidance and mentorship. In addition to helping me with my research, your belief in me has helped me increase my self-confidence and feel more positive about myself. For that, I am forever grateful to you.

I also need to thank **Thea** for being more than a supervisor and office roommate; you became a real friend. You have been an enormous support, reassured me each time I needed it, and made me laugh every day. I will dearly miss the time spent with you.

Thank you to all my colleagues at CEED for making such a pleasant working environment. I want to thank especially **Mat** and **Morgan** for helping with our research but also for correcting and explaining some English to me. We all know it is a tremendous task to check English for French people!

Particular attention also goes to my colleagues on the third floor, **Agata, Ella, Eirik, Florence, Madeleine, Manfredo, Manon, Morgan, Nils,** and **Sara(s)**, for all the sweet and exciting discussions during our coffee and lunch breaks.

A special thank goes to my collaborators during this project, **Dana Royer** and the "French team" led by **Yves Goddéris**, for the great job done on organizing meetings and writing articles together while in lockdown.

When I think about this life achievement, one particular person comes to mind: my elementary school teacher **Viviane Crouvizier.** Thank you so much for helping the little girl that arrived at your school in 2000. You probably have no idea what your kindness has meant to me.

It's time to thank the most important persons in my life for their everlasting and ever stronger support: my lovely mom **Marie**, my amazing sister **Léa** and my kind dad **Denis**. Thank you for always being there for me and showering me with love whenever I need it. I am very lucky to have you. *Merci la Famille!*

Last but not least, I would like to thank my exceptional husband, **Ørjan**, for supporting and loving me every minute of this Ph.D. (and hopefully for many many years after it!). You never let me down, and you are, by far, the best public I could have dreamed of for practicing my presentations. No one else can make me as happy as you can, thank you for being you. *Elsker deg.*

Summary

Atmospheric carbon (pCO_2) has fluctuated considerably over geological time, with solar, tectonic, and biological forcings driving changes in concentrations. However, proxies for past CO_2 concentrations have high uncertainties and are mostly limited to Devonian and younger times, which means that complementary methods such as modelling play a key role in reconstructing past climate fluctuations. Models for the long-term (>10 million years; Myrs) carbon cycle aim to capture the various forces (i.e., sources and sinks) to predict past variations in atmospheric CO_2. Those models assume that the total degassing is compensated in the long term by total weathering. However, the different methods used to estimate this CO_2 degassing are numerous and give very different flux estimates. Consequently, model simulations show very different CO_2 levels over the Phanerozoic and generally calculate lower CO_2 values compared to the ones constructed from proxies for most of the Mesozoic and Cenozoic times.

The most important contribution of this thesis is the refinement of two important forcings in long-term carbon cycle models, namely consumption by silicate weathering and carbon degassing, in order to test their effects on paleoclimate changes over time. We present new estimates of solid Earth degassing for the Phanerozoic from two different proxies for seafloor production. We estimate carbon degassing for the past 490 Myrs using subduction flux from full-plate models as a proxy. Then, for the first time, we used the subduction flux to scale and normalize the arc-related zircon age distribution (reflecting continental arc-activity), which allows us to estimate carbon degassing in a much deeper time. Using arc-activity as a proxy for carbon degassing brings Mesozoic model estimates closer to CO_2 proxy values.

In parallel, through the construction of continental flooding maps for the past 520 Myrs, we have estimated exposed land area relative to the present-day and the fraction of exposed land area undergoing silicate weathering. The latter is based on the amount of exposed land within the tropics (±10°) plus the northern/southern wet belts (40-50°N/S) relative to today, which are the prime regions for silicate weathering. We also have refined those land estimates and potential weatherability by examining the distribution of climate-sensitive indicators. We then translate those estimates into new paleogeographic forcing for long-term carbon models.

Furthermore, we used a spatially resolved climate-carbon cycle Earth system model with refined continental reconstructions and new estimates of solid Earth degassing to simulate and

understand the Ordovician global cooling event. We investigated the respective roles of paleogeography and degassing separately. Our experiments show that, although early Ordovician high temperatures can be replicated within error margins, our new constraints cannot explain the intense cooling over the Mid to Late Ordovician, even if a progressive enhancement in Earth surface weatherability is taken into account. Using GEOCLIM in an inverse modelling approach, the theoretical degassing necessary to reach proxy-derived temperatures for the Early Ordovician was calculated and estimated to be three to five times higher than modern values. Further, to simulate the following Ordovician cooling trend, the solid Earth degassing must be reduced to modern-day values in only 30 Myr. We conclude that, if accepting the veracity of the high early Ordovician temperatures, alternative sources but also sinks of carbon must be considered to explain the climatic cooling shift over this period.

Finally, the development of exposed land provided the opportunity to estimate global flooding. Using the hypsometric method, we developed a new eustatic (global) sea-level curve for the past 520 Myrs. We tested the influence of changing hypsometric slopes on sea levels through time during Pangea. We identified a first-order "supercontinent" cycle of 250 Myr and second-order cycles of 20 and 40 Myrs, which were previously thought to be undetectable using paleogeography. Our new global sea-level curve shares strong similarities with stratigraphic constraints and correlates with some seafloor production proxies throughout the Phanerozoic.

Sammendrag

Atmosfærisk karbondioksid (pCO_2) har svingt betydelig over geologisk tid på grunn av solenergi variasjoner og tektoniske-biologiske påvirkninger som driver endringer i konsentrasjoner. Proxies for CO_2-konsentrasjoner i jordens oldtid har høye usikkerheter og er stort sett begrenset til Devon og yngre perioder, noe som betyr at komplementære metoder som modellering spiller en nøkkelrolle i å rekonstruere tidligere klimaforandringer. Modeller for den langsiktige karbonsyklusen (>10 millioner år) tar sikte på å fange opp de ulike kreftene (dvs. karbonkilder og karbonlagre) som kan forutsi tidligere variasjoner i atmosfærisk CO_2. Disse modellene forutsetter at den totale avgassingen på lang sikt kompenseres av total forvitring. Imidlertid er det flere forskjellige metoder til å estimere CO_2-avgassing og de kan gi svært forskjellige fluksestimater. Følgelig viser modeller svært forskjellige CO_2-nivåer gjennom Fanerozoikum og generelt beregner lavere CO_2-verdier sammenlignet med de som er konstruert fra proxies for det meste av Mesozoikum og Kenozoikum.

Det viktigste bidraget i denne avhandlingen er å forbedrede estimat av silikatforvitring og karbonavgassing, og ved hjelp av langsiktig karbonsyklusmodellering har vi testet deres effekt på klimaendringer gjennom Fanerozoikum. Vi presenterer nye estimater for avgassing ved hjelp av to forskjellige proxies for havbunnsproduksjon for de siste 490 millioner år. Den første metoden bruker subduksjonsfluks fra fullplate modeller som en proxy for å estimere karbonavgassing. Den andre metoden, og for første gang utviklet i denne avhandlingen, er basert på frekvensen av zirkon-aldre fra konvergerende marginer (gjenspeiler subduksjon langs kontinentalmarginer) som ble skalert og normalisert fra estimert subduksjonsfluks for de siste 410 millioner år. Denne metoden kan brukes i mye dypere tider, kanskje over milliarder av år. Bruken av zirkon-frekvens som proxy for estimere karbonavgassing bringer Mesozoiske modellestimater i bedre samsvar med CO_2-proxy-verdier.

Parallelt, gjennom konstruksjon av kontinentale flomkart for de siste 520 millioner år, har vi estimert eksponert landareal i forhold til dagen nivå og andelen av landareal som har gjennomgått silikatforvitring. Sistnevnte er basert på andelen av eksponert land innenfor tropene (±10°) pluss de nordlige/sørlige våtbeltene (40-50°N/S) som i dag er de viktigste områdene for silikatforvitring. Vi har også forbedret disse land-anslagene og potensiell forvitring ved å

undersøke fordelingen av klimasensitive indikatorer. Vi deretter brukte disse nye estimatene for forvitringspotensiale til å forbedre våre langsiktige karbonmodeller.

Videre brukte vi en klima-karbonsyklus jordsystemmodell med forbedrede kontinentale rekonstruksjoner og nye estimater for avgassing for å simulere og forstå den globale avkjølingen gjennom Ordovicium. Vi undersøkte de respektive rollene til paleogeografi og avgassing separat. Basert på våre eksperimenter kan høye temperaturer i tidlig Ordovicium oppnås innenfor feilmarginene, men vi kan ikke forklare den intense avkjølingen over midtre til sen Ordovicium, selv med at en progressiv økning av jordoverflatens forvitringspotensiale tas i betraktning. Ved å bruke GEOCLIM i en invers modelleringstilnærming, ble den teoretiske avgassingen som er nødvendig for å oppnå estimerte proxy temperaturer for tidlig Ordovicium beregnet og estimert til tre-til-fem ganger høyere enn moderne estimater. Videre, for å simulere den påfølgende Ordoviciske avkjøling trenden, må avgassingen reduseres til dagens verdier over kun 30 millioner år. Vi konkluderer med at hvis vi aksepterer høye temperaturene i tidlig Ordovicium, må alternative avgassingskilder, men også kilder for å redusere atmosfærisk karbon vurderes for å forklare avkjølingen over denne perioden.

Avslutningsvis brukte vi våre nye kart for eksponerte landområder til å estimere globale flomkart og vi utviklet en ny global havnivåkurve for de siste 520 Myr ved hjelp av den hypsometriske metoden. Vi testet også påvirkningen av estimerte havnivå ved å endre hypsometriske parametere i forbindelse med dannelsen av superkontinent Pangea. Vi identifiserte en førsteordens "superkontinent" syklus på 250 millioner år, men også andreordens sykluser på 20 og 40 millioner år, som tidligere er antatt uoppdagelig ved bruk av paleogeografiske metoder. Vår nye globale havnivåkurve har store likheter med stratigrafiskbaserte kurver og korrelerer med noen havbunnsproduksjons proxies gjennom Fanerozoikum.

Scientific outputs

First author papers:

Marcilly, C. M et al. (2022). Understanding the early Paleozoic carbon cycle balance and climate change from modelling. Earth and Planetary Science Letters, 594, 117717.

Marcilly, C. M et al. (2022). Global Phanerozoic sea levels from paleogeographic flooding maps. Gondwana Research, 110, 128-142.

Marcilly, C. M. et al. (2021). New paleogeographic and degassing parameters for long-term carbon cycle models. Gondwana Research, 97, 176-203.

First author conference proceedings:

Marcilly, C. M., Maffre, P., Le Hir, G., Pohl, A., Fluteau, F., Goddéris, Y., Donnadieu, Y., Heimdal, T.H., Torsvik, T.H. (2022, July). New constraints on early Paleozoic carbon cycle balance and climate change from modelling. Hybrid Goldschmidt. Poster and flash talk.

Marcilly, C. M., Torsvik, T. H., Domeier, M., & Royer, D. L. (2021, April). Revising key parameters for long-term carbon cycle models. EGU General Assembly Conference Abstracts (pp. EGU21-2794).

Marcilly, C. M., Torsvik, T. H. (2021, January). Refining key parameters for long-term carbon cycle models. Nordic winter meeting, Online.

Marcilly, C. M., Torsvik, T. H. (2020, June). The impact of paleogeography on long-term CO_2 models. Virtual Goldschmidt.

Marcilly, C. M., Torsvik, T. H. (2020, January). Improving long-term CO_2 models for the Phanerozoic: What can be done? Nordic winter meeting, Oslo

Outreach: CEED blog post

Global sea level in deep time: https://www.mn.uio.no/ceed/english/about/blog/2022/global-sea-level-in-deep-time.html

Investigating the causes of the Ordovician cooling: https://www.mn.uio.no/ceed/english/about/blog/2022/causes-of-the-ordovician-cooling.html

Table of contents

PART I : Introduction

1. Motivation and approach

Constraining the processes acting on the Earth's climate is crucial not only to understand our planet's past, and how it has recovered from intense changes, but also to the challenges ahead, which may affect our planet on geological timescales. To fully understand the long-term consequences of the current carbon emissions, we need to look back in time. Indeed, May 2022 marked the passage of the atmospheric CO_2 to 420 parts per million (ppm), 50% greater than the pre-industrial values (280 ppm). This CO_2 level has not been recorded on Earth for the past three Myrs and projections show that we are likely to reach or surpass the 500 ppm mark by the middle of this century (Tierney et al., 2020). The Earth has not experienced those values for tens of millions of years (Cui et al. 2020). The Earth went through and recovered from intense climate changes and crises throughout the past four billion years of uninterrupted life on Earth. Investigating the forcings responsible for triggering the changes and recovering from them will help us understand the current climate change and teach us how climate systems work at high atmospheric CO_2 concentrations. Moreover, it is well established that higher CO_2 levels in the atmosphere lead to higher temperatures (Bonan, 2015) and the current rise in temperatures is leading our planet towards major tipping points (Lenton, 2013, Lenton & Williams, 2013). Therefore, identifying how tipping points were triggered in the past, and how our planet subsequently adapted, is of prime importance to assess the next states that some components of the planet might face in the next millions of years to come.

This study aims to explore the effects of plate tectonics and paleogeography on climatic evolution throughout the Phanerozoic and over different timescales. With models, this study aims to bridge different parts of the Earth system by linking plate tectonics, paleogeography, and the carbon cycle. The project is separated into three sections. The first part assesses the global effect on CO_2 levels of changing solid Earth degassing and land availability through continental drift over the Phanerozoic. This was achieved using the simple box model GEOCARBSULFvolc (Fig. 1 & **article 1**). The second part assesses the role of those forcings on a smaller timescale (over 70 Myrs) and linked it to an intense change in the Earth's climate. For this part, we used the GEOCLIM model to understand the role of plate tectonics during the Ordovician, which culminated with the end-Ordovician Hirnantian Glaciation (Fig. 1 & **article 3**).

Each part of this project uses exposed land maps that were developed over the Phanerozoic. Those maps were then translated into estimations of land availability in areas of potential high weathering activity in **article 1** and used as base input in **article 3**. Additionally, this exercise allowed us, **in article 2**, to develop global flooding estimates for the Phanerozoic and constrain the hypsometric method for calculating sea levels in deep time. Global sea level plays an important role in modern climatic and oceanographic models. In this way, improving our understanding of global sea level in deep time may allow us, to not only understand Earth's paleoclimates, but also predict future climatological and sea level changes.

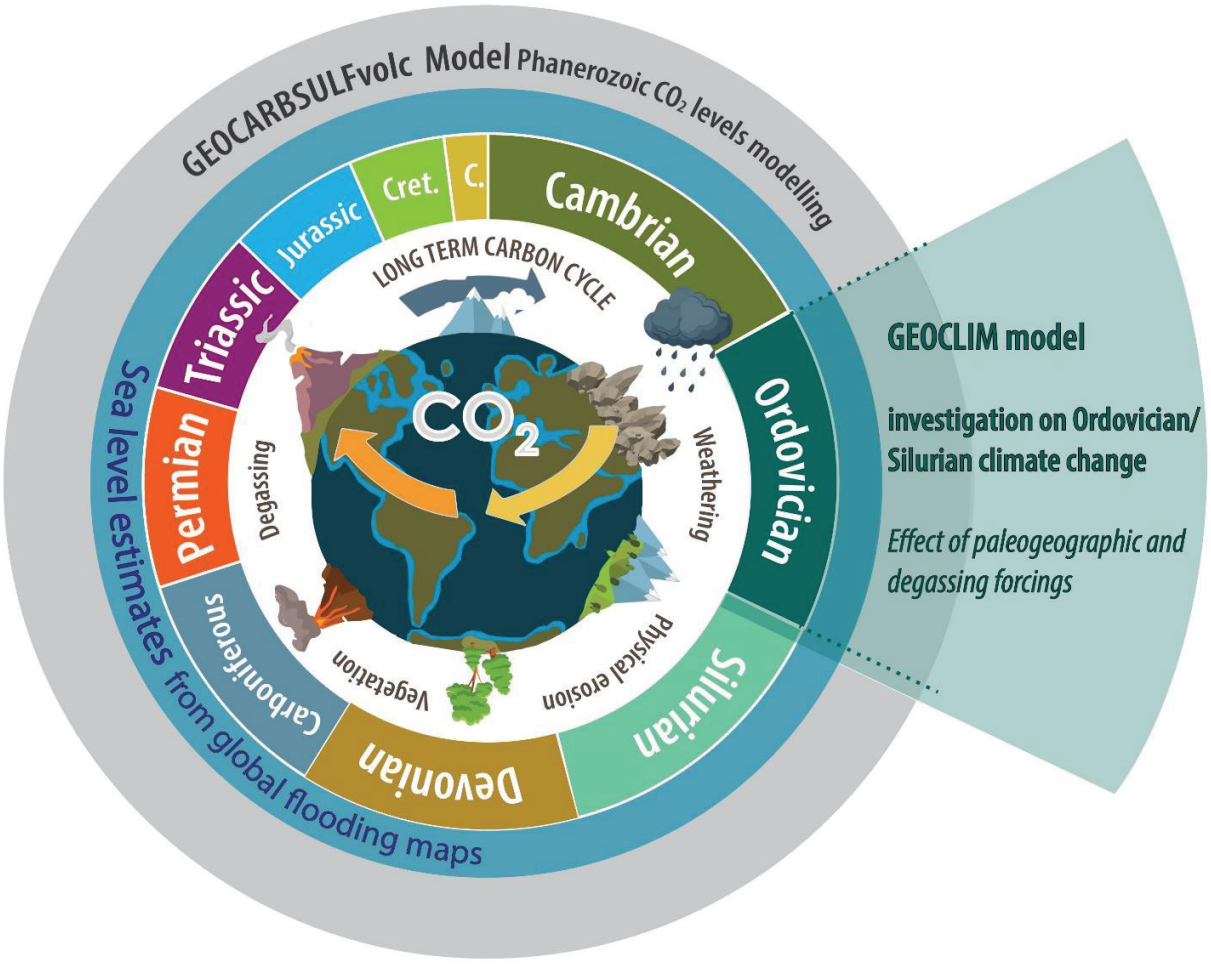

Figure 1: Schematic summary illustration of the project, including a short description of each part.

2. Scientific background

2.1 Climate drivers over time

Changes in the climate and environment are driven by multiple sources, operating on many timescales (Fig. 2), from slow changes in the Sun's strength, which eventually will make our planet inhabitable, to instantaneous processes (impacts). Climate changes therefore occur on many different timescales, from billions of years to hours, and played a central role in the formation, evolution, and extinction of life on our planet. Computer models have been developed independently to assess the effect of the different Earth processes affecting the climate through atmospheric CO_2 concentrations also called pCO_2. Here, we discuss the importance of some parameters for long-term carbon models and climate changes over timescales larger than one Myr as many models run with a time step of 10 Myr.

2.1.1 Climate drivers over billions of years

On billion-year timescales, climate changes are largely governed by the variation in the solar luminosity, the composition of the atmosphere, the radiogenic heat flow and the Earth's rotation rate (changes in the length of the day), which is related to the distance between the Earth and our moon. These forcings are too slow to cause recordable changes in the short-term climate but crucial for the long-term climatic evolution of our planet (Fig. 2)

The Earth-Sun distance and the present inventory of atmospheric greenhouse gases make the current surface temperatures optimal for complex life. However, the Sun is estimated to have been ~25% weaker than present-day during planetary formation (Sagan & Mullen, 1972; Ribas, 2009). The solar insolation was therefore weaker, and the early Earth was not at an ideal distance from the Sun, resulting in a cooler Earth that was essentially frozen for the first 50% of its existence. However, geological evidence suggests that the Archean climate (4–2.5 Ga) was warm enough to sustain liquid oceans and primitive life in the form of prokaryotic microbes (e.g., Kasting, 1989). This mismatch between a cool climate and evidence of liquid water is known as the "faint young sun paradox" (Sagan and Mullen, 1972). The subsequent increase in sun activity with time is included in most new versions of long-term carbon models as it influences the calculation of temperature through time (Berner, 2006; Lenton et al., 2018; Donnadieu et al., 2006).

The weak solar insolation during the Archean was probably compensated by magma oceans and early volcanic degassing that led to an early Earth atmosphere dominated by greenhouse gases [NH_3, CO_2, CH_4, H2O and carbonyl sulfide (OCS)] (Catling & Zahnle, 2020; Ueno et al., 2009; Sagan & Chyba, 1997). These gases formed a significant proportion of the Archean atmosphere, after H_2, as the oxygen levels were very low or non-existent before the great oxidation event at 2.4 Ga (Bekker et al. 2004), although the first rise of oxygen, produced by cyanobacteria (the inventors of oxygenic photosynthesis), is by some reconstructed from about 2.8 Ga (Olson, 2006).

Another hypothesis is that a higher radiogenic heat flux compensated the low solar insolation. The heat flow from the Earth's interior derives primarily from two major factors: energy from planetary accretion and differentiation but also radiogenic heat from the decay of long-lives radionuclides (i.e., ^{40}K, ^{232}Th, $^{235,238}U$). Even if primordial energy from secular cooling lead to a significant portion of the planet's current global heat loss, geochemical and geophysical models highlight the role of radioactive isotopes in powering mantle convection. Indeed, this flux could have generated more than five times the energy produced today (Arevalo et al., 2009). A third hypothesis exterior to the Earth system was proposed by Arbab (2009) analyzing the rotation rate of the Earth. In the early Archean when the Earth-Moon distance was much smaller, a day may have lasted just a few hours as the rotation was faster. This rapid rotation would have increased the Coriolis effect, which has been shown in models to increase the pole to equator temperature gradient by narrowing the Hadley cells and thereby decreasing albedo due to cloud cover (Way et al., 2018; Jansen et al., 2019). Earth is in fact the only terrestrial planet with a large natural satellite (stabilizing its rotation and axis tilt), and as the Moon is slowly moving away, the effect of a slower spinning Earth includes a widening of the tropics, and a change in the climate gradients. Yet another hypothesis is that fewer continents decreased the albedo and early Earth might essentially have been a water planet.

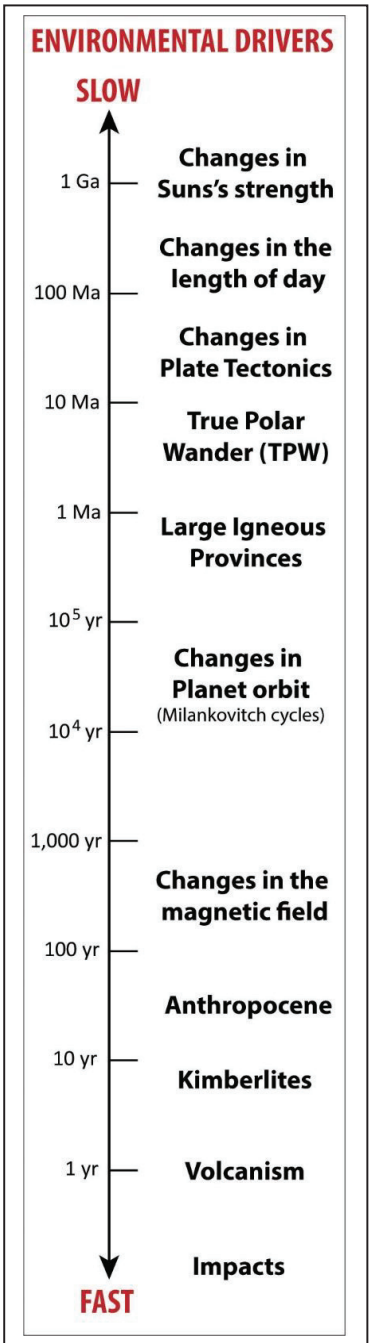

Figure 2: Some environmental and climatic drivers with their timescale of action from fast to slow processes.

2.1.2 Climate drivers over geological timescales: long-term carbon cycle

The Earth system on million-year timescales is at the heart of this study as long-term carbon cycle models run on time steps greater than 1 Myr and, more generally,>10 Myrs. However, processes on longer timescales, as mentioned earlier, also apply to those models. On geological timescales, the climate is mostly regulated by the long-term carbon cycle, also called geological carbon cycle, through the balance between its sources and sinks. This cycle involves the exchange of carbon between rocks and the Earth's surface (Kasting, 1989) (Fig. 3a). It is tied to plate tectonics, which regulates interior temperatures but also, by extension, atmospheric greenhouse gas concentrations and surface temperatures.

Subduction enables the recycling of volatile elements between the surface and the mantle and probably is essential for sustaining planetary habitability. Plate tectonics has not been identified on other terrestrial planets where cooling largely occurs by conduction through a stagnant lid. Estimates for *when* plate tectonics started range from the Hadean (>4 Ga) to 700 Ma and depend on *how* plate tectonics is defined (Korenaga, 2013; Stern, 2018 and references therein). Knowing the tectonic regimes of the deep time is essential to reconstructing past climates, as solid Earth outgassing is considered proportional to the amount of seafloor production (Berner, 2004).

The Phanerozoic Earth was generally characterized by greenhouse conditions with high predicted pCO_2 levels, interrupted by three main periods of icehouse conditions (Fig. 3b): the End-Ordovician (Hirnantian ~445 Ma), Late Paleozoic (330-260 Ma), and the second half of the Cenozoic (34 Ma to present). Low atmospheric CO_2 is a principal factor in controlling continental-scale glaciations (Royer, 2006), but the short-lived Hirnantian cooling event and apparent association with high modeled atmospheric CO_2 (Fig. 3b) levels in some carbon-cycle models may appear contradictory. However, proxies for past CO_2 concentrations have high uncertainties and are mostly limited to Devonian and younger times; therefore the accuracy of long-term carbon models takes a central role in deeper time.

Over millions of years, carbon transfers to and from rocks may result in changes in atmospheric CO_2 that cannot be attained by short-term processes (Berner, 2004) because so much more carbon is stored in rocks compared to oceans, atmosphere, biosphere, and soils combined (Table 1).

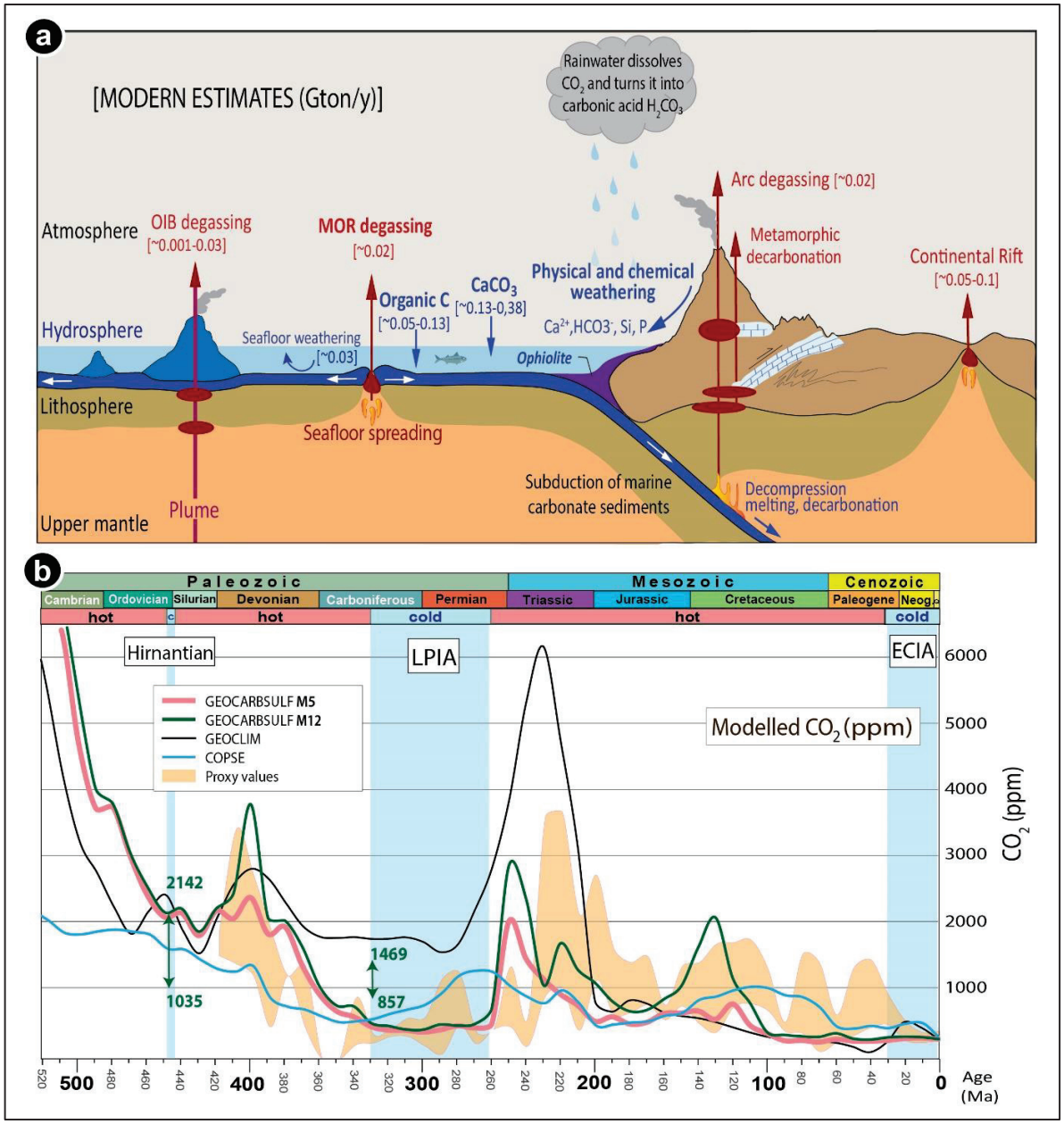

Figure 3: (a) Simplified long-term carbon cycle with depicted main sources and sinks as well as the corresponding fluxes in Gton carbon per year. Those estimates are taken from Lee et al. (2020). **(b)** CO_2 simulations with GEOCARBSULFvolc using revised paleogeography weathering parameters (with correction for aridity) and arc activity (zircons) as a proxy for degassing (Model **M5**: pink thick curve) and with weatherability only at ±10° and hybrid proxy for degassing (Model M12: green curve). GEOCLIM (GEOCLIMTec in Goddéris & Donnadieu., 2019; Goddéris et al., 2014), and COPSE (Mills et al., 2019) are also plotted against CO_2 proxy values from Foster et al. (2017) with 95% standard deviation confidence envelopes for each 10 Myrs interval. The green arrows with numbers at the onset of the Hirnantian and Late Paleozoic Ice Age are estimated CO_2 thresholds to initiate continental-scale glaciations with a fainter sun back in time and assuming a modern threshold of 500 ppm for recent times (Royer, 2006), and considering temperature changes due to luminosity only. High and low numbers assume a climate sensitivity of 3°C and 6°C per doubling of CO_2.respectively Simulated CO_2 levels for the Cambrian-Early Ordovician exit the scale of the diagram (levels reaching above 6000 ppm) but can be found in Tables S2 and S3 of the supplementary data 2 of Marcilly et al. (2021). The main glaciations of the Phanerozoic are shown as blue zones.

As an example, burning all terrestrial life and equilibrating the resulting CO_2 with the oceans would result in less than a 25% increase from the present-day level (Berner, 1989) whereas changes in the long-term carbon cycle likely resulted in increases of more than ten times present-day levels (Crowley and Berner, 2001).

The long-term carbon cycle (Fig. 3a) describes the exchange of carbon between rocks and the surficial system, which consists of the ocean, atmosphere, biosphere, and soils. The long-term carbon cycle is the main controller of the concentration of atmospheric CO_2 and (along with the sulfur cycle) atmospheric oxygen over geological timescales (Berner, 2004; Garrels et al., 1973; Holland, 1978). It can be represented by the generalized reactions below:

Silicate weathering

$$CaSiO_3 + H_2O + 2CO_2 \leftrightarrow Ca^{2+} + 2HCO_3^- + SiO_2 \quad \text{(Eq. 1)}$$

Carbonate weathering

$$CaCO_3 + H_2O + CO_2 \leftrightarrow Ca^{2+} + 2HCO_3^- \quad \text{(Eq. 2)}$$

Photosynthesis and respiration

$$CO_2 + H_2O \leftrightarrow CH_2O + O_2 \quad \text{(Eq. 3)}$$

During the weathering of silicate rocks (Eq.1), two moles of CO_2 are removed from the atmosphere for each mole of $CaSiO_3$ weathered. This reaction supplies calcium and bicarbonate ions to the ocean (or freshwaters), where they precipitate as calcium carbonates ($CaCO_3$) in sediments. This reaction releases one mole of CO_2 and the other mole is buried as CaCO3, resulting in a long-term sink for carbon.

Once exposed on continents, carbonates may also weather (Eq.2) using one mole of CO_2 for each mole of CaCO3 weathered. Calcium and bicarbonate ions will also be supplied to the ocean and precipitated once more as carbonates using one mole of CO_2. Therefore, contrarily to silicate weathering, the weathering and deposition of carbonates result in a null cycle with no net effect on long-term atmospheric CO_2, as long as both processes remain balanced.

Equation (3) is a simplification of photosynthesis (left to right) trapping carbon in organic matter, and respiration (right to left) releasing CO_2 back to the surficial system. These reactions

are part of the organic sub-cycle of the long-term carbon cycle, where organic matter burial and weathering are involved as a secondary factor affecting atmospheric CO_2.

Table 1: The main reservoirs and flux of the short-term and long-term carbon cycles. Italic processes highlight fluxes and bold estimates represent outputs of carbon. Modified from Lee et al. (2020)

Part of the Earth system	Flux (Gton C/y)	Reservoir (Gton C)	
ATMOSPHERE		560	
Biosphere atmosphere exchange	60		
Surface Ocean –atmosphere exchange	70		
OCEANS		$3.7- 3.9 \times 10^4$	
Marine sediments		3150	
Surface – deep ocean exchange	100		
Carbonate precipitation (silicate weathering)	0.13 – 0.38		
Oceanic crust weathering (seafloor)	0.03		
TERRESTRIAL BIOSPHERE AND SOILS		$2 - 2.3 \times 10^3$	
Organic carbon burial	0.05 – 0.13		
Carbonate weathering	**0.22 – 0.25**		
Organic carbon weathering	**0.0043 – 0.050**		
Metamorphic degassing	**0.036 – 0.200**		
CRUST AND MANTLE			
Continental crust		$4.2 \times 10^7 – 2.6 \times 10^8$	
Continental lithospheric mantle		$< 4.8 \times 10^7$	
Oceanic crust and lithospheric mantle		1.4×10^7	
Mantle degassing (total)	**0.036 – 0.200**		
MOR	0.0158 – 0.0163		
Ocean islands	0.001 – 0.030		
Arcs	0.018 – 0.147		
Modern continental rift	0.05 – 0.10		

Main carbon sources

The long-term climate is largely controlled by plate tectonics, and the most important regions of magmatic-related degassing (*sourcing*) are mid-ocean ridges, island arcs, continental arcs and continental rifts (Fig. 3a). The global inputs from these *non-plume* carbon sources today is at least ~0.5 Gt/yr, which is about 50 times less than anthropogenic CO_2 emissions from fossil fuels and cement production (Lee et al., 2020). Continental arcs due to their magmatic interaction with ancient crustal carbonates stored in continents may at times emit more CO_2 than island arcs, hence their distribution through time may lead to an increase in global volcanic fluxes for some periods (Lee et al., 2020). Metamorphic decarbonation does not only happen over continental extension zones and is actually more prevalent over subduction and continental collision zones. However, reconstructing estimates of metamorphic CO_2 over the Phanerozoic is extremely complicated as

metamorphic degassing is diffuse and spatio-temporally heterogeneous (Lee et al. 2020). Non-plume magmatic-related degassing is probably today at one of the lowest Phanerozoic levels, but probably varied significantly in the past due to changes in (e.g.) seafloor production and variations in metamorphic decarbonation (e.g., in continental arcs). Intra-plate volcanic degassing is also low today, but in the past, the largest Large Igneous Provinces (LIP) eruptions may have generated 100,000 Gt of carbon emitted over timescales of 10^2–10^5 years, whereas large kimberlite clusters may have emitted 1000 Gt of carbon over just a few years (Torsvik et al., 2021).

Weathering of ancient carbonates and organic carbon represents another large input of carbon in the system (Table 1). The reaction involves the dissolution of carbonates or oxidation of organic carbon. However, over timescales longer than 10 kyrs, the dissolution and precipitation of carbonates balance each other and so do the oxidation versus burial of organic carbon. Therefore, those processes are thought to have a negligible influence over long timescales (Berner, 2004).

Main carbon sinks

Atmospheric CO_2 reacts with water to form carbonic acid but is also taken up by plants during photosynthesis (Eq. 1, 2). Organic matter then builds up in soils, and during sedimentary burial, part of the organic carbon is taken out of the system and represents a long-term carbon sink. The carbon isotopic composition of seawater and abundance of organic matter in sedimentary rocks can be used to calculate burial rates. According to both methods, organic burial increased during the Carboniferous and Permian due mainly to the growth of large land plants containing microbial-resistant lignin and coastal lowlands conducive to coal basin formation (Berner, 2004).

The microbial decomposition of organic matter also generates organic acid. These organic acids and carbonic acid react with minerals in rocks to liberate cations and acid anions. The organic acid anions are then oxidized into bicarbonate. The dissolved species are carried out of the system by groundwater and rivers toward basins. In the oceanic basins, Ca^{2+} and HCO_3^- are precipitated as calcium carbonate and the silicic acid as biogenic silica, and later buried in sediments as depicted by equation (1).

Over multimillion-year timescales, only Ca and Mg silicate weathering has a direct and significant effect on CO_2 making it an important feedback regulating the Earth's climate over time (Berner, 2004). However, its strength as a climate forcing feedback mechanism and its evolution during land surface reorganizations is debated. One long-standing hypothesis is that increases in CO_2 emissions via solid Earth outgassing cause a rise in surface temperature due to the greenhouse effect, enhancing silicate weathering through warmer conditions and amplifying the hydrological cycle, thus leading to an increased drawdown of atmospheric CO_2 (Fig. 4) (Walker et al., 1981; Berner & Caldeira, 1997). The dependency of silicate weathering on temperature has been observed in many laboratory-based experiments and field studies (Brantley & Chen, 1995; West, 2012; Velbel, 1993a,b; Li et al., 2016). However, those studies lack perspectives in terms of large spatial and temporal scales due to the covariation of other factors with temperature (Deng et al., 2022). In a study, Deng et al. (2022) demonstrated the primary control of temperature on silicate weathering while controls of precipitation or topographic-lithological factors were identified as regional and subordinate based on an abundant modern dataset covering a large environmental gradient (Fig. 5).

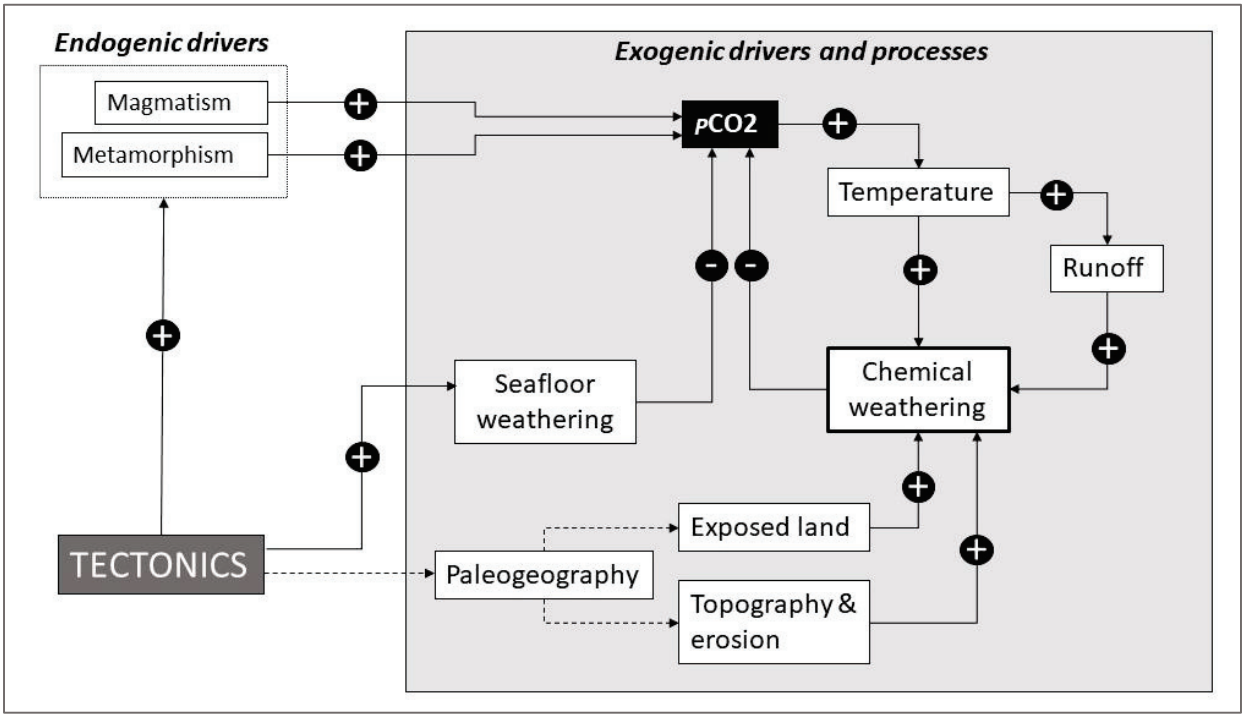

Figure 4: Feedback loops describing the silicate weathering feedback on the exogenic carbon system (i.e. occurring at the Earth's surface). Full arrows indicate transfer function while stippled arrows indicates a direct influence but not directly correlated. Positive and negative symbols represent positive and negative feedbacks, respectively. Modified from Lee et al (2020).

Many studies consider other forcing mechanisms on the climate-weathering feedback to be essential such as hydrologic regulation (Maher & Chamberlain, 2014), tectonic uplift, and related physical erosion (Raymo & Ruddiman, 1992). But due to the lack of robustness in the weathering proxy records through time, the validation of these hypotheses remains challenging (Deng et al., 2022).

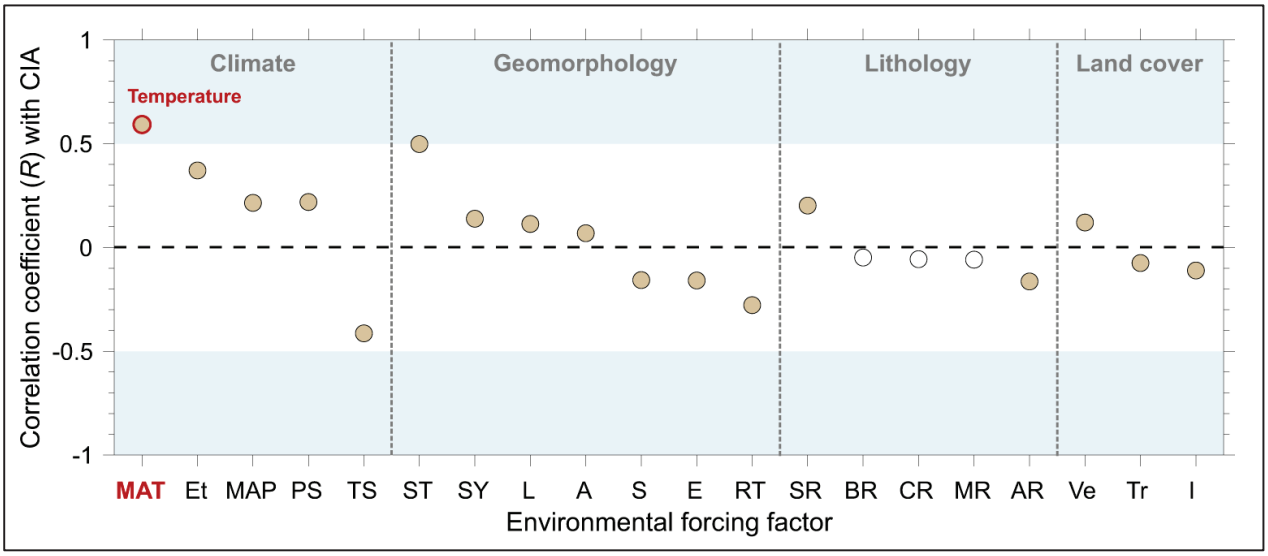

Figure 5*:* Correlation between weathering and environmental forcing factors (after Deng et al. 2022). Correlations with p value of >0.001 are shown as white symbols. The order of forcing factors in each category is sorted by correlation coefficient with CIA. Negative values mean a negative correlation. Most of |R| are lower than 0.5, indicating a subordinate control of these factors on weathering intensity over a global scale. Mean annual temperature (MAT) is the only factor with |R | of >0.5. Climatic metric: MAT-mean annual temperature (°C), Et-actual evapotranspiration (m/yr), MAP-mean annual precipitation (m/yr), PS-precipitation seasonality (coefficient of variation, %), TS-temperature seasonality (standard deviation, °C); geomorphic metric: ST-upland hillslope soil thickness (m), SY-modeled sediment yield (t/km^2/yr) using BQART model29, L-flow length (km), A-drainage area (km^2), S-mean local slope (°), E-mean elevation (m), RT-upland hillslope regolith thickness (m); lithological metric: SR-clastic sedimentary rock area (%), BR-basic rock area (%), CR-carbonate rock area (%), MR-metamorphic rock area (%), AR-acidic-intermediate rock area (%); land cover metric: Ve-vegetation cover area (%), Tr-tree cover area (%), I-ice and snow cover area (%).

2.2 Carbon cycle modelling

2.2.1 Carbon cycle models

Models for the long-term carbon cycle aim to capture the various forces (sources and sinks) to predict past variations in atmospheric CO_2 (e.g., Berner, 2004; 2006; Royer, 2006; Royer et al. 2014; Goddéris et al., 2012; van der Meer et al. 2014; Mills et al., 2014; 2019, 2021; Lenton et al. 2018).

Models for the long-term carbon cycle compute both atmospheric CO_2 and O_2 as the processes affecting their levels are coupled. Currently, the most widely used models are non-dimensional box models meaning that at the global level, each process and reservoir is represented by a single variable. These models are therefore limited by their ability to represent surface properties such as temperature, runoff, and erosion as a single value at a global scale. However, those models have the advantage of being able to run over Phanerozoic timescales, as they do not rely on spatially resolved 3D Earth system models to simulate surface properties. Indeed, due to their complexity, 3D models cannot be run over such timescales, even at low resolution (Mills et al., 2021).

Two main types of box models for the long-term carbon cycle have been developed to simulate fluctuations of CO_2 through geologic time. They use proxies and implement the processes linked to the emission and uptake of carbon in an inverse and forward way (Fig. 6, Royer et al., 2014). Inverse models such as GEOCARBSULF are data-driven and parametrized by isotopic data (Fig. 6a). For example, $\delta^{13}C$, $\delta^{34}S$, or $^{87}Sr/^{86}Sr$ proxy records and associated assumptions are integrated to model how they are related to key processes for CO_2 – O_2 sources and sinks (Lenton et al., 2018; Berner, 2004). Forward models, such as COPSE (Fig. 6b), aim to predict the isotopic records for comparison to data (Lenton et al., 2018). This approach produces quantitative models independent of proxy data constraints. The GEOCARBSULF (inverse) and COPSE (forward) models incorporate similar forcings under different parameters affecting the reservoirs of CO_2 (ocean, atmosphere, soil, and biota). Both model types assume that the total degassing is compensated in the long-term by the total weathering. However, the different methods to estimate this total degassing are numerous and give very different flux estimates (Fig. 7). Consequently, the models show very different CO_2 levels over the Phanerozoic and generally calculate lower CO_2 values compared to the ones constructed from proxies for most of the Mesozoic and Cenozoic (Fig.3b).

Other models such as GEOCLIM (Goddéris et al., 2012, 2014) or SCION (Mills et al., 2021) integrate spatially resolved Earth system models with box models. The GEOCLIM model uses General Circulation Model (GCM) simulations to inform its biogeochemical model (i.e., COMBINE) about the surface processes (Fig. 6b). After the box model calculates the CO_2 concentration, it interpolates between GCM runs to determine an approximate grid of continental runoff and surface temperature to calculate terrestrial weathering. The main limitation of GEOCLIM is that it produces only steady-

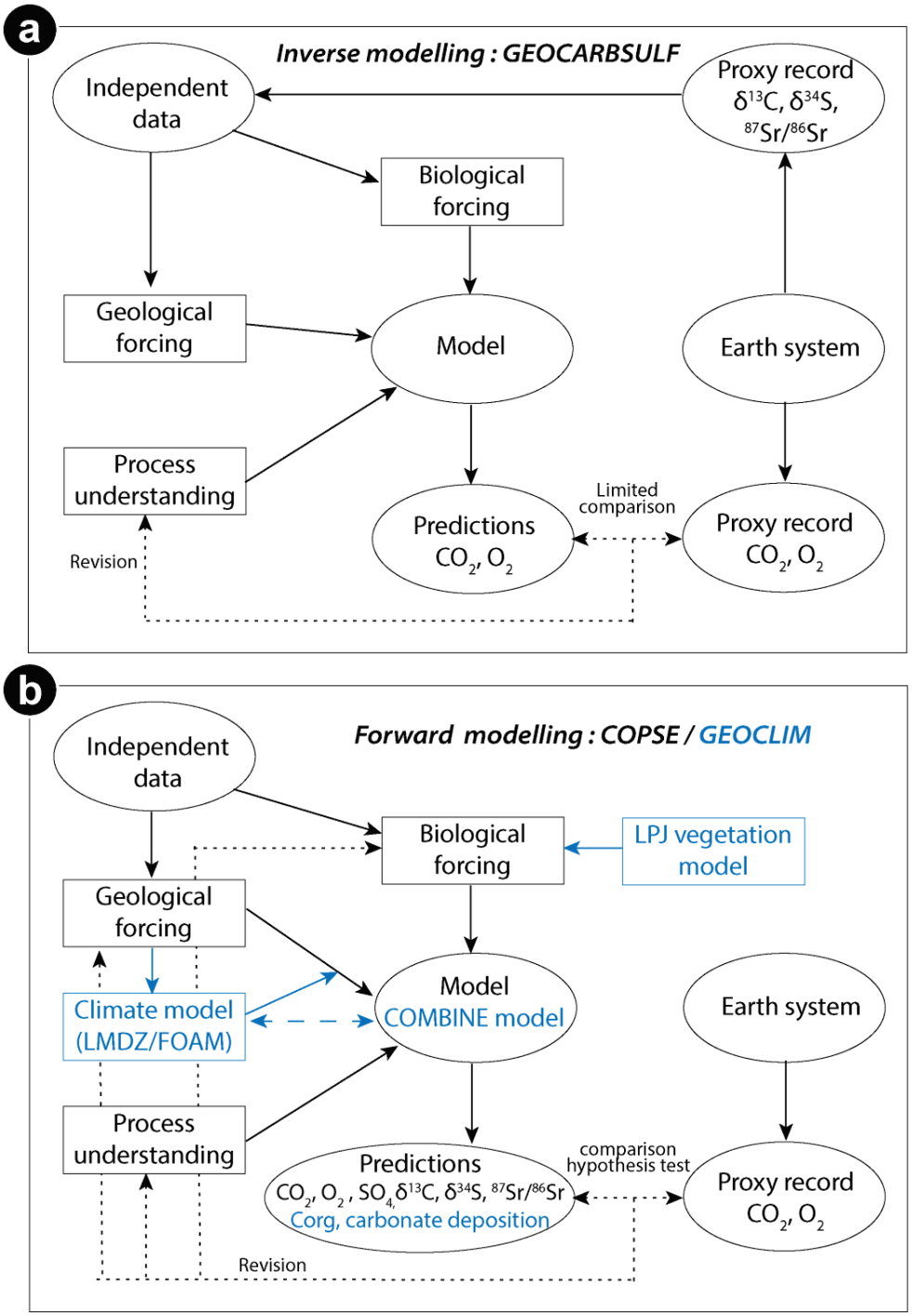

Figure 6: Different approaches to model Phanerozoic biogeochemical cycling: **(a)** inverse modelling approach as GEOCARBSULF **(b)** forward modelling approach as COPSE. GEOCLIM is closer to COPSE in its development but with slight additions indicated in blue. Indeed GEOCLIM work as three boxes (here in blue) linked to each other: the vegetation model LPJ, climate model either LMDZ or FOAM and carbon model COMBINE. Modified from Lenton et al. (2018).

state snapshots of the Earth system. This is the main difference with the newly developed SCION model, since this model links the spatial climate modelling procedures of GEOCLIM with long-term biogeochemical processes of COPSE and can produce continuous predictions for 540 Myrs.

2.2.2 Modelling of the solid Earth degassing

In many carbon models, such as the ones used here (GEOCARBSULF and GEOCLIM), changes in rates of volcanic and metamorphic global degassing are assumed to be directly proportional to rates of seafloor creation, a.k.a. seafloor spreading or production (Fig. 7). All degassing except hotspot degassing is assumed to be driven by fluctuations in seafloor production rates. Such degassing is often referred to as solid Earth degassing. However, the quantification of solid Earth degassing rates excludes intra-plate volcanism such as LIPs from the calculation, which potentially could have been massive during the Cretaceous. LIP degassing triggered by deep plumes could therefore have led to extra high CO_2 emissions, potentially explaining the Cretaceous warming (Larson, 1991; Kaiho & Saito; 1994, Tajika, 1998, 1999; Wallmann, 2001, Berner 2004).

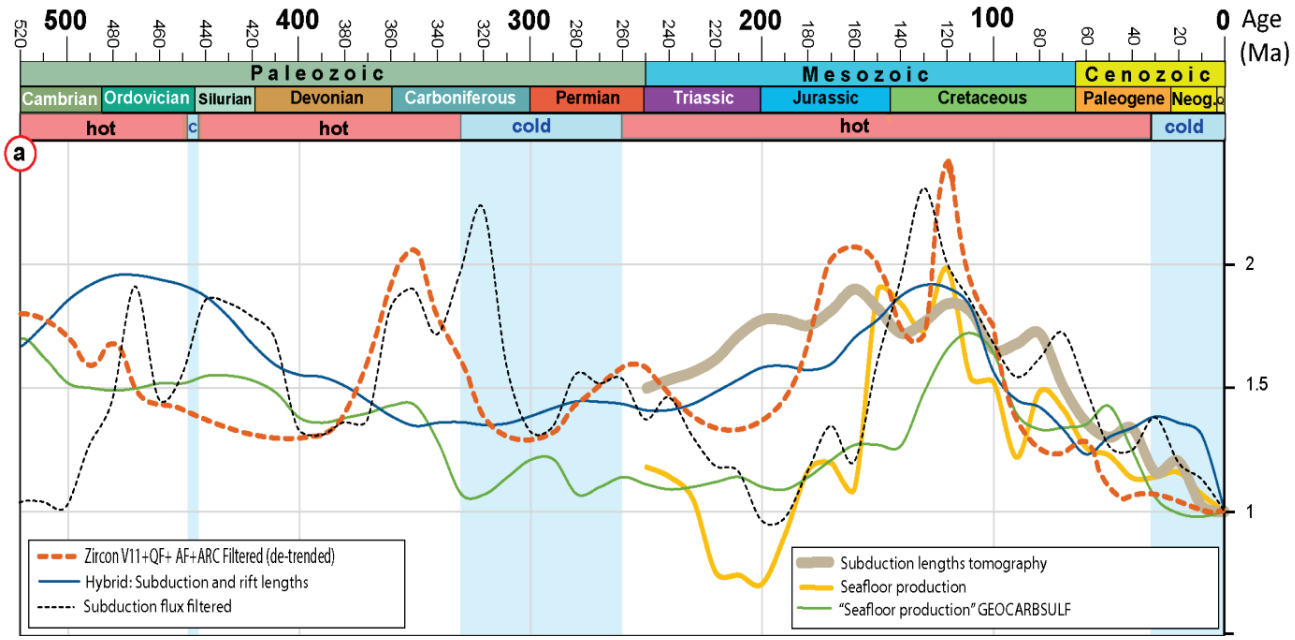

Figure 7: Solid Earth degassing reconstructions from different methods (from Marcilly et al., 2021, **Article 1**). The hybrid subduction fluxes-arc zircon curve developed in **article 1** is in orange. Only three other curves have been estimated for the entire Phanerozoic: the subduction fluxes from the full plate model of Merdith et al. (2021), the "seafloor production" curve of Berner (2004) from sea level inversion, which is the default f_{SR} in GEOCARBSULF and the hybrid curve of Mills et al. (2019) used in COPSE. The blue zones represent the main glaciations of the Phanerozoic.

The oldest *in-situ* seafloor is ~180 Ma. Before that time, direct measurements of seafloor production are severely limited and models must rely on indirect proxies. Many different techniques for estimating seafloor production have been developed over the past decades, such as inversion of sea level (Berner, 2004), subduction or continental rift lengths (van der Meer et al., 2014; Mills et al., 2014, Mills et al., 2019), or subduction fluxes (Coltice et al. 2013). However, most subduction fluxes are derived from full plate models holding large uncertainties before Pangea (Domeier & Torsvik, 2019; Merdith et al., 2021). Another promising proxy is the age-frequency relationship of detrital zircons that mostly track past continental arc systems since zircon-fertile rocks are primarily produced along continental subduction zones. Indeed, their production is argued to mimic true variations in the subduction flux, both regionally and globally (Domeier et al., 2018), and a link between plate tectonic degassing and greenhouse vs. icehouse climates has, e.g., been proposed by McKenzie et al. (2016).

Article 1, revising key parameters for long-term carbon models**,** describes and discusses the accuracy of the current proxies used for solid Earth degassing as well as their potential use in carbon models. This paper presents a new composite curve of degassing from subduction fluxes and, for the first time, a normalized proxy curve based on zircon age distributions. These proxies are then used in subsequent articles to highlight the role of seafloor production in changes in sea levels (**article 2**), and as a parameter in simulations to understand the role of the degassing forcing on the climate change of the Ordovician (**article 3**).

2.2.3 Modelling of silicate weathering

Most agree that minerals dissolve faster with high temperatures and runoff (e.g., Jenny, 1941; Berner, 2004). This is the base for the Earth thermostat theory of Walker et al. (1981), where changes in weathering rate induced by CO_2 level fluctuations serve as negative feedback for stabilizing global temperature.

Today's distribution of high runoff and high temperature are mostly located around the equator (±10°) but also within the northern and southern wet belts (±40-50 NS). However, it is widely accepted that climate gradients through geological times may have been very different from the present ones, and therefore their effects on weathering rate are even more difficult to identify. One solution is to rely on GCM simulations coupled to a carbon model such as in GEOCLIM (e.g.,

Godderis et al., 2012, 2014,2017; Donnadieu et al., 2006). However, this exercise is difficult to constrain due to extensive limitations:

Firstly, to run climatic simulations, the past distribution of not only continental units but also their exposed land through time must be known. Before Pangea, the error linked to paleogeography is increasingly more important as fewer-and-fewer fossil and paleoclimate indicators are available. We test the difference in the integration of climatic parameters between the model GEOCLIM using GCM simulations and the model GEOCARBSULF based on proxy data in **article 1** and in **article 3**.

Second, as runoff is dependent on topography, the maps used in the GCM need such metadata. Here as well, the topography is difficult to constrain through time, both in geographical location and in altitude as no real constraint between relief and sediment accumulation on a global scale can be drawn to this day.

The third limitation builds on this as it concerns the atmospheric circulation, which is also affected by topography on a smaller scale. Indeed, to model precipitation and runoff, the atmospheric currents need to be implanted in the models and are currently considered similar, or close to the modern ones, which most likely constitute a misrepresentation.

Other factors affect the rate of the weathering process. For example, land plants are well known to accelerate chemical weathering (Berner et al., 2003) as rootlets and their microflora symbionts secrete organic acids and chelates that attack primary minerals to reach nutrients such as Ca, K, and Mg. A study by Arthur and Fahey (1993) demonstrated that the presence of trees accelerates the weathering process by a factor of four in a granitic site in Colorado. However, it is often stated that plant roots protect the land from erosion and therefore could inhibit denudation and further weathering from supply-limited conditions. This is only true in lowland areas, in moderate slope areas plants hold soil against erosion and allow moisture to be absorbed more efficiently, which in turn enables the continued dissolution of primary minerals (Berner, 2004). This parameter is particularly important during the Devonian as the plant cover over the Earth spread worldwide and roots started to develop. Therefore, the evolution of plants through time is an important factor influencing weathering in the long-term carbon cycle models and needs to be considered (Berner, 2004, Lenton et al., 2016, 2018). In addition, physical erosion must be kept at a certain level to prevent regolith from developing and limiting weathering and CO_2 drawdown.

Consequently topography is also a factor of acceleration of weathering as it may bring or restrict fresh surfaces available from physical erosion.

The most important forcing on silicate weathering in long-term carbon cycle models is paleogeography, as the actual site where weathering occurs will depend on the local climate, itself dictated by climatic belts and plate tectonics. The size of a continent and its latitudinal location will define the runoff and temperature regimes. A simple argument, whereby a landmass is moved from the pole to the equator, illustrates how a modification in location can lead to a great difference in the rate of CO_2 uptake by silicate weathering through changes in temperature and runoff linked to the residency of climatic belts (Worsley and Kidder, 1991).

One approach to constrain climate change due to changing paleogeography is to assume that the present latitudinal climate zones existed in the past (Berner, 2004). We use this method in **article 1**. For this purpose, we created a set of exposed land maps from 520-70 Ma in 10 Myr increments (Marcilly et al., 2021). Two additional maps for 540 and 530 Ma have subsequently been constructed to complete the Phanerozoic (see appendix 1). These maps are associated with a specially developed *in-house* land tool in GPLATES, which extracts the land area over selected latitudes and translates it into parameters for the long-term carbon cycle model GEOCARBSULFvolc.

Other models such as GEOCLIM, and by extension GEOCARBSULFvolc as it uses GEOCLIM's paleogeography parameters in its default version, use GCMs to model the distribution of runoff and temperature that is later incorporated into the weathering model. This is the method we use in **article 3** when investigating the link between paleogeographic forcing and Ordovician climate change.

Lithology is also an important parameter when assessing the chemical weathering rate. Indeed, the dominant source of dissolved Ca and Mg during silicate weathering is Ca contained in plagioclase (Mackenzie and Garrels, 1966; Garrels, 1967), Mg from pyroxenes, amphiboles, and biotites, and both Ca and Mg in volcanic glass. Several studies reveal that basalt weathers much faster than granites or other acidic igneous or metamorphic rocks (Meybeck, 1987; Taylor and Lasaga, 1999; Dessert et al., 2003; Porder et al., 2007). This is the primary parameter in the study of MacDonald et al. (2019) in attempting to understand the Ordovician cooling. They argue for the existence of many volcanic arcs islands and obducted arcs as zones of 'fresh' basalt undergoing

intense physical erosion, leading to enhancement in weathering itself and resulting in a CO_2 drawdown. However, in **article 3**, we discuss the limitations of this hypothesis and illustrate with some simple model simulations.

Lastly, large igneous provinces (LIPs) can also influence the long-term carbon cycle (Jones et al., 2016). These large eruptions of continental basalt or basaltic oceanic plateaus might erupt in pulses over geologically short periods between 1-5 Myrs, but potentially can have a much longer lifespan up to 50 Myrs (e.g., Bryan and Ernst, 2008; Morgan, 1971; Ridley and Richards, 2010). LIPs have been linked to mass extinctions due to the release of greenhouse gases such as methane and CO_2 through magmatic degassing and volatile release during contact metamorphism (Svensen et al., 2004; Svensen et al., 2007, Wignall, 2001, Wignall et al., 2005; Heimdal et al., 2019, 2021).

The long-term climatic effect of LIPs is yet to be robustly defined. Johansson et al. (2018) argued for a strong long-term correlation between the weathering of certain LIPs (e.g., CAMP) and CO_2 proxies. This was questioned by Torsvik et al. (2021), and Mills et al. (2014) showed a rather small influence of the LIPs on the global weathering budget, except for the Ontong-Java Plateau, one of the largest oceanic LIPs that may have existed on Earth. Complementary to continental silicate weathering, seafloor weathering is considered an important negative feedback to increased pCO_2 (Mills et al., 2014; Krissansen-Totton & Catling, 2017) and could be significantly enhanced by the emplacement of oceanic LIPs. As there is no consensus on the rate of seafloor weathering over the Phanerozoic, the effect of those events on global atmospheric CO_2 levels is even harder to constrain. Seafloor weathering is integrated into several long-term carbon cycle models, e.g., GEOCARBSULF (Berner, 2004) or COPSE (Mills et al., 2014) and is directly linked to seafloor spreading activity.

Another parameter that is commonly not considered in long-term climate models and that could have a large impact on the silicate-weathering rate is true polar wander (TPW). TPW is the reorientation of the Earth to align its greatest non-hydrostatic principal axis of inertia with its spin axis, causing the geographic locations of the poles to change (Torsvik et al., 2012). It corresponds to the rotation of the entire solid silicate Earth (mantle and crust). This phenomenon will change the geography of continents with respect to climatic zones and may have had significant impacts on global climate and biological evolution (Evans, 2003). It mostly arises from the redistribution of density heterogeneities in the mantle (subduction) and the corresponding changes in the Earth's moment of inertia (Steinberger & Torsvik, 2008, Torsvik et al., 2012). During TPW, some areas

may change their latitude, whilst a location near the rotation axis (0ºN, 11ºE; Torsvik et al. 2012) does not move at all. Our reconstructions are based on paleomagnetic data that record both 'continental drift' and TPW, and thus the effects of TPW are accounted for in our models.

2.3 Modelling of global sea level

Eustatic (global) sea level changes can be quantified using stratigraphic methods and other paleoenvironmental indicators (e.g., Miller et al., 2005). Fossil corals provide high precision constraints for the past few million years and indicate rates of sea level rise as high as 40 mm/yr (Lambeck et al., 2014), an order of magnitude higher than Anthropocene-driven changes (~3 mm/yr). In deep time (i.e.,> 100 Ma), the number of methods that can be used to reconstruct sea level is limited. They are essentially restricted to methods associated with stratigraphy, which uses fossil markers and sedimentary facies changes to assess the position of the shoreline through time (e.g., Haq & Al-Qahtani, 2005; Haq & Schutter, 2008; Miller et al., 2005, Hardenbol et al., 1998) and plate tectonic reconstructions, which assess changes to the depth and the extent of ocean basins (e.g., Vérard et al., 2015; Conrad, 2013). However, plate tectonic methods require full-plate polygons with age estimates for the oceanic lithosphere that are mainly synthetic ("made up") before the Cretaceous.

Developing a set of maps of exposed land through the Phanerozoic allowed us to estimate the extent of flooded land through time. Measurements of global flooding represent averages across great continental extents, making them less sensitive than stratigraphic analyses to regional-scale vertical land motion, such as from dynamic topography, and hence more reliable for estimating eustatic sea level. This method can also help identify local deviations caused by regional uplift or subsidence and constrain geodynamic mechanisms for sea-level change. Our new sea-level reconstruction usefully tracks global variations in Phanerozoic eustatic sea level but also opens opportunities to estimate such variations in deeper time.

In **article 2**, we present those new estimates and redefine flooding under two terms: "modern land flooding" and "continental flooding" depending on the reference lower base for the calculation. We have now developed maps for 540 and 530 Ma and thus estimate flooding over the entire Phanerozoic (see appendix 2). By adapting the hypsometric method (Forney, 1975, Algeo & Wilkinson, 1991; van der Meer et al., 2017; Bond, 1979; Harrison, 1990) with new values for the hypsometric slope we calculated sea levels over the Phanerozoic (Fig. 8).

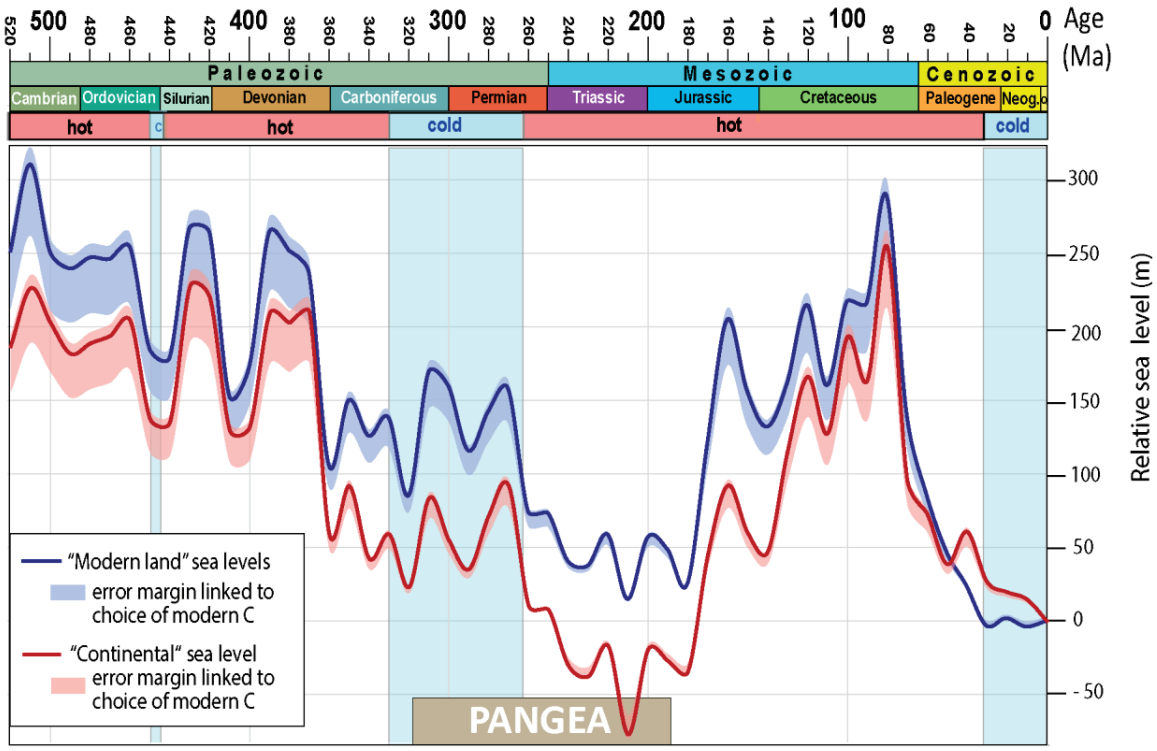

Figure 8: "Modern-land" and "continental" sea levels with error margins linked to the choice of modern day hypsometry from ETOPO1 (applying different corrections for "bed", "ice" in Amante & Eakins (2009) and an additional geoid correction (Vérard, 2017)). The blue zones represent the main glaciations of the Phanerozoic.

3. Summary of papers

3.1 Paper 1

The first paper is an invited paper published in the Elsevier journal *Gondwana Research* and is entitled **"New paleogeographic and degassing parameters for long term carbon cycle models"**. This paper reviews the current state of research on the two most important parameters of the long-term carbon cycle, paleogeographic forcing on silicate weathering and degassing forcing, and presents new estimates for the Phanerozoic. We revised the paleogeographic forcing by compiling new flooding maps for the past 520 Ma, estimated the exposed land area relative to the present-day (f_A), and the fraction of exposed land area undergoing silicate weathering (f_{AW}-f_A). The latter is based on the amount of exposed land within the tropics (±10°) plus the northern/southern wet belts (40-50 °N/S) relative to today, which are the prime regions for silicate weathering. We also estimated carbon degassing for the past 410 Myr using subduction flux from full-plate models as a proxy. For the first time, we then used the subduction flux to scale and normalize the arc-related zircon age distribution (arc-activity), allowing us to estimate carbon degassing in a much deeper time. The effect of these refined modelling parameters for weathering and degassing was then tested in the GEOCARBSULFvolc model, and the results were compared to other carbon models and CO_2 proxies.

3.2 Paper 2

The second paper published in the Elsevier journal *Gondwana Research* is entitled **"Global Phanerozoic sea levels from paleogeographic flooding maps".** In this study, we used the maps developed in the first paper associated with the hypsometric method to calculate sea levels from flooding estimates throughout the Phanerozoic. A first-order "supercontinent" cycle of 250 Myrs in sea level estimates was recognized but we also documented second-order cycles of 20 and 40 Myrs, which were previously thought to be undetectable using paleogeography. The hypsometric slope is critical for reconstructing past sea levels, and steepening the hypsometric slope during Pangea assembly requires dramatically larger sea-level fluctuations. Our new sea-level curve shares strong similarities with stratigraphic constraints and correlates with some seafloor production proxies throughout the Phanerozoic. By contrast, sea level curves based on reconstructions of past plate motions diverge from our curve, and each other, notably in the Paleozoic, and probably reflect large model uncertainty. Because measurements of global flooding

represent averages across great continental extents, they are less sensitive than stratigraphic analyses to regional-scale vertical land motion, such as from dynamic topography. Our new sea-level reconstruction thus usefully tracks global variations in Phanerozoic eustatic sea level. It can be used to identify local deviations caused by regional uplift or subsidence and constrain geodynamic mechanisms for sea-level change.

3.3 Paper 3

The third paper, published in the Elsevier journal *Earth and Planetary Science Letters*, is entitled **"Understanding the early Paleozoic carbon cycle balance and climate change from modelling".** There we present a new CO_2 and temperature simulations for the early Paleozoic using a spatially resolved climate-carbon cycle Earth system model, fed with refined continental reconstructions and new estimates of solid Earth degassing. Based on our simulations we show that, although early Ordovician high temperatures can be replicated within error margins, our new constraints cannot explain the intense cooling over the Mid to Late Ordovician, even if a progressive enhancement in Earth surface weatherability is taken into account. By using GEOCLIM in an inverse modelling approach, we then calculated that the theoretical degassing necessary to reach proxy-derived temperatures for the Early Ordovician is three-to-five times higher than modern values. Further, to simulate the following Ordovician cooling trend, the solid Earth degassing must be reduced to modern-day values in only 30 Myrs.

4. Discussion: Linking the research topics and results

The research behind the articles composing this thesis is built on each other and the base is presented in **article 1**. In this article, we introduce the land maps we built to constrain the amount of land potentially exposed to weathering. This was initiated after realizing that the long-term carbon models using both latitudinal and GCM-based distribution of land undergoing weathering tend to overestimate the amount of exposed land, mostly over South China. We therefore constructed a new set of paleo-maps integrating the latest constraints in terms of paleogeography of continents and terranes, lithofacies associated with specific climatic environments (e.g., tillites, coal, evaporites, bauxites), and paleobiology. The creation of these exposed land maps as opposed to continental contour maps, allowed us to estimate flooding through time. Therefore, in **article 2** we discuss the use and accuracy of global flooding maps to estimate sea level through time.

The heart of this thesis is about long-term carbon models and how paleogeography influences their simulations and by extension, how it may have affected past climates. To test this, we used the proportion of land under latitudes of high temperature and runoff in the maps to quantify the land parameters associated with GEOCARBSULFvolc. This study revealed that changes in land availability do not greatly affect CO_2 levels. However, after further refinements linked to aridity development during Pangea, we achieved promising results in improved proxy-model matches.

As highlighted in **article 1**, all major glaciations of the Phanerozoic tend to occur after an increase in land availability for weathering (Fig. 9), creating a drawdown in CO_2. This mechanism has been discussed as being a trigger mechanism for the Ordovician glaciation (e.g., Kump et al., 1999; Macdonald et al., 2019). To test this link, we pursued a focused study around the Hirnantian glaciation with new paleogeographic reconstructions over seven time slices **(article 3)**.

In **article 3**, the simulations are run in GEOCLIM, which uses a GCM that models the distribution of runoff and therefore aridity, but also by extension, silicate weathering. GCM simulations require the use of a supercomputer and consequently, simulating climatic components for the entire Phanerozoic would have been unrealistic to fit into the lifetime of this thesis. Therefore, we chose to study the highly debated and problematic climatic changes of the Ordovician.

Our hypothesis is built upon the work of Nardin et al. (2011) suggesting that increased weathering linked to paleogeographic distribution facilitated the onset of the Hirnantian glaciation. In our study, we used our new maps to test further this hypothesis, but instead found that paleogeography, through the given land availability to weathering, on its own imposes warming and that cooling is principally brought by changes in degassing. However, we also highlighted the limitations of the model and one of the main ones is the dependency of the model on topography to simulate runoff and by extension weathering. Topography is extremely difficult to constrain through time, both in terms of geography and altitude.

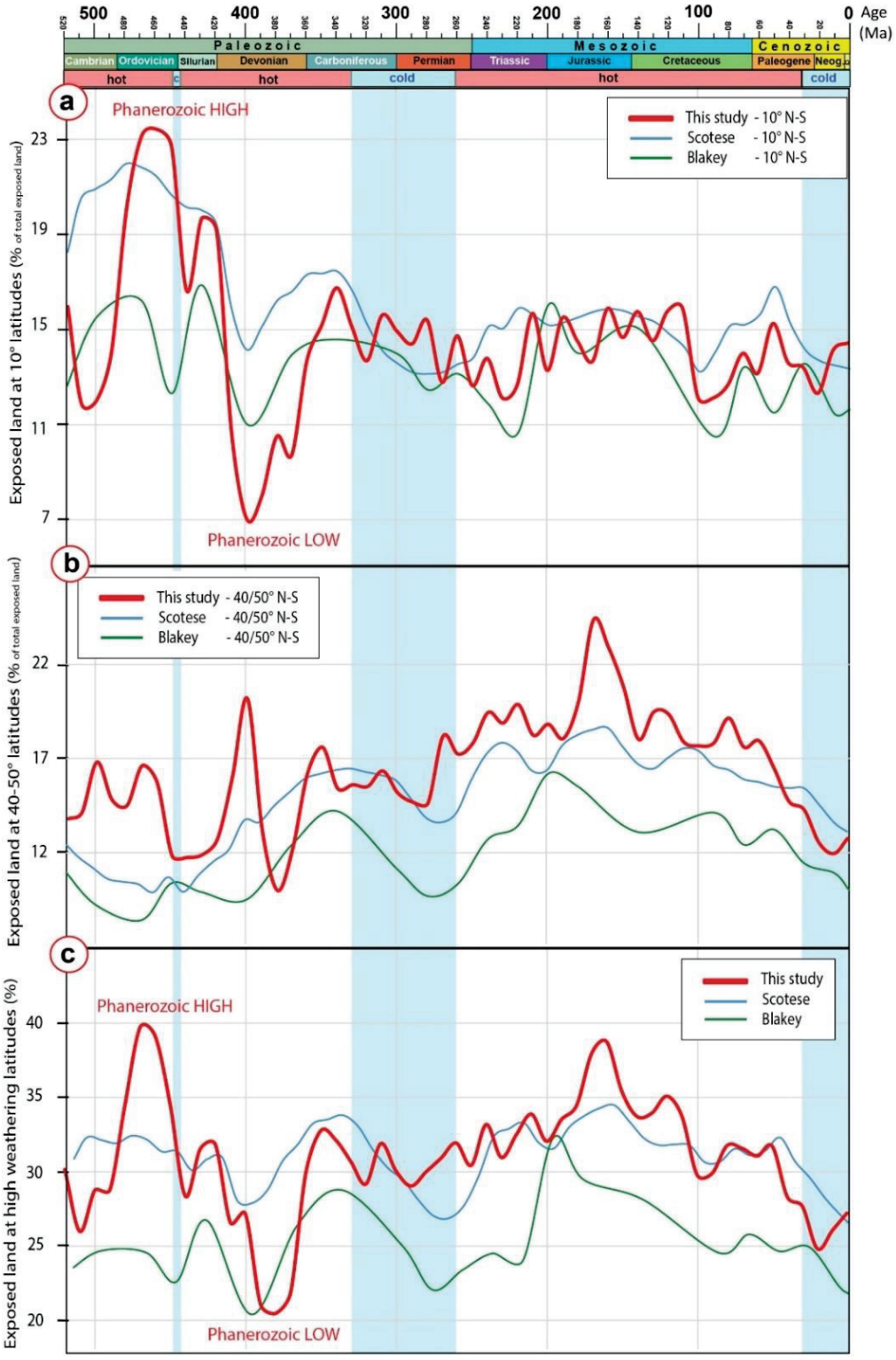

Figure 9: (a) Curves of exposed land at ±10° latitudes for three different reconstructions. The red curve displays the values estimated from our maps. The blue curve was calculated from the reconstructions of Scotese (2016) and the green curve was estimated from the reconstructions used in GEOCLIM (Blakey, 2009). **(b)** Same as in panel a but for latitudes ±40-50°. **(c)** Panels a and b combined, showing theoretical weathering activity in the tropics and the northern/southern wet belts The blue zones represent the main glaciations of the Phanerozoic..

5. Unresolved and future work

5.1 Topography

One of the major challenges in paleogeography and its potential effect on paleoclimates is constraining topography. Even if the geological record provides us evidences of past subduction and collisions, the exact locations of past orogenies are difficult to identify. It is well known that the presence of mountain ranges can greatly affect regional climatic gradients (Schmittner et al., 2011; Maffre et al., 2018) and the rainfall distribution, and can trigger the aridification of large land areas and consequently influence the weathering flux (Maffre et al., 2018). In long-term carbon models, the effect of topography on silicate weathering is often kept at minimum and represents only the effect of the supercontinent cycle as this parameter is based on marine carbonate $^{87}Sr/^{86}Sr$ ratio or rock abundance compilations. In future work we aim to restore the topographic forcing for single orogenic events and bring more constraints on the evolution of this forcing through time. Our first planned investigation will focus on the late Paleozoic (~330-260 Ma) since (e.g.) Godderis et al. (2017) suggest the onset and ending of the ice age is related to the build-up and collapse of the Variscan orogeny during Pangea formation. However, their simulations are only based on five time-slices over a 100 Myrs period, and partly based on outdated paleogeographical reconstructions.

Constraining topography is also crucial for calculating sea levels with the hypsometric method. This is particularly true for supercontinents such as Pangea and the large Gondwana landmass that can also be described as a supercontinent. Constraining topography through time allows for the development of a more accurate representation of hypsometric curves and gradients to apply in the calculations. In an ideal model version, each continent could have its own hypsometry, allowing us to calculate a more accurate global sea level curve.

5.2. Parameters and error propagation in GEOCARBSULFvolc

The current propagation of error in GEOCARBSULFvolc is based on Monte Carlo simulations where 10,000 values are generated for each 10 Myrs time step. However, this process is linked to an embedded error as 85% of the simulations are commonly rejected but values are kept partially for the next simulation leading to a general error of on average 1000 ppm CO_2 between Monte Carlo runs and simple simulations. It is therefore important to revise the error propagation.

Moreover, much of the uncertainty on estimated CO_2 values is attributable to two input parameters in the model: the climate sensitivity and the influence of plants on silicate weathering in terms of plant evolution and the timing of evolutionary progress. Both of these processes can be better constrained through further research.

In addition, a recent study demonstrated that temperature is the primary factor affecting the efficiency of silicate weathering (Deng et al., 2022). However, the temperature change through time is one of the least constrained parameters in GEOCARBSULF (where it is called GEOG). The default values suggest a rather cold environment in the early Paleozoic, which is at odds with many studies.

5.3. Constraining climate gradients and tropical exposed land through time

In long-term carbon models, the paleogeographic forcing is based on the amount of exposed land within selected latitude bands or using GCMs. Both of those methods have limitations. One of the main limitations of relying on latitudinal distribution to assess weatherability is that climate gradients are rarely distributed in simple latitudinal belts. GCM are able, in theory, to recreate climate gradients with the simulation of runoff and temperature distribution over the planet. The main limitation is that those simulations are computationally expensive but also that they rely largely on topography distribution, which is one of the least constrained elements in paleogeographic reconstructions. In future work we want to test a new way of integrating those climate gradients in long-term carbon models. We will use an updated dataset of climatically sensitive lithofacies (i.e., coal, bauxite, kaolinite, evaporites and tillites) to reconstruct those climate gradients, mostly the tropical belts through time. However, the time step of the maps produced is generally 20 Myrs and for periods of intense climatic changes, such as the late Paleozoic, this is too coarse to identify some climate-sensitive processes. Moreover, plant fossil indicators should be added to make the dataset more complete and more applicable to shorter time steps.

These newly reconstructed climate gradients will then be used to extract the amount of land under tropical settings and will be first tested over the late Paleozoic period. Indeed, this period is perfect to test this new definition of the paleogeographic forcing as massive climate change took place and climate gradients were changing greatly. An interesting case would be to compare the use of reconstructed climatic belts to estimate land availability in a box model such as COPSE

against the use of a spatially resolved model such as in SCION, as the use of GCM simulations tends to overestimate the amount of land due to their coarse grid size.

5.4. LIPs and climate

LIPs are commonly emplaced in a short time period (a few million years or less), aerosol-generating SO_2 may trigger initial global cooling over a few years whereas CH_4 and CO_2 can lead to global warming over timescales of 10^2–10^5 yrs. (Fig. 2). A causal link between LIPs and mass extinctions has long been postulated but LIPs have been argued to potentially have a large impact on the longer-term climate since vast areas of juvenile basalt may have been exposed to tropical conditions, which will enhance the global weathering activity (Jones et al., 2016; Johansson et al., 2018). Their impact was investigated by Johansson et al. (2018) by comparing CO_2 proxy data with the areal extent of LIPs within ± 5, ± 10 and ±15° latitudes. However, tropical settings are unlikely to have been restricted to those latitudes during the Phanerozoic and in future work we will revise the tropical belts as outlined above (section 5.3) and test the long-term climate effect of tropical LIPs using the biogeochemical model COPSE with a revised LIP input table brought by our newly reconstructed climate gradients.

Before being tested for the entire Phanerozoic, the revised LIP input table will first be tested for the late Paleozoic period. Indeed, the demise of the late Paleozoic ice age is partly attributed to Permian LIP activity (Zhang & Torsvik, 2022).

5.5. Improving the proxy record

Atmospheric CO_2 proxies are numerous but restricted in deep time. A challenging part of the proxy records we faced concerned our papers dealing with early Paleozoic climates and notably the Ordovician climates as no reliable CO_2 proxies exist before the Early Devonian (~420 Ma). Well-known Devonian proxies for atmospheric CO_2 include paleosols and stomata, which are commonly combined with liverworts, alkenones and boron for the younger geological record to derive a mean proxy curve (Fig. 3). Proxy-based CO_2 estimates, however, are notably coarse in the 420-340 Ma and 260-240 Ma periods (~2 per 10 Myr interval) leading to critical gaps in our general understanding of the Earth's climate. This included the transition to icehouse conditions during the Late Paleozoic Ice Age as well as the shift back to greenhouse conditions. Other types of proxies do exist, e.g., the C3 plant method (Cui et al., 2020), and it is essential to fill crucial gaps in order to undertake a joint analysis of multiple proxies and carbon-cycle models.

5.6. Improved estimates of solid Earth degassing

Subduction fluxes derived from full-plate models provide a powerful means of estimating plate tectonic CO_2 degassing (sourcing) through time. A key challenge is to develop reliable full-plate models in deep time, but we also expect refinements in subduction fluxes for Mesozoic-Cenozoic times as more advanced ocean-basin models with intra-oceanic subduction are being developed and properly implemented in full-plate models. Relative degassing estimates based on subduction flux rates are too low to match proxy CO_2 levels for parts of the Mesozoic and notably the early Cenozoic (Fig. 3). Implementing intra-oceanic subduction histories, adding fluxes from continental rifts and/or explicitly considering the intersection of continental magmatic arcs with carbonate-filled basins through time would almost certainly increase plate tectonic degassing and minimize existing model-proxy CO_2 mismatches but such *hybrid* models are not trivial to develop.

5.7. Paleogeography, degassing & carbon cycle during the "boring billion" and Snowball Earth events

After the "Great Oxygenation Event" and the birth of the modern atmosphere during the early Proterozoic, there are no known glaciations for about 1.5 billion years. This greenhouse stage includes the so-called "boring billion" (1.8-0.8 Ga), incidentally contemporaneous with the first two supercontinents on Earth (Nuna and Rodinia). The boring billion was therefore a tectonically active period, which culminated in the initial dispersal of Rodinia at around 750 Ma and was accompanied by dramatic cooling events (Snowball Earths). In most paleogeographic models, Rodinia was equatorially centred and undergoing rifting at tropical latitudes, potentially leading to extensive silicate weathering and cooling. With a high theoretical weatherability, the emplacement of a LIP at tropical latitudes may have accelerated weathering and triggered Snowball Earth conditions (Godderis et al., 2003). However, enhanced silicate weathering is just one of many explanations (Stern & Miller, 2019), and alternative explanations include both biotic and tectonic causes, such as reduced continental arc-activity (McKenzie et al., 2016; Williams et al., 2019). In **article 1** we developed novel ways to quantify volcanic arc degassing in deep time from the zircon record, and as a supplement to computationally intensive 3D climate simulations, we also parameterized theoretical silicate weathering for most of the Phanerozoic based on the latitudinal distribution of exposed land from our paleogeographic maps. We have now extended our maps to 540 Ma to cover the entire Phanerozoic, but we anticipate extending those maps further back in time (pending data availability) to estimate silicate weathering efficiency and global sea levels.

This may vastly improve carbon cycle modelling in deep time and perhaps allowing us to expose the cause(s) for the onset and termination of Snowball Earth climates.

6. References

Algeo, T. J., & Wilkinson, B. H. (1991). Modern and ancient continental hypsometries. J. Geol. Soc. Lond, 148(4), 643-653.

Amante, C., Eakins, B.W., (2009). ETOPO1 1 Arc-Minute Global Relief Model: Procedures, Data Sources, and Analysis. NOAA Tech. Memo. NESDIS NGDC-24. http://dx.doi.org/10.7289/V5C8276M.

Arbab, A. I. (2009). The length of the day: A cosmological perspective.Progress in Physics, 1(1), 8-11.

Arevalo Jr, R., McDonough, W. F., & Luong, M. (2009). The K/U ratio of the silicate Earth: Insights into mantle composition, structure and thermal evolution. Earth and Planetary Science Letters,278(3-4), 361-369.

Arthur, M. A., & Fahey, T. J. (1993). Controls on soil solution chemistry in a subalpine forest in north-central Colorado. Soil Science Society of America Journal, 57(4), 1122-1130.

Bekker, A., Holland, H. D., Wang, P. L., Rumble, D. I. I. I., Stein, H. J., Hannah, J. L., ... & Beukes, N. J. (2004). Dating the rise of atmospheric oxygen. Nature, 427(6970), 117-120.

Berner, R. A. (1989). Biogeochemical cycles of carbon and sulfur and their effect on atmospheric oxygen over Phanerozoic time. Global and Planetary Change,1(1-2), 97-122.

Berner, E. K., Berner, R. A., & Moulton, K. L. (2003). Plants and mineral weathering: present and past. Treatise on geochemistry, 5, 605.

Berner, R. A. (2004).The Phanerozoic carbon cycle: CO2 and O2. Oxford University Press on Demand.

Berner, R. A. (2006). GEOCARBSULF: a combined model for Phanerozoic atmospheric O2 and CO2.Geochimica et Cosmochimica Acta,70(23), 5653-5664.

Berner, R. A., & Caldeira, K. (1997). The need for mass balance and feedback in the geochemical carbon cycle. Geology, 25(10), 95

Blakey, R. (2009). Molleweide plate tectonic maps. https://deeptimemaps.com/

Bonan, G. (2015). Ecological climatology: concepts and applications. Cambridge University Press.

Bond, G.C. (1979). Evidence of some uplifts of large magnitude in continental platforms. Tectonophysics 61:285–305

Brantley, S.L., and Chen, Y., (1995). Chemical weathering rates of pyroxenes and amphiboles. Min. Soc. Am. Rev. Mineral 31:119–172.5-956.

Bryan, S. E., & Ernst, R. E. (2008). Revised definition of large igneous provinces (LIPs). Earth-Science Reviews, 86(1-4), 175-202.

Catling, D. C., & Zahnle, K. J. (2020). The archean atmosphere. Science Advances, 6(9), eaax1420.

Coltice, N., Seton, M., Rolf, T., Müller, R. D., & Tackley, P. J. (2013). Convergence of tectonic reconstructions and mantle convection models for significant fluctuations in seafloor spreading. Earth and Planetary Science Letters, 383, 92-100.

Conrad, C.P., (2013). The solid Earth's influence on sea level. Geol. Soc. Am. Bull. 125: 1027–1052, doi:10.1130/B30764.1.

Crowley, T. J., & Berner, R. A. (2001). CO2 and climate change. Science, 292(5518), 870-872.

Cui, Y., Schubert, B. A., & Jahren, A. H. (2020). A 23 my record of low atmospheric CO2. Geology, 48(9), 888-892.

Deng, K., Yang, S., & Guo, Y. (2022). A global temperature control of silicate weathering intensity. Nature communications, 13(1), 1-10.

Dessert, C., Dupré, B., Gaillardet, J., François, L. M., & Allegre, C. J. (2003). Basalt weathering laws and the impact of basalt weathering on the global carbon cycle. Chemical Geology, 202(3-4), 257-273.

Domeier. M., Magni, V., Hounslow, M.W., Torsvik, T.H. (2018). Episodic zircon age spectra mimic fluctuations in subduction. Scientific Reports 8:1747. doi:10.1038/s41598-018-35040-z

Domeier, M., & Torsvik, T. H. (2019). Full-plate modelling in pre-Jurassic time. Geological Magazine, 156(2), 261-280.

Donnadieu, Y., Goddéris, Y., Pierrehumbert, R., Dromart, G., Fluteau, F., & Jacob, R. (2006). A GEOCLIM simulation of climatic and biogeochemical consequences of Pangea breakup. Geochemistry, Geophysics, Geosystems,7(11).

Evans, D. A. (2003). True polar wander and supercontinents. Tectonophysics, 362(1-4), 303-320.

Forney, G. G. (1975). Permo-Triassic sea-level change. The Journal of Geology, 83(6), 773-779.

Foster, G. L., Royer, D. L., & Lunt, D. J. (2017). Future climate forcing potentially without precedent in the last 420 million years. Nature communications, 8(1), 1-8.

Garrels, R.M., (1967). Genesis of some ground waters from igneous rocks. In: P.H. Abelson, ed., Researches in geochemistry. Wiley, New York, pp. 405–420.

Garrels, R. M., Perry, E. A., & Mackenzie, F. T. (1973). Genesis of Precambrian iron-formations and the development of atmospheric oxygen. Economic Geology,68(7), 1173-1179.

Goddéris, Y., Donnadieu, Y., Nédélec, A., Dupré, B., Dessert, C., Grard, A., ... & François, L. M. (2003). The Sturtian 'snowball'glaciation: fire and ice. Earth and Planetary Science Letters, 211(1-2), 1-12.

Goddéris, Y., Donnadieu, Y., Lefebvre, V., Le Hir, G., & Nardin, E. (2012). Tectonic control of continental weathering atmospheric CO2, and climate over Phanerozoic times. Comptes Rendus Geoscience, 344(11-12), 652-662.

Goddéris, Y., Donnadieu, Y., Le Hir, G., Lefebvre, V., & Nardin, E. (2014). The role of palaeogeography in the Phanerozoic history of atmospheric CO2 and climate. Earth-Science Reviews, 128, 122-138.

Goddéris, Y., Donnadieu, Y., Carretier, S., Aretz, M., Dera, G., Macouin, M., & Regard, V. (2017). Onset and ending of the late Palaeozoic ice age triggered by tectonically paced rock weathering. Nature Geoscience, 10(5), 382-386.

Godderis, Y., & Donnadieu, Y. (2019). A sink-or a source-driven carbon cycle at the geological timescale? Relative importance of palaeogeography versus solid Earth degassing rate in the Phanerozoic climatic evolution. Geological Magazine, 156(2), 355-365.

Hardenbol, J., Thierry, J., Farley, M.B., Jacquin, T., de Graciansky, P.-C., Vail, P.R., (1998). Mesozoic and Cenozoic sequence stratigraphy of European basins. SEPM Spec. Publ. 60, 3–13.

Harrison, C. G. A., (1990), Long term eustasy and epeirogeny in continents, in Sea Level Change: U.S. National Research Council Geophysics study Committee (Washington D.C.), p. 141-158.

Haq, B. U., & Al-Qahtani, A. M. (2005). Phanerozoic cycles of sea level change on the Arabian Platform.GeoArabia,10(2), 127-160.

Haq, B.U., Schutter, S.R., (2008). A chronology of Paleozoic sea level changes. Science 322: 64–68. http://dx.doi.org/10.1126/science.1161648.

Heimdal, T. H., Callegaro, S., Svensen, H. H., Jones, M. T., Pereira, E., & Planke, S. (2019). Evidence for magma–evaporite interactions during the emplacement of the Central Atlantic Magmatic Province (CAMP) in Brazil. Earth and Planetary Science Letters, 506, 476-492.

Heimdal, T. H., Goddéris, Y., Jones, M. T., & Svensen, H. H. (2021). Assessing the importance of thermogenic degassing from the Karoo Large Igneous Province (LIP) in driving Toarcian carbon cycle perturbations. Nature communications, 12(1), 1-7.

Holland, H. D. (1978). The Chemical Evolution of the Atmosphere and Oceans. Hoboken.

Jansen, T., Scharf, C., Way, M., & Del Genio, A. (2019). Climates of warm Earth-like planets. II. Rotational "Goldilocks" zones for fractional habitability and silicate weathering. The Astrophysical Journal,875(2), 79.

Jenny, H., (1941). Factors of soil formation. McGraw-Hill, New York.

Johansson, L., Zahirovic, S., & Müller, R. D. (2018). The interplay between the eruption and weathering of large igneous provinces and the deep-time carbon cycle. Geophysical Research Letters, 45(11), 5380-5389.

Jones, M.T., Jerram, D.A., Svensen, H.H., Grove C. (2016). The effects of large igneous provinces on the global carbon and sulphur cycles. Palaeogeography, Palaeoclimatology, Palaeoecology 441, 4-21.

Kaiho, K., & Saito, S. (1994). Oceanic crust production and climate during the last 100 Myr. Terra Nova, 6(4), 376-384.

Kasting, J. F. (1989). Long-term stability of the Earth's climate. Global and planetary change, 1(1-2), 83-95.

Korenaga, J. (2013). Initiation and evolution of plate tectonics on Earth: theories and observations.Annual review of Earth and planetary sciences,41, 117-151.

Krissansen-Totton, J., & Catling, D. C. (2017). Constraining climate sensitivity and continental versus seafloor weathering using an inverse geological carbon cycle model. Nature communications, 8(1), 1-15.

Kump, L. R., Arthur, M. A., Patzkowsky, M. E., Gibbs, M. T., Pinkus, D. S., & Sheehan, P. M. (1999). A weathering hypothesis for glaciation at high atmospheric pCO2 during the Late Ordovician. Palaeogeography, Palaeoclimatology, Palaeoecology, 152(1-2), 173-187.

Lambeck, K., H. Rouby, A. Purcell, Y. Sun, and M. Sambridge (2014), Sea level and global ice volumes from the Last Glacial Maximum to the Holocene, PNAS, 111(43), 15296-15303, doi:10.1073/pnas.1411762111.

Larson, R. L. (1991). Geological consequences of superplumes. Geology, 19(10), 963-966.

Lee, C-T A., Jiang, H., Dasgupta, R., Torres, M. (2020). A Framework for Understanding Whole-Earth Carbon Cycling. In Ordcutt, B.N., Daniel. I., Dasgupta, R. (Eds.) DEEP CARBON Past to Present. Cambridge University Press, UK, pages 313-357.

Lenton, T. M. (2013). Environmental tipping points. Annual Review of Environment and Resources, 38, 1-29.

Lenton, T. M., & Williams, H. T. (2013). On the origin of planetary-scale tipping points. Trends in Ecology & Evolution, 28(7), 380-382.

Lenton, T. M., Dahl, T. W., Daines, S. J., Mills, B. J., Ozaki, K., Saltzman, M. R., & Porada, P. (2016). Earliest land plants created modern levels of atmospheric oxygen. Proceedings of the National Academy of Sciences, 113(35), 9704-9709.

Lenton, T. M., Daines, S. J., & Mills, B. J. (2018). COPSE reloaded: An improved model of biogeochemical cycling over Phanerozoic time. Earth-Science Reviews, 178, 1-28.

Li, G., Hartmann, J., Derry, L. A., West, A. J., You, C. F., Long, X., ... & Chen, J. (2016). Temperature dependence of basalt weathering. Earth and Planetary Science Letters, 443, 59-69.

Maffre, P., Ladant, J. B., Moquet, J. S., Carretier, S., Labat, D., & Goddéris, Y. (2018). Mountain ranges, climate and weathering. Do orogens strengthen or weaken the silicate weathering carbon sink?. Earth and Planetary Science Letters, 493, 174-185.

Maher, K., & Chamberlain, C. P. (2014). Hydrologic regulation of chemical weathering and the geologic carbon cycle. Science, 343(6178), 1502-1504.

Macdonald, F. A., Swanson-Hysell, N. L., Park, Y., Lisiecki, L., & Jagoutz, O. (2019). Arc-continent collisions in the tropics set Earth's climate state. Science, 364(6436), 181-184.

Mackenzie, F.T., and Garrels, R.M., (1966). Chemical mass balance between rivers and oceans. Am. J. Sci. 264:507–525.

Marcilly, C. M., Torsvik, T. H., Domeier, M., & Royer, D. L. (2021). New paleogeographic and degassing parameters for long-term carbon cycle models. Gondwana Research, 97, 176-203.

McKenzie, N. R., Horton, B. K., Loomis, S. E., Stockli, D. F., Planavsky, N. J., & Lee, C. T. A. (2016). Continental arc volcanism as the principal driver of icehouse-greenhouse variability. Science, 352(6284), 444-447.

Merdith, A. S., Williams, S. E., Collins, A. S., Tetley, M. G., Mulder, J. A., Blades, M. L., ... & Müller, R. D. (2021). Extending full-plate tectonic models into deep time: Linking the Neoproterozoic and the Phanerozoic. Earth-Science Reviews, 214, 103477.

Meybeck, M., (1987). Global chemical weathering of surficial rocks estimated from river dissolved loads. Am. J. Sci. 287:401–428.

Miller, K. G., Kominz, M. A., Browning, J. V., Wright, J. D., Mountain, G. S., Katz, M. E., ... & Pekar, S. F. (2005). The Phanerozoic record of global sea level change. Science, 310(5752), 1293-1298.

Mills, B., Daines, S. J., & Lenton, T. M. (2014). Changing tectonic controls on the long-term carbon cycle from Mesozoic to present. Geochemistry, Geophysics, Geosystems, 15(12), 4866-4884.

Mills, B. J., Krause, A. J., Scotese, C. R., Hill, D. J., Shields, G. A., & Lenton, T. M. (2019). Modelling the long-term carbon cycle, atmospheric CO2, and Earth surface temperature from late Neoproterozoic to present day. Gondwana Research, 67, 172-186.

Mills, B. J., Donnadieu, Y., & Godderis, Y. (2021). Spatial continuous integration of Phanerozoic global biogeochemistry and climate. Gondwana Research, 100, 73-86.

Morgan, W. J. (1971). Convection plumes in the lower mantle. Nature, 230(5288), 42-43.

Nardin, E., Goddéris, Y., Donnadieu, Y., Hir, G. L., Blakey, R. C., Pucéat, E., & Aretz, M. (2011). Modeling the early Paleozoic long-term climatic trend. Bulletin, 123(5-6), 1181-1192.

Olson, J. M. (2006). Photosynthesis in the Archean era.Photosynthesis research,88(2), 109-117.

Porder, S., Hilley, G. E. & Chadwick, O. A. (2007). Chemical weathering, mass loss, and dust inputs across a climate by time matrix in the Hawaiian Islands. Earth Planet. Sci. Lett. 258, 414–427.

Raymo, M. E., & Ruddiman, W. F. (1992). Tectonic forcing of late Cenozoic climate. nature, 359(6391), 117-122.

Ribas, I. (2009). The Sun and stars as the primary energy input in planetary atmospheres.Proceedings of the International Astronomical Union,5(S264), 3-18.

Ridley, V. A., & Richards, M. A. (2010). Deep crustal structure beneath large igneous provinces and the petrologic evolution of flood basalts. Geochemistry, Geophysics, Geosystems, 11(9).

Royer, D. L. (2006). CO2-forced climate thresholds during the Phanerozoic. Geochimica et Cosmochimica Acta,70(23), 5665-5675.

Royer, D. L., Donnadieu, Y., Park, J., Kowalczyk, J., & Godderis, Y. (2014). Error analysis of CO2 and O2 estimates from the long-term geochemical model GEOCARBSULF. American Journal of Science, 314(9), 1259-1283.

Sagan, C., & Chyba, C. (1997). The early faint sun paradox: Organic shielding of ultraviolet-labile greenhouse gases.Science,276(5316), 1217-1221.

Sagan, C., & Mullen, G. (1972). Earth and Mars: Evolution of atmospheres and surface temperatures.Science,177(4043), 52-56.

Schmittner, A., Silva, T. A., Fraedrich, K., Kirk, E., & Lunkeit, F. (2011). Effects of mountains and ice sheets on global ocean circulation. Journal of Climate, 24(11), 2814-2829.

Scotese, C. R. (2016). PALEOMAP PaleoAtlas for GPlates and the PaleoData Plotter Program PALEOMAP Project (2016)(http://www.earthbyte.org/paleomap-paleoatlas-for-gplates/)

Steinberger, B., & Torsvik, T. H. (2008). Absolute plate motions and true polar wander in the absence of hotspot tracks. Nature, 452(7187), 620-623.

Stern, R. J. (2018). The evolution of plate tectonics.Philosophical Transactions of the Royal Society A: Mathematical, Physical and Engineering Sciences,376(2132), 20170406.

Stern, R.J. & Miller, N.R. (2019). Neoproterozoic Glaciation—Snowball Earth Hypothesis. Encyclopedia of Geology, 2nd edition. https://doi.org/10.1016/B978-0-12-409548-9.12107-4

Svensen, H., Planke, S., Malthe-Sørenssen, A., Jamtveit, B., Myklebust, R., Rasmussen Eidem, T., & Rey, S. S. (2004). Release of methane from a volcanic basin as a mechanism for initial Eocene global warming. Nature, 429(6991), 542-545.

Svensen, H., Planke, S., Chevallier, L., Malthe-Sørenssen, A., Corfu, F., & Jamtveit, B. (2007). Hydrothermal venting of greenhouse gases triggering Early Jurassic global warming. Earth and Planetary Science Letters, 256(3-4), 554-566.

Tajika, E. (1998). Mantle degassing of major and minor volatile elements during the Earth's history.Geophysical research letters,25(21), 3991-3994.

Tajika, E. (1999). Carbon cycle and climate change during the Cretaceous inferred from a biogeochemical carbon cycle model. Island Arc, 8(2), 293-303.

Taylor, A.S., and Lasaga, A.C., (1999). The role of basalt weathering in the Sr isotope budget of the oceans Chem. Geol. 161:199–214.

Tierney, J. E., Poulsen, C. J., Montañez, I. P., Bhattacharya, T., Feng, R., Ford, H. L., ... & Zhang, Y. G. (2020). Past climates inform our future. Science, 370(6517), eaay3701.

Torsvik, T. H., Van der Voo, R., Preeden, U., Mac Niocaill, C., Steinberger, B., Doubrovine, P. V., ... & Cocks, L. R. M. (2012). Phanerozoic polar wander, palaeogeography and dynamics. Earth-Science Reviews, 114(3-4), 325-368.

Torsvik, T. H., Svensen, H. H., Steinberger, B., Royer, D. L., Jerram, D. A., Jones, M. T., & Domeier, M. (2021). Connecting the deep Earth and the atmosphere. In Mantle Convection and Surface Expressions (Edited by Hauke Marquardt, Maxim Ballmer, Sanne Cottaar and Jasper Konter). Geophysical Monograph 263, 413-453. American Geophysical Union. DOI: 10.1002/9781119528609.ch16.

Ueno, Y., Johnson, M. S., Danielache, S. O., Eskebjerg, C., Pandey, A., & Yoshida, N. (2009). Geological sulfur isotopes indicate elevated OCS in the Archean atmosphere, solving faint young sun paradox.Proceedings of the National Academy of Sciences,106(35), 14784-14789.

Van Der Meer, D. G., Zeebe, R. E., van Hinsbergen, D. J., Sluijs, A., Spakman, W., & Torsvik, T. H. (2014). Plate tectonic controls on atmospheric CO2 levels since the Triassic. Proceedings of the National Academy of Sciences, 111(12), 4380-4385.

Van der Meer, D. G., van Saparoea, A. V. D. B., Van Hinsbergen, D. J. J., Van de Weg, R. M. B., Godderis, Y., Le Hir, G., & Donnadieu, Y. (2017). Reconstructing first-order changes in sea level during the Phanerozoic and Neoproterozoic using strontium isotopes. Gond. Res., 44, 22-34.

Velbel, M. A. (1993a). Constancy of silicate-mineral weathering-rate ratios between natural and experimental weathering: implications for hydrologic control of differences in absolute rates. Chemical Geology, 105(1-3), 89-99.

Velbel, M. A. (1993b). Temperature dependence of silicate weathering in nature: How strong a negative feedback on long-term accumulation of atmospheric CO2 and global greenhouse warming?. Geology, 21(12), 1059-1062.

Vérard, C., Hochard, C., Baumgartner, P. O., Stampfli, G. M., & Liu, M. (2015). 3D palaeogeographic reconstructions of the Phanerozoic versus sea-level and Sr-ratio variations. J. Palaeogeogr., 4(1), 64-84.

Vérard, C. (2017). Statistics of the Earth's Topography. Open Access Library Journal, 4(06), 1.

Walker, J. C., Hays, P. B., & Kasting, J. F. (1981). A negative feedback mechanism for the long-term stabilization of Earth's surface temperature. Journal of Geophysical Research: Oceans, 86(C10), 9776-9782.

Wallmann, K. (2001). Controls on the Cretaceous and Cenozoic evolution of seawater composition, atmospheric CO2 and climate. Geochimica et Cosmochimica Acta, 65(18), 3005-3025.

Way, M. J., Del Genio, A. D., Aleinov, I., Clune, T. L., Kelley, M., & Kiang, N. Y. (2018). Climates of warm Earth-like planets. I. 3D model simulations.The Astrophysical Journal Supplement Series,239(2), 24.

Wignall, P. B. (2001). Large igneous provinces and mass extinctions. Earth-science reviews, 53(1-2), 1-33.

Wignall, P. B., Newton, R. J., & Little, C. T. (2005). The timing of paleoenvironmental change and cause-and-effect relationships during the Early Jurassic mass extinction in Europe. American

Williams, J.J., Mills, B.J.W. & Lenton, T.M. (2019). A tectonically driven Ediacaran oxygenation event. *Nature Communications* 10:2690 |

Worsley, T. R., & Kidder, D. L. (1991). First-order coupling of paleogeography and CO2, with global surface temperature and its latitudinal contrast. Geology, 19(12), 1161-1164.

West, A. J. (2012). Thickness of the chemical weathering zone and implications for erosional and climatic drivers of weathering and for carbon-cycle feedbacks. Geology, 40(9), 811-814.

Zhang, H., & Torsvik, T. H. (2022). Circum-Tethyan magmatic provinces, shifting continents and Permian climate change.*Earth and Planetary Science Letters*, *584*, 117453.

PART II : Scientific contributions

New paleogeographic and degassing parameters for long-term carbon cycle models.

Chloé M. Marcilly, Trond H. Torsvik, Mathew M. Domeier and Dana L. Royer.

Gondwana Research 97 (2021) 176-203.

Gondwana Research 97 (2021) 176–203

Contents lists available at ScienceDirect

Gondwana Research

journal homepage: www.elsevier.com/locate/gr

GR Focus Review

New paleogeographic and degassing parameters for long-term carbon cycle models

Chloé M. Marcilly [a,*], Trond H. Torsvik [a,b], Mathew Domeier [a], Dana L. Royer [c]

[a] Centre for Earth Evolution and Dynamics (CEED), University of Oslo, 0315 Oslo, Norway
[b] School of Geosciences, University of Witwatersrand, Johannesburg 2050, South Africa
[c] Department of Earth and Environmental Sciences, Wesleyan University, Middletown, CT 06459, USA

ARTICLE INFO

Article history:
Received 22 February 2021
Revised 21 May 2021
Accepted 21 May 2021
Available online 26 May 2021
Handling Editor: M. Santosh

Keywords:
Carbon cycle
Modelling
Paleoclimate
Phanerozoic
Paleogeography
Degassing

ABSTRACT

Long-term carbon cycle models are critical for understanding the levels and underlying controls of atmospheric CO_2 over geological time-scales. We have refined the implementation of two important boundary conditions in carbon cycle models, namely consumption by silicate weathering and carbon degassing. Through the construction of continental flooding maps for the past 520 million years (Myrs), we have estimated exposed land area relative to the present-day (f_A), and the fraction of exposed land area undergoing silicate weathering ($f_{AW\text{-}fA}$). The latter is based on the amount of exposed land within the tropics (±10°) plus the northern/southern wet belts (±40–50°) relative to today, which are the prime regions for silicate weathering. We also evaluated climate gradients and potential weatherability by examining the distribution of climate-sensitive indicators. This is particularly important during and after Pangea formation, when we reduce f_{AW}-f_A during times when arid equatorial regions were present. We also estimated carbon degassing for the past 410 Myrs using the subduction flux from full-plate models as a proxy. We further used the subduction flux to scale and normalize the arc-related zircon age distribution (arc-activity), allowing us to estimate carbon degassing in much deeper time. The effect of these refined modelling parameters for weathering and degassing was then tested in the GEOCARBSULFvolc model, and the results are compared to other carbon cycle models and CO_2 proxies. The use of arc-activity as a proxy for carbon degassing brings Mesozoic model estimates closer to CO_2 proxy values but our models are highly sensitive to the definition of f_{AW}-f_A. Considering only variations in the land availability to weathering that occur in tropical latitudes (corrected for arid regions) and the use of our new degassing estimates leads to notably higher CO_2 levels in the Mesozoic, and a better fit with the CO_2 proxies.

Contents

* Corresponding author.
E-mail address: c.f.m.marcilly@geo.uio.no (C.M. Marcilly).

https://doi.org/10.1016/j.gr.2021.05.016
1342-937X/

1. Introduction

Atmospheric CO_2 concentrations have fluctuated considerably over geological time, driven by time-dependent solar, tectonic, and biological forcings. A history of those fluctuations can be reconstructed from proxies of past CO_2 concentrations that extend back into the Paleozoic, but these proxy records are fragmentary and often associated with large uncertainties (Foster et al., 2017). In contrast, models for the long term carbon cycle, e.g. GEOCARBSULF (volc) (e.g., Berner, 2004; 2006; Royer et al., 2014), COPSE (e.g. Bergman et al., 2004; Lenton et al., 2018), and GEOCLIM (e.g., Goddéris et al., 2012, 2014; Donnadieu et al. 2006), aim to capture the principal forcings on CO_2 (the time-dependent balance of sources and sinks) to formulate retrodictions of its past atmospheric concentration. Modelling, therefore, plays a key role in not only reconstructing past CO_2 fluctuations (as a complement to the proxy record) but also our attempt to understand their causes.

The relative importance of different carbon *sinks* and *sources* is debated, and variations in forcing factors are mostly estimated by indirect methods. CO_2 *sinks* include silicate weathering and burial of carbonates and organic carbon (e.g., Berner et al., 1983; Berner, 2004; Walker et al., 1981; Worsley and Kidder, 1991; Otto-Bliesner, 1995; Goddéris et al., 2012, 2014). The strength of the silicate weathering feedback is largely tied to relief and climate, which in turn is linked to plate tectonics and continental paleogeography (Worsley and Kidder, 1991; Gibbs et al., 1999; Berner, 2004; Donnadieu et al., 2006; Goddéris et al., 2014; Goddéris and Donnadieu, 2017). For example, continents located at tropical latitudes, and their associated warm and wet climates, promote CO_2 consumption by silicate weathering. Constraining the paleogeographic input in long-term carbon cycle models is therefore fundamental (Donnadieu et al., 2006; Pohl et al., 2014; Goddéris et al., 2014; Goddéris and Donnadieu, 2017). Remarkably, Charles Lyell proposed such a link between paleogeography and the climate in 1830 (Lyell, 1830), long before Alfred Wegener presented his revolutionary theory of continental drift in 1912.

Plate tectonics plays an important role in shaping the long-term climate at both regional and global scales by controlling the distribution of continents and oceans (paleogeography), and erecting and dismantling mountain ranges, thereby modulating the intensity of weathering, but also by powering arc-volcanism, the main *source* of CO_2 (e.g., Gyllenhaal et al., 1991; Zhang et al., 2012; Lagabrielle et al., 2009; Hay et al., 1990; Horton et al., 2010; Barron et al., 1989; Otto-Bliesner, 1995). Volcanic emissions and metamorphic decarbonation in continental arcs, island arcs, mid-ocean ridges, and continental rifts can loosely be referred to as solid Earth or plate tectonic degassing (Berner, 2004). There is no clear consensus on how to estimate (or even how to parameterize) such degassing through geological time, but in the GEOCARBSULF model (Berner, 2004) there is a time-dependent parameter for *'seafloor production'* (f_{SR}) that can be considered as a proxy of plate tectonic activity and thus solid Earth CO_2 degassing relative to present-day. Ironically, CO_2 degassing from spreading ridges is probably trivial with respect to degassing from magmatic arcs and continental arcs in particular. However, on a planet that is not expanding or shrinking, seafloor production must compensate the global subduction flux (to first order; i.e. neglecting intraplate deformation), and thus f_{SR} should present a useful approximate measure of global arc activity and thus solid Earth CO_2 degassing.

Seafloor production can be estimated directly from present-day seafloor age grids derived from marine geophysical data (magnetic anomalies), but this only provides f_{SR} estimates back to the Cretaceous. For earlier times, f_{SR} may be indirectly inferred from stratigraphically derived global sea-level fluctuations because variations in seafloor spreading (mid-ocean ridge volume) are the most important driver of global sea-level change (Conrad, 2013; Karlsen et al., 2020). However, this inversion is complicated by the many other time-dependent contributions to sea-level and by the difficulty of separating global (eustatic) signals from local ones. Another approach is to estimate seafloor production in deep time from full-plate models. The locations of subduction zones are generally better defined than the location of ridges in these models, so it is more sensible to estimate and discuss the subduction flux directly. Note that full-plate models, although powerful in being constrained by multiple independent sources of data, are nevertheless simplifications with significant uncertainties that grow backward in time. With respect to the subduction flux in particular, the occurrence of intra-oceanic subduction zones may be underrepresented (van der Meer et al., 2012). Recently, McKenzie et al. (2016) and Domeier et al. (2018) suggested that apparent variations in zircon production through time could mimic real fluctuations in the global subduction flux, and so analyses of zircon age spectra may provide an independent pathway toward estimating solid Earth CO_2 degassing through time.

Some authors have argued that the rate of seafloor production (and thus the subduction flux) has not varied significantly for the past 180 Ma (e.g. Rowley, 2002; Cogné and Humler, 2006), but that view has been repeatedly refuted by examination of extant marine magnetic anomalies (e.g., Larson, 1991; Conrad and Lithgow-Bertelloni, 2007; Seton et al., 2009; Coltice et al., 2013) and both continental (e.g., Engebretson, 1992) and full-plate tectonic models (Domeier et al. 2018; Torsvik et al. 2020). A particular triumph of the view that the seafloor production rate varies has been the recognition of a conspicuous peak in seafloor production in the Early Cretaceous (Seton et al., 2009). In this context, it is important to point out that several recent papers have attempted to estimate the past subduction flux by simply normalizing global subduction lengths (e.g. van der Meer et al., 2014; Mills et al., 2014, 2019; Wong et al. 2019), but this implicitly assumes a constant globally averaged rate of convergence. Continental rift lengths (Brune et al., 2017), or combinations of subduction and continental rift

lengths, have also been used as measures for plate tectonic degassing (Mills et al. 2019; Wong et al., 2019), but are overly simplified for the same reason—they assume the globally averaged rates of spreading and convergence (i.e. cm/yr per unit arc/ridge length) to have remained static through time.

In this study, we explore alternative ways to constrain CO_2 sources and sinks through geological time, with a particular focus on estimating plate tectonic degassing and the silicate weathering potential. We explore the latter by mapping out the areas of exposed land for the past 520 Myrs (Section 2) and determining how much of it was within latitude bands of high theoretical 'weatherability'. We use the term 'weatherability' to refer to the potential in silicate weathering intensity, which is controlled by the availability of land in equatorial regions and the northern and southern wet belts. For estimating plate tectonic degassing, we use the subduction flux as a proxy back to the Early Devonian (410 Ma), estimated from full-plate tectonic models (Section 3). In an attempt to proceed even further backward in time, we re-analyzed the age distribution of arc-related zircons to explore the possibility that they grossly mimic the subduction flux. Observing a good temporal correspondence between the zircon age distribution and the subduction flux since the Early Devonian, we re-scale the former to the latter to estimate absolute values of plate tectonic degassing in deeper geologic time, when plate models become increasingly uncertain. Finally, we demonstrate how the GEOCARBSULFvolc carbon cycle model responds to our updated estimates of the time-dependent exposed land area, the fraction of that area undergoing chemical weathering, and the rate of plate tectonic degassing (Sections 4 and 5).

2. Paleogeographical maps

2.1. Methods

2.1.1. Building maps of exposed land

To better constrain the amount of exposed and flooded land areas through time we have created a set of new maps based on the geological record, namely sedimentological data and fossil distributions. The maps were constructed in 10 Myr intervals from the Cambrian (520 Ma) to the Late Cretaceous (70 Ma). The exposed land maps were built following the same workflow as the maps of the PALEOMAP project (Scotese 2014a, b, 2016). As such, the main framework is a combination of geological lithofacies (Scotese, 2014a, b, 2016) and paleoclimatic reconstructions (Moore and Scotese, 2010, Scotese and Moore, 2014, Boucot et al., 2013) adapted to our plate tectonic framework (Torsvik and Cocks, 2017). However, our maps differ from those of Scotese and co-workers in several important ways, because we use a different plate tectonic framework and we integrate additional data. The PALEOMAP project is based on the plate tectonic model of Scotese (2016) (http://www.earthbyte.org/paleomap-paleoatlas-for-gplates/), whereas our reconstructions are based on Torsvik and Cocks (2017) with minor refinements in the Paleo- and Neotethys domain during the late Paleozoic and early Mesozoic. Consequently, there are large discrepancies between our continental reconstructions and those of Scotese and co-workers, both in terms of absolute longitude and latitude. These differences have a major impact on the area of land estimated to lie within latitudes of high theoretical weatherability, i.e. in the tropics and the northern/southern wet belts (~±10° and ±40–50°) (Gibbs et al., 1999; Torsvik and Cocks, 2017), and so are expected to yield distinctive silicate weathering histories in carbon cycle models like GEOCARBSULF-volc or COPSE (Berner, 2004, 2006; Royer et al., 2014; Lenton et al., 2018; Mills et al., 2014, 2019).

For the construction of exposed land maps, we prioritized the paleoenvironmental reconstructions of Torsvik and Cocks (2017) as the main source (when available); for areas and periods lacking coverage, we used reconstructions from the PALEOMAP project and other sources (Fig. 1; see supplementary data 1 for details). Additional mapping was done, notably for North Africa and Europe, using detailed maps from the peri-Tethys (Dercourt et al., 2000), Tethys project (Dercourt et al., 1993), the geological atlas of Western and Central Europe (Ziegler, 1990) and the Middle East Basins evolution program (Barrier and Vrielynck, 2008).

With the base maps of exposed land area, we modified the time-dependent coastlines of the land blocks, here called polygons, according to the distribution of climatically sensitive facies. For this, we employed a database of coal, bauxites, evaporites, and tillites based on Boucot et al. (2013) but with added data and refined time-calibration (Torsvik and Cocks, 2017). We used (for example) evaporites as indicators for the location of coastal shallow basins. This method helped to constrain coastlines when we did not have matching data between the paleogeographic reconstructions of Torsvik and Cocks (2017), the PALEOMAP project and other sources. However, evaporites could also represent lake deposits and we therefore considered only large concentrations of deposits, together with gradients reflecting a transition from coast to land (using also bauxite and coal deposits, for example).

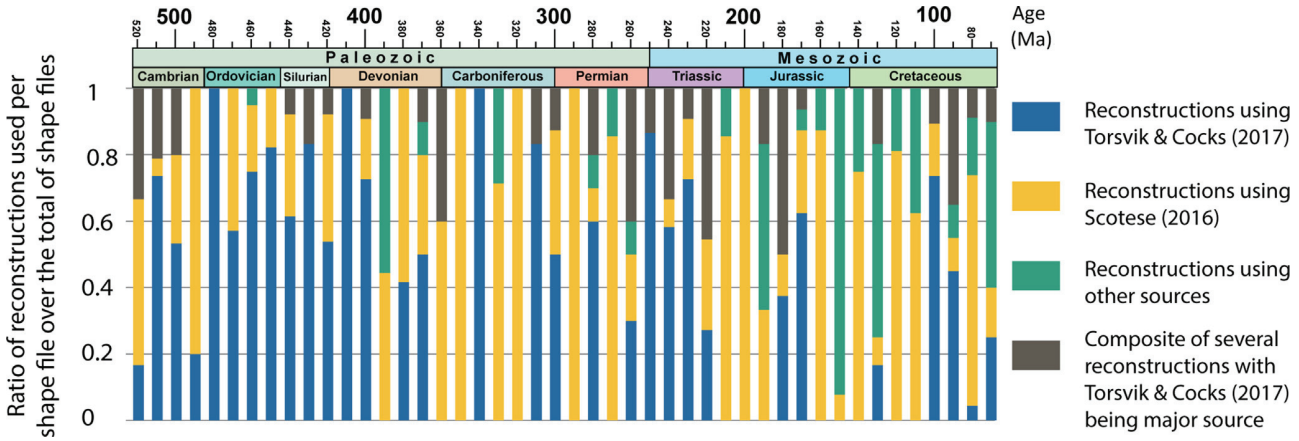

Fig. 1. Phanerozoic timescale and background information for the reconstructions used to build the exposed land maps (Fig. 2). The reconstructions of Torsvik and Cocks (2017) with minor refinements are always used to define the location of the continents, and the definition of land follows those maps when that information is available. The second most used source is Scotese (2016) exported in Gplates. "Composite of several reconstructions" represents the use of multiple sources in defining the land area (a complete list of sources per plate can be found in the supplementary data 1).

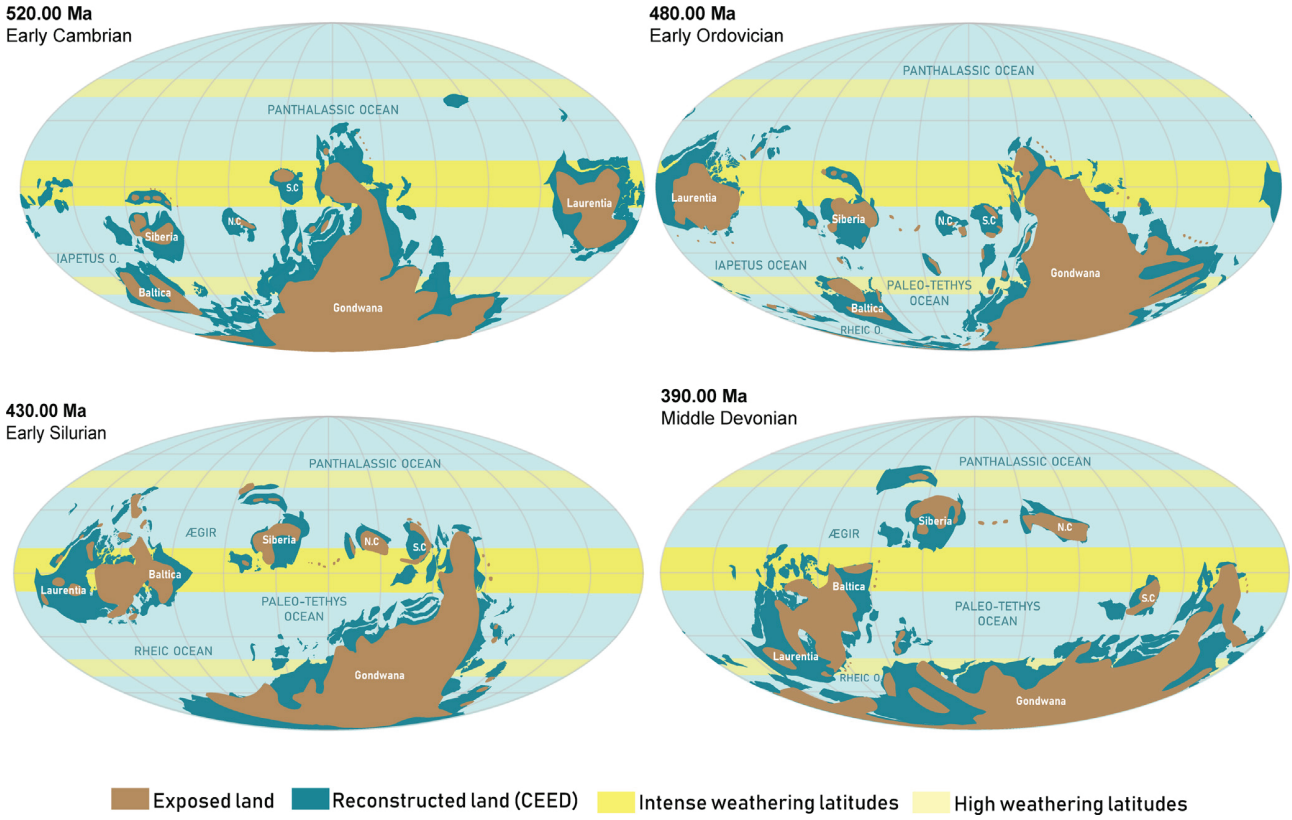

Fig. 2. Maps of reconstructed exposed land for the Phanerozoic (520–70 Ma). The maps are here presented for every ~50 Myrs but are originally made in 10 Myrs intervals (can be downloaded from http://www.earthdynamics.org/climate/exposed_land.zip). The blue shapes represent the contours of continents and microcontinents (CEED model: Torsvik and Cocks 2017 with updates). The brown shapes represent the exposed land, i.e. above sea-level. Three yellow bands denote the high weatherability latitudes. The more intense yellow band at ± 10° of the equator represents the latitudes of most intense chemical weathering (i.e. silicate weathering for CO2 models).

We constructed maps every 10 Myrs, although some of the underlying datasets have a coarser resolution. In some instances, a given 10 Myr interval was based in part on the extrapolation of patterns from before or after the interval (e.g., Early Carboniferous: Tournaisian; Late Triassic-Early Jurassic: Rhaetian to Sinemurian; Early Jurassic: Oxfordian). In terms of spatial uncertainty, our maps are generally continental in scale but also contain microcontinents and island arcs when available. However, they do not include all local variations that potentially could have an impact on the climate system (e.g., islands or microcontinents in the latitudes located within 10° of the equator).

Our maps of exposed land (Fig. 2) were constructed in GPlates and then used to compute the total area of exposed land at a given time, as well as the fraction of that area positioned within certain latitude bands. We also computed the same parameters from the reconstructions of Scotese (2016) and Blakey (2009). We assume that the maps of Blakey (2009), which were used for Paleozoic time in the GEOCLIM model (Goddéris et al., 2012, 2014), reflect exposed land and not total land area. Note that our maps with reconstructed land areas are constructed between 520 and 70 Ma, but we have extended our exposed land maps from 60 Ma to present-day using the maps of Golonka et al. (2006). These were digitized in Heine et al. (2015) and we used their digital outlines of exposed land transferred to the reconstructions of Torsvik and Cocks (2017). All our maps were crosschecked with the occurrences of terrestrial and marine fossils (www.paleobiodb.org) and the 60, 40 and 20 Ma maps underwent some refinements according to Poblete et al. (2021).

2.1.2. Estimating theoretical silicate weathering strength

Weathering plays a key role in the consumption of CO_2 (e.g., Walker et al. 1981), as first recognized by Ebelmen (1845), and Berner et al. (1983) and Marshall et al. (1988) were among the first to introduce weathering as a key parameter in geological carbon cycle modeling. Since then many studies have re-affirmed and further explored the linkages between weathering and carbon consumption (e.g. Francois and Walker, 1992: Goddéris and François, 1995; Goddéris and Joachimski, 2004; Goddéris et al., 2014, Mills et al., 2014), and systematic investigations of these linkages have been especially facilitated by the development of general circulation models (GCMs) (Barron et al., 1989; Otto-Bliesner, 1995).

The intensity of silicate weathering is dependent on rates of physical erosion and temperature but mostly on continental runoff, and is thus ultimately tied to plate tectonics and paleogeography through the changing of relief and the shifting of continental latitudes (White and Blum, 1995; Gibbs et al., 1999; West et al., 2005). Runoff is defined as the amount of discharge (mm/year) to the ocean relative to the amount of exposed land in a particular latitudinal band. Modern observations show that runoff is the highest, on average, in tropical latitudes between 10°N and 10°S and between 30 and 60°N (Oki and Kanae, 2006).

For large continents, and especially supercontinents such as Pangea, inland rainfall is strongly reduced and runoff is then limited by evaporation (Gibbs et al., 1999; Goddéris et al., 2014). Intervals associated with large continental assemblies, such as the late Paleozoic formation of Pangea, will thus tend to increase continentalisation of the climate, leading to aridity and the limiting of

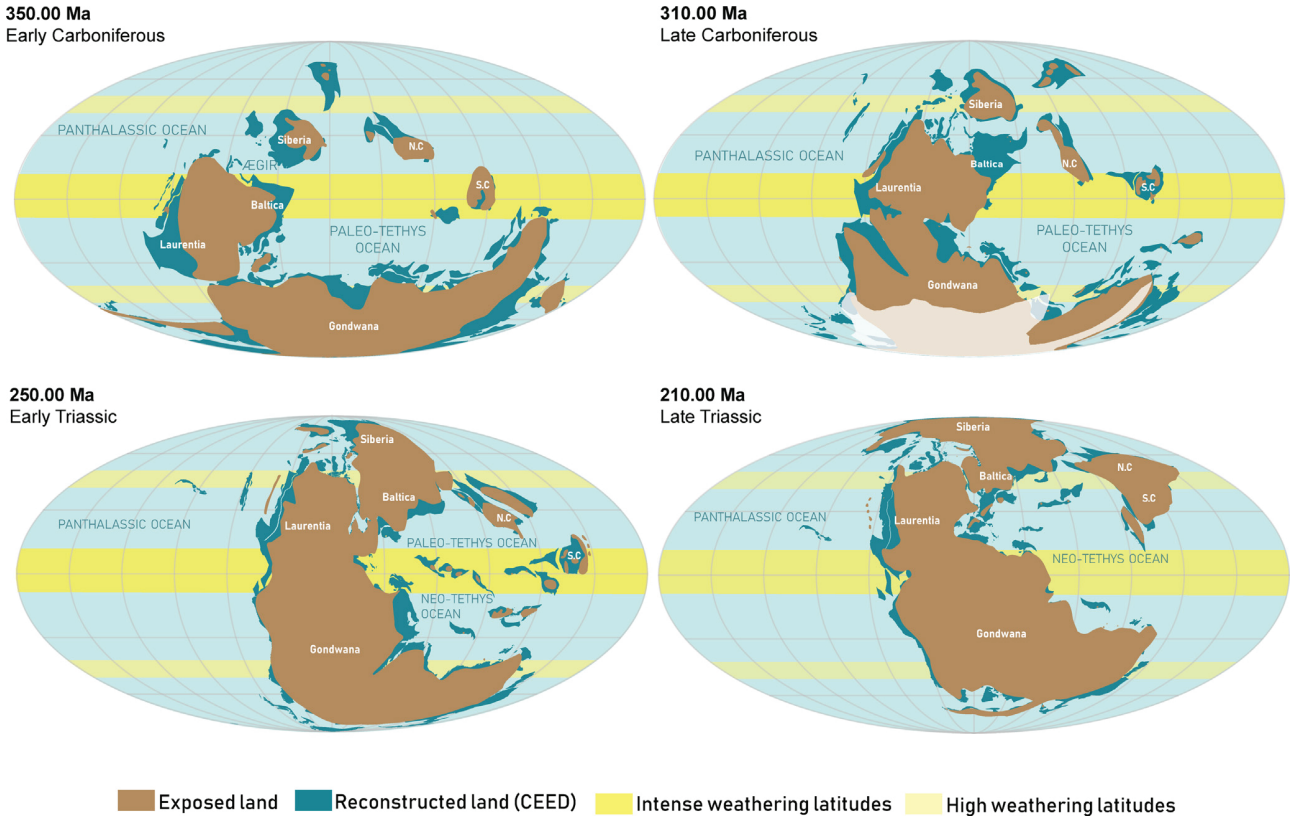

Fig. 2 (*continued*)

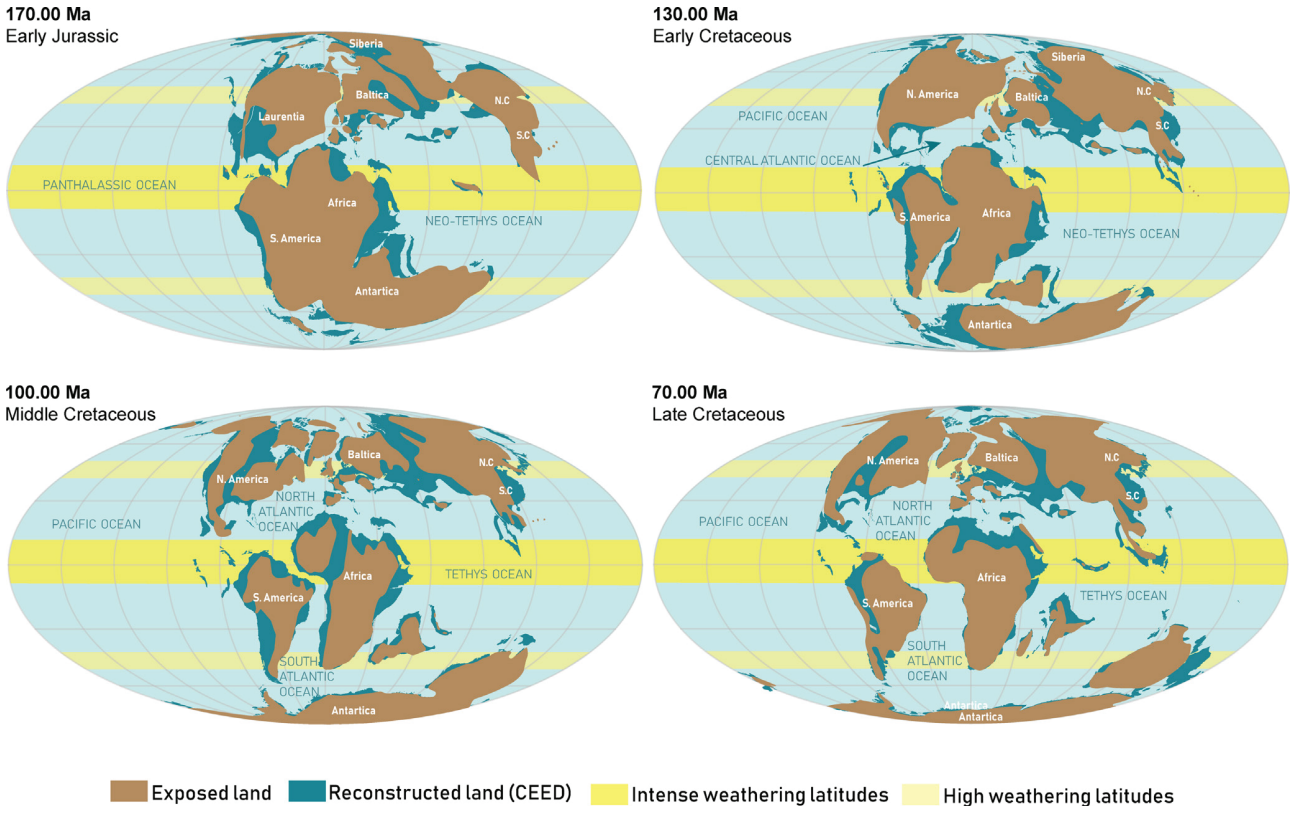

Fig. 2 (*continued*)

Table 1
Overview of the longitude filter applied to the land area calculation to assess the effect of aridity associated with continentality during and following Pangea assembly and lasting beyond its break-up (270–110 Ma) on the ±10° latitude band.

Time (Ma)	Filtered Longitudes	Exposed land Area (10^6.km^2)	Weighted Latitude	ABS Weighted Latitude	Land 10Deg (10^6.km^2)	Land 10Deg (%)
270	−45 to 20	113.79	−16.07	38.06	7.36	6.47
260	−45 to 20	128.79	−10.70	35.88	7.84	6.09
250	−30 to 5	128.27	−8.15	36.57	7.62	5.94
240	−30 to 0	133.74	−7.22	36.31	9.77	7.30
230	No filter	134.58	−5.52	36.88	16.34	12.14
220	−30 to 15	130.59	−3.52	36.27	7.29	5.58
210	−30 to 15	138.10	3.04	35.14	8.28	6.00
200	−35 to 30	131.17	11.79	37.27	4.73	3.61
190	−35 to 30	132.88	8.73	36.58	7.13	5.37
180	−35 to 30	136.99	6.07	36.97	7.01	5.12
170	−35 to 30	120.71	3.71	37.87	5.16	4.28
160	−35 to 5	106.97	6.99	37.68	5.24	4.90
150	−35 to 10	115.08	4.06	38.50	6.34	5.51
140	−35 to 10	119.59	4.57	39.37	6.97	5.83
130	−35 to 10	114.85	6.25	39.94	6.11	5.32
120	−40 to 10	105.28	12.43	40.08	5.56	5.28
110	−40 to 10	115.45	10.22	40.56	6.80	5.89

silicate weathering, and hence lower CO_2 consumption (Michel et al., 2015; Mujal et al., 2018). We tested the effect of Pangea continentalisation on simulated CO_2 levels using GEOCARBSULFvolc in Section 5. For this, we reduce the availability of land to weathering by removing from our calculations longitude bands which include land exposed at ±10° latitudes (Table 1). The longitudes removed were so chosen according to the distribution of evaporites and coal.

We furthermore test two ways of evaluating weatherability (i.e. the potential of silicate weathering activity linked to paleogeography). We first consider weatherability restricted to the equatorial latitudes between 10°N and 10°S, corresponding to the region of most intense silicate weathering. We then consider a revised approach that also considers the exposed land between ±40 and 50°, in addition to the equatorial band. This revision is based on recent studies that have used the GEOCLIM model linking paleogeography and climate, which suggest that an important contribution to the global weatherability is provided by these mid-latitudes (Goddéris et al., 2014; Goddéris and Donnadieu, 2017; Hilley and Porder, 2008; Hartman and Richards, 2014). Note that because the continents were largely confined to the southern hemisphere in the early Paleozoic, estimates of exposed land area between ±40 and 50° latitude are exclusively derived from the southern hemisphere before 340 Ma (Fig. 3b). After Pangea formation, the mean continental latitude shows a systematic northward shift (Fig. 3a) and it is only from the Early to Mid-Jurassic that the amount of exposed land is similar for the northern and southern wet belts (Fig. 3b).

In Section 2.2.4, we compare reconstructions in terms of the amount of exposed land and in particular exposed land at latitudes with a high potential for silicate weathering (i.e high runoff and high temperature) for the different sets of reconstructions outlined in Section 2.1.1. Notably, these reconstructions do not consider relief, which greatly impacts weathering intensity, the development of thick regoliths that can limit silicate weathering efficiency (Ollier and Pain, 1996) or the occurrence of extensive lava blankets on the Earth's surface (following the emplacement of large igneous provinces) that can enhance silicate weathering. The estimation and implementation of such parameters into our paleogeographic model thus remains an important opportunity for future work.

2.2. Paleogeographic reconstructions and weatherability

2.2.1. Early Paleozoic (Cambrian to Silurian)

In the early Paleozoic, nearly all the continents were located in the southern hemisphere (Fig. 2, plate 1: 520–420 Ma; Fig. 3a). Gondwana, the largest continental unit, which mostly formed in the late Neoproterozoic, stretched from the South Pole to the equator (western Australia) for most of the Paleozoic. Multiple other continents (including Baltica, Siberia, and North China) drifted progressively northward during the early Paleozoic, resulting in a string of independent landmasses along the equator in Ordovician and Silurian time. However, the then-northern part of Gondwana (western Australia) and Laurentia formed most of the exposed land at the equator for most of the early Paleozoic.

The northern hemisphere was dominated by the Panthalassic Ocean at this time, but another large ocean was present in the southern hemisphere, the Iapetus Ocean, which separated Laurentia from Baltica and Gondwana. The Iapetus had reached its zenith in the Cambrian and then progressively shrank during the Ordovician (Fig. 2, plate 1: 520–440 Ma) before disappearing entirely during the mid-Silurian collision of Baltica, Avalonia, and Laurentia that formed Laurussia (Fig. 2, plate 1: 420 Ma). Another important ocean, the Rheic Ocean, opened at ~480 Ma between Gondwana and Avalonia and remained an important ocean until ~320 Ma when Gondwana, Laurussia, and intervening terranes collided to form the supercontinent Pangea (Fig. 2, plate 2: 310 Ma).

The total exposed land area ($Land_{EXP\_TOTAL}$) was relatively small and stable during the early Paleozoic (Fig. 4a) but the exposed land within ±10° of the equator and between ±40 and 50°, i.e. latitudes with potentially high weatherability ($Land_{EXP\_Wtot}$), increased sharply between 510 and 460 Ma. A Phanerozoic maximum of 39% of the total exposed land (Fig. 4b, black curve) was reached by 460 Ma before declining again to only 20% by 380 Ma. Throughout this time, the latitudes between ±40–50° held a relatively low proportion of exposed land ($Land_{EXP\_W40/50}$, Fig. 4b, blue curve) compared with the remainder of the Phanerozoic, but also note that most continents were essentially located in only one hemisphere in the early Paleozoic (Fig. 3a). We observe particularly low values for $Land_{EXP\_W40/50}$ at 440 Ma, associated with a more than 5% drop from the Late Ordovician. Conversely, the area of exposed land within ±10° ($Land_{EXP\_W10}$) peaks sharply in the Middle-Late Ordovician, when it reached the highest theoretical tropical weathering contribution for the entire Phanerozoic (~23% of $Land_{EXP\_TOTAL}$) (Fig. 4b, red curve).

Some global sea-level curves suggest sea-levels increased during the early Paleozoic (peaking in the Late Ordovician) but this is not supported by our flooded land estimates (the inverse of the total exposed land), which are indicative of high but fluctuating sea-levels throughout the early and mid-Paleozoic (Fig. 4c). A low of about 23% of flooded land between 450 and 440 Ma coincides

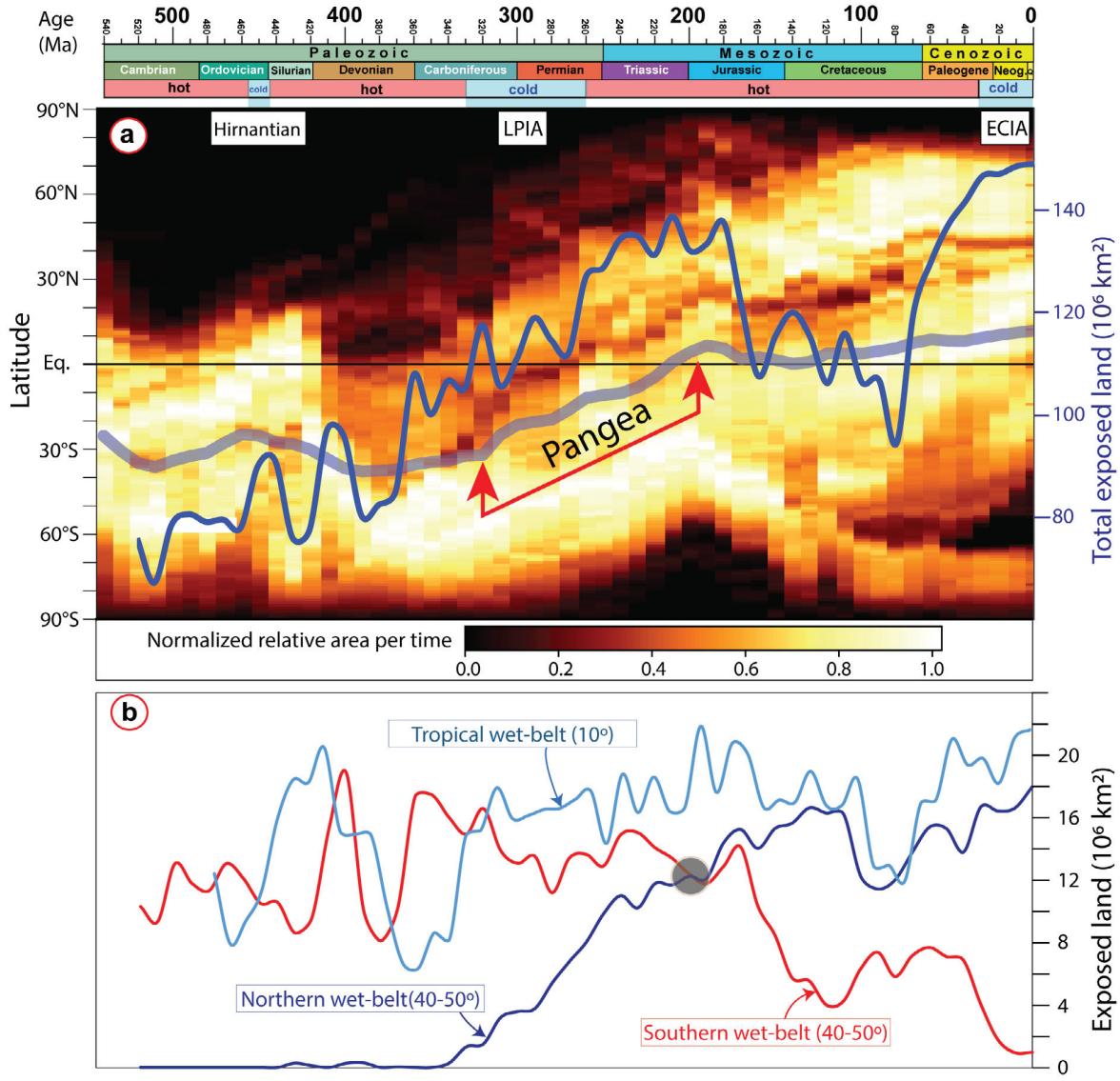

Fig. 3. (a) Phanerozoic timescale with greenhouse (hot) versus icehouse (cold) conditions. We consider three main icehouses (i.e Hirnantian, Late Paleozoic Ice age LPIA and End Cenozoic ice age ECIA). However, glacial deposits of latest Devonian, earliest Carboniferous age and the Middle-Late Jurassic probably witnessed episodes of cold climate (Dera et al., 2011). The heat-map shows the latitudinal distribution of continental area (lighter regions) as a function of time (Torsvik et al., 2020). The south polar areas remain dark even though it was occupied by continents several times in the past (including at present-day) because its area is small compared to the area of lower latitudes (the pole itself has no area). The thick grey curve shows the average continental paleolatitude (weighted by area) while the blue curve corresponds to the percentage of exposed land (10^6 km^2). Our model covers the period from 520 to 70 Ma followed by a revision of the model from Golonka et al. (2006; digitized in Heine et al., 2015) and Poblete et al. (2021) after 70 Ma. (b) Exposed land in the southern and northern hemisphere belts between 40 and 50° (wet belts) as well as within ±10°. Note the total lack of exposed land in the northern belt until the Carboniferous (~340 Ma) because all the continents were essentially located in the southern hemisphere during the early Paleozoic (panel (a)). During the Early Jurassic, the amount of exposed land is similar in the northern and southern wet belts and from the mid-Jurassic (~170 Ma); the northern wet belt starts to dominate over the southern wet belt. The grey circle highlights that 'cross-over'.

with the end-Ordovician (Hirnantian) icehouse, which may have lasted less than a million years (Cocks and Torsvik, 2020).

2.2.2. Late Paleozoic (Devonian to Permian)

By Early Devonian time, Gondwana had rotated such that South Africa occupied the South Pole, but the landmass still stretched from the pole to the equator (western Australia) and the largest part of its exposed land was located between 40 and 90°S (Fig. 2, Plate 1: 390 Ma). Siberia and North China continued drifting northward in Devonian time, vacating the equatorial positions they had in the Ordovician and Silurian, and reached latitudes of 10–40°N by the early Carboniferous (Fig. 2, Plate 2, 350 Ma). At 350 Ma, only the northern areas of Laurussia and South China were located between 10°N and 10°S. The Rheic Ocean between Laurussia and Gondwana had narrowed considerably by this time, and closed completely during the late Carboniferous formation of Pangea at 320 Ma (Fig. 2, plate 2, 310 Ma).

Pangea drifted slowly northwards (Fig. 3a) and brought the interior of the former Laurussia to an equatorial position by the late Carboniferous. By the beginning of the Permian (300 Ma), the continents were widely spread in latitude (stretching from the South Pole to at least 60°N) but restricted in longitude. Most

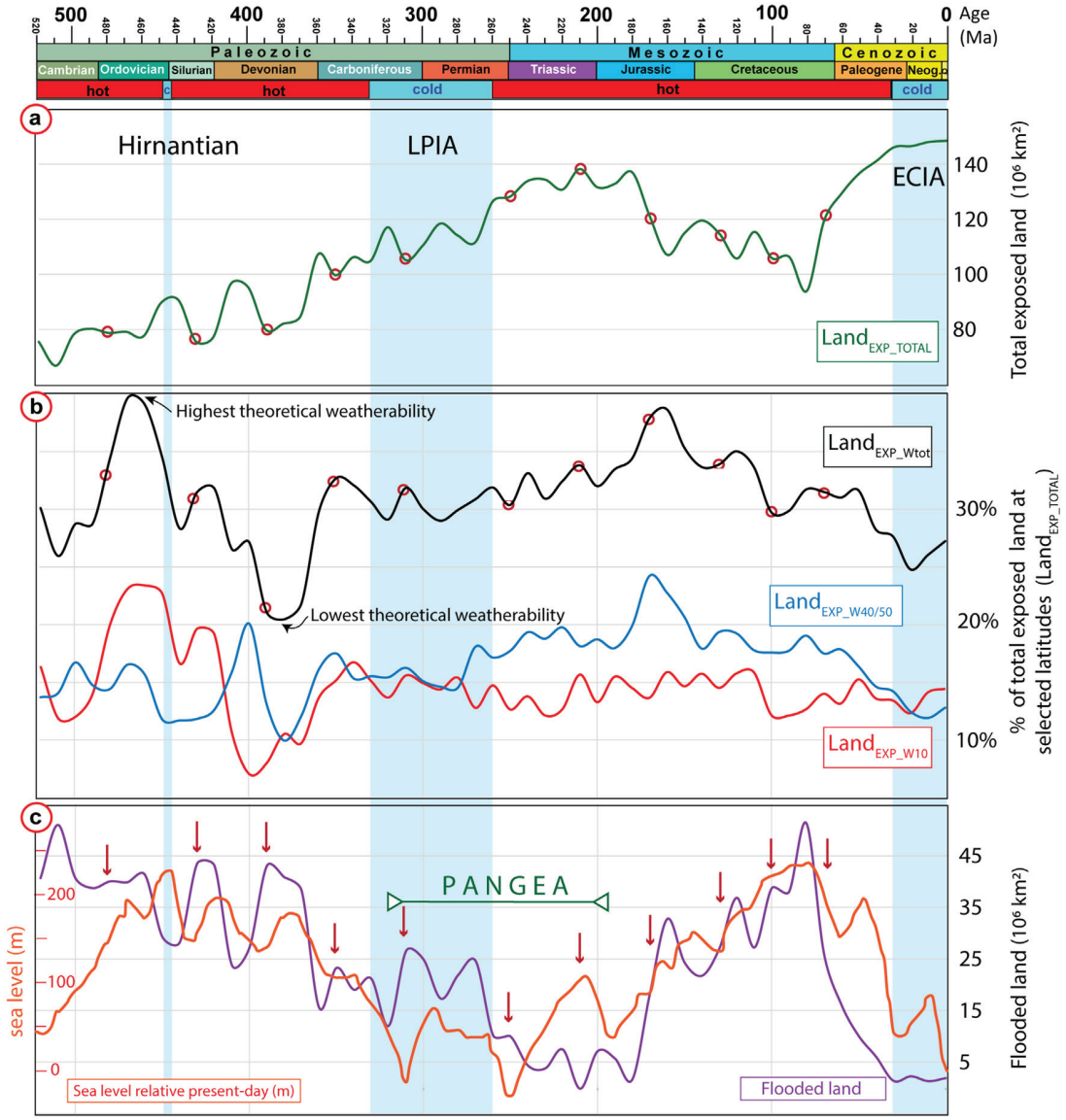

Fig. 4. Timescale with greenhouse (hot) versus icehouse (cold) conditions for the past 520 Myrs (see Fig. 3 caption) and (a) $Land_{EXP\_TOTAL}$, the total amount of exposed land (in millions of square kilometers: 10^6 km^2). (b) Amount of exposed land for selected latitude bands of high theoretical weatherability, i.e. $Land_{EXP\_W10}$ at the tropics (±10°, red curve) and $Land_{EXP\_W40/50}$ at the northern and southern wet belts (±40–50°, blue curve) expressed as a percentage of total exposed land. The black curve, $Land_{EXP\_Wtot}$, is the total theoretical weatherability (combining ±10° and ±40–50°). (c) Relative sea-level curve (stratigraphic-based: Haq and Al-Qahtani 2005; Haq and Schutter 2008) compared with our estimates of flooded land (in millions of square kilometers: 10^6 km^2). Flooded land (Total land - Exposed land) is scaled so that highs and lows mimic the global sea-level curve. The red arrows and red circles (panel a-b-c) represent times of reconstructed maps in Fig. 2. ECIA, End Cenozoic Ice Age; LPIA, Late Paleozoic Ice Age.

of the landmasses were located between 60°W and 60°E (Fig. 2, plate 2) and Pangea was surrounded on three sides by the large Panthalassic Ocean. To the east, Pangea was flanked by the wedge-shaped Paleotethys Ocean. Pangea never actually included all continental crust, and several Asian continental blocks were separated from the supercontinent by the Paleotethys (Fig. 2, plate 2: 310 Ma). In the early Permian, a string of terranes spalled off the northeastern margin of Gondwana, commencing the opening of the Neotethys Ocean, which then grew quite wide already by 250 Ma at the expense of a narrowing Paleotethys (Fig. 2, plate 2, 250 Ma).

During the Early Devonian, from 410 to 390 Ma, $Land_{EXP\_TOTAL}$ declined by ~17 mill. km^2 (15%) (Fig. 4a). At the same time, $Land_{EXP\_W10}$ dropped sharply and only 8% of $Land_{EXP\_TOTAL}$ occurred within those tropical latitudes from 400 to 390 Ma (Fig. 4b, red curve), reducing $Land_{EXP\_Wtot}$ to about 20% of $Land_{EXP\_TOTAL}$ and marking the lowest theoretical weatherability recorded for the entire Phanerozoic (Fig. 4b, black curve). In the Late Devonian $Land_{EXP\_TOTAL}$ increased again by more than 30 mill. km^2 (30%), reaching values above 112 mill. km^2 by 360 Ma, and then fluctuated around 115 mill. km^2 during the Carboniferous and Permian (Fig. 4a). $Land_{EXP\_Wtot}$ likewise climbed sharply in the Late Devonian to earliest Carboniferous and then fluctuated around 33% of $Land_{EXP\_TOTAL}$ for the remainder of the late Paleozoic (Fig. 4b). This marked increase in $Land_{EXP\_TOTAL}$ occurred seemingly in concert with decreasing sea-levels (Haq and Al-Qahtani, 2005; Haq and Schutter, 2008) which appears to have started 10 Myrs before, and is displayed by both our flooded land estimates and reconstructed sea-levels (Fig. 4c). The lowest sea-level (and

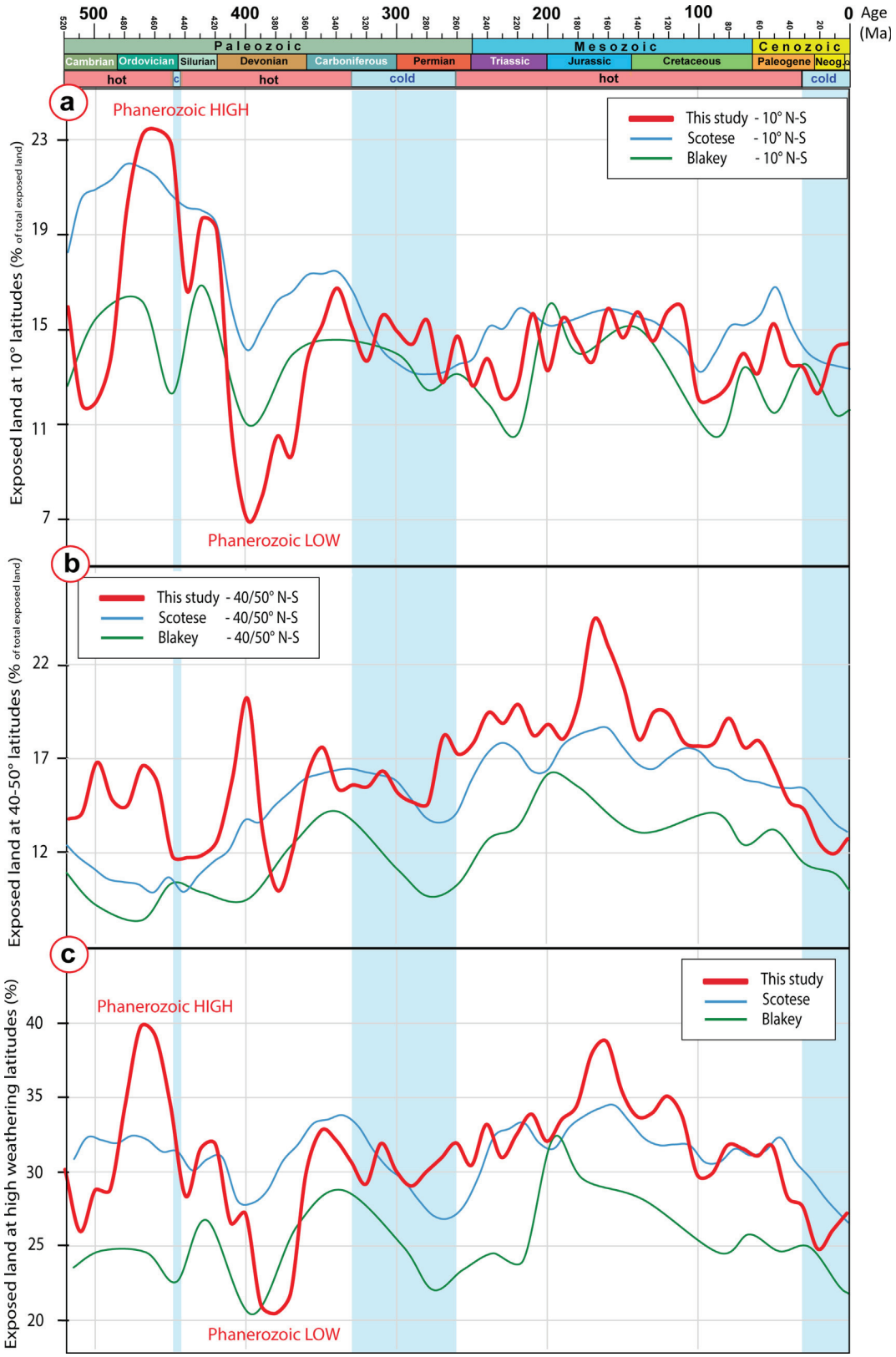

Fig. 5. Timescale with greenhouse (hot) versus icehouse (cold) conditions for the past 520 Myrs (see Fig. 3 caption) and (a) curves of exposed land at ±10° latitudes for three different reconstructions. The red curve displays the values estimated from our maps (as in Fig. 4b). The blue curve was *calculated* from the reconstructions of Scotese (2016) and the green curve was *estimated* from the reconstructions used in GEOCLIM (Blakey, 2009). (b) Same as in (a) but for latitudes ±40-50°. (c) Panels (a) and (b) combined, showing theoretical weathering activity in the tropics and the northern/southern wet belts.

correspondingly largest area of exposed land) from Paleozoic time was reached around 250 Ma, at the transition between the Paleozoic and Mesozoic eras.

2.2.3. Mesozoic-Cenozoic

Pangea drifted slowly but continuously northwards after it formed (Fig. 3a), and by the early Mesozoic the continents were spread in latitude from pole-to-pole (Fig. 2, plate 2, 250 Ma). Laurentia abandoned its equatorial position during the Triassic, whereas the northern part of Gondwana (North Africa and South America) migrated progressively into the equatorial realm. Three oceans dominated: the Panthalassic surrounded Pangea on three sides, whereas to the east the Paleotethys was shrinking and the Neotethys widening by the northwards movement of the Cimmerian and Sibumasu blocks (Fig. 2, plate 2, 250 Ma).

The most important phase of Pangea breakup started when the Central Atlantic Ocean opened in the Early Jurassic (~195 Ma), and by around 170 Ma the former Laurussia and Gondwana were separated by 250–400 km (Fig. 2, plate 3 170 Ma). Around that time, Gondwana also started to break up, leading to the separation of India, Madagascar, East Antarctica, and Australia from the rest of Gondwana (Fig. 2, Plate 3, 130 Ma). At the same time that Gondwana was disintegrating, Eurasia was amalgamating, and East Asia became fully part of Eurasia at around 130 Ma, when the opening of the South Atlantic started. By the Late Cretaceous, India had separated from Madagascar (Fig. 2, Plate 3, 70 Ma). During most of the Mesozoic, Africa and South America did not move much in latitude and their northern parts occupied the equatorial regions.

$Land_{EXP\_TOTAL}$ was high (~130 mill. km^2) from the late Permian to the mid-Jurassic but dramatically decreased between 180 and 160 Ma (Fig. 4a). However, $Land_{EXP\_Wtot}$ increased greatly during the late Paleozoic and early Mesozoic, reaching a peak at 160 Ma (Fig. 4b, black curve). During the Mesozoic, $Land_{EXP\_W10}$ showed less variability and fluctuated between 12% and 16% of $Land_{EXP\_TOTAL}$ (Fig. 4b, red curve). Conversely, $Land_{EXP\_W40/50}$ increased sharply between 190 and 170 Ma (blue curve in Fig. 4b), reaching the Phanerozoic maximum of around 22% of $Land_{EXP\_TOTAL}$ and producing the aforementioned peak in $Land_{EXP\_Wtot}$ (black curve in Fig. 4b). $Land_{EXP\_TOTAL}$ increased sharply (by ~60%) between 80 and 40 Ma before stabilizing close to present values for the rest of the Cenozoic (Fig. 4a). Conversely, $Land_{EXP\_Wtot}$ remained similar during the same period before decreasing between 50 and 20 Ma from 31 to 27% of $Land_{EXP\_TOTAL}$ (black curve in Fig. 4b).

Eustatic curves suggest that sea-level rose continuously over the Mesozoic (Haq and Al-Qahtani, 2005; Haq and Schutter, 2008), from the Phanerozoic low at 250 Ma to the Phanerozoic high in the Late Cretaceous (Fig. 4c). Sea-level then dropped precipitously in the latest Cretaceous and through to the present-day. These first-order eustatic trends (which are relatively well-defined for the Mesozoic-Cenozoic) are closely reflected by the flooded continental area curve derived from our exposed land maps.

2.2.4. Comparison of reconstructed weatherability with other studies

In Fig. 5 we have compared our estimated theoretical weatherability with those derived from the reconstructions of Blakey (2009) and Scotese (2016), and the diagram is separated into % exposed land at tropical latitudes (Fig. 5a), the northern/southern wet belts (Fig. 5b) and the total theoretical weatherability (Fig. 5c). In general, our model shows more variability than the two others do. In terms of total theoretical weatherability (Fig. 5c), our model shows a pronounced increase in the early Paleozoic, peaking in the Late Ordovician (40%), just before the Hirnantian glaciation. Although that peak in the total theoretical weatherability begins to abate before the onset of the Hirnantian glaciation, we note that the peak in the weatherability at 10° latitudes is sustained until the glaciation began (Fig. 5a). We consider this to reflect a meaningful link between that glacial event and weatherability, and more specifically the amount of land between the latitudes of 10°N and 10°S, where silicate weathering is about 20 times more intense than in the northern and southern wet belts (Goddéris et al., 2014). Enhanced continental weathering and CO_2 drawdown may therefore have been a contributing factor to the onset of that end-Ordovician glaciation (e.g., Kump et al., 1999; Goddéris et al., 2017). According to our model, this Late Ordovician peak of high theoretical weatherability is the highest recorded in the Phanerozoic, but it is absent in the two other models. This discrepancy is principally linked to the different positions of Siberia and Laurentia. In our reconstruction, Laurentia and Siberia but also the northern part of Baltica are included in the calculation of land available within the 10° latitudes whereas in reconstructions from Scotese and Blakey, they are above and below this 10° boundary.

During the Silurian and Devonian, there is a general (but oscillating) decrease to about 20% of all exposed land near the Devonian-Carboniferous boundary (~360 Ma), which is the lowest recorded for the Phanerozoic in our reconstruction. However, the three models show a drop immediately before in the ±10° latitudes triggering a general low for the reconstructions of Scotese and Blakey at 400 Ma. All three models then show a sharp increase in the total theoretical weatherability up to the mid-Carboniferous (Fig. 5a), with a peak in the ±10° latitudes just prior to the initiation of the Late Paleozoic Ice Age (LPIA). We consider the main LPIA phase to have lasted from 330 to ~275 Ma (Torsvik and Cocks, 2017) but minor glacial deposits can be tracked to about 260 Ma (e.g., Fielding et al., 2008; Montañez and Poulsen, 2013; Soreghan et al., 2019; Scotese et al., 2021). Both the Scotese and Blakey reconstructions display a drop in land at weatherability latitudes during the LPIA, whereas ours stay stable. The cause for this discrepancy is the difference in the modelled flooded area around Gondwana mostly in the latitudes 40-50°S and additionally over Laurussia and northern Gondwana for Scotese's reconstructions.

In the early Mesozoic, our model of total theoretical weatherability oscillates about a gradually increasing trend and ends with a pronounced peak in the Late Jurassic at 160 Ma (Fig. 5c, red curve). By comparison, the model of Scotese shows a more modest peak due to smaller fluctuations in the ±40–50°. However, the model of Blakey shows an earlier peak of total theroritical weatherability at 200 Ma before engaging a decrease lasting into the Cenozoic. This decrease is also observed in our reconstructions and Scotese's but from the mid-Jurassic.

Our model shows the highest variability during the early and mid-Paleozoic and is dominated by changes in exposed land at low latitudes (±10° red curve in Fig. 5a). The three models show very different characteristics but the reconstructions of Blakey (2009) show generally much less land in latitudes of potentially high weatherability compared to both our study and that of Scotese (2016) (Fig. 5c). This smaller proportion of land would lead to an underestimation of the silicate weathering potential and linked CO_2 sink in long-term climate models with the use of this model compared to Scotese's or ours. Generally, the large difference observed can be attributed to more flooding modelled on the coast of Gondwana as well as to the fact that many fewer islands and microcontinent are mapped in the work of Blakey (2009). However, this could also be due to the extrapolation necessary between the available maps of Blakey over the Phanerozoic which has a lower time resolution than the two other models discussed here.

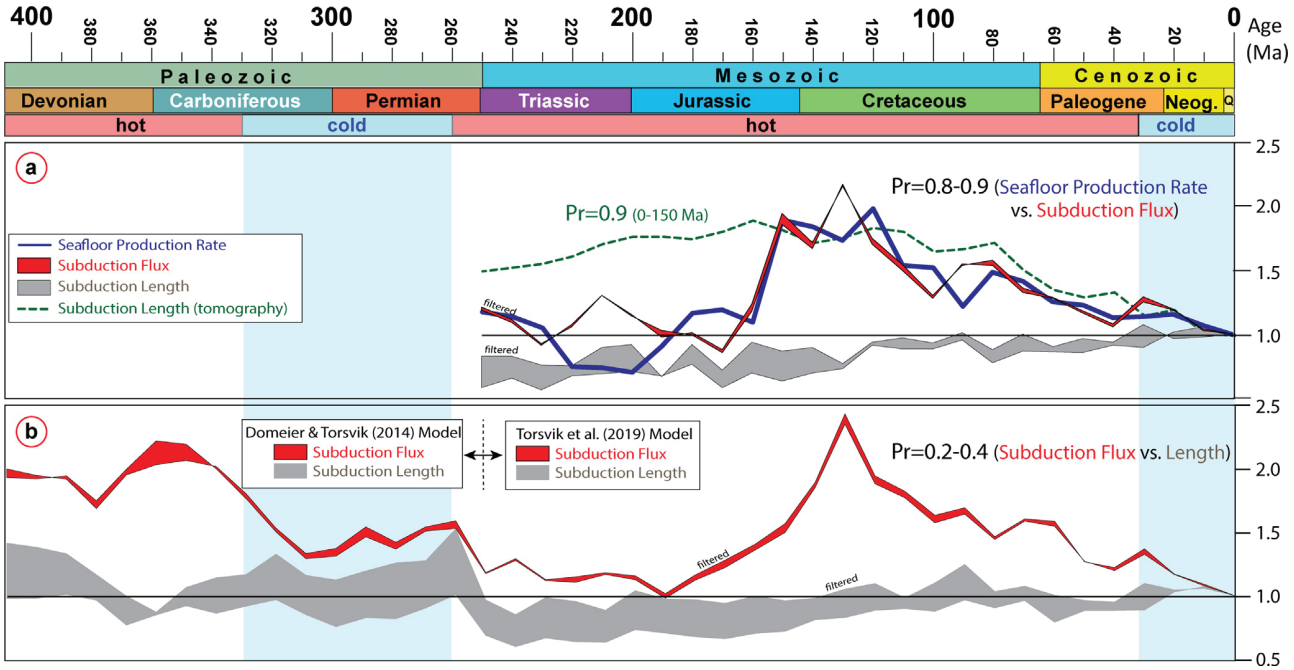

Fig. 6. Timescale with greenhouse (hot) versus icehouse (cold) conditions for the past 410 Myrs (see Fig. 3 caption). (a) Seafloor production rate from Coltice et al. (2013) (thick blue line) compared with our calculations of subduction lengths and fluxes from the same full-plate model (extension of the Seton et al. 2012 model) and subduction lengths from seismic tomography from van der Meer et al. (2014) (stippled green curve). Lengths and fluxes are shown with (upper part of shaded regions) and without filter cut-offs (see text). P_r is the Pearson product-moment correlation coefficient (r), a dimensionless index ranging from −1.0 to 1.0 that reveals the extent of a linear relationship between two data sets. Seafloor production rate and subduction flux are well correlated for the past 160 Myrs with P_r = 0.84 (unfiltered) and P_r = 0.86 (filtered). For the past 250 Myrs P_r = 0.76 (unfiltered) and P_r = 0.79 (filtered). Notice that subduction lengths from this full-plate model show much less variability through time and are strikingly different from that of van der Meer et al. (2014). Van der Meer et al. (2014) and Coltice et al. (2013) curves compare well for the past 150 Myrs (P = 0.9). (*b*) Calculated subduction lengths and fluxes from Domeier & Torsvik (2014) and Torsvik et al. (2019; Model R) after 250 Ma. Subduction fluxes and lengths are non-correlated (P = 0.2–0.4 depending on filtering), implying that variation in fluxes depends on rate-variations and not lengths. Note a change in subduction lengths when switching between the two full-plate models.

3. Estimating degassing for long-term carbon models

The most important long-term solid Earth degassing occurs at continental arcs (including metamorphic decarbonation; Caldeira, 1992; Lee and Lackey 2015) and continental rifts, and to a lesser extent at island arcs and mid-ocean ridges (Lee et al., 2020). The global inputs from these non-plume carbon sources vary on geological timescales, predominantly due to changes in seafloor production/-consumption rates, and those rates are thus commonly employed in long-term CO_2 models as a proxy for degassing on geologic time scales (Berner, 2004; Berner, 2006; Royer et al., 2014; Goddéris and Donnadieu 2017; Mills et al., 2019). However, the specific estimates of those rates which have been widely employed in carbon cycle models are rather poorly constrained. The longest such proxy estimations have been derived from global sea-level fluctuations, given that changes in spreading rates (and thus mid-ocean ridge volume) are the most important driver of sea-level variations (Conrad, 2013). In long-term carbon cycle models, this parameterization of degassing is expressed as a time-dependent rate relative to present-day and dubbed f_{SR} in GEOCARBSULFvolc. This term was originally defined as the '*seafloor creation rate*' but is now more generally treated as a proxy for rates of 'plate tectonic degassing', 'plate tectonic activity' or 'solid Earth degassing'. In accordance with its established use, we also adopt the term f_{SR} to describe the degassing rate for long-term carbon models in this study.

3.1. Degassing since 250 Ma: Rates of crustal production and destruction vs. subduction lengths

Back to 83 Ma, seafloor production rates can be calculated with a high degree of confidence from oceanic lithospheric age-grids derived from marine magnetic anomalies. Coltice et al. (2013) estimated Mesozoic-Cenozoic seafloor spreading rates (f_{SR}) by computing the 0–8 Myrs area from oceanic age-grids, as a moving average over the studied period, using an extension of the Seton et al. (2012) full-plate model. Normalized to today (=1), their estimation of f_{SR} shows modern-day-like rates (within a factor of ±0.3) between 250 and 160 Ma, peak rates in the Late Jurassic-Early Cretaceous, and then, after 120 Ma, a gradual decline to modern-day rates (blue curve in Fig. 6a). In our models developed using GPlates, seafloor production rate and subduction flux must be equal due to the continental area being held fixed, and so any differences observed between them are due to the application of filters (see below). The subduction flux calculated from the same but unfiltered full-plate model used by Coltice et al. (2013), when compared against their seafloor production curve, yields a Pearson r-correlation (P_r) of 0.8 and 0.9 over the 0–250 Ma and 0–160 Ma range, respectively (where P_r can range from −1 to 1 and P_r = 1 denotes a perfect positive relationship). Although expected, this confirms that the rate of seafloor spreading and the subduction flux, as computed from the same model, closely correspond (Fig. 6a).

In contrast to the direct computation of f_{SR} or the subduction flux, van der Meer et al. (2014) proposed that those fluxes could be more simply estimated from the time-dependent length of subduction zones. They mapped out the lateral extent of slabs from seismic tomography and then converted those to time-dependent subduction zone lengths using a geometrical correction based on a model of mantle density increasing with depth. By assuming the present-day, globally averaged rate of convergence (6 cm/yr., Schellart et al., 2008) to be constant through time, they estimated a normalized subduction flux that grossly matched the f_{SR} curve of

Coltice et al. (2013) for the past 150 Ma (P_r = 0.9, green stippled curve in Fig. 6a). However, if we repeat the same experiment on the plate model used by Coltice et al. (2013), we find that the time-dependent length of subduction zones shows very little variation with time (grey-shaded curves in Fig. 6a). This means that the variations earlier observed in the direct subduction flux calculation must be associated with changes to global convergence rates *and not subduction lengths* as suggested by van der Meer et al. (2014). By extension, this also means that variations in the rate of seafloor production are not simply due to changing ridge/rift lengths, but also to fluctuations in the globally averaged spreading rate. Many other studies employ normalized subduction lengths, continental rift lengths, or a hybrid combination of these two measures, to derive estimates of plate tectonic degassing (e.g. Mills et al. 2014, 2017), but the availability of full-plate models should now permit the community to work with convergence/divergence fluxes rather than boundary lengths. Interestingly, however, the coincidentally good correlation that van der Meer et al. (2014) observed between subduction lengths (assuming a constant average convergence rate) and the seafloor production rate curve of Coltice et al. (2013) back to 150 Ma implies there are important intra-oceanic subduction zones lengths which are missing (not represented) in the model used by Coltice et al. (2013).

To constrain the seafloor production rate through time we calculated the subduction flux directly from full-plate models, after some filtering (as described in Domeier et al., 2018) to remove artefacts associated with kinematic imperfections that are invariably present in full-plate models. For example, many transform boundaries are not perfect small-circles, and will therefore have some small component of transpression or transtension that is unlikely to have resulted in true subduction/spreading and should therefore be filtered out. Similarly, subduction zones and spreading centers may, for some short time-interval, exhibit unrealistic relative motions of small magnitude (e.g. divergence along a subduction zone). It is also important to average calculations over a time interval that is commensurate with the temporal resolution of the model itself. Our calculations were conducted in 10 Myr intervals and we imposed both orthogonal velocity (0–1 cm/yr.) and transform (0–20°) cut-off filters. However, it is worth noting that the subduction flux calculation is rather insensitive to even moderate filtering (as the filtered contributions are normally of very small magnitude), whereas the estimation of subduction lengths is much more sensitive to such filtering (Fig. 6a); incidentally, this is another reason why convergence/divergence fluxes present a better proxy for plate tectonic degassing.

3.2. Degassing since the Early Devonian (410 Ma) based on subduction fluxes

Investigation of a more recent full-plate model (Fig. 6b), corrected for published flaws in the reconstruction of the Pacific-Panthalassic (Torsvik et al., 2019), also demonstrates that the subduction flux and subduction lengths are uncorrelated (P_r = 0.2–0.4, dependent on filtering). In fact, all published full-plate models (e.g., Torsvik et al. 2010; Seton et al. 2012; Matthews et al., 2016; Torsvik et al. 2019) that we have analysed show that the subduction flux is linked to variations in the average convergence rate whilst subduction lengths vary little with time (Fig. 6).

In Fig. 6b, subduction fluxes and lengths were calculated from two separate models, i.e. the Mesozoic-Cenozoic model of Torsvik et al. (2019), which is based on refinements of the Matthews et al. (2016) model for the past 250 Myrs, and the late Paleozoic model of Domeier and Torsvik (2014), which extends backwards from 250 to 410 Ma. The subduction flux curve is almost identical to that calculated in Domeier et al. (2018) and Torsvik et al. (2020). During the Devonian and early Carboniferous (410–340 Ma), the degassing rate was approximately twice that of present-day, and during the late Carboniferous and Permian, the degassing rate was approximately 1.5 times present-day rates. Interestingly, the mid-Carboniferous transition between those distinct rates (decline from >2 to <1.5 present-day rates) started shortly before the onset of the Late Paleozoic Ice Age (LPIA) at ~330 Ma, and continued until shortly after Pangea assembly at ~320 Ma. Following a mostly stable but slowly rising flux in the late Carboniferous and Permian (through the LPIA), there was a sharp drop at the Paleozoic-Mesozoic boundary, whereafter the subduction flux reached the lowest levels of the Phanerozoic (around 1.2) during the Triassic and Early Jurassic (Fig. 6b). Conspicuously, subduction lengths, which otherwise show very little variation with time, also show a pronounced drop near the Paleozoic-Mesozoic transition at around 250 Ma; we therefore suspect that this is an artefact of the switch between the different full-plate models. During the Jurassic, there was a systematic increase in the subduction flux, which peaked in the Early Cretaceous, at 130 Ma (Fig. 6b). Subsequently, in the remainder of the Mesozoic and Cenozoic, the subduction flux progressively waned toward modern times.

3.3. Constraining degassing in deep time: The use of detrital zircon ages

Plate models generally become increasingly uncertain with increasing time. Prior to Jurassic time the reconstructed oceanic lithosphere is entirely synthetic (Torsvik et al., 2010) and before Pangea formed (~320 Ma) the longitudinal location of the continents is not strictly known. In recent years, a method using deep mantle structures as a reference frame for surface movements to resolve paleolongitude has emerged (Torsvik et al., 2014). That method is exploited in the reconstructions herein, as well as in the full-plate model of Domeier and Torsvik (2014), but the validity of this method in deep time is debated. It is therefore prudent to seek additional, complementary methods that can quantify the subduction flux and thus solid Earth degassing in deep time. One exotic pathway could be to consider the history of geomagnetic reversals, which may be tied to the global subduction budget since subducted slabs affect the core-mantle boundary heat flow and thus the geodynamo (Hounslow et al. 2018). However, the history of geomagnetic polarity is not generally well-defined prior to the Permian, and the specifics of this relationship are still poorly resolved. Another more promising pathway is to consider the age-frequency relationship of detrital zircons, the production of which may mimic true variations in the subduction flux, both regionally and globally (Domeier et al., 2018). Indeed, the use of zircon abundances to infer changes in plate tectonic degassing and greenhouse vs. icehouse climates has already been pioneered by McKenzie et al. (2016).

Here we further explore the use of detrital zircon age distributions to estimate the subduction flux. To accomplish this we queried the large global zircon database of Voice et al. (2011; V11). Although there are larger, more recent databases available (e.g. Puetz et al. 2018), we elected to use V11 because it includes convenient tectonic environment metadata tags, which make it easier to extract zircon ages that can be linked to arc environments. V11 and the database of Puetz et al. (2018), however, are broadly similar, with highs and lows in zircon abundance observed at approximately the same ages throughout Earth history (see also Domeier et al. 2018), and they yield a P_r correlation of 0.92 over the entire studied age range.

The V11 database was first quality-filtered to eliminate imprecise/poor data, which was achieved by removing: *(i)* all results associated with a one-sigma (1σ) level error that exceeded 20% of the best-estimated age of the grain, *(ii)* all results with a best-estimated age less than the youngest-estimated depositional age

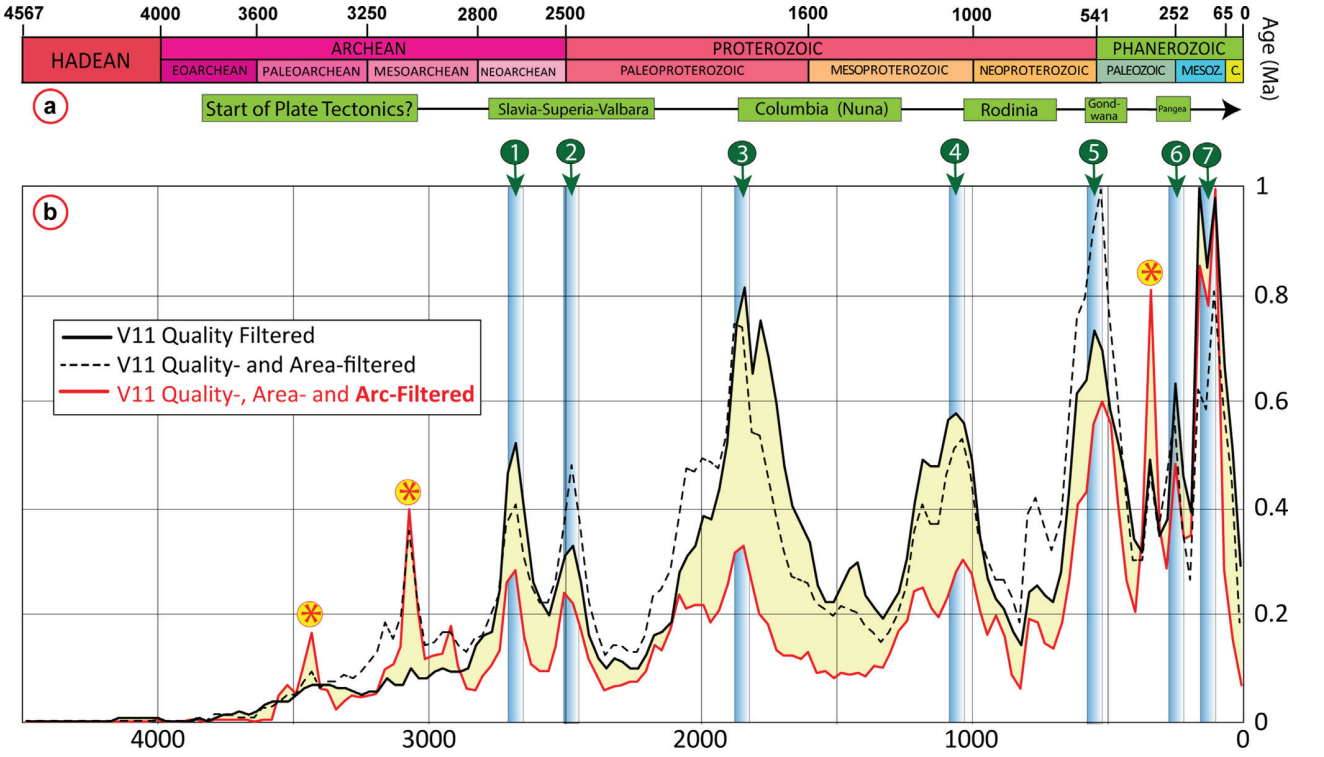

Fig. 7. (a) Timescale over the past 4,500 Myrs and the estimated assembly/dispersal of super-cratons/superterranes (Slavia, Superia, Valbara, and Gondwana) and supercontinents (Columbia, Rodinia, and Pangea; after Torsvik & Cocks, 2017). Note that the main phase of Gondwana took place during late Neoproterozoic-early Paleozoic times but the core of this superterrane lasted until merging with Laurussia to form Pangea at around 320 Ma. (b) Normalized zircon age frequency (Voice et al. 2011; V11), *first* quality-filtered (black curve), *then* area-filtered (stippled black curve), and *finally* arc-filtered (red curve) (see text for details). The quality-filtered curve shows seven major peaks since the late Archean. Those peaks are also seen after area filtering but the main Cretaceous quality-filtered peak (peak 6) is shifted to the early Cambrian (540 Ma, i.e. during Gondwana formation). There is also an additional peak in the early Mesoarchean. The latter is also pronounced after arc filtering that also shows a minor peak in the Paleoarchean and an additional peak at around 350 Ma (prior to Pangea assembly). Yellow shading shows the difference between quality-filtered and area + arc-filtered curves.

of the strata minus the one-sigma error of the grain age, and *(iii)* ages older than the age of the solar system and Earth (>4567 Ma). These filtering steps reduced the total number of zircon ages by ~3% (leaving 186,812 entries) but did not result in a significant alteration of the shape of the age distribution. This post-filtering distribution (shown using 30 Myr bins in Fig. 7) is similar to that of Domeier et al. (2018) except that ages in excess of 3.6 Ga were excluded from their histograms. There are seven main age-frequency peaks, the two oldest (peaks 1 and 2) are contemporaneous with some major craton interactions starting at ~2.7 Ga, whilst peaks 3 to 5 broadly coincide with the assembly of the two first supercontinents—Columbia (1.9–1.8 Ga) and Rodinia (1.1–1.0 Ga)—and the formation of the large landmass of Gondwana (peak 5). In Phanerozoic time, one peak is approximately coincident with Pangea formation, but the largest age-frequency peak is observed in the Early Cretaceous, when Pangea was rapidly disintegrating (peak 7 in Fig. 7).

We also applied an area-scaling to the V11 dataset in an attempt to compensate for the very uneven geographic distribution of the zircon sampling. The area scaling adds more weight to under-sampled regions (or equivalently, reduces the weight of over-sampled regions). The effect of this area scaling (stippled curve in Fig. 7) is significant, especially in reducing the amplitude of the peaks of the last ~300 Myr (mostly coming from North America) and in increasing some of the older peaks; for example, the peak around 540 Ma coincident with Gondwana assembly.

A third filtering step was applied to reduce the signal from non-arc related contributions. All entries in V11 are tagged with a tectonic environment, and of the eight varieties, three environments (fore-, back- and retro-arc basins) are directly associated with arc volcanism. We therefore removed all other entries from the quality- and area-filtered version of the dataset (Fig. 7), leaving 47,231 entries. There are some notable caveats to be mentioned with regard to this last filter. First, in addition to igneous rocks, both sedimentary and metamorphic rocks can exist in arc-related environments, and thus recycled zircons are not entirely stricken from the dataset by this filter. Second, most 'arc-related' zircons now exist in non-arc-related environments (e.g., recycled into passive margin sediments). We note that the general shape of the arc-, quality- and area-filtered V11 curves remain similar, but two new peaks appear in the Precambrian after application of the last filter. There is also a notable augmentation of a formerly subtle inflection in the age-frequency curve at around 350 Ma (red curve in Fig. 7). Finally, we de-trended the age-frequency curve, assuming the background monotonic decrease in zircon frequency with increasing age to be a reflection of preservation issues, but the slope (−0.0004) over the past 800 Ma is minor, and consequently the de-trended and non-trended curves are almost identical. In Fig. 7, the zircon age-frequency histograms resulting from these various filtering steps are compared after being scaled to their highest individual peaks.

As observed by Hounslow et al. (2018), we find that the shape of our final V11 zircon age-frequency distribution resembles the directly computed subduction flux of the last 410 Ma, with a minor temporal offset (Fig. 8a; see also Domeier et al. 2018). Specifically, since the start of the Phanerozoic, the zircon age-frequency distribution shows five main peaks. The oldest, in the Cambrian at around 520 Ma (P#1, Fig. 8a), is too old to be compared against

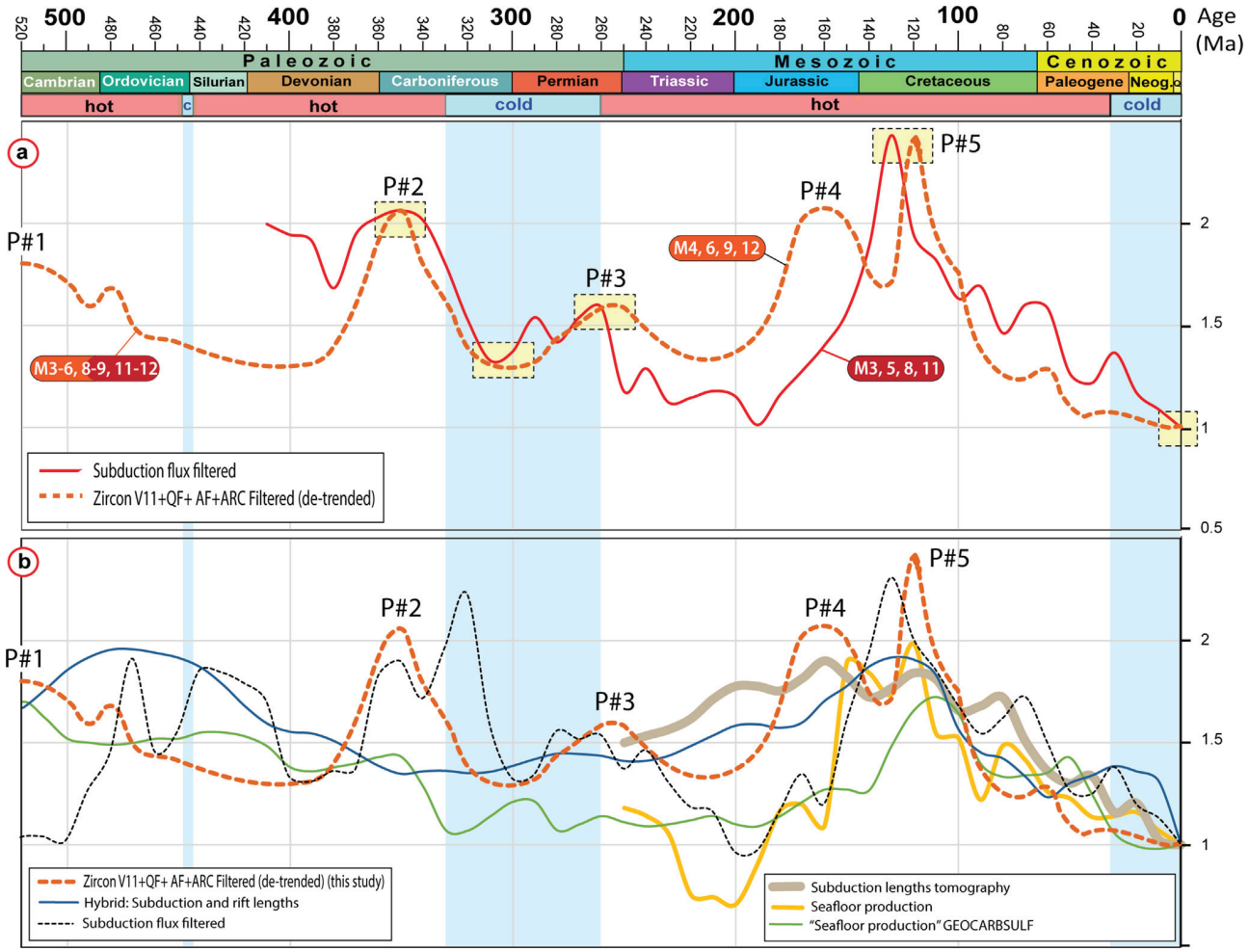

Fig. 8. Timescale with greenhouse (hot) versus icehouse (cold) conditions for the past 520 Myrs (see Fig. 3 caption) and (a) revised f_{SR} (this study) based on two degassing proxies, i.e. subduction flux from full-plate models (red curve) and scaled arc-zircons (stippled orange). Subduction flux (filtered) for the past 410 Myrs (0–250 Ma also shown in Fig. 7b) shows peaks in the early Carboniferous (340–360 Ma), late Permian (~260 Ma), and the Early Cretaceous (~130 Ma). Two lows (late Carboniferous and Recent times) coincide with icehouse conditions whilst a third low in subduction flux (~190 Ma) coincides with greenhouse conditions. Subduction flux is compared with the frequency of arc-related zircons (Voice et al. 2011, V11) that have been quality- and area-filtered. Assuming that the general trend of decreasing zircon frequencies through time may reflect real preservation problems we have de-trended (with very little effect) the arc-zircons curve for the past 800 Myrs (slope = −0.004). The arc-zircon curve was then *rescaled* to the subduction flux by fitting three peaks of approximately the same age (P#2, #3, and #5) and a Permo-Carboniferous low at around 300 Ma (yellow boxes). The zircon data were binned in 10 Myrs intervals. Values for present-day and 10 Ma were set equal to unity (=today). The M# labels refer to the models including the presented proxy for their simulations (see Table 2). (b) Comparison of scaled arc-zircons and other proxies for f_{SR}. Only three have been estimated for the entire Phanerozoic. The "seafloor production" curve of Berner (2004) from sea level inversion, is the default f_{SR} in GEOCARBSULF(volc) whereas the hybrid curve of Mills et al. (2019) is the default in COPSE. For comparison we also plotted the subduction fluxes calculated from the full-plate model of Merdith et al. (2021) (stippled black curve).

the subduction flux curve, but a second peak observed in the early Carboniferous (P#2) and a smaller high in the late Permian (P#3) are both comparable to similar inflections in the subduction flux. A fourth peak observed in the zircon age-frequency distribution, in the Middle Jurassic (P#4), is not evident in our subduction flux, whilst the fifth peak (P#5 at 120 Ma, Fig. 8a) is observed about 10 Myrs after the subduction flux peak. Both peaks P#3, P#5, and a Permo-Carboniferous low show an offset of about 10–15 Myrs, which is similar to the temporal offsets found by Domeier et al. (2018), who conducted comparisons between zircon age-frequency distributions and the subduction flux on a regional scale.

Given the first-order correspondence of these independent datasets since the late Paleozoic, we postulate that the zircon age-frequency distributions of earlier time may present a useful subduction flux proxy (and thus a proxy for 'plate tectonic activity' or solid Earth degassing). However, to use the arc-zircon record as a potential measure of the relative subduction flux we must re-scale the arc-filtered zircon curve to the subduction flux curve since 410 Ma. We did this by fitting *(i)* early Carboniferous to Early Triassic highs and lows (360–250 Ma; yellow box in Fig. 8a), *(ii)* Early Cretaceous peaks at 130 and 115 Ma, and *(iii)* normalizing the zircon distribution by the youngest value (giving the youngest bin a value of 1). The latter is important because the zircons generated by recent-to-ongoing arc-activity have mostly not been accounted for, since the formation of a zircon, and subsequent uplift and exposure of its host lag behind ongoing subduction. Thus, one cannot assign present-day or very recent zircon counts as representative of today.

4. Revision of paleogeographic and degassing input parameters in GEOCARBSULFvolc

GEOCARBSULFvolc is a popular long-term carbon and sulfur cycle model (Berner, 2006). This model estimates atmospheric CO_2 and O_2 levels by reconstructing the important long-term

sources and sinks through time (Royer et al., 2014; Berner 2004, 2006). If sources are defined mostly through the degassing input (translated by f_{SR}), the sinks are more highly parameterized and are mostly represented by silicate weathering intensity and carbon burial through time. The silicate weathering activity is constrained by different forcings affecting its rate, such as land plant evolution (translated by LIFE, GYM and FERT parameters), land temperature (GEOG), runoff (f_D), effect of relief on the weathering rate (f_R), and is scaled in its expression by the land area parameters that we revise here. The GEOCARBSULFvolc model has 68 input parameters, 12 of which are time-dependent. Our study concerns three of these time-dependent variables, namely (1) f_A, the exposed land area, (2) $f_{AW}\_f_A$, the fraction of exposed land undergoing chemical weathering and (3) f_{SR}, the seafloor creation rate (=subduction flux), as discussed above. f_A is expressed as the time-dependent total exposed land area relative to the presently exposed land area, for which we use a value of 149×10^6 km^2 in Eq. (1):

$$f_A = \frac{exposed\ \ land_t}{149 * 10^6} \quad (1)$$

For $f_{AW}\_f_A$ we estimate the amount of exposed land at latitudes with a high theoretical weatherability through time. We consider both ±10° only (called $f_{AW10}\_f_A$), and ±10° plus ±40–50° (called $f_{AW}\_f_A$), and its expression can be written as in Eq. (2):

$$f_{AW}\_f_A = \frac{\left(\frac{exposed\ \ land\ \ at\ \ high\ \ weathering\ \ latitudes_t}{total\ \ exposed\ \ land_t}\right)}{\left(\frac{exposed\ \ land\ \ at\ \ high\ \ weathering\ \ latitudes_{t=0}}{total\ \ exposed\ \ land_{t=0}}\right)} \quad (2)$$

The considered present-day ratio values are 0.26 for $f_{AW}\_f_A$ and 0.145 for $f_{AW10}\_f_A$. Those values are based on our paleogeographic model at time zero.

This parameter was first introduced by Royer et al. (2014) in view to depict more realistically the expression of chemical weathering in the model. The resulting "Goddéris" version of the parameter in Royer et al. (2014) uses simulations from GEOCLIM (Goddéris et al., 2012) to select the fraction of land area that had non-zero runoff (based on paleoreconstructions of land and topography) to calculate $f_{AW}\_f_A$. If this version of the parameter is valuable progress for the model, as it allows to exclude cold and

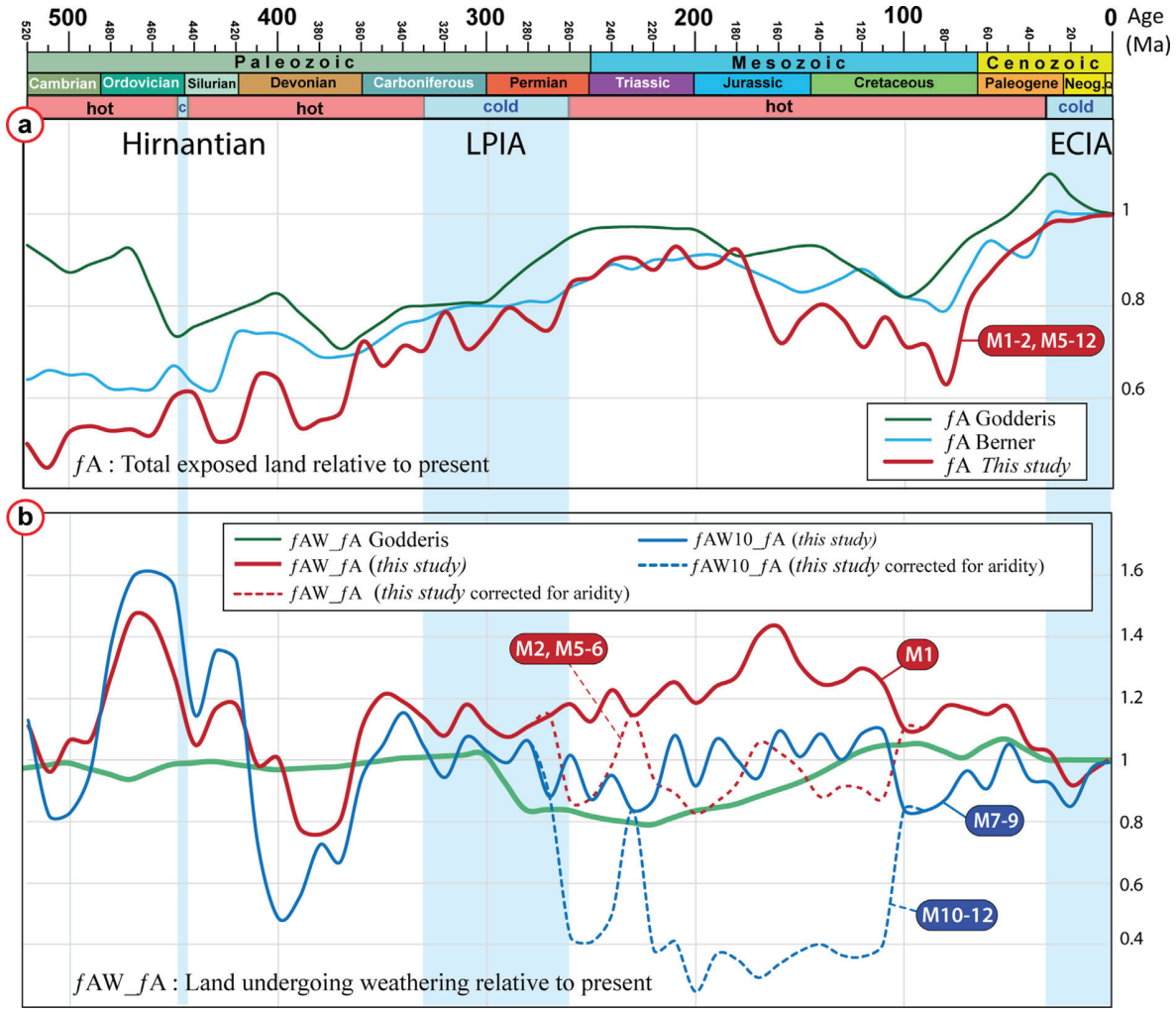

Fig. 9. Timescale with greenhouse (hot) versus icehouse (cold) conditions for the past 520 Myrs (see Fig. 3 caption). (a) Revised f_A (this study) compared with the two different options available in GEOCARBSULFvolc, i.e. Berner or Goddéris weathering parameters (Royer et al. 2014). (b) Revised $f_{AW\text{-}fA}$ (this study) compared with the Goddéris values in GEOCARBSULFvolc (Berner is set to 1 for the entire period). Two considerations of weatherability are here tested. The red curve corresponds to the total weatherability formed at latitudes of ±10° & ±40–50°, whereas the red curve displays the weatherability only at ±10° (f_{AW10}-f_A). From the mid-late Permian to the mid-Cretaceous, climate gradients were much different from today, with arid tropical areas; we have excluded those areas between 280 and 100 Ma, and the resultant f_{AW}-f_A is shown by the stippled curves for both definitions of weatherability considered. All values for the parameters are presented in the Table S1 of the supplementary data 2. The M# labels refer to the models including the proxy selected in their simulations. A list of the models is presented in Table 2. ECIA, End Cenozoic Ice Age; LPIA, Late Paleozoic Ice Age.

dry environments from the calculation of weathering, it also creates some limitations. The coarse grid size used in the model from Goddéris et al. (2012) retricts the integration of the effect of microcontinents and volcanic islands in their climatic simulations and linked weathering calculation. Those small land areas are particularly important in the early Paleozoic for example. Moreover, the input for those simulations comprised only 22 maps used to represent the entire Phanerozoic, and thus large extrapolations were required. Furthermore, the land availability was overestimated and the runoff simulations were based on extremely poorly constrained paleotopography, leading to an increased (and highly uncertain) silicate weathering activity throughout the Phanerozoic.

Here, we used a more simplified definition of land availability through time by extracting the amount of land, including some microcontinents and islands, located in specific latitudes. This assumes that climate gradients are constant through geological time (e.g. wet and warm tropics) and that runoff is globally similar to that determined from GEOCLIM reconstructions, both of which are important limitations. However, the distinct advantage of this approach is that we are able to evaluate the underlying effects of paleogeography, which is relatively well-constrained (and further improved herein), independently of the significant but poorly constrained effects of changing relief and climate zonation (which are ultimately tied back to paleogeography). In other words, we seek an improved understanding of the relationship between well-determined base paleogeography and climate, providing a framework on which progressively more sophisticated analyses can build.

4.1. Revision of f_A and $f_{AW}\_f_A$

The GEOCARBSULFvolc model can be operated in two different modes in the most recent R-code: '*Berner*' and '*Goddéris*' (Royer et al., 2014). These modes have different weathering-related parameters, based on Berner (2004) and Goddéris et al. (2014), respectively. In Fig. 9a, we compare the *'Goddéris'* and *'Berner'* values for f_A against our own (calculated from the total land area estimations and their fluctuations as detailed in Section 2). There are broad similarities from the early Carboniferous to the Early Jurassic (about 360–180 Ma) but there are relatively large differences in the early and mid-Paleozoic (520–360 Ma) and during the Late Jurassic and Cretaceous. It is also noteworthy that the f_A values of *'Goddéris'* are systematically higher than the *'Berner'* values. All models hold similar levels during and directly following the LPIA as the low sea-level maximized the amount of exposed land (Figs. 9a & 4c).

Our estimates of $f_{AW}\_f_A$, calculated from the estimations of exposed land area in selected latitude bands (Section 2) extend from 520 Ma (we use the original GEOCARBSULFvolc parameters from 570 to 520 Ma) (Fig. 9b). They are very different from '*Goddéris*' (green curve in Fig. 9b), as well as the '*Berner*' model, which holds $f_{AW}\_f_A$ always = 1 (Fig. 9b; Supplementary data 2, Table S1). In the model of '*Goddéris*', $f_{AW}\_f_A$ shows hardly any differences from the Cambrian to the late Carboniferous, whereas our estimation exhibits strong fluctuations, including both the Phanerozoic maximum and minimum. Near the Carboniferous-Permian boundary, during the LPIA, the $f_{AW}\_f_A$ of '*Goddéris*' exhibits a distinct reduction to about 0.8 that lasted until the Early Jurassic. By contrast our estimation of $f_{AW}\_f_A$ exhibits a gradual increase

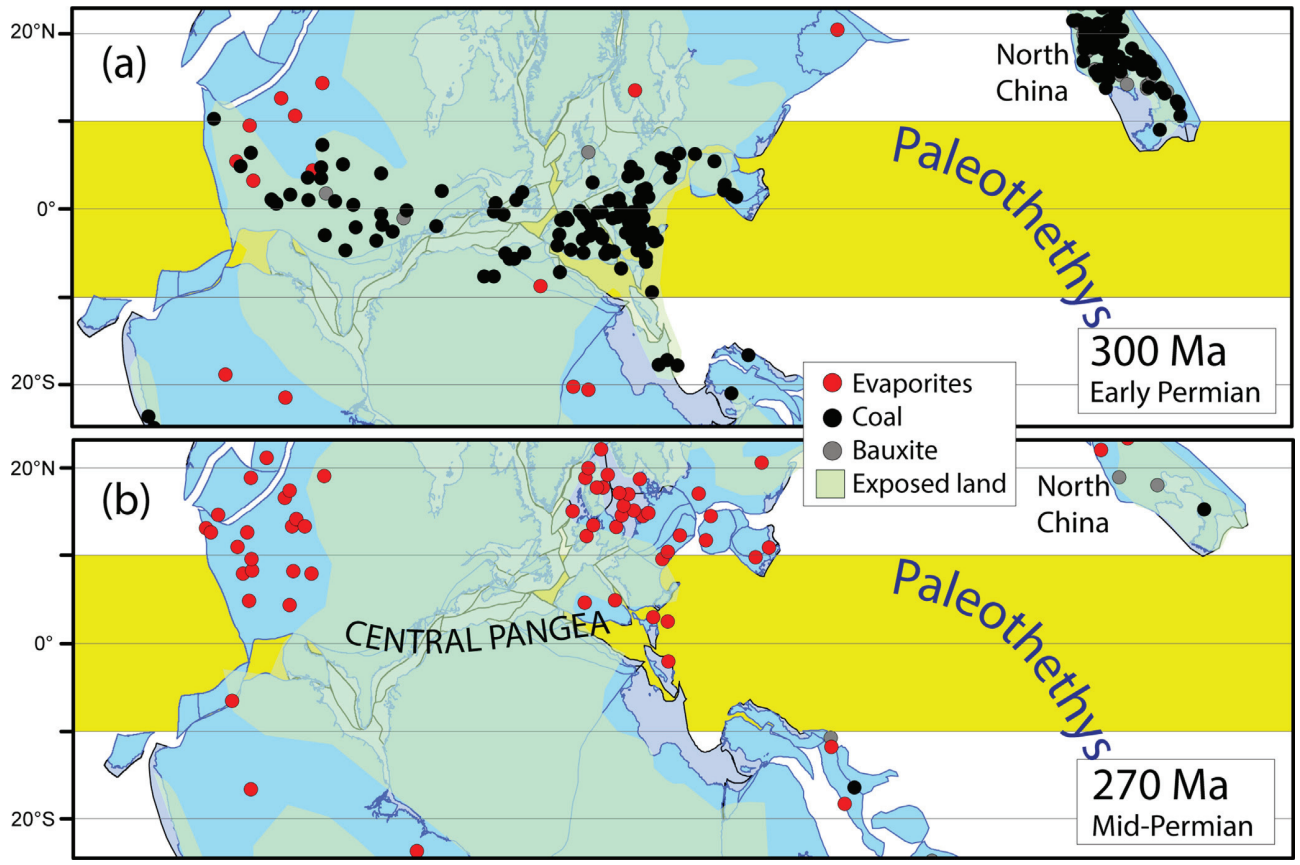

Fig. 10. Reconstruction of Central Pangea and the western parts of the Paleotethys together with exposed land and the distribution of evaporites, coal, and bauxite at (a) 300 Ma and (b) 270 Ma. Both reconstructions are in the paleomagnetic reference frame and the theoretical low-latitude belt of high weatherability is shaded yellow (±10°).

throughout that interval, and thus the estimates of f_{AW}–f_A by '*Goddéris*' are consistently lower than ours from the early Permian to the mid-Cretaceous (compare green and red solid curve in Fig. 9b). From ~100 Ma to present-day the curves are in closer agreement.

Paleogeographic biome maps for the early phase of the LPIA and Pangea assembly (Fig. 10a) suggest that climate gradients then were grossly similar to those of the present-day (Torsvik and Cocks, 2017). However, as the Pangean climate aridified in response to growing continentality, the rain forests collapsed and were eventually replaced by seasonally dry biomes in the early Permian (Sahney et al. 2010). Subsequently, in middle-late Permian time, an expansive arid region extended across much of Pangea (Fig. 10b), spanning both northern and southern latitudes, and crossing both the Americas and Europe (Boucot et al. 2013; Torsvik and Cocks, 2017; Torsvik et al. 2020). Low global climatic gradients and a low latitude arid region traversing most of central Pangea characterized the Triassic and Jurassic, but even long after Pangea breakup, many equatorial regions appeared arid until about 100 Ma.

To account for the low climate gradients between 270 and 110 Ma, revised calculations of exposed land at high weathering latitudes were made by removing exposed land polygons where paleoclimate indicators (evaporites) suggest low-latitude (±10° arid conditions (Table 1). This reduces f_{AW}–f_A considerably (stippled red curve in Fig. 9b), and brings it into closer agreement with the '*Goddéris*' curve (green line in Fig. 9b).

Considering that numerical simulations suggest that CO_2 consumption by silicate weathering in the tropics is perhaps 20 times higher than that achieved by the northern/southern wet belts (Goddéris et al. 2014), we also explore the use of f_{AW10}–f_A (Fig. 9b blue curves). This has some important consequences: f_{AW10}–f_A is about 1.6 times higher than present-day values in the mid-Late Ordovician compared to 1.45 for f_{AW}–f_A. The latter is already the highest potential CO_2 sink by silicate weathering observed from the entire Phanerozoic, but it becomes even higher with f_{AW10}–f_A. A steep decline immediately follows this peak, coincident with the Hirnantian icehouse. Conversely, f_{AW10}–f_A values during the LPIA and the End Cenozoic Icehouse Age (ECIA) remain comparable to the original values (f_{AW}–f_A around 1). The values during the Devonian, which already had the lowest Phanerozoic f_{AW}–f_A, become even lower. However, if we further adjust f_{AW10}–f_A for the effects of equatorial aridity between 270 and 110 Ma (''adjusted f_{AW10}–f_A''), then the late Permian to mid-Cretaceous greenhouse is characterized by the lowest recorded Phanerozoic f_{AW10}–f_A values (around 0.4). In fact, these refinements made to account for aridity in the adjusted f_{AW10}–f_A result in a lowering of the values to less than half of that of the present-day for the majority of the Mesozoic (Fig. 9b). Given the large differences exhibited by these alternative estimations of f_{AW}–f_A, the specific selection of f_{AW10}–f_A unsurprisingly has a profound influence on CO_2 modelling (Section 5).

4.2. Revised degassing (f_{SR})

For CO_2 modelling (Section 5) we have defined f_{SR} in two different ways. In the first case, we use a hybrid version where f_{SR} is estimated from the subduction flux back to 350 Ma and then we switch to using the normalized zircon age distribution (hereafter 'arc-activity') as a measure of f_{SR} for all earlier times. In the second case, we simply use arc-activity as a measure of f_{SR} for the entire time range (Fig. 8a; Supplementary data 2, Table S1). Continental arc-activity has been argued to play an important role in regulating long-term climate changes, and McKenzie et al. (2016) argued that reduced continental arc activity explains all icehouse climates. Only the LPIA, however, shows a clear relation with the zircon record, and the ECIA occurred long after the onset of a large reduction in arc activity which started in the Cretaceous. In our analysis, there is a general decrease in arc activity during the Ordovician but the short-lived end-Ordovician (Hirnantian) icehouse was not preceded by any notable changes in the arc activity curve, which continued descending until reaching a minimum during the Devonian (Fig. 8a). That was at a time when the climate was generally warm, although there are rocks of glacial origin in the latest Devonian and earliest Carboniferous of South America (Torsvik and Cocks, 2017). Another minimum in arc activity that coincided with prevailing greenhouse conditions occurred during the Triassic-Early Jurassic. Thus, variations in plate tectonic activity/degassing cannot alone explain greenhouse versus icehouse conditions.

Over the past few years, f_{SR} has been estimated in many ways, and in Fig. 8b we compare our estimate of f_{SR}, using normalized arc activity (as in Fig. 8a) as a proxy, with two other estimates that are available for the entire Phanerozoic (and older times): the standard f_{SR} in GEOCARBSULF (Berner, 2004) and a hybrid f_{SR} estimate based on subduction and rift lengths (Mills et al., 2019). Our estimates of f_{SR} (based on arc activity) show a minimum during the late Neoproterozoic (Cryogenian) Snowball Earth events (not shown in the diagram), followed by a steady increase in the late Precambrian-early Cambrian, and peak at 520 Ma (P#1 in Fig. 8). A corresponding f_{SR} value of about 1.8 is similar to the two other estimates but the f_{SR} curves are very different for most of the Paleozoic. The Hirnantian Icehouse (probably lasting less than a million years) is not recognized in any of the curves for f_{SR} (Fig. 8b) and our f_{SR} values vary between 1.5 and 1.4 during the Ordovician. Our arc activity peak in the early Carboniferous (P#2, Fig. 8b) is not recognized in the two other curves but a general low during the LPIA is seen in all curves. During the Mesozoic, the hybrid curve of Mills et al. (2019) is close to our curve, whilst the Berner (2004) seafloor production curve is much lower. All curves peak in the Early Cretaceous with f_{SR} values of 2.4–1.5, followed by decreasing values toward recent times. Our arc activity peaks P#3 and P#4 are not reflected in the two other curves, but on average the trend of the f_{SR} curve of Mills et al. (2019) follows our arc activity curve (Fig. 8b). Note, however, that we have shown subduction lengths from full-plate models to be an over-simplified measure of f_{SR} (Section 3.3) and thus the hybrid f_{SR} estimate of Mills et al. (2019) may be less reliable prior to 200 Ma.

Merdith et al. (2021) recently published a full-plate model for the past one billion years, from which we can extract a subduction flux. Some similarities to our subduction flux in the late Paleozoic could be anticipated given that this model is based on the model of Young et al. (2019), which in turn modified the model of Domeier and Torsvik (2014). Young et al. (2019) made substantial changes to the model of Domeier and Torsvik (2014), but several of these involved latitudinal adjustments that violated paleomagnetic constraints and were subsequently reverted by Merdith et al. (2021), so the latter model more closely resembles that of Domeier and Torsvik (2014). However, significant differences remain in the assignment of longitudes between these models (see below). For 500–410 Ma, the Merdith model is adapted from two regional models (Domeier, 2016, 2018) and in earlier time it connects with the Neoproterozoic model of Merdith et al. (2019).

Differences in the late Paleozoic subduction flux (Fig. 8b) between Merdith et al. (2021) and this study, most notably a peak at 320 Ma (start of LPIA), result largely from longitudinal changes made with respect to the model of Domeier and Torsvik (2014). The observation of a large difference at 320 Ma might initially appear counterintuitive since Pangea is assembled by this time in both models, and positioned at similar longitudes (although note Merdith et al. (2021) reconstruct Pangea farther north than what the bulk of paleomagnetic data suggest at this time). Recalling that the subduction fluxes shown in Figs. 6 and 8 are scaled (relative to

Table 2
Overview of the 12 different models we have used to estimate atmospheric CO_2 in the GEOCARBSULFvolc program. All parameters as in Royer et al. (2014) except time-dependent changes in f_{SR}, f_A and $f_{AW\_}f_A$. In the original GEOCARBSULF code these parameters are described as *"Seafloor creation rate at time (t) relative to the present-day"* (f_{SR}), *"Land area at time (t) relative to the present-day"* (f_A) and *"Fraction of land area undergoing chemical weathering"* ($f_{AW\_}f_A$ & $f_{AW10\_}f_A$). For the latter two parameters we use those of Royer et al. (2014) before 520 Ma.

Model	Revised parameter descriptions (others as in Royer et al. 2014)
M1	Revised f_A and $f_{AW\_}f_A$ scaled by exposed land within ±10° and between 40 and 50°N/S (Fig. 11a, 9)
M2	As M1 but $f_{AW\_}f_A$ adjusted for arid equatorial regions (Fig. 11a, 9)
M3	Revised f_{SR} (arc-zircon model) (Fig. 11b, 8a)
M4	Revised f_{SR} (hybrid model: Subduction flux 0–350 Ma and arc-zircon model for older times) (Fig. 11b, 8a)
M5	M2 + M3 (Fig. 11c, 13a)
M6	M2 + M4 (Fig. 11c)
M7	Revised f_A and $f_{AW10\_}f_A$ (Fig. 12a, 9)
M8	M7 + M3 (Fig. 12a, 9)
M9	M7 + M4 (Fig. 12b, 9)
M10	As M7 but $f_{AW10\_}f_A$ adjusted for arid equatorial regions (Fig. 12b, 9)
M11	As M8 but $f_{AW10\_}f_A$ adjusted for arid equatorial regions (Fig. 12b, 9)
M12	As M9 but $f_{AW10\_}f_A$ adjusted for arid equatorial regions (Fig. 12b, 9, Fig. 13a)

present-day rates), this difference arises because the model of Domeier and Torsvik (2014) includes stronger longitudinal motions prior to Pangea formation necessitated by the absolute reference frame (Torsvik et al., 2014). By contrast, the models of Merdith et al. (2021) and Young et al. (2019) are not longitudinally anchored, and therefore have generally smaller rates of tectonic motion for all times prior to Pangea formation.

In early Paleozoic time, the subduction flux from Merdith et al. (2021) shows large fluctuations in the late Cambrian and Early Ordovician, and very low (as today) rates in the earlier Cambrian. Interestingly, an accelerated subduction flux (increased CO_2 sourcing) occurs during the Hirnantian glaciation, although this signal is not recognized in any other models (Fig. 8b). Importantly, this subduction flux does not resemble the normalized arc-related zircon age distribution prior to 400 Ma. Although improving plate models certainly hold the promise of providing stronger constraints on solid Earth degassing in such deep time, there remain substantial uncertainties and ambiguities in global paleogeography in Ediacaran and earliest Paleozoic time (e.g. Abrajevitch and Van der Voo, 2010), which have a direct impact on reconstructions extending into the early Paleozoic. We therefore consider the normalized arc-related zircon age distribution to be a presently better proxy for arc-activity and potential carbon degassing in deep time.

5. CO_2 modelling

The most recent GEOCARBSULFvolc model (described in Royer et al., 2014) can be run with two different sets of paleogeographic parameters (that we here revised) but also runoff (f_D) and temperature (GEOG) input parameters ('*Berner*' or '*Goddéris*' in Royer et al., 2014). We used the *Goddéris* weathering parameters (f_D and GEOG, Fig. 1 in Royer et al., 2014) with our modifications of f_A, $f_{AW\_}f_A$, and f_{SR} to generate new CO_2 estimates presented here. The code and resampling strategy were applied as in Royer et al. (2014): the model was run with 10,000 iterations for each of our tests. Following the strategy of Royer et al. (2014), each revised parameter was tested separately with decreasing error percentage applied, from 50 to 30% on average, until the model failure rate reached levels below 5%. The presented simulations estimate atmospheric CO_2 for the past 570 Myrs in 10 Myr intervals and assume a steady state between those time steps (Berner, 2004). Only simulations between 520 Ma and present-day are shown here to coincide with the resolution of our paleogeographic reconstructions and therefore our revised paleogeographic input.

We tested many different scenarios to assess the relative influence of the revised input parameters (Table 2). We first tested separately the influence of paleogeography by changing only the paleogeographic inputs, as well as considering revised climate gradients for parts of the late Paleozoic and Mesozoic. We then tested the influence of two different proxies for degassing (i.e. subduction flux vs. arc activity). Finally, we tested different combinations of changes in paleogeography and degassing. Revised simulations (Models 1–12) are shown in Figs. 11 and 12 and reconstructed CO_2 levels are plotted together with proxies extending back to the Early Devonian (Foster et al., 2017) as well as the GEOCARBSULFvolc simulation of Royer et al. (2014) for comparison.

5.1. Phanerozoic CO_2 fluctuations from GEOCARBSULFvolc model simulations (Royer et al., 2014)

The Royer et al. (2014) model predicts very high CO_2 levels in the early Cambrian (520 Ma), close to 5000 ppm on average, which peak at 6000 ppm at 540 Ma (see supplementary data 2, Table S2). Those values drop rapidly throughout the late Cambrian and Early to mid-Ordovician to about 2000 ppm, followed by a further drop in the Late Ordovician-early Silurian to about 1800 ppm. The early Paleozoic, therefore, witnessed a reduction in CO_2 levels of about 4000 ppm (Fig. 11, blue curve). During the late Silurian-Early Devonian, there is an increase in CO_2 levels to about 2400 ppm before a major decline to about 350 ppm by the early Carboniferous (350 Ma). This major shift in Earth history is contemporaneous with the origin and expansion of Devonian forests (Berner, 1997), and the reduction in modelled CO_2 (Fig. 11, blue curve) closely follows that of the proxies (red stippled curve with yellow confidence envelope).

CO_2 levels average 357 ppm between the early Carboniferous (350 Ma) and the late Permian (260 Ma). Those low values (extending throughout the LPIA) are comparable to 'modern-day' CO_2 levels. Near the Permo-Triassic boundary, there is a sharp increase in modelled CO_2 levels from about 380 ppm at 260 Ma to about 1250 ppm at 250 Ma. This increase is due to the combined effect of low land-availability for silicate weathering and low runoff triggering a low weathering activity, but also to the low values in the isotopic time series of $\delta^{13}C$ and $\delta^{34}S$ used to track carbon burial through time (Fig. 1b,c,h in Royer et al. 2014). This important reduction of the CO_2 sinks with stable degassing (Fig. 1k in Royer et al. 2014) lead to the simulation of this peak. Furthermore, the peak is partly driven by a drop in climate sensitivity from 6 °C per doubling of CO_2 during the LPIA (330–260 Ma in the GEOCARBSULFvolc code) to 3 °C from 250 Ma and onwards (until 30 Ma and the start of the end-Cenozoic Ice Age); a lower climate sensitivity leads to larger changes in atmospheric CO_2 due to weaker associated silicate weathering feedbacks. This change in climate sensitivity implemented in GEOCARBSULFvolc is based on geological evidence of a long-term climate sensitivity of 6 °C or higher during

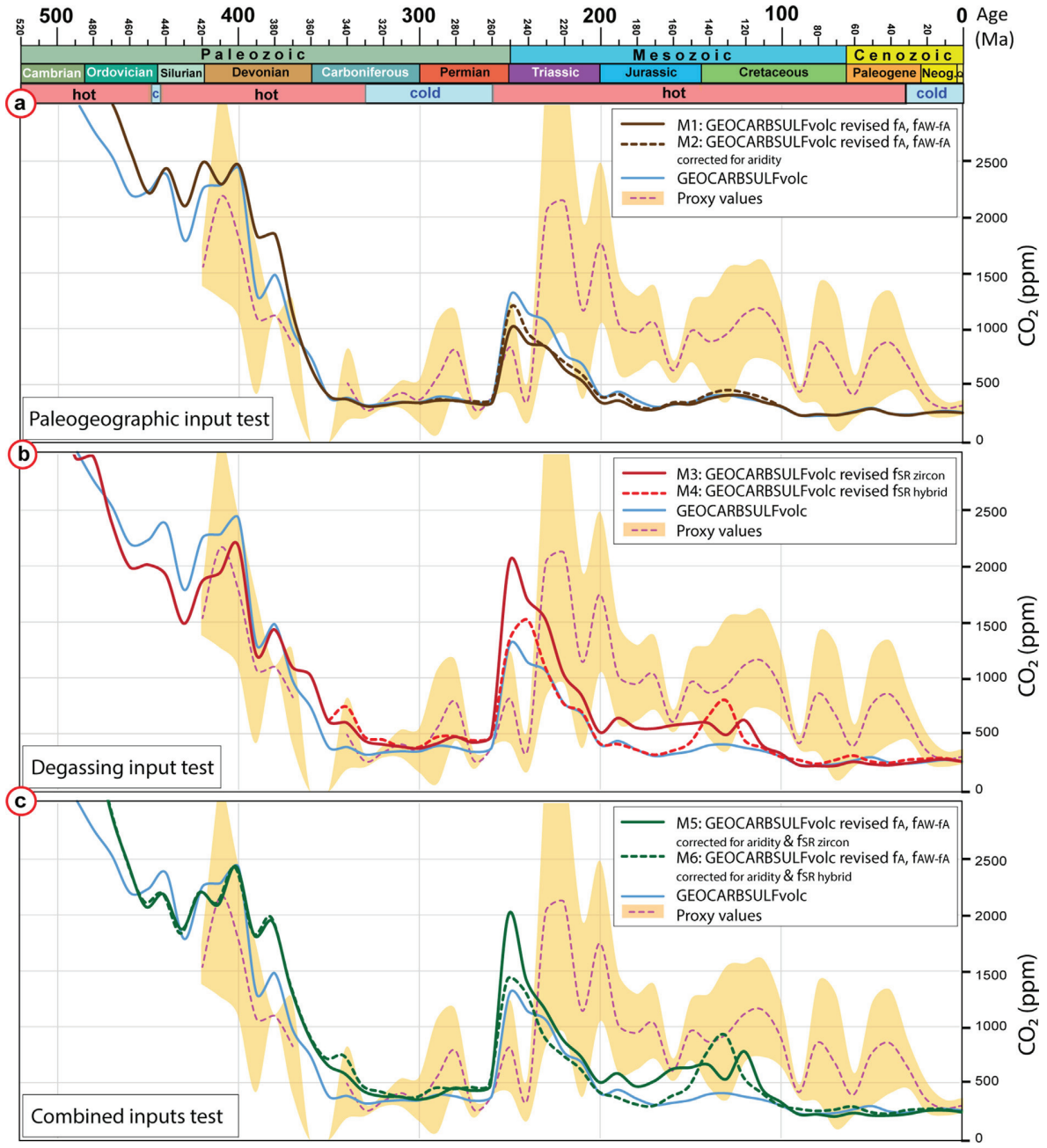

Fig. 11. Timescale with greenhouse (hot) versus icehouse (cold) conditions for the past 520 Myrs (see Fig. 3 caption) and modelled CO_2 levels with GEOCARBSULFvolc (a) Simulations with revised input for paleogeography (full line) and reduced exposed land due to arid climate during Pangea (dotted line) (b) Simulations with revised degassing input parameter with arc zircons as a proxy (full line) and subduction flux (dotted line). (c) Simulations with both revised parameters from a) and b). The yellow shaded area corresponds to CO_2 proxy values from Foster et al. (2017). The purple dashed line shows the median value of the proxies. Simulated CO_2 levels for the Cambrian-Early Ordovician exit the scale of display (levels reaching above 6000 ppm) but can be found in Table S2 in the supplementary data 2. The blue curve in a) b) and c) is the simulation for the Phanerozoic using GEOCARBSULFvolc as in Royer et al. (2014).

those icehouses (Hansen et al., 2008; Pagani et al., 2010; Park and Royer, 2011; Rohling et al., 2012; in Royer et al., 2014). Subsequently, a drop in modelled CO_2 levels follows the 250 Ma peak and CO_2 levels in the Royer et al. (2014) model remain below 500 ppm from the Early Jurassic onward.

5.2. Revised models

When considering only the revised paleogeographic (weathering related) input parameters, i.e. f_A and with total weatherability taken to be $f_{AW}f_A$ (brown line in Fig. 11a, Model M1), we observe two notable changes in the modelled CO_2 levels compared to the previous GEOCARBSULFvolc model (blue curve, Fig. 11a). First, modelled CO_2 levels in the early Paleozoic (Caldeira, 1992; Hansen et al., 2008; Pagani et al., 2010; Rohling, 2012) are on average 300 ppm higher until the Late Devonian. Second, the Permo-Triassic peak at 250 Ma is reduced by 500 ppm. The revised quantification of exposed land being weathered at low latitudes in 'Central Pangea' from 270 Ma due to aridity (Fig. 9b, red stippled curve), only result in marginally higher CO_2 levels during the late

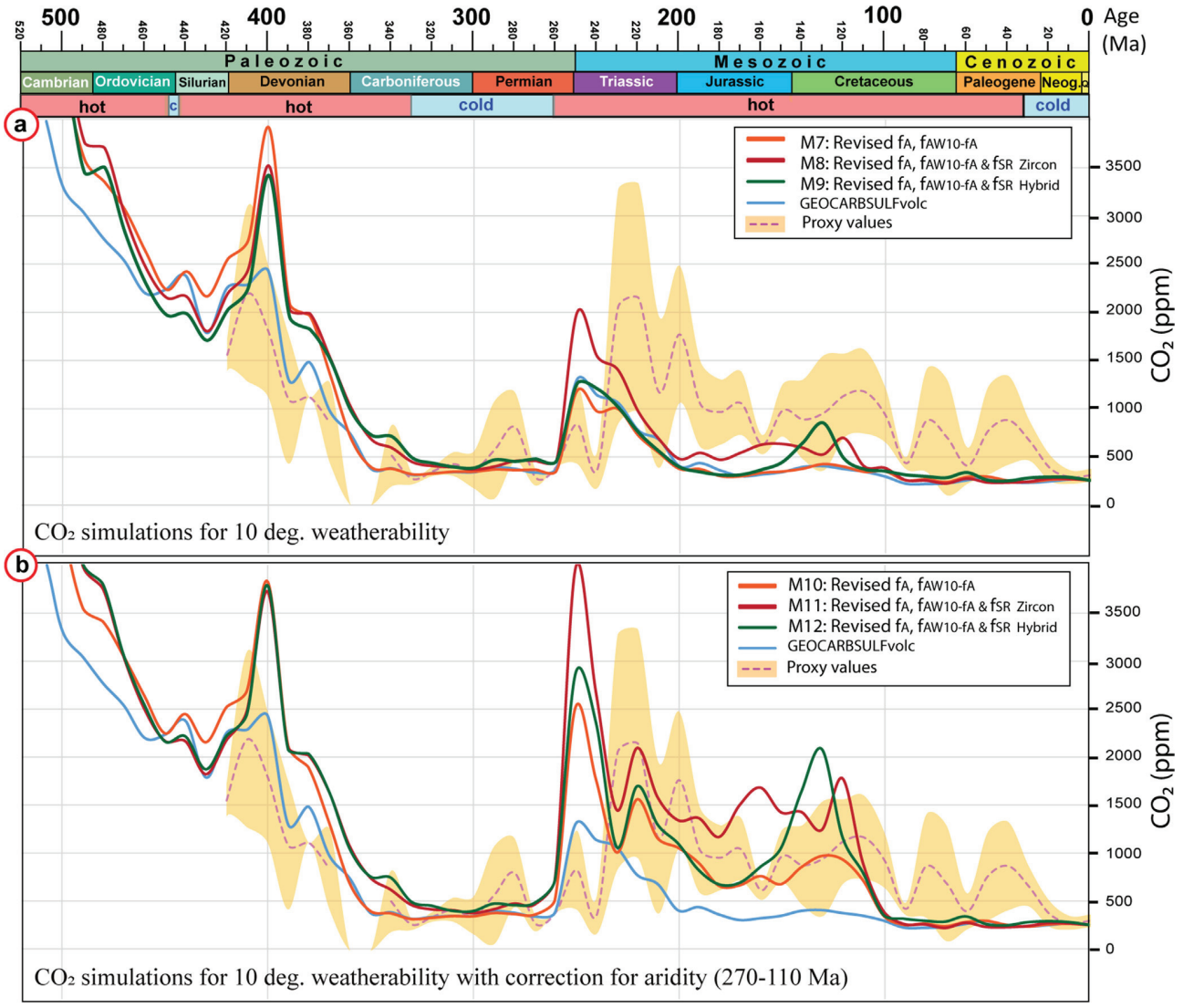

Fig. 12. Timescale with greenhouse (hot) versus icehouse (cold) conditions for the past 520 Myrs (see Fig. 3 caption) and (a) simulations with revised paleogeographic input for only the ±10° latitudes as weatherability (orange curve), together with new degassing input using zircon as a proxy (red curve) or hybrid subduction flux/zircon as a proxy (green curve). The yellow shaded area corresponds to CO_2 proxy values from Foster et al. (2017). The purple dashed line shows the median value of the proxies. Simulated CO_2 levels for the Cambrian-Early Ordovician exit the scale of display (levels reaching above 6000 ppm) but can be found in Table S3 in the supplementary data 2. (b) Similar simulations as in panel (a) but with additional refinements in paleogeographic input due to arid tropical areas between 270 and 110 Ma. The blue curve in both a) and b) is the simulation for the Phanerozoic using GEOCARBSULFvolc as in Royer et al. (2014). Simulated CO_2 levels for the Cambrian-Early Ordovician exit the scale of display (levels reaching above 6000 ppm) but can be found in Table S3 in the supplementary data 2.

Paleozoic and Mesozoic. Indeed, CO_2 levels are only 50 ppm higher on average after 250 Ma, even though these revisions reduce the weathering sink quite considerably (Fig. 11a, Model M2).

The revision of the degassing parameter (f_{SR}) leads to a different response compared with the reference model of Royer et al. (2014) (blue curve in Fig. 11b). Our revised model(s) show lower CO_2 levels during the early Paleozoic (except for the Cambrian) and higher levels during the late Paleozoic and Mesozoic until the mid-Cretaceous (Fig. 11b, red curves). We modelled CO_2 with two different estimates of f_{SR}: In the first case, we used subduction flux as a proxy back to 350 Ma and then continued backward in time with the use of arc activity as a proxy for f_{SR} (hybrid version; stippled red curve in Fig. 11b, Model M4). In the second case, we only used arc activity for the f_{SR} proxy (thick red curve in Fig. 11b, Model M3). Both cases yield similar CO_2 levels for the Paleozoic results, whilst the Permo-Triassic CO_2 peak and Mesozoic levels differ more markedly (Fig. 11b). Using arc activity as a proxy for degassing leads to higher CO_2 estimates at the Permo-Triassic boundary with values above 2000 ppm, whilst the subduction flux proxy yields levels around 1500 ppm. This drop is probably linked to the switch in the full-plate models used to calculate the subduction flux (Fig. 8a). Globally, the use of arc activity as f_{SR} proxy leads to higher CO_2 levels during Triassic to Early Cretaceous times and brings the modelled CO_2 estimates closer to the envelope of proxy values for CO_2. Subduction flux as a proxy for degassing during the Mesozoic (Model M4) leads to a single pronounced CO_2 peak at 130 Ma compared with the standard model (Fig. 11b).

When used simultaneously, the use of our revised input parameters (i.e. f_{AW} f_A and f_{SR} together) leads to higher CO_2 levels in the Cambrian and Early Ordovician (570–450 Ma) with levels on average 1500 ppm higher than the previous model (Fig. 11c and Supplementary data 2, Table S2 for the early Cambrian). During the mid-Ordovician to Devonian, the levels are similar to the previous GEOCARBSULFvolc model (Fig. 11c). From the mid-Devonian, the

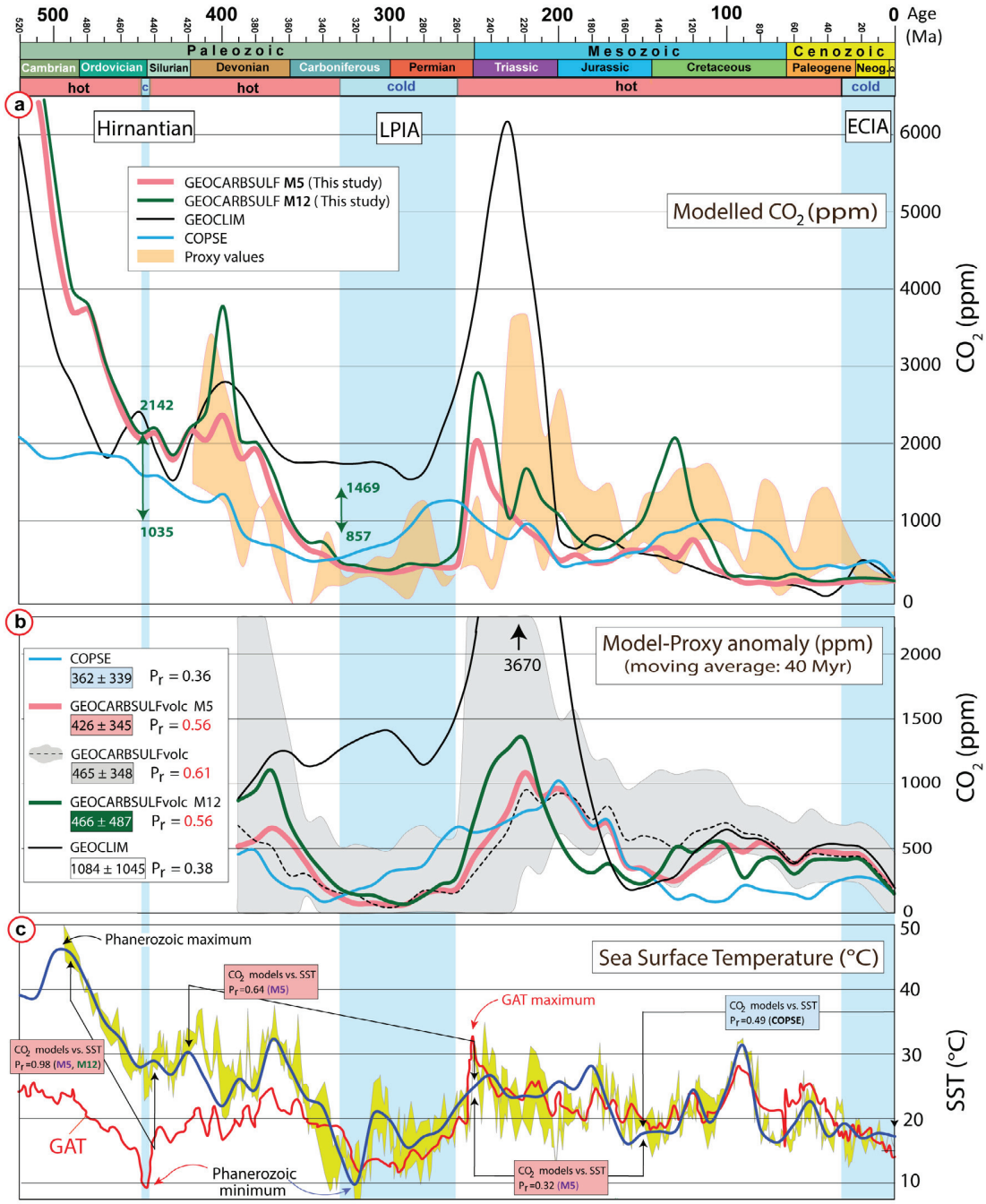

Fig. 13. Timescale with greenhouse (hot) versus icehouse (cold) conditions for the past 520 Myrs (see Fig. 3 caption) and (a) CO_2 simulations with GEOCARBSULFvolc using revised paleogeography weathering parameters (with correction for aridity) and arc activity (zircons) as a proxy for degassing (Model M5: red thick curve; Tables S2-S3 of the supplementary data 2), and with weatherability only at ±10° and hybrid proxy for degassing (Model M12: green curve). GEOCLIM (GEOCLIMTec in Goddéris and Donnadieu, 2017; Goddéris et al., 2014), and COPSE (Mills et al., 2019) are also plotted against CO_2 proxy values from Foster et al. (2017) with 95% standard deviation confidence envelopes for each 10 Myrs interval. The green arrows with numbers at the onset of the Hirnantian and Late Paleozoic Ice Age are estimated CO_2 thresholds to initiate continental-scale glaciations with a fainter sun back in time and assuming a modern threshold of 500 ppm for recent times (Royer, 2006), and considering temperature changes due to luminosity only. High (low) numbers assume a climate sensitivity of 3 °C (6 °C) per doubling of CO_2. Simulated CO_2 levels for the Cambrian-Early Ordovician exit the scale of the diagram (levels reaching above 6000 ppm) but can be found in Tables S2 and S3 of the supplementary data 2. (b) Model-Proxy anomalies for all the models in panel a plus GEOCARBSULFvolc (Royer et al., 2014) shown with 95% confidence envelopes. Anomalies have been smoothed with a moving window (40 Myrs) and thus start at 400 Ma. (c) Sea surface temperatures (SSTs) shown as 95% confidence envelope in yellow shading (Song et al., 2019) and a filtered running mean (5 Myr window) SST curve (blue line) extended back to 520 Ma (see Section 6 for details). The red line is the temperature (GAT) curve of Scotese et al. (2021), extensively based on the SSTs of Song et al. (2019), but modified (most notably for the Paleozoic) by adding or subtracting temperatures from the SSTs based on geological and paleontological criteria according to the authors. The labels refer to the Pearson coefficient analysis ran between the two curves mentioned in the label and over the interval shown between the arrows linked to the label.

use of our revised parameters leads to higher modelled CO_2 levels, and the response is even higher for the small peak simulated at 380 Ma where levels go up by 500 ppm (Fig. 11c). This increase in CO_2 can clearly be attributed to the change in paleogeographic input as simulations remain similar to the previous GEOCARBSULFvolc model (blue curve) when testing the effect of degassing in M3 or M4 (Fig. 11 b). However, higher estimates in the Mesozoic clearly relate to the choice of degassing input. Even associated with the revised paleogeographic input, the use of arc activity as a proxy for degassing leads to a higher estimated peak in CO_2 at 250 Ma, and generally higher CO_2 levels throughout the Jurassic and Early Cretaceous (solid green line in Fig. 11c, Model M5).

To assess the impact of the definition of weatherability, we also ran simulations wherein weatherability was restricted to the equator where silicate weathering potential is at its maximum (if physical erosion allows it). With this definition, we recalculated $f_{AW}\_f_A$ by only considering exposed land near the equator (±10°, e.g. using $f_{AW10}\_f_A$) and tested its influence with and without refinement linked to aridity that developed across central Pangea, as well as combined with our revised degassing estimates. This change from $f_{AW}\_f_A$ to $f_{AW10}\_f_A$ does not drastically change the CO_2 estimates, even when associated with our degassing revisions, but intensifies the CO_2 peak at 400 Ma (Fig. 12a, orange curve, Model M7) and results in a minor elevation of modelled CO_2 levels during Triassic-Jurassic time. However, when refined for aridity in the equatorial belt (Models M10-12), changes in $f_{AW10}\_f_A$ make the models highly responsive and sensitive to changes in degassing (Fig. 12b).

Indeed, the reduction of exposed land available to weathering during Pangea times is translated into a sharp rise in CO_2 levels (orange curve in Fig. 12b) and the additional effect of elevated degassing leads to much higher CO_2 estimates for most of the Mesozoic (Fig. 12b). The increased CO_2 levels lead overall to a better apparent fit with the proxy values, even if the peaks simulated are higher than the proxy values between 160 and 120 Ma (Fig. 12b). A particularly good fit is observed between the estimates and the proxy values between 230 and the peak at 220 Ma, which is triggered by a rebound in land availability and is notably absent in the previous GEOCARBSULFvolc model of Royer et al. (2014) (Figs. 12b & 9b).

6. Discussion

In Fig. 13 we compare two of our GEOCARBSULFvolc models (M5 and M12; see supplementary data 2, Tables S2 and S3 for times before 520 Ma) with (*i*) two other long-term carbon cycle models (GEOCLIM and COPSE), (*ii*) proxies for CO_2 (when available), and *(iii)* sea surface temperatures (SSTs). SSTs are plotted in 10 Myrs intervals and each mean temperature is calculated over a five Myr window (blue thick curve in Fig. 13c). We use the dataset of Song et al. (2019), assuming an invariant oxygen isotope composition of seawater to calculate SSTs, and data-selection includes only $\delta^{18}O$ from phosphate fossils (apatite conodonts) before the Mesozoic. We have extended the dataset of Song et al. (2019) to ~520 Ma with $\delta^{18}O$ data from phosphatic Siberian brachiopods (Wotte et al. 2019). To assure that we only included fossils that once thrived in (shallow) seas at low latitudes, we excluded reconstructed fossil locations above ±30°. Because of this and the fact that our SST curve is smoothed our mean values may at times not overlap with the 95% confidence envelope of Song et al. (2019). The mean reconstructed latitude is 16 ± 9° for the past 520 Myrs (based on own reconstruction parameters) and mean latitudes are similar for Paleozoic (14 ± 8°) and Mesozoic/Cenozoic times (17 ± 9°).

Table 3
Pearson correlation coefficients for different time-series. (a) Testing correlation between models and CO_2 proxies for different time periods. (b) Testing correlation between models. (c) Testing correlation between models and sea surface temperature for different time periods. All the revised paleogeographic inputs include corrections for aridity (Models M5 and M12; see Table 1 and Fig. 13a). In Table 3a we have also averaged model-proxy differences over selected time periods (see also Fig. 13c). [#1]Royer et al. (2014); [#2]Goddéris and Donnadieu (2017); [#3]Mills et al. (2019).

(a) Pearson C - models versus CO_2 proxies (Coverage 420–0 Ma)

Time period (Ma)	M5 (this study)	M12 (this study)	GEOCARBSULFvolc[#1]	GEOCLIM[#2]	COPSE[#3]
Late Paleozoic (420–250)	0.87	0.83	0.94	0.41	0.53
Paleozoic selection (420–270)	0.91	0.89	0.95	0.76	0.62
Mesozoic/Cenozoic (230–0)	0.78	0.61	0.79	0.76	0.40
Cenozoic (70–0)	−0.95	−0.43	−0.29	−0.29	0.11
Phanerozoic (420–0)	0.56	0.57	0.61	0.38	0.36
Mean Model-Proxy offsets (in ppm) and standard deviation (1σ)					
Phanerozoic (420–0)	426 ± 345	467 ± 487	465 ± 348	1084 ± 1045	363 ± 339*
Paleozoic selection (420–270)	290 ± 271	428 ± 482	305 ± 308	1174 ± 374	351 ± 270
Mesozoic/Cenozoic selection (230–0)	476 ± 332	382 ± 307[#]	554 ± 325	726 ± 932	349 ± 386*

(b) Pearson C – Our new models against other models

	M5 vs GEOCARSULFvolc	M12 vs GEOCARBSULFvolc	M5 vs GEOCLIM	M5 vs COPSE
Early Paleozoic (540–420)	0.92	0.92	0.86	0.82
Late Paleozoic (420–250)	0.96	0.93	0.65	0.41
Early Mesozoic (250–150)	0.93	0.85	0.71	0.84
Late Mesozoic (150–70)	0.86	0.90	0.88	−0.02
Cenozoic (70–0)	0.17	−0.17	0.89	0.17
PHANEROZOIC (520–0)	0.98	0.96	0.67	0.86

(c) Pearson C- models versus sea surface temperature (SST, coverage 520–0 Ma)

	M5	M12	GEOCARBSULFvolc	GEOCLIM	COPSE	Proxies vs SST
Early Paleozoic (520–420)	0.70	0.70	0.61	0.50	0.72	
'Ordovician' (490–440)	0.97	0.99	0.93	0.66	0.83	
Late Paleozoic (420–250)	0.65	0.55	0.56	0.34	0.12	0.53 (0.94 for 370–320 Ma)
Early Mesozoic (250–150)	0.32	0.27	0.44	0.31	0.10	0.12
Late Mesozoic (150–70)	−0.17	−0.33	−0.26	−0.32	0.49	−0.42
Cenozoic (70–0)	−0.17	0.00	0.52	−0.35	−0.36	0.27
PHANEROZOIC (520–0)	0.82	0.77	0.81	0.44	0.73	0.40 (420–0 Ma)

Models M5 and M12 are especially highlighted because they yield the lowest model-proxy residuals, notably for the Mesozoic (Fig. 12 and Table 3a). Model M5 also has low residuals (mean = 290 ± 271 ppm) during the late Paleozoic (420–270 Ma). Conversely, M12 has comparatively low residuals over the last 230 Myrs (382 ± 307 ppm; Table 3a). As a reminder, model M5 incorporates changes in both paleogeographic/weathering (f_A and f_{AW}–f_A scaled by exposed land within the warm/wet tropics and the northern/southern wet-belts, and corrected for arid equatorial regions) and degassing (f_{SR}) parameters. The latter is based on normalized arc-activity (zircons) and this f_{SR} proxy is available for the entire Phanerozoic. Model M12 differs in two ways: f_{AW}–f_A is only scaled by exposed land within the warm/wet tropics (f_{AW10}–f_A), and as a proxy for f_{SR} we use the hybrid model (Table 3). To quantitatively compare different models against proxy CO_2, we compute the residuals for each step as well as the Pearson's correlation coefficients (P_r) (Table 3). We also show graphically a 40 Myr moving average of the residuals in Fig. 13b. Over the last 420 Myrs, COPSE has a slightly lower P_r than GEOCLIM (0.36 and 0.38, respectively) (Fig. 13b), whilst the GEOCARBSULFvolc models provide higher values (P_r = 0.56–0.61; Table 3a). However, CO_2 models are associated with considerable uncertainties (not shown for our models), and one sigma errors in the GEOCARBSULFvolc model (e.g., Royer et al., 2014) averages to 350 ppm for the past 570 Myrs. Thus, most of the model and proxy CO_2 values (Fig. 13a,b) overlap within error at the 95% confidence level.

There are no reliable CO_2 proxies before the Early Devonian and therefore the reliability of long-term carbon cycle models is more difficult to evaluate for the early Paleozoic. Although CO_2 proxies based on marine organic matter have been presented by Witkowski et al. (2018), we note that there are outstanding questions concerning the fidelity of these proxies under conditions of high CO_2, and we therefore disregard them (Witkowski et al., 2019).

All models, including ours, suggest a systematic decrease in CO_2 levels of 3000–4000 ppm in the early Paleozoic (Fig. 13a, supplementary data 2, Tables S2-S3). This decrease corresponds to an increase in theoretical weatherability (Fig. 5c, red curve), and notably exposed land within the warm and wet tropics (Fig. 5a, red curve). This drop in CO_2 levels coincides with a strong reduction in sea surface temperatures (SSTs) from ~500 Ma (Fig. 13c), reaching a low just prior to the short-lived Hirnantian icehouse at ~445 Ma. In our analysis, this cooling correlates with a peak in land availability to weathering in the Late Ordovician but also to a reduction in arc-activity during the early Paleozoic (Fig. 8). Thus, the combination of enhanced silicate weathering and decreased degassing can explain a global cooling towards the end-Ordovician in our models.

The Hirnantian cooling event has been considered paradoxical due to its apparent association with high CO_2 levels (e.g., Vandenbroucke et al., 2010, Crowley and Baum,1995), as observed in all our tested carbon cycle models (1620–2430 ppm, Fig. 13a; Supplementary data 2, Tables S2-S3). Low atmospheric CO_2 is a principal variable in controlling continental-scale glaciations, but the solar energy was lower (by 3–5%) in the Late Ordovician (Crowley and Baum, 1995). Consequently, the CO_2 threshold for nucleating ice sheets during this period may have been 4–8 times higher than pre-industrial levels of ~280 ppm (Gibbs et al. 2000; Herrmann et al. 2003; Royer, 2006; Lowry et al. 2014). The study of the response of temperature per doubling of atmospheric CO_2, i.e climate sensitivity, can help us to estimate the threshold for glaciation initiation. The combined study of CO_2 proxies and temperature generally show climate sensitivities of about 3 °C per CO_2 doubling during ice-free periods, and about 6 °C per doubling CO_2 with land ice (Royer, 2016). Estimated CO_2 thresholds to initiate continental-scale glaciations with a fainter sun in the end-Ordovician varies between 1035 and 2142 ppm (Fig. 13a) based on a climate sensitivity of 6 °C and 3 °C per doubling of CO_2, respectively. These estimates assume a modern threshold of 500 ppm for recent times (Royer, 2006) and only consider temperature changes due to luminosity differences. All models are within or close to the theoretical threshold values (Fig. 13a). In our GEOCARBSULFvolc simulations, we used a constant climate sensitivity of 3.0 ± 1.25 °C per CO_2 doubling, except during glacial periods (LPIA, ECIA) where climate sensitivity doubles to 6 °C as in Royer et al. (2014).

The proxy record shows high levels at 410 Ma followed by a decrease in CO_2 levels toward the LPIA (Fig. 13a), whereas all models suggest a peak at 400 Ma. Considering uncertainties in both proxies and models, CO_2 levels in our GEOCARBSULFvolc model M5 and COPSE overlap with CO_2 proxy levels for the late Paleozoic and with strong to moderate P_r's of 0.87 and 0.53, respectively (420–250 Ma, Table 3a). Our GEOCARBSULFvolc simulations suggest a strong decrease of more than 2500 ppm during the Devonian and early Carboniferous and bring CO_2 levels under 500 ppm during the LPIA, as also indicated by the proxies (Fig. 13a, b). The GEOCLIM model shows a more modest drop of 1000 ppm and modelled CO_2 levels are above 1500 ppm during the LPIA, twice that of the proxy estimates, and the P_r for the late Paleozoic is poorer (P_r = 0.41, Table 3a) than the other models for the period 420–250 Ma. However, new simulations using GEOCLIM that focus specifically on the late Paleozoic yield lower CO_2 levels (down to 400 ppm for some simulations) during the LPIA (Goddéris et al., 2017), more in line with with simulations using GEOCARBSULFvolc, including ours, and the proxy record.

SSTs and modelled CO_2 (GEOCARBSULFvolc and GEOCLIM) correlate well for the early Paleozoic (520 to 420 Ma, see also Cocks and Torsvik, 2020) yielding a P_r of 0.6 (0.70 for our revised models M5 & M12) and 0.5, respectively (Table 3a). During the Devonian (400–370 Ma) a marked increase in SSTs (9 °C) occurs 30 Myrs after a prominent increase in CO_2 levels. Afterwards, both SSTs and CO_2 levels declined progressively towards the initiation of the LPIA in the mid-Carboniferous.

The link between CO_2 levels and tropical climate change on million-year timescales has been debated (e.g., Crowley, 1991). The Song et al. (2019) SST curve (yellow confidence envelope in Fig. 13c) included temperature ($\delta^{18}O$) data from fossils that once lived at tropical and subtropical latitudes (<40°N/S). In our reconstructions, a small number of their data points come from paleolatitudes in excess of 40° and so we have restricted the Song et al. (2019) SST curve to only include temperature data from those fossils which lived at latitudes below 30°N/S (Fig. 13c, see supplementary data 3 for SST values). When comparing those selected and smoothed SST data (averaged over 5 Myr bins) to CO_2 proxies for different time intervals over the period 420–0 Ma, we observe a similar trend between SST and CO_2 proxies (P_r = 0.55, Table 3c) until the late Carboniferous, with a close fit between 370 and 320 Ma (P_r = 0.94). However, for the rest of the Phanerozoic major discrepancies arise between these time series (P_r in Table 3c). Some of these discrepancies could be related to underlying inconsistencies in the data, associated with parameters such as seawater pH, age and the spatial distribution of the SST and CO_2 proxies. In addition, the presence of continental ice caps and diagenetic alteration can also affect the accuracy of oxygen isotope paleothermometry (e.g., Song et al., 2019; Scotese et al., 2021; Goldberg et al., 2021). The SST curve also assumes that the sampled organisms lived at shallow water depths and we have assumed an invariant oxygen isotope composition of seawater.

There are also other types of temperature curves such as global average temperatures (GATs), which are an area-scaled integration of all the climate belts. The most recent GAT curve of Scotese et al. (2021) combines geological constraints (e.g., biome maps) and iso-

topic temperature data. This curve shows many similarities to SSTs (Fig. 13c), but its pre-Carboniferous estimates differ radically from high early Paleozoic SSTs, which they reject (but see Goldberg et al. 2021). As a consequence, the GAT curve of Scotese et al. (2021) exhibits minimum temperatures during the Hirnantian Icehouse and maximum temperatures near the Permo-Triassic boundary (Siberian Traps temperature anomaly).

During the mid-late Carboniferous and Permian, GEOCARBSULFvolc models and COPSE simulate low and stable CO_2 levels, which are well below the CO_2 threshold for nucleating ice sheets during the LPIA (1020–2100 ppm; Fig. 13a). GEOCLIM yields substantially higher CO_2 levels during the LPIA followed by a sharp CO_2 increase at the end of the LPIA. GEOCARBSULFvolc model M5 yields a noticeable CO_2 spike of 2000 ppm at 250 Ma linked to the reduction of CO_2 sinks and change in climate sensitivity at this time. This peak is also sensitive to the choice of degassing (see Fig. 11b, c) and is most pronounced when using arc-activity (zircons) as a proxy for f_{SR}. The GEOCARBSULFvolc model peak is 20 and 30 Myrs older than the peak in the GEOCLIM model and the proxy peak, respectively. This particular feature but also the difference in intensity of the peak between GEOCARBSULFvolc and GEOCLIM are discussed in Goddéris et al. (2014) and are attributed to the expression of silicate weathering in the models, and how it relates to runoff. Theoretical weatherability is rather constant during the Permian and early Mesozoic (Fig. 9b, red curve) or lowered from about 270 Ma if we consider an arid equator across central Pangea. However, even with variations in the f_{AW}_f_A parameter, the GEOCARBSULFvolc model is not very sensitive at the Permo-Triassic boundary (Fig. 11a) and it is the increase in degassing (f_{SR}, Fig. 8a) that controls the increased CO_2 levels in the model.

Whilst there are first-order, long-term correlations between modelled CO_2 levels (GEOCARBSULFvolc and to some extent GEOCLIM), SSTs, CO_2 proxies, and the geologic record (continental glaciations) during parts of the Paleozoic (see Pearson correlations in Table 3c), the transition from the LPIA to super-greenhouse conditions at the dawn of the Mesozoic is intriguing. The three carbon cycle models predict very different CO_2 levels during this transition; at 230 Ma, for example, modelled CO_2 levels vary by more than 5000 ppm. Furthermore, while COPSE shows a peak in the middle Permian, GEOCARBSULFvolc shows a peak (250 Ma) near the Permo-Triassic boundary and GEOCLIM peaks in the mid-Triassic. Note, however, that the elevated CO_2 levels in the GEOCARBSULFvolc models (250 Ma) coincide with a reduction in imposed climate sensitivity (from 6 °C to 3 °C), and the large changes in f_{AW}_f_A (M10-12; Fig. 9c), which we impose from 280 Ma, have a relatively negligible effect on modelled CO_2 (Fig. 13a; green line 280–260 Ma) at high climate sensitivity.

From the Jurassic until the Late Cretaceous, CO_2 proxy levels remain relatively stable around 1000 ppm, whereas model values for GEOCARBSULFvolc and GEOCLIM are closer to 500 ppm. COPSE, on the other hand, shows an increase in CO_2 from 500 ppm in the Jurassic to 1000 ppm during the mid-Cretaceous (Fig. 13a) and is more compatible with proxy data (Fig. 13b). Our GEOCARBSULFvolc M12 but particularly M5 simulations with revised degassing yield higher CO_2 estimates and better match the Mesozoic proxies compared with Royer et al., (2014). However, P_r for both models are poor (Table 3c) and modelled CO_2 levels are consistently lower than the proxy values (as with the GEOCLIM model, Fig. 13a).

When including all our revised parameters (f_A, f_{AW}_f_A, and f_{SR}), one notable difference from the Royer et al. (2014) model is the elevated CO_2 levels in the Early Cretaceous, which visually appear to better fit the proxies, but P_r's remain quite similar for all the GEOCARBSULFvolc models (Table 3a). We have, for some reconstruction times, made rather dramatic changes to estimates of the area of exposed land, but surprisingly, GEOCARBSULFvolc is not very sensitive to these changes, except in the early to mid Paleozoic (until the Late Devonian; Fig. 13a) and at the Permo-Triassic boundary. GEOCARBSULFvolc is more sensitive to our degassing rate (f_{SR}) modifications, notably during the Ordovician-Silurian, Carboniferous, Early Triassic and Early Cretaceous.

The testing of a more reduced weatherability (f_{AW10}_f_A) with refinement for aridity (Fig. 12b) highlights the lack of sensitivity of the model to changes in paleogeography. Indeed, strong differences between the models arise only when the f_{AW}_f_A is changed by a factor $\geq$2, as for the peak at 400 Ma between M (1–2, 5–6) and M (7–12) and for the Mesozoic between M (7–9) and M (10–12) with the refinements for aridity (Figs. 11 and 12). Park and Royer (2011) observed this need for a strong reduction in land-availability to achieve a better fit in the model/proxy levels but discarded this option. However, we show here that with refinement due to climate gradients, such a reduction may be reasonable.

With respect to the past 230 Ma, the GEOCARBSULFvolc model with our f_{AW}_f_A and f_{SR} (hybrid model) revisions yields the lowest model-proxy difference (382 ± 307 ppm; Table 3a, M12). P_r's, however, remain quite similar between the GEOCARBSULFvolc models. Models using land within ± 10° as a measure of land-area undergoing chemical weathering (e.g. M10 to 12 in Figs. 12b, 13a) are the first simulations that show high CO_2 levels in the early Mesozoic and a peak at 220 Ma that better fit the proxy values. However, some important discrepancies remain with the proxy records. Most notably, our refinements for aridity for the models M10-12 lead to very high CO_2 being simulated at the Permo-Triassic boundary due to a strong response of the models to the reduced paleogeographic input associated with the already existing low CO_2 sinks (i.e., carbon burial and runoff, see Section 5.1) and high climate sensitivity.

The Jurassic is commonly portrayed as a greenhouse world, but episodes of cooler climates have been argued from SSTs (notice the reduction in our smoothed SST curve from about 180 Ma in Fig. 13c; blue thick curve), notably during the Middle and Late Triassic (Dera et al., 2011). Model M12 shows an early Mesozoic low of about 670 ppm in the Middle Jurassic, and proxy data also show a low towards the end of the Jurassic, followed by increasing CO_2 levels during the Early Cretaceous. A major discrepancy remains during the late Mesozoic and the Cenozoic between the CO_2 proxies (averaging to 500 ppm) and lower simulated levels of CO_2 from all of our models (averaging to 250 ppm) (Figs. 11 and 12). The proxy record shows two peaks at 80 and 40 Ma with a mean average value of 800 ppm, whereas our models remain stable at 250 ppm. This discrepancy, notably in the Eocene, was investigated by Park and Royer (2011), who observed an improvement with an enhanced climate sensitivity and a reduction in land availability. On the contrary, our estimations suggest a sharp increase of exposed land during the same time period, leading to greater CO_2 consumption (with the caveat that a change of model occurs at 70 Ma) (Fig. 9). In conjunction with that increased CO_2 consumption, we also implement a sharp decline in degassing values from 120 Ma (Fig. 8), creating even lower simulated CO_2 levels during the Cenozoic.

7. Conclusions and challenges

By mapping out the areas of exposed land and reconstructing their spatial distribution for the past 520 Myrs, we have estimated the theoretical silicate weathering potential linked to land availability, here called 'total weatherability' (i.e. the equatorial regions and the northern and southern wet belts). Our new model predicts much larger variations in weatherability than previous models, notably for the Paleozoic, where we estimate the Phanerozoic maximum during the Ordovician and minimum during the Devonian.

This variability largely results from the amount of exposed land within the equatorial regions (±10°), and for most of the Paleozoic the continents were largely restricted to the southern hemisphere and there was no land in the northern continental wet belt.

The difference between exposed and total land at a given time provides an estimate of flooded land through time, which should closely track eustatic changes. The trends in our estimates of flooded land exhibit many similarities to the sea-level curve of Haq and Al-Qahtani (2005) and Haq and Schutter (2008) (Fig. 4c). Both show high values, albeit fluctuating, during mid-Ordovician to mid-Devonian times, lows during the time of Pangea (although somewhat offset in time), and a remarkably similar increase during Jurassic and Cretaceous times. This correspondence provides us with some additional confidence that our maps of exposed land provide reliable estimates.

To constrain plate tectonic degassing, we argue that normalized subduction flux is a reliable proxy. Subduction flux has been calculated from full-plate models back to the Early Devonian (410 Ma), and we observe two notable peaks during the early Carboniferous (~350 Ma) and the Early Cretaceous (~130 Ma), both periods of mild greenhouse conditions, whereas the LPIA and ECIA are characterized by a reduced subduction flux. As noted previously (e.g. Domeier et al. 2018), age distributions of arc-related zircons appear to grossly mimic subduction fluxes, and here we present a new approach to estimate degassing through time by rescaling the global zircon age distribution to the subduction flux. Importantly, this approach permits estimation of plate tectonic degassing in deep time when full-plate models become increasingly unreliable. Since the Late Devonian, there are some noticeable differences between the subduction flux and arc-activity, but mostly in the early Mesozoic, which could in part be an artefact of the plate model transition.

In general, our revised estimates for f_A and $f_{AW}\_f_A$ (leaving all other parameters as in Royer et al. 2014) do not radically change modelled CO_2 levels but lead to somewhat higher levels in late Cambrian to Late Devonian times. Our results are (still) consistently lower than proxy estimates for the Mesozoic and especially Cenozoic times. However, if we normalize $f_{AW}\_f_A$ to the amount of exposed land within the tropics (±10°, $f_{AW10}\_f_A$), i.e. the regions with the highest potential CO_2 consumption by silicate weathering, and correct for arid equatorial areas between 270 and 110 Ma (as judged from biome maps), then there are rather dramatic changes in modelled CO_2. This results in a better model-proxy fit over the Mesozoic, but important discrepancies remain at 400 Ma and at the Permo-Triassic boundary. This better fit with refinements for aridity suggests that estimates of theoretical weatherability which assume static climatic belts (similar to those of the modern-day) could lead to poor estimation of land availability through time. Therefore, future enhancements in paleogeographic maps should focus on constraining climate gradients and linked land availability to weathering through time.

Leaving parameters as in Royer et al. (2014) and only implementing changes in f_{SR} (based on normalized subduction flux to 380 Ma and thereafter normalized arc-activity) leads to rather lower CO_2 levels from the mid-Ordovician to the Early Devonian, slightly higher levels from the Devonian to the late Permian, and elevated highs in the Early Triassic (~250 Ma) and the Early Cretaceous (~130 Ma). The use of normalized arc-activity as a proxy for f_{SR} improves slightly the model-proxy differences for Triassic to mid-Cretaceous times.

If we implement our changes in both f_{SR} and $f_{AW}\_f_A$ in the GEOCARBSULFvolc model, improvements in the CO_2 model-proxy fit only occur in models constraining weatherability to ± 10° latitudes. These result in higher modelled CO_2 for the early to mid-Mesozoic and are in closer agreement with proxies. This is most evident in late Permian to mid-Cretaceous times, when (except for the elevated CO_2 peak at 250 Ma) modelled CO_2 levels for all our simulations are within the CO_2 proxies uncertainties envelope.

In conclusion, we consider our new estimates of f_{SR} and $f_{AW}\_f_A$ to be important improvements to some of the key parameters in deep time CO_2 modelling. Nevertheless, CO_2 model-proxy mismatches remain, and clearly indicate a need for further revisions. Future research in enhancing long-term carbon cycle models should focus on constraining climate sensitivity through time, as well as better resolving the time-dependence of major CO_2 sinks and their dynamics, including carbon burial, the effects of plants on weathering (LIFE, GYM, FERT, and their time dependencies) and other poorly constrained parameters elaborated by Royer et al. (2014).

Declaration of Competing Interest

The authors declare that they have no known competing financial interests or personal relationships that could have appeared to influence the work reported in this paper.

Acknowledgments

We acknowledge financial support from the Research Council of Norway (RCN), through its Centres of Excellence funding scheme, project 223272 (CEED), and through RCN project 250111 to M.D. We also thank Tim Horscroft for this invited contribution. We thank Douwe van der Meer and two anonymous reviewers for their constructive comments that helped to improve the manuscript.

Appendix A. Supplementary material

Supplementary data to this article can be found online at https://doi.org/10.1016/j.gr.2021.05.016.

References

Abrajevitch, A., Van der Voo, R., 2010. Incompatible Ediacaran paleomagnetic directions suggest an equatorial geomagnetic dipole hypothesis. Earth Planet. Sci. Lett. 293 (1–2), 164–170.
Barrier, É., & Vrielynck, B. (2008). Paleotectonic maps of the Middle East: tectono-sedimentary-palinspatic maps from Late Norian to Pliocene, 14 maps, Comm. la Cart. Geol. du monde.
Barron, E.J., Hay, W.W., Thompson, S., 1989. The hydrologic cycle: a major variable during Earth history. Palaeogeo. Palaeoclim. Palaeoecol. 75 (3), 157–174.
Bergman, N.M., Lenton, T.M., Watson, A.J., 2004. COPSE: a new model of biogeochemical cycling over Phanerozoic time. Am. J. Sci. 304 (5), 397–437.
Berner, R.A., Lasaga, A.C., Garrels, R.M., 1983. The carbonate silicate geochemical cycle and its effect on atmospheric carbon dioxide over the past 100 million years. Am. J. Sci. 283, 641–683.
Berner, R.A., 2004. The Phanerozoic carbon cycle: CO2 and O2. Oxford University Press on Demand.
Berner, R.A., 2006. Inclusion of the weathering of volcanic rocks in the GEOCARBSULF model. Am. J. Sci. 306 (5), 295–302. https://doi.org/10.2475/05.2006.01.
Blakey, R. (2009). Molleweide plate tectonic maps. Available "on purchase" at https://deeptimemaps.com/.
Brune, S., Williams, S.E., Mueller, R.D., 2017. Potential links between continental rifting, CO2 degassing and climate change through time. Nature Geosci. 10 (12), 941–946.
Boucot, A.J., Xu, C., Scotese, C.R., Morley, R.J., 2013. Phanerozoic paleoclimate: an atlas of lithologic indicators of climate. SEPM (Society for Sedimentary Geology). ISBN:978-1-56576-282-4.
Cocks, L.R.M., Torsvik, T.H., 2020. Ordovician palaeogeography and climate change. Gond. Res. doi: 10.1016/j.gr.2020.09.008.
Caldeira, Ken, 1992. Enhanced Cenozoic chemical weathering and the subduction of pelagic carbonate. Nature 357 (6379), 578–581. https://doi.org/10.1038/357578a0.
Cogné, J.P., Humler, E., 2006. Trends and rhythms in global seafloor generation rate. Geochem. Geophys. Geosys. 7 (3).
Coltice, N., Seton, M., Rolf, T., Müller, R.D., Tackley, P.J., 2013. Convergence of tectonic reconstructions and mantle convection models for significant

fluctuations in seafloor spreading. Earth Planet. Sci. Lett. 383, 92–100.
Conrad, C.P., Lithgow-Bertelloni, C., 2007. Faster seafloor spreading and lithosphere production during the mid-Cenozoic. Geology 35, 29–32. https://doi.org/10.1130/G22759A.1.
Conrad, C.P., 2013. The solid Earth's influence on sea-level. GSA Bull. 125 (7–8), 1027–1052.
Crowley, T.J., 1991. Past CO2 changes and tropical sea surface temperatures. Paleoceanography 6 (3), 387–394.
Crowley, T.J., Baum, S.K., 1995. Reconciling Late Ordovician (440 Ma) glaciation with very high (14X) CO2 levels. J. Geophys. Res. 100, 1093–1101.
Dera, G., Brigaud, B., Monna, F., Laffont, R., Pucéat, E., Deconinck, J.F., Pellenard, P., Joachimski, M.M., Durlet, C., 2011. Climatic ups and downs in a disturbed Jurassic world. Geology 39 (3), 215–218.
Dercourt, J., Ricou, L.E., Vrielynck, B., (Eds.), 1993. Atlas Thethys Palaeoenvironmental Maps. Gauthier-Villars, Paris, 307p., 14 maps, 1 pl.
Dercourt, J., Gaetani, M., Vrielynck, B., Barrier E., Biju-Duval B., Brunet M.F., Cadet J. P., Crasquin, S., Sandulescu, M., (Eds.), 2000Atlas Peri-Thethys, Palaeogeographical maps. CCGM/CGMW, Paris: 24 maps and explanatory notes: I-XX; 1-269.
Domeier, M., Torsvik, T.H., 2014. Plate tectonics in the late Paleozoic. Geosci. Front. 5 (3), 303–350.
Domeier, M., 2016. A plate tectonic scenario for the Iapetus and Rheic oceans. Gond. Res. 36, 275–295. https://doi.org/10.1016/j.gr.2015.08.003.
Domeier, M., Magni, V., Hounslow, M.W., Torsvik, T.H., 2018. Episodic zircon age spectra mimic fluctuations in subduction. Sci. Rep. 8, 1747. https://doi.org/10.1038/s41598-018-35040-z.
Domeier, M., 2018. Early Paleozoic tectonics of Asia: Towards a full-plate model. Geosci. Front. 9, 789–862. https://doi.org/10.1016/j.gsf.2017.11.012.
Donnadieu, Y., Pierrehumbert, R., Jacob, R., Fluteau, F., 2006. Modelling the primary control of paleogeography on Cretaceous climate. Earth Planet. Sci. Lett. 248 (1–2), 426–437.
Ebelmen, J.J., 1845. Sur les produits de la decomposition des especes minirales de la famille des silicates. Annales des Mines 7, 3–66.
Engebretson, D.C., 1992. 180 million years of subduction. GSA today 2, 100.
Fielding, C.R., Frank, T.D., Isbell, J.L., 2008. The late Paleozoic ice age — A review of current understanding and synthesis of global climate patterns. In: Fielding, C. R., Frank, T.D., Isbell, J.L. (Eds.), Resolving the Late Paleozoic Ice Age in Time and Space. GSA Special Paper, 441, 343-354, doi: 10.1130/2008.2441(24).
Foster, G.L., Royer, D.L., Lunt, D.J., 2017. Future climate forcing potentially without precedent in the last 420 million years. Nature Commun. 8, 14845.
Francois, L.M., Walker, J.C., 1992. Modelling the Phanerozoic carbon cycle and climate: constraints from the 87Sr/86Sr isotopic ratio of seawater. Am. J. Sci 292 (2), 81–135.
Gibbs, M.T., Bluth, G.J., Fawcett, P.J., Kump, L.R., 1999. Global chemical erosion over the last 250 my; variations due to changes in paleogeography, paleoclimate, and paleogeology. Am. J. Sci. 299 (7–9), 611–651.
Gibbs, M.T., Bice, K.L., Barron, E.J., Kump, L.R., 2000. Glaciation in the early Paleozoic 'greenhouse': the roles of paleogeography and atmospheric CO2. In: Huber, B.T., MacLeod, K.G., Wing, S.L., Eds., Warm Climates in Earth History. Cambridge, Cambridge University Press, pp. 386-422.
Goddéris, Y., François, L.M., 1995. The Cenozoic evolution of the strontium and carbon cycles: relative importance of continental erosion and mantle exchanges. Chem. Geol. 126 (2), 169–190.
Goddéris, Y., Joachimski, M.M., 2004. Global change in the Late Devonian: modelling the Frasnian-Famennian short-term carbon isotope excursions. Palaeogeo. Palaeoclim. Palaeoecol. 202 (3–4), 309–329.
Goddéris, Y., Donnadieu, Y., Lefebvre, V., Le Hir, G., Nardin, E., 2012. Tectonic control of continental weathering, atmospheric CO_2, and climate over Phanerozoic times. C. R. Geo. 344 (11–12), 652–662. https://doi.org/10.1016/j.crte.2012.08.009.
Goddéris, Y., Donnadieu, Y., Le Hir, G., Lefebvre, V., Nardin, E., 2014. The role of paleogeography in the Phanerozoic history of atmospheric $CO_2$and climate. Earth Sci. Rev. 128, 122–138. https://doi.org/10.1016/j.earscirev.2013.11.004.
Goddéris, Y., Donnadieu, Y., 2017. A sink- or a source-driven carbon cycle at the geological timescale? Relative importance of paleogeography versus solid Earth degassing rate in the Phanerozoic climatic evolution. Geol. Mag. 156 (2), 355–365. https://doi.org/10.1017/S0016756817001054.
Goddéris, Y., Donnadieu, Y., Carretier, S., Aretz, M., Dera, G., Macouin, M., Regard, V., 2017. Onset and ending of the late Palaeozoic ice age triggered by tectonically paced rock weathering. Nature Geosci. 10 (5), 382–386.
Goldberg, S.L., Present, T.M., Finnegan, S., Bergmann, K.D., 2021. A high-resolution record of early Paleozoic climate. PNAS 118, (6) e2013083118.
Golonka, J., Krobicki, M., Pajak, J., Van Giang, N., Zuchiwwicz, W., 2006. Global Plate Tectonics and Paleogeography of Southeast Asia, Faculty of Geology. Geophysics and Environmental Protection. AGH University of Science and Technology, Arkadia, Krakow, Poland.
Gyllenhaal, E.D., Engberts, C.J., Markwick, P.J., Smith, L.H., Patzkowsky, M.E., 1991. The Fujita-Ziegler model: a new semi-quantitative technique for estimating paleoclimate from paleogeographic maps. Palaeogeo., Palaeoclim., Palaeoecol. 86 (1–2), 41–66.
Hansen, James, Sato, Makiko, Kharecha, Pushker, Beerling, Davis, Berner, Robert, Masson-Delmotte, Valerie, Pagani, Mark, Raymo, Maureen, Royer, Dana L., Zachos, James C., 2008. Target Atmospheric CO2: Where Should Humanity Aim? Open Atmospheric Science Journal 2, 217–231. https://doi.org/10.2174/1874282300802010217.
Haq, B.U., Al-Qahtani, A.M., 2005. Phanerozoic cycles of sea-level change on the Arabian Platform. GeoArabia 10 (2), 127–160.
Haq, B.U., Schutter, S.R., 2008. A chronology of Paleozoic sea-level changes. Science 322 (5898), 64–68.
Hartman, G., Richards, M., 2014. Mapping and defining sources of variability in bioavailable strontium isotope ratios in the Eastern Mediterranean. Geochim. Cosmochim. Acta 126, 250–264.
Hay, W.W., Barron, E.J., Thompson, S.L., 1990. Global atmospheric circulation experiments on an Earth with polar and tropical continents. J. Geo. Soc. 147 (5), 749–757.
Heine, C., Yeo, L.G., Müller, R.D., 2015. Evaluating global paleoshoreline models for the Cretaceous and Cenozoic. Aust. J. Earth Sci. 62 (3), 275–287.
Herrmann, A.D., Patzkowsky, M.E., Pollard, D., 2003. Obliquity forcing with 8–12 times preindustrial levels of atmospheric pCO_2 during the Late Ordovician glaciation. Geology 31, 485–488.
Hilley, G.E., Porder, S., 2008. A framework for predicting global silicate weathering and CO2 drawdown rates over geologic time-scales. Proc. Natl. Acad. Sci. USA 105 (44), 16855–16859.
Horton, D.E., Poulsen, C.J., Pollard, D., 2010. Influence of high-latitude vegetation feedbacks on late Palaeozoic glacial cycles. Nat. Geosci. 3 (8), 572–577.
Hounslow, M.W., Domeier, M., Biggin, A., 2018. Subduction flux modulates the geomagnetic polarity reversal rate. Tectonophysics 742, 34–49.
Karlsen, K.S., Domeier, M., Gaina, C., Conrad, C.P., 2020. A tracer-based algorithm for automatic generation of seafloor age grids from plate tectonic reconstructions. Comput.Geosci. 104508.
Kump, L.R., Arthur, M.A., Patzkowsky, M.E., Gibbs, M.T., Pinkus, D.S., Sheehan, P.M., 1999. A weathering hypothesis for glaciation at high atmospheric pCO2 during the Late Ordovician. Palaeogeo. Palaeoclim. Palaeoecol. 152 (1–2), 173–187.
Lagabrielle, Y., Goddéris, Y., Donnadieu, Y., Malavieille, J., Suarez, M., 2009. The tectonic history of Drake Passage and its possible impacts on global climate. Earth Planet. Sci. Lett. 279 (3–4), 197–211.
Larson, R.L., 1991. Geological consequences of superplumes. Geology 19 (10), 963–966.
Lee, C.T.A., Lackey, J.S., 2015. Global continental arc flare-ups and their relation to long-term greenhouse conditions. Elements 11 (2), 125–130.
Lee, C-T.A., Jiang, H., Dasgupta, R., Torres, M., 2020. A framework for understanding whole-earth carbon cycling. In: Orcutt, B., Daniel, I., Dasgupta, R. (Eds.), DEEP CARBON: Past to Present. Cambridge University Press, pp. 313–357. doi:10.1017/9781108677950.
Lenton, T.M., Daines, S.J., Mills, B.J., 2018. COPSE reloaded an improved model of biogeochemical cycling over Phanerozoic time. Earth Sci. Rev. 178, 1–28.
Lowry, D.P., Poulsen, C.J., Horton, D.E., Torsvik, T.H., Pollard, D., 2014. Thresholds for Paleozoic ice sheet initiation. Geology 42, 627–630.
Lyell, C. (1830). Principles of geology, being an attempt to explain the former changes of the Earths surface, by reference to causes now in operation. London, John Murray, Volume 1.
Marshall, H.G., Walker, J.C., Kuhn, W.R., 1988. Long-term climate change and the geochemical cycle of carbon. J. Geophys. Res.: Atmospheres 93 (D1), 791–801.
Matthews, K., Maloney, K.T., Zahirovic, S., Williams, S.E., Seton, M., Müller, R.D., 2016. Global plate boundary evolution and kinematics since the late Paleozoic. Glob. Planet. Chang. 146, 226–250.
McKenzie, N.R., Horton, B.K., Loomis, S.E., Stockli, D.F., Planavsky, N.J., Lee, C.-T.A., 2016. Continental arc volcanism as the principal driver of icehouse-greenhouse variability. Science 352 (6284), 444–447. https://doi.org/10.1126/science.aad5787.
Merdith, A.S., Williams, S.E., Brune, S., Collins, A.S., Müller, R.D., 2019. Rift and plate boundary evolution across two supercontinent cycles. Glob. Planet. Chang. 173, 1–14.
Merdith, A.S., Williams, S.E., Collins, A.S., Tetley, M.G., Mulder, J.A., Blades, M.L., Young, A., Armistead, S.E., Cannon, J., Zahirovic, S., Müller, R.D., 2021. Extending full-plate tectonic models into deep time: Linking the Neoproterozoic and the Phanerozoic. Earth Sci. Rev. 214. https://doi.org/10.1016/j.earscirev.2020.103477.
Michel, L.A., Tabor, N.J., Montañez, I.P., Schmitz, M.D., Davydov, V.I., 2015. Chronostratigraphy and paleoclimatology of the Lodève Basin, France: evidence for a pan-tropical aridification event across the Carboniferous-Permian boundary. Palaeogeo. Palaeoclim. Palaeoecol. 430, 118–131.
Mills, B., Daines, S.J., Lenton, T.M., 2014. Changing tectonic controls on the long-term carbon cycle from Mesozoic to present. Geochem. Geophys. Geosys. 15 (12), 4866–4884.
Mills, B.J., Scotese, C.R., Walding, N.G., Shields, G.A., Lenton, T.M., 2017. Elevated CO 2 degassing rates prevented the return of Snowball Earth during the Phanerozoic. Nat. comm. 8 (1), 1–7.
Mills, B.J.W., Krause, A.J., Scotese, C.R., Hill, D.J., Shields, G.A., Lenton, T.M., 2019. Modelling the long-term carbon cycle, atmospheric CO_2, and Earth surface temperature from late Neoproterozoic to present day. Gond. Res. 67, 172–186.
Montañez, I.P., Poulsen, C.J., 2013. The Late Paleozoic Ice Age: An Evolving Paradigm. Annu. Rev. Earth Planet. Sc. 41, 629–656. https://doi.org/10.1146/annurev.earth.031208.100118.
Moore, T.L., Scotese, C.R., 2010. The Paleoclimate Atlas (ArcGIS), GSA, 2010 Annual Meeting. Abstracts with Programs 42, 598.
Mujal, E., Fortuny, J., Marmi, J., Dinarès-Turell, J., Bolet, A., Oms, O., 2018. Aridification across the Carboniferous-Permian transition in central equatorial Pangea: the Catalan Pyrenean succession (NE Iberian Peninsula). Sediment. Geol. 363, 48–68.
Ollier, C., Pain, C., 1996. Regolith, Soils and Landforms. John Wiley & Sons.
Oki, T., & Kanae, S. (2006). Global hydrological cycles and world water resources. Science, 313(5790), 1068–1072.

Otto-Bliesner, B.L., 1995. Continental drift, runoff, and weathering feedbacks: implications from climate model experiments. J. Geophys. Res. 100 (6), 11537–11548.
Pagani, Mark, Liu, Zhonghui, laRiviere, Jonathan, Ravelo, Ana Christina, 2010. High Earth-system climate sensitivity determined from Pliocene carbon dioxide concentrations. Nature Geoscience 3, 27–30. https://doi.org/10.1038/ngeo724.
Park, J., Royer, D.L., 2011. Geologic constraints on the glacial amplification of Phanerozoic climate sensitivity. Am. J. Sci. 311 (1), 1–26.
Poblete, F., Dupont-Nivet, G., Licht, A., Van Hinsbergen, D.J., Roperch, P., Mihalynuk, M.G., et al., 2021. Towards interactive global paleogeographic maps, new reconstructions at 60, 40 and 20 Ma. Earth Sci. Rev. 103508.
Pohl, A., Donnadieu, Y., Le Hir, G., Buoncristiani, J.F., Vennin, E., 2014. Effect of the Ordovician paleogeography on the (in) stability of the climate. Clim. Past 10 (6), 2053–2066.
Puetz, S.J., Ganade, C.E., Zimmermann, U., Borchardt, G., 2018. Statistical Analyses of Global U-Pb Database 2017. Geosci. Front. 9, 121–145.
Rohling, E et al.PALAEOSENS Project Members, 2012. Making sense of palaeoclimate sensitivity. Nature 491, 683–691. https://doi.org/10.1038/nature11574.
Rowley, D.B., 2002. Rate of plate creation and destruction: 180 Ma to present. GSA Bull. 114 (8), 927–933.
Royer, D.L., 2006. CO2-forced climate thresholds during the Phanerozoic. Geochim. Cosmochim. Acta 70 (23), 5665–5675. https://doi.org/10.1016/j.gca.2005.11.031.
Royer, D.L., Donnadieu, Y., Park, J., Kowalczyk, J., Goddéris, Y., 2014. Error analysis of CO2 and O2 estimates from the long-term geochemical model GEOCARBSULF. Am. J. Sci. 314 (9), 1259–1283.
Royer, D.L., 2016. Climate sensitivity in the geologic past. Annu. Rev. Earth Planet Sci., 44
Sahney, S., Benton, M.J., Falcon-Lang, H.J., 2010. Rainforest collapse triggered Carboniferous tetrapod diversification in Euramerica. Geology 38 (12), 1079–1082.
Schellart, W., Stegman, D., Freeman, J., 2008. Global trench migration velocities and slab migration induced upper mantle volume fluxes: constraints to find an Earth reference frame based on minimizing viscous dissipation. Earth Sci. Rev. 88, 118–144.
Scotese, C.R., 2014a. The PALEOMAP Project PaleoAtlas for ArcGIS, version 2, Volume 1, Cenozoic Plate Tectonic, Paleogeographic, and Paleoclimatic Reconstructions, Maps 1-15. PALEOMAP Project, Evanston.
Scotese, C.R., 2014b. Atlas of Paleogene Paleogeographic Maps (Mollweide Projection), Maps 8–15, Volume 1, The Cenozoic, PALEOMAP Atlas for ArcGIS. Evanston, IL, USA: PALEOMAP Project.
Scotese, C.R., Moore, T.L., 2014. Atlas of Phanerozoic Ocean Currents and Salinity (Mollweide Projection),Volumes 1-6, PALEOMAP Project PaleoAtlas for ArcGIS, PALEOMAP Project, Evanston, IL.
Scotese, C.R., 2016. PALEOMAP PaleoAtlas for GPlates and the PaleoData plotter program. In: GSA Abstracts with Programs, vol. 48, No. 5.
Scotese, C.R., Song, H., Mills, B.J.W., van der Meer, D.G., 2021. Phanerozoic paleotemperatures: The Earth's changing climate during the last 540 million years. Earth Sci. Rev.
Seton, M., Gaina, C., Müller, R.D., Heine, C., 2009. Mid-Cretaceous seafloor spreading pulse: fact or fiction?. Geology 37 (8), 687–690.
Seton, M., Müller, R.D., Zahirovic, S., Gaina, C., Torsvik, T.H., Shephard, G., Talsma, A., Gurnis, M., Turner, M., Chandler, M., 2012. Global continental and ocean basin reconstructions since 200 Ma. Earth Sci. Rev. 113, 212–270.
Song, H., Wignall, P.B., Song, H., Dai, X., Chu, D., 2019. Seawater temperature and dissolved oxygen over the past 500 million years. J. Earth Sci. 30 (2), 236–243.
Soreghan, G.S., Soreghan, M.J., Heavens, N.G., 2019. Explosive volcanism as a key driver of the late Paleozoic ice age. Geology 47, 600–604. https://doi.org/10.1130/G46349.1.
Torsvik, T.H., Steinberger, B., Gurnis, M., Gaina, C., 2010. Plate tectonics and net lithosphere rotation over the past 150 My. Earth Planet. Sci. Lett. 291, 106–112.
Torsvik, T.H., van der Voo, R., Doubrovine, P.V., Burke, K., Steinberger, B., Ashwal, L. D., Trønnes, R.G., Webb, S.J., Bull, A.L., 2014. Deep mantle structure as a reference frame for movements in and on the Earth. Proc. Natl. Acad. Sci. USA 111, 8735–8740. https://doi.org/10.1073/pnas.1318135111.
Torsvik, T.H., Cocks, L.R.M., 2017. Earth History and Palaeogeography. Cambridge University Press. 317 pp..
Torsvik, T.H., Steinberger, B., Shephard, G.E., Doubrovine, P.V., Domeier, M., Gaina, C., Conrad, C., Sager, W.W., 2019. Pacific-Panthalassic reconstructions: Overview, errata and the way forward. Geochem. Geophys. Geosys. 20. https://doi.org/10.1029/2019GC008402.
Torsvik, T.H., Svensen, H.H., Steinberger, B., Royer, D.L., Jerram, D.A., Jones, M.T., Domeier, M., 2020. Connecting the Deep Earth and the Atmosphere. AGU book chapter.
Vandenbroucke, T.R., Armstrong, H.A., Williams, M., Paris, F., Zalasiewicz, J.A., Sabbe, K., et al., 2010. Polar front shift and atmospheric CO2 during the glacial maximum of the Early Paleozoic Icehouse. Proc. Natl. Acad. Sci. 107 (34), 14983–14986.
Van der Meer, D.G., Torsvik, T.H., Spakman, W., Van Hinsbergen, D.J.J., Amaru, M.L., 2012. Intra-Panthalassa Ocean subduction zones revealed by fossil arcs and mantle structure. Nat. Geo. 5 (3), 215–219.
Van der Meer, D.G, Zeebe, R., van Hinsbergen, D.J.J., Sluijs, A., Spakman, W., Torsvik, T.H., 2014. Plate tectonic controls on atmospheric CO2 levels since the Triassic. Proc. Natl. Acad. Sci. doi:10.1073/ pnas.1315657111.
Voice, P.J., Kowalewski, M., Eriksson, K.A., 2011. Quantifying the timing and rate of crustal evolution: global compilation of radiometrically dated detrital zircon grains. J. Geol. 119, 109–126.
Walker, J.C.G., Hays, P.B., Kasting, J.F., 1981. A negative feedback mechanism for the long-term stabilization of Earth's surface temperature. J. Geophys. Res. 86, 9776–9782.
Wegener, A., 1912. Die Entstehung der Kontinente. Dr. A. Petermanns Mitteilungen aus Justus Perthes geographischer Anstalt, 58, 185–195, 253–256, 305–309.
West, A.J., Galy, A., Bickle, M., 2005. Tectonic and climatic controls on silicate weathering. Earth Planet. Sci. Lett. 235 (1–2), 211–228.
White, A.F., Blum, A.E., 1995. Effects of climate on chemical_ weathering in watersheds. Geochim. Cosmochim. Acta 59 (9), 1729–1747.
Witkowski, C.R., Weijers, J.W., Blais, B., Schouten, S., Damsté, J.S.S., 2018. Molecular fossils from phytoplankton reveal secular PCO2 trend over the Phanerozoic. Sci. Adv. 4(11), eaat4556.
Witkowski, C.R., Agostini, S., Harvey, B.P., Van Der Meer, M.T., Sinninghe Damsté, J. S., Schouten, S., 2019. Validation of carbon isotope fractionation in algal lipids as a pCO 2 proxy using a natural CO 2 seep (Shikine Island, Japan). Biogeosciences 16 (22), 4451–4461.
Wong, K., Mason, E., Brune, S., East, M., Edmonds, M., Zahirovic, S., 2019. Deep carbon cycling over the past 200 million years: a review of fluxes in different tectonic settings. Front. Earth Sci. 7, 263. https://doi.org/10.3389/feart.2019.00263.
Worsley, T.R., Kidder, D.L., 1991. First-order coupling of paleogeography and CO sub 2, with global surface temperature and its latitudinal contrast. Geology 19(12). doi: 10.1130/0091-7613(1991)019<1161: FOCOPA>2.3.CO; 2.
Wotte, T., Skovsted, C.B., Whitehouse, M.J., et al., 2019. Isotopic evidence for temperate oceans during the Cambrian Explosion. Sci. Rep. 9, 6330.
Young, A., Flament, N., Maloney, K., Williams, S., Matthews, K., Zahirovic, S., Müller, R.D., 2019. Global kinematics of tectonic plates and subduction zones since the late Paleozoic Era. Geosci. Front. 10, 989–1013. https://doi.org/10.1016/j.gsf.2018.05.011.
Zhang, X., Prange, M., Steph, S., Butzin, M., Krebs, U., Lunt, D.J., Schulz, M., 2012. Changes in equatorial Pacific thermocline depth in response to Panamanian seaway closure: Insights from a multi-model study. Earth Planet. Sci. Lett. 317, 76–84.
Ziegler, P.A., 1990. Geological atlas of western and central Europe. Shell Internationale Petroleum Maatschappij BV, 239 pp.

Chloé M. Marcilly PhD research fellow at the Centre for Earth Evolution and Dynamics (CEED), at the Department of Geosciences, University of Oslo since 2019. She completed a MSc in sedimentology/geochemistry from the University of Oslo in 2016. She is working within the field of paleoclimate reconstructions and long-term carbon cycle modelling. Her main research interest is the effect of changing paleogeography and carbon degassing on climate over geological timescales.

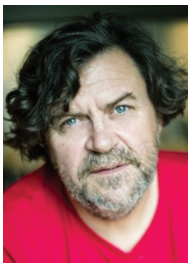

Trond H. Torsvik Professor of Geodynamics and Director of the Centre for Earth Evolution and Dynamics (CEED), University of Oslo (Norway). He is also a Professor at Wits University (Johannesburg, South Africa) and with particular interests in paleomagnetism, paleogeography, Earth history and long-term climate evolution.

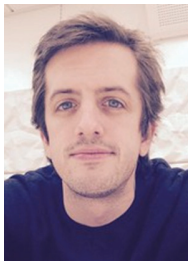

Mathew Domeier Researcher at the Centre for Earth Evolution and Dynamics (CEED) at the University of Oslo (Norway) since 2013, with research interests in tectonics, paleogeography and paleomagnetism.

Dana L. Royer Professor of Earth and Environmental Sciences at Wesleyan University (USA). He is interested in CO_2 proxies, long-term carbon cycle models, and understanding patterns of CO_2 and climate sensitivity over the Phanerozoic.

Global Phanerozoic sea levels from paleogeographic flooding maps.

Chloé M. Marcilly, Trond H. Torsvik, Clinton P. Conrad.

Gondwana Research 110 (2022) 128-142.

NB: Table 1 column 5 values have been corrected compared to the published version (now in green) due to errors. An erratum has been requested to Gondwana Research but with no success to this date.

Gondwana Research 110 (2022) 128–142

Contents lists available at ScienceDirect

Gondwana Research

journal homepage: www.elsevier.com/locate/gr

Global Phanerozoic sea levels from paleogeographic flooding maps

Chloé M. Marcilly [a,*], Trond H. Torsvik [a,b], Clinton P. Conrad [a]

[a] Centre for Earth Evolution and Dynamics (CEED), University of Oslo, 0315 Oslo, Norway
[b] School of Geosciences, University of Witwatersrand, Johannesburg 2050, South Africa

ARTICLE INFO

Article history:
Received 3 January 2022
Revised 22 April 2022
Accepted 20 May 2022
Available online 1 June 2022
Handling Editor: R. D. Nance

Keywords:
Phanerozoic sea level
Paleogeographic reconstructions
Global flooding
Global hypsometry

ABSTRACT

The validity of sea level estimates based on stratigraphic correlations has been debated since the 1990 s as relative sea level curves differ between sites due to local tectonics, different deposition rates and changes in dynamic topography. Here, we offer a new eustatic (global) sea level curve for the past 520 million years (Myrs) based on observations of global flooding. We use paleogeographic reconstructions to measure the area of today's exposed land that was flooded in the past (*modern-land flooding*). We then apply the modern global hypsometric slope to reconstruct the sea level history. We find minimum sea levels (comparable to today's level) towards the end of Pangea (210 Ma) and peak levels (~280 m higher than today) at 80 Ma when Pangea was widely dispersed. A first-order "supercontinent" cycle of 250 million years (Myrs) is recognized but we also document a second-order cycle of 37 Myrs that was previously thought to be undetectable using the hypsometric method. The hypsometric slope is critical for reconstructing past sea levels, and steepening the hypsometric slope during Pangea assembly implies dramatically larger sea level fluctuations. Our new sea level curve shares strong similarities with stratigraphic constraints and correlates with seafloor production proxies throughout the Phanerozoic. Measurements of global flooding represent averages across great continental extents, making them less sensitive than stratigraphic analyses to regional-scale vertical land motion, such as from dynamic topography and hence more reliable for estimating eustatic sea level. This method can also help to identify local deviations caused by regional uplift or subsidence and serves to constrain geodynamic mechanisms for sea level change. Our new sea level reconstruction usefully tracks global variations in Phanerozoic eustatic sea level, but also opens opportunities to estimate such variations in deeper time.

1. Introduction

Sea level and its fluctuations over various timescales are indicators of changes across multiple earth processes, including climatic and tectonic changes as well as time-dependent mantle dynamics. Eustatic or global sea level variations may be driven by changes in the volume of water in the oceans, controlled by the amount of water stored on land in glaciers and groundwater. On timescales of 10 s to 100 s of Myrs, water exchange with Earth's mantle contributes to large sea level fluctuations (Karlsen et al., 2019). Eustatic changes on such timescales also result from plate tectonics and mantle processes that create volcanoes, mid oceanic ridges, and continental orogeny, which vertically deflect the seafloor or change its area (e.g., Conrad, 2013). Stresses associated with mantle flow can also trigger up to a kilometer (km) of dynamically supported topography that affects eustatic sea level as well as coastal (i.e., local) observations of sea level (e.g., Moucha et al., 2008; Conrad and Husson, 2009).

Eustatic sea level changes can be quantified using stratigraphic methods and other paleoenvironmental indicators (e.g., Miller et al., 2005). Fossil corals provide high precision constraints for the past few million years, and indicate rates of sea level rise as high as 40 mm/yr (Lambeck et al., 2014), an order of magnitude higher than Anthropocene-driven changes (~3 mm/yr). In deep time (i.e., > 100 Ma), the number of methods that can be used to reconstruct sea level is limited. They are essentially restricted to methods associated with stratigraphy, which uses fossil markers and sedimentary facies changes to assess the position of the shoreline through time (e.g., Haq & Al-Qahtani, 2005; Haq & Schutter, 2008; Miller et al., 2005, Hardenbol et al., 1998) and plate tectonic reconstructions, which assess changes to the depth and the extent of ocean basins (e.g., Vérard et al., 2015; Conrad, 2013). However, plate tectonic methods require full-plate polygons with age-estimates for the oceanic lithosphere that are mainly synthetic before the Cretaceous.

* Corresponding author.

https://doi.org/10.1016/j.gr.2022.05.011
1342-937X/

Most stratigraphy-based Phanerozoic sea level curves show consistent long-duration fluctuations (Fig. 1) with (1) high (200 to 400 m) sea levels in the early Paleozoic, (2) low (50 to −25 m) sea levels during Pangea times (320–250 Ma), (3) peak sea level in the Late Cretaceous (~250 m at 100–80 Ma) and (4) declining sea levels during Late Cretaceous and Cenozoic times (from 200 m to present-day level). Most variations are within the 200 m range, but some studies yield variations up to 400 m above and 50 m below present-day levels (e.g., Hallam, 1992; Snedden & Liu, 2010, 2011). Although the reported amplitudes of the early Paleozoic and late Mesozoic sea level high-stands vary significantly, the relative consistency of the temporal variations in the different stratigraphic curves suggests that they can place practical constraints on the plate tectonic processes that largely control them. Nevertheless, stratigraphy-based sea level curves have been challenged because they simultaneously measure eustatic sea level change and local uplift or subsidence at the observation location (Kominz et al., 2016; Gurnis, 1993a,b), which can result in over- or under-estimation of global-scale fluctuations. Indeed, the relative sea level assessment is often based on measurement along one or more coastlines and can be affected by the local dynamic topography of the region (Müller et al., 2008; Gurnis et al. 1998; Spasojevic et al., 2008).

Compared to regional stratigraphic observations, global flooding estimates represent averages of sea level change across large areas, making these estimates less sensitive to modification by regional uplift or subsidence. Here, we calculate eustatic sea level change directly from flooding maps using the hypsometric method, which converts continental flooding into changes in sea level using the landmass-specific hypsometric curve (Forney, 1975, Algeo & Wilkinson, 1991; van der Meer et al., 2017; Bond, 1979; Harrison, 1990). This method provides estimates of sea level fluctuations with coarser time-resolution than can be obtained from other methods (e.g., seismic or stratigraphic analysis). However, the hypsometric method holds the significant advantage of being applicable over long periods (>10 Myrs), such as the entire Phanerozoic (Algeo & Wilkinson, 1991). However, this method relies on the accuracy of the flooding estimates. In previous studies, both global continental crust flooding (e.g., Kocsis and Scotese, 2021; Scotese and Golonka, 1992) and 'upper shelf to coastal' flooding (e.g., Ronov, 1994; Smith et al., 2004) are engulfed in the term "flooding". This can lead to confusion and faulty comparisons as these estimates utilize different measurements, and may be subjected differently to corrections for isostatic processes. Furthermore, while the upper limit of the flooded area can usually be identified through time, the lower limit is usually more poorly defined, and needs clarification. We here develop clear terms and definitions for flooding estimates and express the main differences and limitations between two chosen definitions. We also refined flooding estimates based on paleogeographic maps of exposed land (Marcilly et al. 2021). Based on our analyses of flooded land, we here present a new global sea level curve over most of the Phanerozoic with improved accuracy.

2. Methods

2.1. Definition of flooding

The quality of sea level estimates derived from the hypsometric method primarily depends on quantifying the size of flooded land areas over time. This study tests two different definitions of flooding, "*modern-land*" and "*continental*" flooding. "*Modern-land*" flooding is here simply defined as the areal difference between exposed land at a certain time in the past (exposed but moved in time according to the tectonic reconstruction) versus the total land area exposed today. For example, the brown and light blue areas in Fig. 2a are the exposed area today for the reconstructed landmasses, but only the brown areas were exposed at 440 Ma. The light blue areas, therefore, represent land areas flooded at 440 Ma. It should be noted that some of the land flooded today is considered exposed at certain times in the past (pink areas), e.g., within landmasses interior to Gondwana (Fig. 2a) that were juxtaposed in the past. We here consider those areas as shallow areas most likely to be exposed within the 10 Myrs of the map life

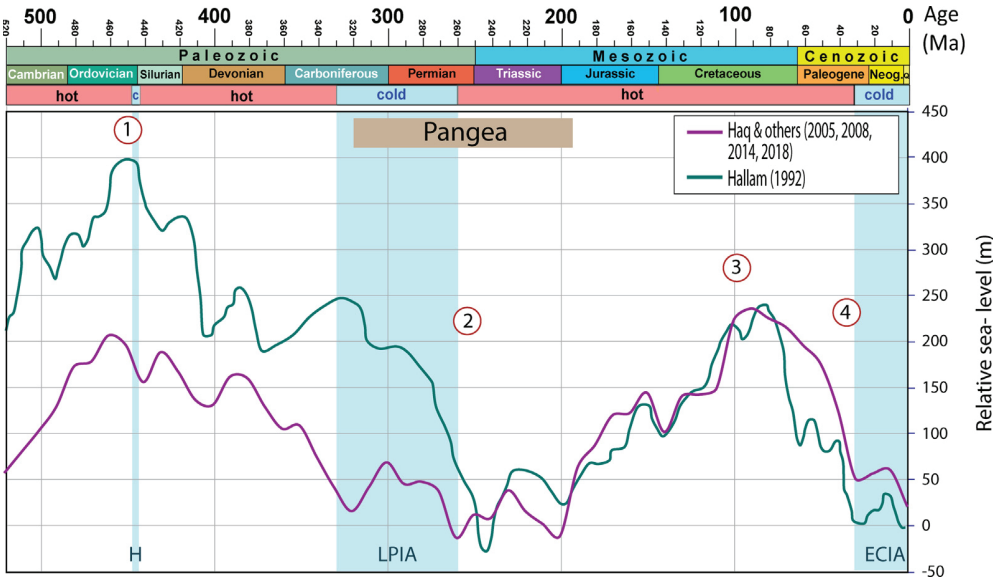

Fig. 1. Timescale with greenhouse (hot) versus icehouse (cold) conditions for the past 520 Myrs and two global sea level curves derived from the use of stratigraphic methods (i.e. Hallam, 1992; Composite curve from: Haq & Al-Qahtani, 2005, Haq & Schutter, 2008, Haq, 2014; 2018). The curve is binned every 10 Myrs to smooth changes in chronostratigraphy (generally less than 4 Myr differences) between studies. Numbers 1 to 4 refer to the description of sea level fluctuations discussed in the text. Bulk Pangea lasted from about 320 to 195 Ma (Veevers, 2004; Torsvik and Cocks, 2017). H, Hirnantian glaciation (end-Ordovician; ~445 Ma); LPIA, Late Paleozoic Ice Age (330–260 Ma); ECIA, End Cenozoic Ice Age (past 30 Myrs). The timing of the main icehouses are extracted from the compilation of Torsvik and Cocks (2016), Fielding et al. (2008), Rocha-Campos et al. (2008), Gaetani et al. (2009), Beerling and Berner (2000), and correspond to periods with large permanent ice-sheets (Scotese et al. 2021).

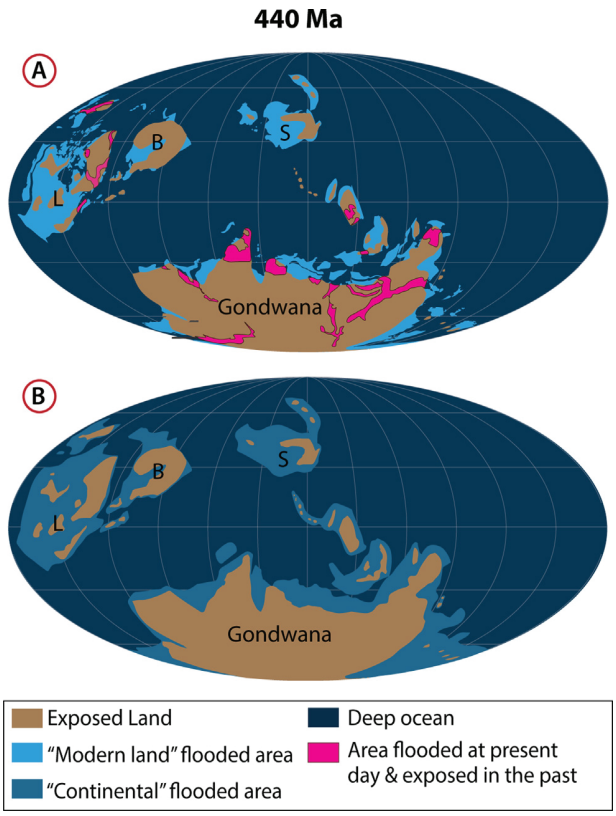

Fig. 2. Plate reconstructions at ~ 440 Ma (early Silurian) with exposed land, deep ocean and **(a)** "*Modern land*" flooded areas (light blue) and exposed land of the past that is currently flooded (pink areas). Our reconstructions assume that small pathways between continents were also exposed in the past, based on lithofacies and fossil distributions over 10 Myr intervals. However, those land areas are not exposed today. **(b)** "*Continental*" flooded area (updated from Marcilly et al., 2021). B, Baltica; L, Laurentia, S, Siberia. (For interpretation of the references to color in this figure legend, the reader is referred to the web version of this article.)

and therefore consider them as exposed. The "*modern-land*" flooding method to estimate global sea levels does not require precise paleogeographic information in terms of absolute latitude and longitude for the continents.

"*Continental*" flooding is here defined as the difference between the area of the continental crust (continental crust polygons modified from Torsvik and Cocks, 2017) and the area of exposed land through time (Fig. 2b). This flooding refers to the inundation of entire continental shelves and includes areas of for example stretched continental crust (pre-breakup extension) along passive margins. Computing the area of flooded continental shelves requires more detailed paleogeographic and plate tectonic knowledge of those areas. Contrarily to the "*modern-land*" flooding estimates, the "*continental*" flooding estimates (Fig. 3a) must be corrected relative to present-day flooding to translate them into relative sea level estimates. The total present-day area of continental crust is estimated to 210.4 mill. km^2 (Cawood et al., 2013), which is almost identical to the areal extent (210.5 mill. km^2) of the continental crust polygon model of Torsvik & Cocks (2017). Based on this continental polygon model, with some revisions, we have mapped out the limit of potential continental crust worldwide for the past 520 Myrs, and the areal extent is listed in Table 1. One simplification in our model is that some areas of exposed oceanic crust today (e.g., Iceland) are incorrectly integrated into the estimates of exposed continental land, leading to an error of 0.08% that is removed from the obtained flooding estimates.

The present-day flooding calculated based on the continental shelves model is ~ 61.5 mill. km^2 which is the difference between present-day area of continental crust (~210.5 mill. km^2) and the exposed land area on Earth (~148.9 mill. km^2). To express the "*continental*" estimates relative to the present, we remove this present-day flooding value (Fig. 3a) from each estimate over the studied period. However, it is worth pointing out that "*continental*" crust estimates through time, as opposed to "*modern-land*" estimates, are often poorly constrained and are the result of a subjective exercise, e.g. how much continental extension took place along a particular rifted margin, how much shortening took place for a specific terrane, and at what time(s) did extension or shortening occur.

The uncertainties linked to the exposed land maps mostly reside in the time-step chosen (i.e 10 Myrs), and some maps, where base-data were lacking, had to be built using extrapolation between the maps ± 10 Myrs around it (Marcilly et al., 2021). It is to be noted that uncertainties are large and numerous for the exposed land reconstructions but nearly impossible to quantify as data become less reliable with time. This is also true when trying to estimate the transition zone between continental and oceanic crust through time (e.g., Torsvik et al. 2009), but this only affects "*continental*" flooding estimates.

2.2. Calculation of sea levels

In order to calculate sea levels from flooding estimates, we used the hypsometric method (Forney, 1975, Bond, 1979) with an estimate of the hypsometric slope that relates continental area to elevation (van der Meer et al., 2017). We consider only one single global and averaged hypsometric slope over Earth's coastal regions, as we aim to calculate global changes in sea level. We therefore do not calculate the slope for each continental landmass separately, unlike previous studies (e.g., Bond (1979); Forney (1975)). To estimate the slope, we used a linear fit over the ETOPO1 global relief model (Amante and Eakins, 2009) corrected for geoid and post-glacial rebound effects (Vérard, 2017). As the elevation for Phanerozoic eustatic fluctuations ranges within a few hundred meters above present sea level, only the low elevation hypsometric curve (i.e., the coastal hypsometry) is required here. The slope of the hypsometric curve is assumed to remain constant in the first few hundred meters (0–200 m) (Forney, 1975; Hallam, 1984). This approximation has been demonstrated as reliable (van der Meer et al. 2017) and enables the following linear relationship:

$$h(t) = F(t) * C \quad (1)$$

F(t) is the time-dependent additional area of continental shelves (in km^2) that will be flooded by sea level rise $h(t)$, while C is the hypsometric slope (in km^2/10^{6}km). In equation (1), the hypsometric curve is used to estimate the eustatic sea level rise that will flood different portions of the continent over time. To use it over the Phanerozoic, we assume that ancient coastal hypsometries were similar to those of the present-day (Forney, 1975). This assumption implies that the shelf margins were identical in slope (albeit located differently across the globe through time).

Models for modern hypsometry suggest different values for C based on whether ice sheets are considered, or if the ice is removed (Amante & Eakins, 2009). A value of 0.0050 km/10^{6}km^2 is estimated by van der Meer et al. (2017) using a model corrected for ice load. However, Vérard (2017) suggests that the slope should additionally be corrected for geoid and post-glacial rebound effects. Furthermore, as we identify variations in sea level that are>200 m (Fig. 1), we recalculated the slope from Vérard (2017) using a linear fit between 0 and 250 m (range of most of the

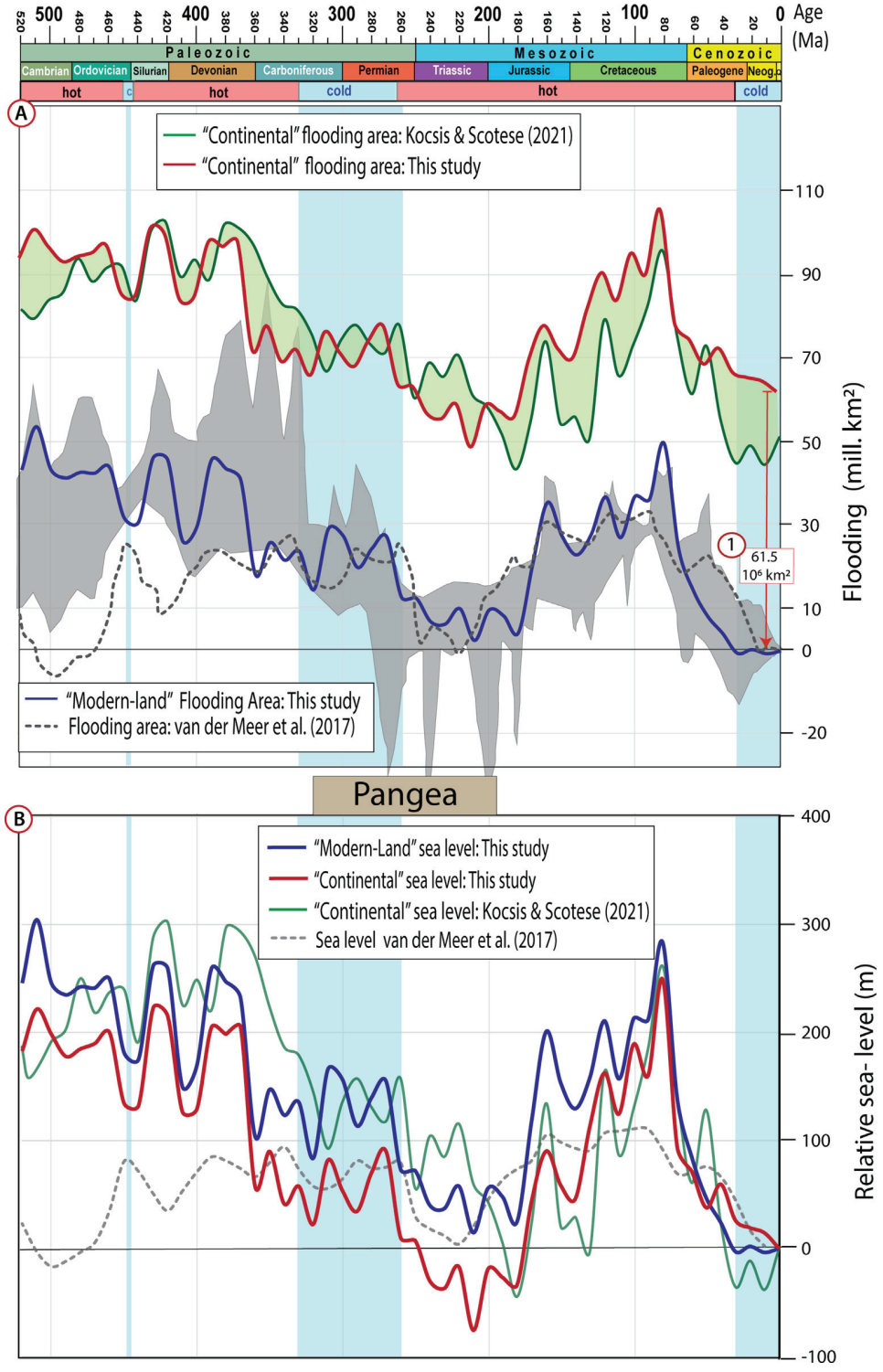

Fig. 3. (a) Time-scale with greenhouse (hot) versus icehouse (cold) conditions for the past 520 Myrs (See Fig. 1 caption for additional details), "*Modern-land*" flooding estimates and our "Continental" flooding estimates (without any corrections) compared with continental flooding estimates of Kocsis & Scotese (2021). The difference between our curve and the one of Kocsis and Scotese (2021) is shaded in green. The offset labeled (1) indicates the correction needed for our "*continental*" estimates to be expressed relative to present. The shaded grey area corresponds to the compilation of flooding areas estimates from different studies compiled by van der Meer et al. (2017). The flooding area from van der Meer et al. (2017; stippled grey line) is based on strontium isotope analysis with correction for weathering processes. **(b)** Estimated "*Modern-land*" (blue curve) and "*Continental*" (red curve) sea levels, compared to sea level reconstructions from Kocsis and Scotese (2021) and van der Meer et al. (2017). (For interpretation of the references to color in this figure legend, the reader is referred to the web version of this article.)

Table 1
Land and flooding areas through time with a 10 Myrs time step, and calculated sea levels for both "modern-land" and "continental flooding". The mismatch between modern land and exposed land during 20-0 Ma is linked to many islands that are mapped in the exposed land model.

Age (Ma)	Continental crust 10^6 km^2	Modern land (corrected for Iceland) 10^6 km^2	Exposed land 10^6 km^2	Modern-land flooding Relative 10^6 km^2	Continental flooding 10^6 km^2	Continental flooding relative to present Relative 10^6 km^2	Modern land sea level (C = 0.0057 km/km^2) Relative m	Continental sea level (C = 0.0057 km/km^2) m	Continental sea level (C = 0.0057 km/km^2) Relative m
520	169.40	116.16	75.61	43.42	93.79	32.30	245.84	531.07	182.88
510	167.57	117.83	66.95	53.74	100.62	39.14	304.32	569.78	221.60
500	174.85	118.88	78.29	43.45	96.55	35.07	246.02	546.74	198.55
490	173.28	119.00	80.37	41.50	92.91	31.42	234.97	526.11	177.92
480	172.98	118.79	78.86	42.79	94.13	32.64	242.32	532.99	184.80
470	174.33	119.07	79.29	42.63	95.03	33.55	241.42	538.12	189.93
460	174.49	118.89	77.69	44.06	96.79	35.31	249.49	548.09	199.91
450	175.03	118.97	89.80	32.03	85.23	23.74	181.37	482.61	134.42
440	175.76	118.98	90.86	30.98	84.90	23.41	175.44	480.75	132.56
430	176.61	119.16	75.77	46.25	100.84	39.36	261.91	571.02	222.84
420	176.84	120.27	77.37	45.76	99.47	37.98	259.14	563.24	215.05
410	180.65	120.40	96.75	26.51	83.90	22.41	150.12	475.08	126.89
400	179.80	122.57	95.50	29.93	84.29	22.81	169.48	477.31	129.12
390	177.74	123.00	80.10	45.76	97.65	36.16	259.14	552.93	204.74
380	178.77	122.96	82.21	43.62	96.56	35.08	246.98	546.78	198.59
370	182.78	123.16	85.04	40.98	97.74	36.25	232.06	553.45	205.26
360	179.20	123.03	107.55	18.35	71.65	10.16	103.89	405.71	57.52
350	177.28	123.06	99.92	26.01	77.36	15.88	147.27	438.06	89.87
340	175.28	125.42	106.48	21.81	68.80	7.31	123.49	389.58	41.40
330	176.77	126.16	105.10	23.93	71.67	10.18	135.49	405.81	57.63
320	182.92	129.36	117.44	14.78	65.47	3.99	83.70	370.75	22.56
310	181.44	131.94	105.51	29.30	75.93	14.45	165.88	429.97	81.79
300	181.73	135.57	110.77	27.66	70.96	9.47	156.62	401.80	53.61
290	186.35	135.98	118.78	20.06	67.57	6.08	113.57	382.62	34.43
280	188.33	136.25	114.45	24.67	73.89	12.40	139.68	418.38	70.19
270	189.27	136.39	111.91	27.34	77.36	15.87	154.80	438.04	89.85
260	190.09	136.89	126.82	12.93	63.27	1.78	73.22	358.26	10.07
250	191.39	138.47	128.62	12.72	62.78	1.29	72.03	355.47	7.29
240	190.50	138.51	134.29	7.08	56.20	−5.28	40.09	318.25	−29.94
230	189.81	138.51	134.84	6.54	54.97	−6.52	37.03	311.26	−36.92
220	189.67	138.52	131.18	10.20	58.49	−2.99	57.74	331.21	−16.98
210	186.81	138.42	138.69	2.59	48.12	−13.36	14.66	272.49	−75.70
200	190.16	139.02	132.04	9.84	58.12	−3.36	55.75	329.12	−19.07
190	190.04	138.86	133.28	8.44	56.76	−4.73	47.81	321.41	−26.78
180	193.00	139.02	137.46	4.42	55.54	−5.95	25.00	314.49	−33.70
170	190.78	139.55	121.50	20.91	69.28	7.80	118.41	392.31	44.12
160	184.81	140.02	107.39	35.49	77.41	15.93	200.95	438.36	90.17
150	187.16	140.02	115.35	27.05	71.81	10.32	153.19	406.62	58.43
140	189.50	140.02	119.88	22.88	69.62	8.13	129.56	394.22	46.03
130	196.52	140.02	115.04	27.97	81.48	20.00	158.39	461.39	113.20
120	196.24	140.02	106.04	37.22	90.20	28.71	210.77	510.76	162.57
110	199.28	140.02	115.77	27.75	83.52	22.03	157.11	472.92	124.73
100	201.06	140.24	106.18	37.59	94.88	33.39	212.83	537.25	189.07
90	196.37	139.98	106.57	37.44	89.79	28.31	212.00	508.45	160.26
80	199.67	140.95	94.19	50.07	105.47	43.99	283.52	597.25	249.06
70	198.08	141.44	119.99	24.52	78.09	16.60	138.84	442.18	93.99
60	203.90	141.36	129.82	14.95	74.09	12.60	84.63	419.52	71.33
50	205.20	142.36	137.04	8.22	68.16	6.68	46.56	385.97	37.79
40	213.66	143.01	141.67	4.20	71.99	10.51	23.81	407.66	59.47
30	212.73	143.27	146.64	-0.51	66.09	4.60	−2.88	374.24	26.05
20	211.93	144.53	147.05	0.34	64.88	3.39	1.94	367.39	19.20
10	212.60	145.07	148.57	-0.64	64.03	2.55	−3.62	362.58	14.39
0	210.49	146.14	149	0.00	61.49	0.00	0.00	348.17	0.00

variations). This results in a value of C = 0.0057 km/10^{6}km^2, which we use here.

Once the hypsometric slope is chosen, relative sea level fluctuations can be calculated by estimating flooding through time. This is obtained by calculating the difference between the exposed land area and the total land area (i.e., "*continental*" or "*modern-land*") at a given time. In this way, we estimated the amount of flooded land for the past 520 Myrs in 10 Myrs intervals (Fig. 3a). By applying this flooding value to equation (1), relative sea level can be expressed as:

$$h = (L_{total} - L_{Exposed}) * C \quad (2)$$

where L_{total} is the total area of land ("*continental*" or "*modern-land*" in km^2), $L_{Exposed}$ (Marcilly et al. 2021) represents the area of exposed land (in km^2), and sea level is expressed relative to present-day (Fig. 3b; Table 1).

Global sea level estimates on 10 to 100 Myrs scales usually need to be adjusted for the isostatic response (Pitman, 1978; Conrad, 2013; van der Meer et al., 2017). Generally, a mantle mass equal to the added water depth is displaced from beneath the oceanic lithosphere (Conrad, 2013), which decreases the sea level change relative to the continents. Since seawater density is ~ 30% of the density of mantle rocks, isostatic compensation of seawater, when fully completed, should cause the observed sea level change to be

only 70% of the changes in water-level rise (Spasojevic and Gurnis, 2012). Isostatic rebound completes within timescales of ~ 10 k years and therefore it is suitable to apply a full isostatic correction for the timescales considered here (>1 Myr). However, our flooding maps (Fig. 2) are derived from a compilation of several local to regional stratigraphic studies that assess the extent of the coastline that we used to draw the exposed land limit. Therefore, those studies already integrate the effect of global isostasy as they measure the eustatic sea level (when compiled globally) and not the water column. For this reason, it is not necessary to adjust our sea level estimates (e.g., equation (2)) to account for isostatic effects. However, the water volume or basin volume changes that are responsible for this isostatically compensated change in eustatic sea level are larger than the observed change (h in equation (2)) by a factor of 1/0.7 = 1.43 (Conrad, 2013; Pitman, 1978).

3. Results and discussion

3.1. Calculated eustatic sea levels

3.1.1. Flooding and sea levels from "Modern-land" flooding

"*Modern-land*" flooding estimates (Fig. 3a) yield early Palaeozoic (520–460 Ma) sea levels that are about 250 m higher than present day levels (Fig. 3b; Table 1). Large reconstructed fluctuations are notable for the Late Ordovician to the Devonian, with a 74 m oscillation in sea level between 460 and 440 Ma, and a 90 m oscillation between 420 and 390 Ma. The drop in sea level around 450 Ma coincides with the Hirnantian glaciation, which likely lasted less than one million years (Torsvik & Cocks, 2017). A more considerable sea level drop (124 m) occurs near the Devonian-Carboniferous boundary at 370–360 Ma (Fig. 3b). This marks the start of a prolonged 100 Myr period of lower sea levels fluctuating around 150 m until 260 Ma, overlapping with the Late Paleozoic Ice Age (LPIA) that lasted from about 330 to 260 Ma. Peak glacial extent, however, occurred between 300 and 290 Ma (Montañez & Poulsen, 2013; Soreghan et al., 2019).

In the late Permian (260 Ma), sea levels dropped by 81 m, followed by a more gentle decrease until reaching the lowest reconstructed value for the entire Phanerozoic at 210 Ma (~14 m). These low sea levels correspond to the time when bulk Pangea may have been centered above TUZO (Fig. 4a), one of the main large low shear-wave velocity provinces (LLSVPs; Garnero et al. 2007, 2016) in the lowermost mantle (today observed beneath Africa). Central Pangea was situated on top of high dynamic topography that may have contributed to the all-time low in global sea levels at 210 Ma (Fig. 4a). A sharp increase in global sea level (~90 m) is recognized between 180 and 160 Ma and occurred during the main and initial break-up phase of Pangea (Torsvik & Cocks, 2017). Peak Phanerozoic sea levels are noticed at around 80 Ma (~283 m) and are followed by a sharp drop in sea levels until the mid-Cenozoic (Fig. 3b, 5a).

3.1.2. Flooding and sea levels from "Continental" flooding

Our "*continental*" flooding estimates (Fig. 3a) are broadly similar to estimates in Kocsis and Scotese (2021), but our model suggests systematically *less* flooding during the Carboniferous and the Triassic, and significantly *more* flooding (averaging 16 mill. km^2) during the Late Jurassic-Cretaceous and parts of the Cenozoic. The discrepancies for the Carboniferous and Triassic (for example) are mostly related to the shelf area around present-day China, where the Kocsis & Scotese (2021) model suggests significantly larger flooded areas than our model (Marcilly et al., 2021), with differences averaging 9 million km^2 and a maximum difference at 360 Ma (nearly 30 million km^2). Kocsis and Scotese (2021) display less present-day continental flooding than is currently observed on Earth (61.5 million km^2). This discrepancy is linked to their choice of definition for the transition from continental to oceanic crust (set at 1400 m isobaths), while our model is based on detailed mapping of the continental-ocean transition zone worldwide using seismic and potential field data (e.g. Torsvik et al. 2009). Kocsis and Scotese (2021) chose to create smaller areas with continental crust along the passive margins compared to our model, explaining the present-day differences.

Continental flooding estimates must be corrected for the present-day value when integrated into equations (1) and (2). The volume of continental crust increased over the Phanerozoic but estimates of the increase in crustal growth differ vividly among different models (2% to 39%; Cawood et al., 2013 and reference therein). Our model considers only the continental area, representing essentially stretched continental crust at passive margins that we here call "shelves", and incorporates negligible, or only minor, additional crustal volumes. For this reason, crustal growth models should not be used to scale our flooding estimates. Instead, we subtracted the modelled present-day flooding (Fig. 3a) from all estimates over the studied period, expressing flooding relative to the present (e.g., Forney, 1975, Bond, 1979, van der Meer et al., 2017 and references therein).

"*Continental*" flooding estimates generally result in lower sea levels (on average −75 m), most notably during Pangea times (Fig. 3b, Table 1), but sea level curves based on "*continental*" and "*modern-land*" flooding estimates are broadly similar with an average sea-level difference of 50 m over the past 520 Myrs.

3.2. Comparison of estimates with other flooding-based sea level curves

Over the past 30 years, numerous estimates of flooding through time have been published (see compilation in van der Meer et al. 2017 based on (Golonka et al., 1994; Ronov,1994; Blakey, 2008; Walker et al., 2002; Scotese, 2016). The overall trends are broadly similar over the Phanerozoic, but there are significant differences in estimated sea levels (grey-shaded background in Fig. 3a).

"*Continental*" flooding-based sea levels calculated here (red curve in Fig. 3b) are mostly within the range of previous estimates but there are clear exceptions during the Hirnantian (~445 Ma) and the Carboniferous (~360–310 Ma) where our reconstructions show lower values than most previous estimates. When calculated with the same hypsometric slope, sea level from the "*continental*" flooding model of Kocsis and Scotese (2021) (green curve in Fig. 3b) implies consistently higher sea levels than our model between 500 and 180 Ma (averaging to 211 m versus 87 m in our model), but lower sea levels during the Early Jurassic and Early Cretaceous (comparable to the present day) (see supplementary material).

"*Modern-land*" calculations represent a better-constrained set of estimates as both the present-day exposed land and the past exposed land are based on physical observations that are used to build the flooding estimates. Our "*modern-land* "flooding and therefore sea level estimates generally plot within the average range from other studies and "*continental*" estimates, except for the Hirnantian and parts of the Carboniferous (Fig. 3). The "*modern-land*" curve is generally higher than the *continental* curve between 180 and 80 Ma.

3.3. "Modern-land" estimates vs stratigraphic and tectonic methods

Our "*modern-land*" sea level curve shows high sea levels in the mid-Cambrian and the Early-Mid-Ordovician, and thus differs significantly from the composite curve from Haq and others, here referred to as the Haq curve (Haq & Al-Qahtani, 2005; Haq and Schutter; 2008, Haq, 2014; 2018), which suggests steadily increas-

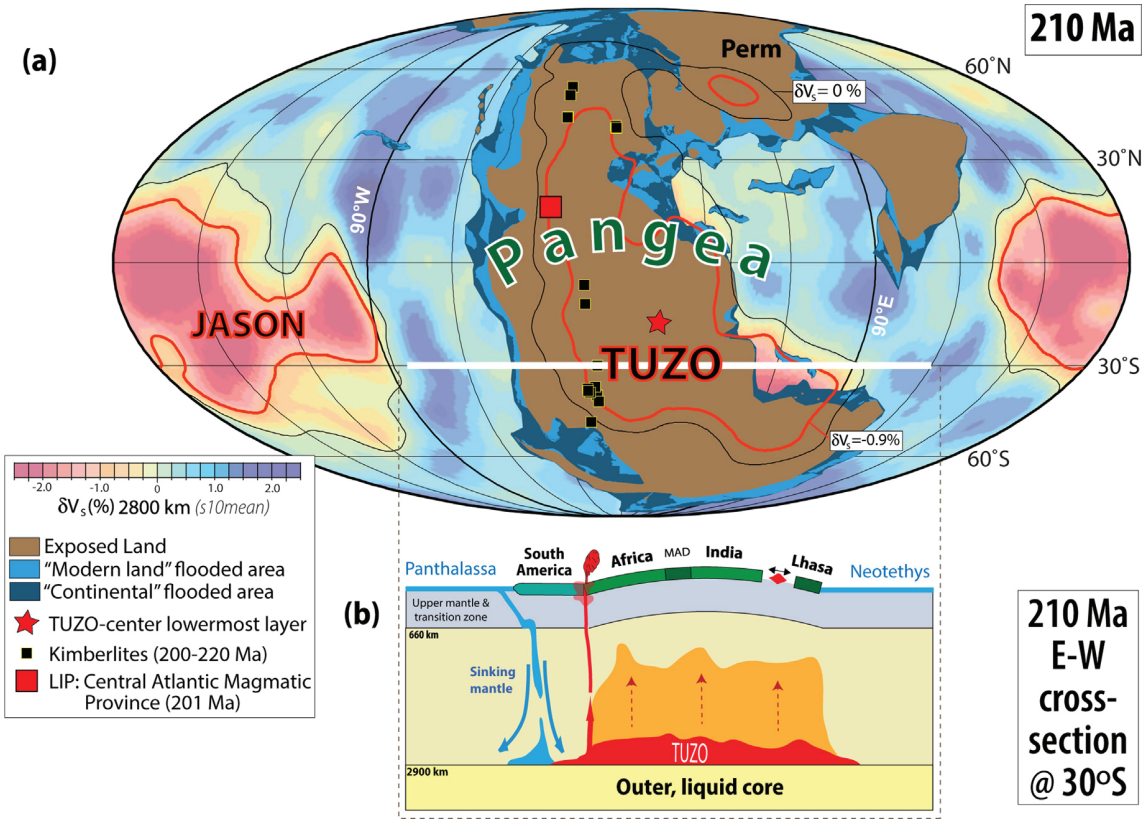

Fig. 4. **(a)** Reconstruction at 210 Ma (in a mantle reference frame; Torsvik & Cocks, 2017) where exposed land (*brown areas*) (Marcilly et al., 2021) and *"Modern land (light blue areas) / Continental (Dark blue areas)"* flooded areas are draped on the *s10mean* tomography model (δV_S%) at 2800 km depth (Doubrovine et al., 2016). Thick red lines are the 0.9% slow contour (largest horizontal gradients in *s10mean*) and the thin black lines are the zero contours. The lowermost mantle is dominated by two large low shear-wave velocity provinces (LLSVPs, Garnero et al. 2007, 2016), named TUZO (beneath Africa) and JASON (beneath the Pacific), which dominate the residual (positive) geoid (Burke et al., 2008; Torsvik et al., 2016). The center of the lowermost TUZO layer is marked by a red star (beneath SW Africa). This juxtaposition assumes that the lower mantle thermochemical piles have remained relatively stable back to 210 Ma (e.g., Torsvik et al. 2010b). At this time, Pangea stretched from pole-to-pole and the bulk of exposed land was centered over TUZO. We estimate some of the lowest sea levels for the Phanerozoic during this time (Fig. 5a). **(b)** 210 Ma east–west cross-section at 30°S from the Panthalassic Ocean to the Neotethys. Surface continents in the cartoon profile of Pangea include S. America, S. Africa, Madagascar (MAD), India and Lhasa, and overlying TUZO, which are warmer but probably also denser and stiffer than the ambient mantle in its lowermost few hundred kilometers (red color). The orange color above TUZO is shown to indicate that the area above TUZO is also warmer than the background mantle, and tends to be overlain by positive dynamic topography anomalies (e.g. Torsvik et al., 2016) as indicated by the "bulged" Pangean lithosphere. A dynamically uplifted Pangea may feature a steeper hypsometric gradient than today's world, lessening Pangean flooding for a given sea level offset (see section 3.4). Between 220 and 200 Ma, plumes sourced from the western margin of TUZO are witnessed by kimberlites and one large igneous province (Central Atlantic Magmatic Province) and older triggering slabs that we relate to subduction along the western margin of the Americas. (For interpretation of the references to color in this figure legend, the reader is referred to the web version of this article.)

ing sea levels until the end Ordovician (Fig. 5a). However, the two curves match reasonably well in trend from the Early Ordovician to the middle Carboniferous. Our curve shows a local low near the End-Ordovician Hirnantian glaciation, very similar to the fluctuations presented by the Haq curve, despite large discrepancies in levels during the early Paleozoic, with on average + 150 m over the peaks at 430 and 390 Ma in our estimates compared to the Haq curve. One of the major differences with the Haq curve is the sharp drop of 150 m that we model between 370 and 350 Ma, whereas the Haq curve suggests a more gradual decrease from 390 to 320 Ma. However, both models reach a low at 320 Ma (Fig. 5a). During the Late Paleozoic, the two curves differ substantially as the Haq curve generally shows much lower sea levels (as much as 90 m), notably near the start of the Pangea assembly. Our curve shows a marked drop in sea level near the end of the LPIA and reaches minimum sea levels at around 210 Ma, whereas the Haq curve models an all-time low between 210 and 200 Ma (Fig. 5a). Contrarily to what is observed at the end-Ordovician glaciation, the peak of the LPIA glaciations (i.e. ~ 300 Ma) does not correspond to a minimum in sea level, either from our method or from stratigraphic methods.

From about 190 Ma (soon after the main Pangea break-up) to 80 Ma, the two curves show gross similarities, and in our estimates, sea levels increased from about 28 m to about 280 m at 80 Ma. Both curves show Phanerozoic peaks in sea levels during the late Cretaceous, but the Haq curve suggests a slightly earlier peak than our reconstructions (i.e. 90 Ma versus 80 Ma). Unlike several other sea level reconstructions (e.g., Hallam, 1992, and Haq and Al-Qahtani, 2005, van der Meer et al. (2017) in Figs. 1 & 5a), our sea level curve does not display any fluctuation during this Cenozoic drop in sea level (Fig. 5a).

van der Meer et al. (2017) flooding estimates, based on an independent method using strontium isotopes, are much lower than our estimates during the early Paleozoic, and the fluctuations seem to occur 10–20 Myrs earlier compared to our reconstruction. Conversely, the Late Paleozoic displays fluctuations and sea levels that compare well with ours. However, from the mid-Jurassic, the strontium-based estimates are once again much lower than both

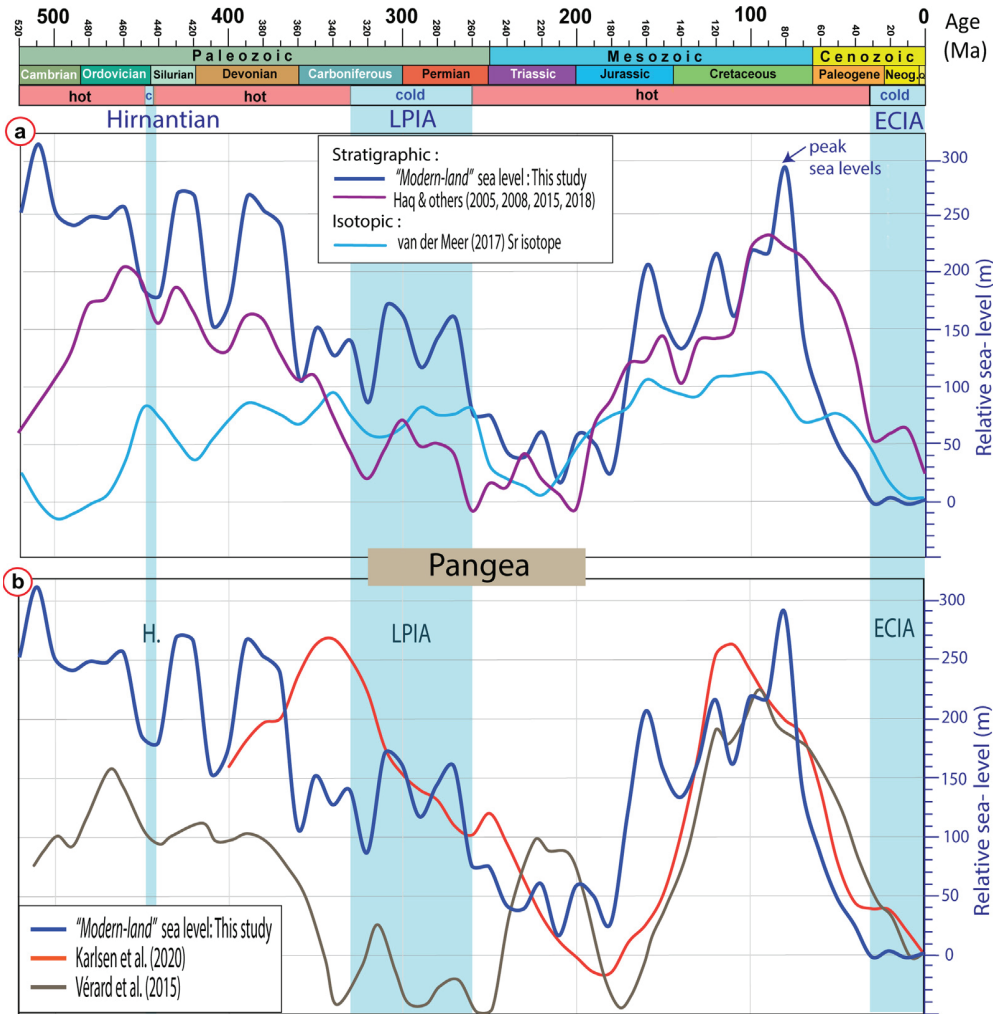

Fig. 5. Time-scale with greenhouse (hot) versus icehouse (cold) conditions for the past 520 Myrs (See Fig. 1 caption for additional details) and "*Modern-land*" sea levels compared with **(a)** the stratigraphically-derived long-term curve from the composite curve of Haq & others (2005, 2008, 2014, 2018) as well as the Sr isotope based estimates from van der Meer et al. (2017). Both curves are binned every 10 Myrs, as is our curve, to facilitate comparisons. **(b)** Comparison to sea level estimates from tectonic models (Karlsen et al., 2020; Vérard et al., 2015).

flooding and stratigraphic methods, even though the global trend is similar for all (Fig. 5a).

Our "modern land" based sea level curve also shows gross similarities with the tectonic-based sea level curves for parts of the Mesozoic and the Cenozoic, but the late Paleozoic curves are markedly different (Fig. 5b). For example, the tectonic-based model of Karlsen et al. (2020) (Fig. 5b) yields very high sea levels (270 m) during the Carboniferous at 340 Ma (just prior to the LPIA), whereas a different tectonic-based model of Vérard et al. (2015) suggests very low sea levels (~40 m). However, tectonic-based sea-level curves are poorly constrained before Pangea (Torsvik et al. 2010), and our flooding-based model, which is not critically dependent on plate reconstructions, suggests intermediate sea levels of about 150 m.

From a global perspective, our "*modern-land*" estimates largely follow stratigraphic models (Fig. 5a) back to the early Mezosoic and only partially agree with tectonic models back to the late Paleozoic (Fig. 5b). However, there is a larger diversity among the tectonic models because tectonic models require full-plate models with ages for the oceanic lithosphere, which can differ significantly, and partly because they account for sea-level changing processes differently (e.g., Karlsen et al. (2019) include water exchange with the mantle while Vérard et al. (2015) do not). The two full-plate models are also fundamentally different. Contrarily, sea level reconstructions based on flooding estimates are either not sensitive or only marginally sensitive to tectonic models based on oceanic crust reconstructions, and thus avoid some of the model uncertainties that can afflict tectonic-based reconstructions. That makes flooding-based sea level reconstructions more reliable, and the close tracking of the stratigraphic and flooding-based curves (Fig. 5a) supports this.

3.4. Sea-levels during Pangea: Effect of changing hypsometric slopes

Assuming a constant hypsometric slope for the 0–250 m elevations for the past 520 Myrs is obviously a simplification. In reality, hypsometric curves change over time due to tectonic and geomorphological processes such as rifting, suturing of landmasses, changing type and age of continental margins, and uplift and peneplation of cratonic interiors (Algeo & Wilkinson, 1991; Gurnis, 1993a, 1993b; Algeo & Seslavinsky, 1995, Bond, 1979). As an example, the mean continental height and crustal thickness should increase during supercontinent formation (e.g., Zhang, 2005), steepening the hypsometric slope (Algeo & Wilkinson, 1991) for perhaps a

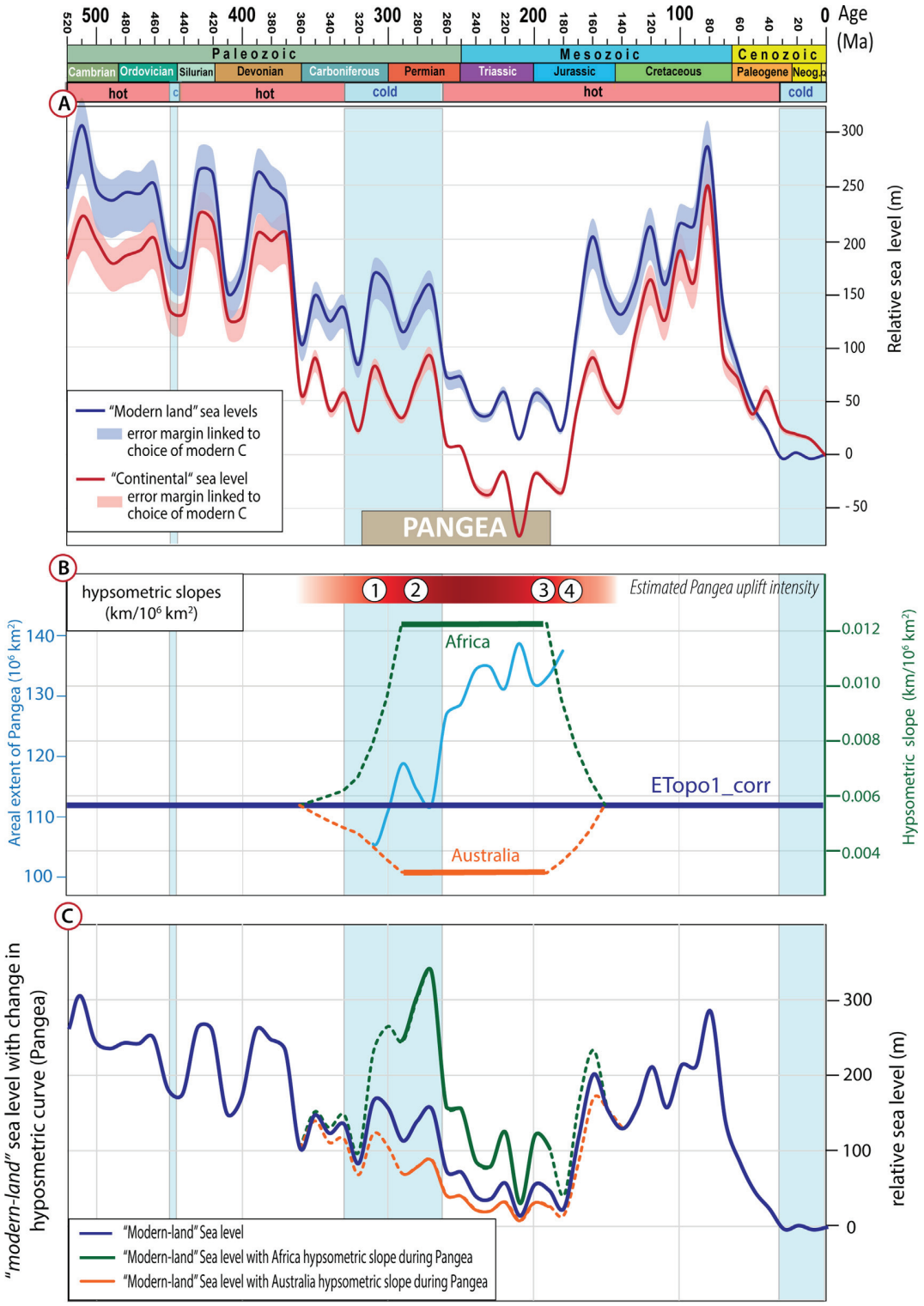

Fig. 6. Time-scale with greenhouse (hot) versus icehouse (cold) conditions for the past 520 Myrs (See Fig. 1 caption for additional details) **(a)** "*modern-land*" and "*continental*" sea levels with error margins linked to the choice of modern day hypsometry from ETOPO1 (applying different corrections for "bed", "ice" in Amante & Eakins (2009) and an additional geoid correction (Vérard 2017)). **(b)** Scenarios tested here with progressive increase and decrease in hypsometric slope during Pangea time. Africa and Australia refer to the slope for the 0–200 m elevation from Harrison et al. (1983) as presented in Algeo & Wilkinson (1991). The choice of time-residency of changes in slope is based on the assembly and break up of Pangea as follows: (1) Initial suturing, Laurussia fused with Gondwana to form Pangea at around 320 Ma, (2) main phase of Pangea assembly and uplift above TUZO, (3) main phase of Pangea break up with the opening of the Central Atlantic ocean at ~ 195 Ma, and (4) break up of Gondwana from 180 to 170 Ma. We also show the areal extent of Pangea (320–195 Ma) in light blue, which includes a late Paleozoic area increase of about 8%, which is mostly related to the merger of Siberia with Pangea. ETOPO1_corr refers to the slope used in our sea level calculations (0.057 km/10^{6}km^2) extracted from Vérard (2017). **(c)** "*Modern-land*" sea level with different choices for hypsometric slope during Pangea time (green curve for Africa and orange for Australia) following the scenarios shown in panel b. (For interpretation of the references to color in this figure legend, the reader is referred to the web version of this article.)

few tens of million years. The increased slope would indicate even higher sea levels to produce the observed flooding that was in place when Pangea formed. Although in many places, periods of large relief are rapidly followed by orogenic collapses and post-collision extension (e.g., Andersen et al., 1991; Stampfli et al., 2013).

Such higher sea levels, however, would have been occurring at a time when we might expect sea level to be depressed. For example, the LPIA glaciation occurred during the first half of Pangea's lifetime (Fig. 6b), and may have lowered eustatic sea level by sequestering water on land. Additionally, we note that Pangea during its zenith assembly (210 Ma) became located above TUZO (Fig. 4a). A persistent upwelling above TUZO would tend to dynamically uplift the continents across supercontinental length scales (Fig. 4b), with Pangea sitting above positive dynamic topography, and on-average low dynamic topography across the surrounding oceans (e.g., Conrad and Husson, 2009). This configuration of relatively deeper oceans would contribute to *lower* sea levels during Pangean time if TUZO has remained fairly stable since Pangea formation (e.g., Torsvik et al. 2014, 2016). Indeed, Conrad (2013) estimated up to ~ 0.5 m/Myr of sea level rise since Pangea breakup as continents move off the dynamic high and the seafloor on average rises. Another sea level-elevating process (e.g., ridge volumes during Pangea that are larger than expected) is thus necessary to offset the sea level depression inherent to the geodynamic positioning of Pangea over broad-scale mantle upwelling (Fig. 4a). Although orogenic events taking place during Pangea formation primarily affected the interior of the continent, and thus may not have significantly influenced coastal hypsometry, we note that positive dynamic topography above TUZO would have uplifted the continent, as it is thought to uplift Africa today (e.g., Lithgow-Bertelloni and Silver, 1998). This dynamic uplift may have contributed to, or even controlled, the steepening of the average hypsometric slope during Pangea formation.

There are no direct records of the variation in the hypsometric curve with time, although modeling studies have attempted to reconstruct such changes (Sømme et al., 2009, Burgess, 2001). However, to account for increased continental height and thickness during Pangea formation, we tested a steepening of the slope (C in Eq. (1)) following supercontinent assembly and uplift (Fig. 6a). The main phase of Pangea assembly started at ~ 320 Ma when Gondwana, Laurussia (including Laurentia and Baltica in Fig. 2) and intervening terranes amalgamated (Torsvik and Cocks, 2017). Pangea constituted ~ 70% of the present-day area of continental crust at that time, but there was a net increase of 8% between 320 and 250 Ma (Fig. 6b).

Algeo and Wilkinson (1991) estimated that Africa, an elevated continent currently positioned above TUZO, has a hypsometric slope that is more than double that of the main continental trend (i.e., average for the globe). Africa is here considered a hypsometric analogue for Pangea, since both are expected to be uplifted continental areas, and we employ its steeper slope of 0.0122 km/10^6km^2 to our calculations of sea level estimates during Pangea (Fig. 6a). During the development of Pangea, we implemented first a small increase in slope from 350 to 320 Ma with values increasing gradually from 0.0057 to 0.0067 km/10^6 km^2 between 350 and 320 Ma. During the most active phase of Pangea, we implemented a sharp but gradual increase of the slope from 0.0067 to 0.0122 km/10^6 km^2 between 320 and 280 Ma (Fig. 6b). However, if the uplift was caused by upwelling above TUZO, it might only have occurred in the central parts of Pangea (Fig. 4a,b), considering that the supercontinent was considerably larger compared to Africa. Therefore, using Africa's hypsometric slope for Pangea might overestimate the slope steepening and thus represents an upper end-value for Pangea's slope.

Table 2
Sea levels calculated using changes in the hypsometric slope. The time interval of change is highlighted in yellow, green for Africa and orange for Australia.

Age	*Scenario of change in hypsometric slope (HS)- AFRICA*	*Modern land sea level with change in HS- AFRICA*	*Scenario of change in hypsometric slope (HS)- AUSTRALIA*	*Modern land sea level with change in HS- AUSTRALIA*
(Ma)	Km/km^2	relative m	Km/km^2	relative m
520	0.0057	245.7	0.0057	245.7
510	0.0057	304.2	0.0057	304.2
500	0.0057	245.9	0.0057	245.9
490	0.0057	234.9	0.0057	234.9
480	0.0057	242.2	0.0057	242.2
470	0.0057	241.3	0.0057	241.3
460	0.0057	249.4	0.0057	249.4
450	0.0057	181.3	0.0057	181.3
440	0.0057	175.4	0.0057	175.4
430	0.0057	261.8	0.0057	261.8
420	0.0057	259.0	0.0057	259.0
410	0.0057	150.1	0.0057	150.1
400	0.0057	169.4	0.0057	169.4
390	0.0057	259.0	0.0057	259.0
380	0.0057	246.9	0.0057	246.9
370	0.0057	232.0	0.0057	232.0
360	0.0057	103.9	0.0057	103.9
350	0.0058	151.5	0.0054	139.5
340	0.0060	130.9	0.0051	111.2
330	0.0062	148.0	0.0049	116.2
320	0.0067	98.5	0.0047	68.8
310	0.0078	229.9	0.0042	122.7
300	0.0095	263.9	0.0038	105.4
290	0.0122	244.0	0.0035	70.1
280	0.0122	300.8	0.0032	79.6
270	0.0122	333.4	0.0032	88.2
260	0.0122	157.7	0.0032	41.7
250	0.0122	155.1	0.0032	41.0
240	0.0122	86.4	0.0032	22.8
230	0.0122	79.7	0.0032	21.1
220	0.0122	124.3	0.0032	32.9
210	0.0122	31.6	0.0032	8.4
200	0.0122	120.1	0.0032	31.8
190	0.0122	103.0	0.0032	27.2
180	0.0095	41.9	0.0036	16.0
170	0.0078	162.1	0.0041	86.1
160	0.0066	232.7	0.0048	169.4
150	0.0057	153.7	0.0057	153.7
140	0.0057	130.0	0.0057	129.6
130	0.0057	158.9	0.0057	158.4
120	0.0057	211.5	0.0057	210.8
110	0.0057	157.6	0.0057	157.1
100	0.0057	213.6	0.0057	212.8
90	0.0057	212.7	0.0057	212.0
80	0.0057	284.5	0.0057	283.5
70	0.0057	139.3	0.0057	138.8
60	0.0057	84.9	0.0057	84.6
50	0.0057	46.7	0.0057	46.6
40	0.0057	23.9	0.0057	23.8
30	0.0057	-2.9	0.0057	-2.9
20	0.0057	1.9	0.0057	1.9
10	0.0057	-3.6	0.0057	-3.6
0	0.0057	0.0	0.0057	0.0

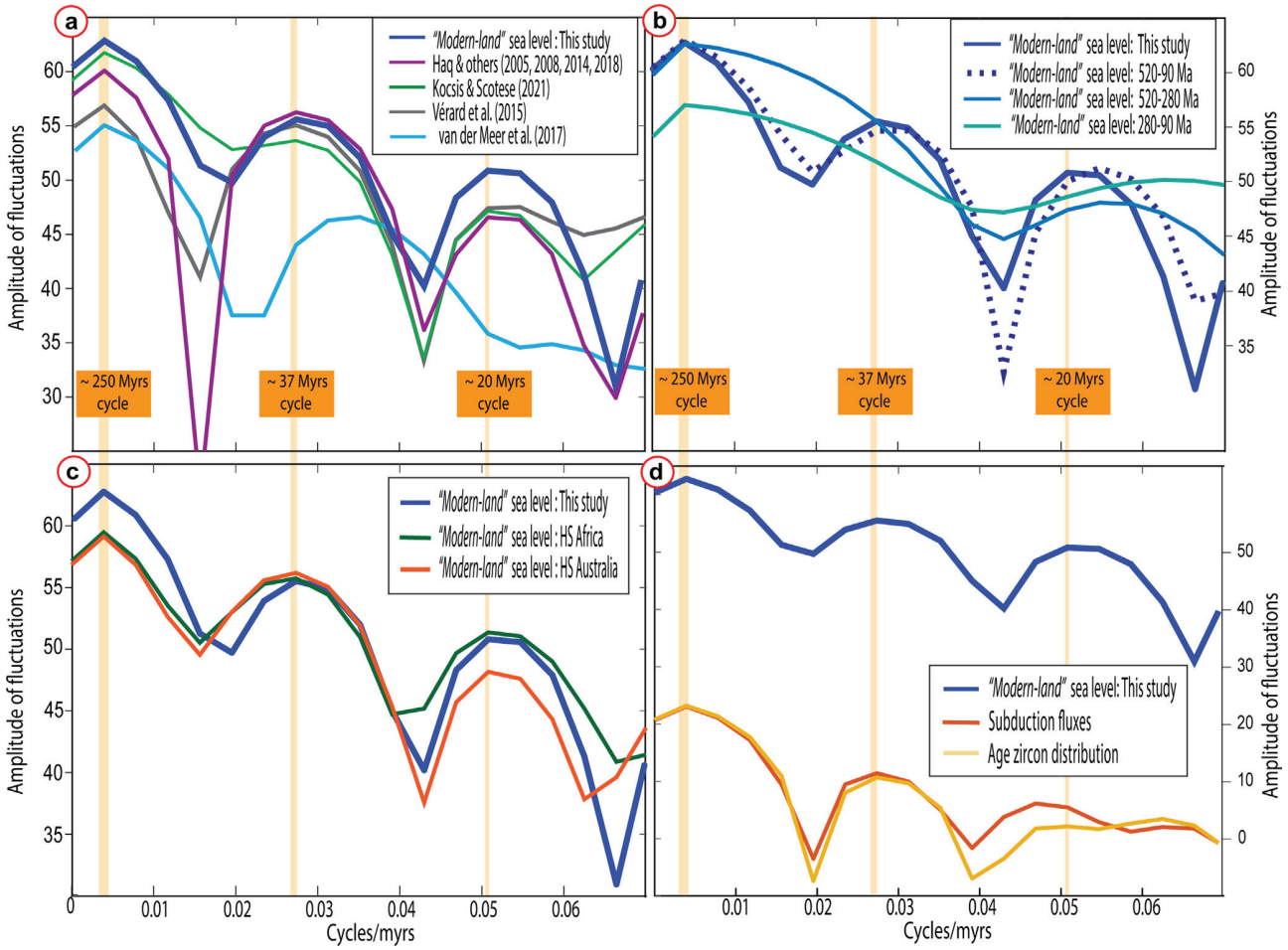

Fig. 7. **(a)** Periodograms derived from stratigraphic (Haq & Al-Qahtani, 2005, Haq & Schutter 2008, Haq, 2014, 2018), tectonic (Vérard et al., 2015) and continental flooding ("Modern-land" sea level from this study; Kocsis & Scotese, 2021) methods. Cycles shorter than 20 Myrs are not considered as the time resolution in our models is 10 Myrs, and estimates used in all the periodograms were binned in 10 Myrs intervals. **(b)** Testing for temporal changes in the cycles. We here test separately the Paleozoic (520–280 Ma) and Mesozoic 280–90 Ma (even if including part of the Permian) as well as the influence of the Cenozoic (compare 520–90 Ma against 520–0 Ma). **(c)** Periodogram showing effects of changed hypsometry during Pangea for both African and Australian slopes. **(d)** Periodogram of proxies for seafloor spreading from Marcilly et al. (2021).

Contrarily, it has been demonstrated that the hypsometric slope in areas of subduction zones is reduced due to sinking slabs pulling the Earth's surface downwards, creating negative dynamic topography (Gurnis, 1993a,b). This was likely also the case for Pangea as the supercontinent was surrounded by subduction zones at several stages of its assembly (Torsvik and Cocks, 2017). Therefore, instead of creating a steepening of the gradient, the development of subduction zones may have instead created a flattening in the gradient. (Gurnis, 1993b) estimated the hypsometric gradient for low-lying (0–200 m) areas near subduction to be close to the value proposed by van der Meer et al. (2017) (0.005 km/10^6km^2) and therefore should not produce significant changes.

To test the hypothesis of a flattened gradient even further, we also applied a flattened gradient of 0.0032 km/10^6 km^2, corresponding to the present-day value for low-lying Australia (Algeo & Wilkinson, 1991) (Fig. 6 b, supplementary material).

After changing the slope of the hypsometric curve from 0.0057 to a gradual increase until 0.0122 km/10^6km^2 (Africa slope, Fig. 6b), *"modern-land"* sea levels rose by + 59 m on average throughout the main uplift period with a maximum increase of + 78 m at 270 Ma compared to an unchanging slope (Fig. 6b & Table 2). Major differences reside in the intensification of large peaks in sea level at 300 and 270 Ma, and minor changes around 220 and 200 Ma increase smaller peaks in sea level. When applying the smaller Australian slope (Fig. 6b), the changes are also initially significant. Indeed, during the maximum decrease of the slope at 270 Ma, the reduction of the peak reaches −66 m (Fig. 6c). These observations suggest that the method used here is highly sensitive to the choice of the hypsometric slope. Such changes can be significant, notably during the end of the Pangea assembly when the hypsometric slope could have reached a maximum. At this period, a substantial discrepancy with other curves arises between our estimates and reference levels (Figs. 1, 5 and 6a, c). Therefore, our use of a fixed slope of 0.0057 km/10^6 km^2 during the Phanerozoic may cause us to underestimate the magnitude of sea-level fluctuations for periods with a steeper slope, or to overestimate them for periods when the hypsometry is flatter. This could potentially explain some of the observed discrepancies with stratigraphic methods (Fig. 5a).

3.5. Cyclicity

In order to identify the cyclicity of sea level changes, we computed the Discrete Fourier Transform (DFT) of the variable sea levels using a fast Fourier transform (FFT) algorithm. As our sea level reconstructions are based on flooding estimates in 10 Myr intervals, only sea level fluctuations ~ 20 Myr or longer can be considered. Fig. 7a displays a significant peak at 250 Myrs, which corresponds to a supercontinent cycle, and this is qualitatively visible by the high sea levels before and after Pangea (Fig. 6a). This ~ 250

Myr first-order peak is generally visible for several other sea level curves (peridograms computed also after binning in 10 Myr intervals, Fig. 7a), as are some shorter-period, second-order cycles.

It has previously been assumed that the hypsometric method is limited to first-order approximations (Hallam, 1984); however, our reconstructions include both first and second-order cycles. Indeed, two smaller peaks are visible in the periodogram but with smaller intensity, and these are second-order cycles (5–50 Myrs) at about 37 and 20 Myrs per cycle (Fig. 7a). These second-order cycles can be observed with ~ 37 Myrs intervals from 510 to 270 Ma and from 200 to 160 Ma. Between 350 and 300 Ma, 270–200 Ma, and 130–80 Ma, cycles are shorter and about 20 Myrs in duration (Fig. 6a). Most other curves considered, computed using a variety of methods, also show similar second-order periodicity (Fig. 7a).

To identify the temporal changes in these cycles we ran the spectral analysis for the Paleozoic and Mesozoic separately (Fig. 7b). Due to the shorter time window, the first order and second order cycles become less clearly identifiable. However, there is still significant power for the longer second order cycles (~37 Myr) during the Paleozoic, while some of the power shifts toward shorter second order cycles during the Mesozoic (Fig. 7b). We additionally analysed the Phanerozoic without the Cenozoic (90–520 Myr), a period without second order fluctuations in our reconstruction. For this case, the peak showing ~ 37 Myr second order cycles becomes sharper and the ~ 20 Myrs cycles peak is displaced towards shorter cycles (Fig. 7b). This suggests that the ~ 20 Myrs cycle may be an artefact linked to the 10 Myrs time step used in our reconstructions. Indeed no shorter cycle than 20 Myrs should be identifiable, as it would be composed of less than 2 points.

A second order cycle with a ~ 37 Myr cycle is thus a recurring strong signal through most of the Phanerozoic (Fig. 7b). We find that this cycle is mostly unchanged by hypsometry, although it becomes more defined and reaches higher power if the hypsometric slope is steeper during Pangea (Fig. 7c). Interestingly, Boulila et al. (2018) also observed cycles with this duration (~36 Myrs), and attributed them to astronomical processes. In particular, they propose that vertical and radial motions of the solar system could induce long-term climatic variations that modulate the ice sheets. To look for a tectonic driver of this cyclicity, we ran the same spectral analysis on two independent datasets from Marcilly et al. (2021) that provide proxies for seafloor spreading (i.e subduction fluxes and age-zircon distributions). This analysis (Fig. 7d) shows a clearly identifiable supercontinental cycle of 250 Myrs, but also tectonic cycles at ~ 37 Myrs. This suggests that tectonic processes may be the source of those second order cycles.

Guillaume et al. (2016) discussed the difficulty for eustatic charts to constrain second order eustatic fluctuations because coastline observations also measure vertical ground motion, due to tectonics or dynamic topography. Furthermore, their analysis of the Permian and Triassic argues that neither tectonic nor glacio-eustatic processes can explain the rates of eustatic change implied by second order cycles during this period. Nevertheless, we have identified a robust second order fluctuation across the Phanerozoic (Fig. 7). This is possible despite Guillaume et al.'s (2016) concerns because our paleogeographic method averages across all coastlines, and therefore is less sensitive to particular tectonic events in any one location.

Furthermore, our identification of a ~ 37 Myr second order cycle (Fig. 7) arises from an analysis of the entire Phanerozoic record, and not just a particular portion of it (e.g., Permian-Triassic). We do observe a correlation with global-scale tectonic indicators (e.g., Fig. 7d and Fig. 8b), but this correlation is more easily explained by tectonic processes generating eustatic change (a global sea level offset), instead of coastline uplift and

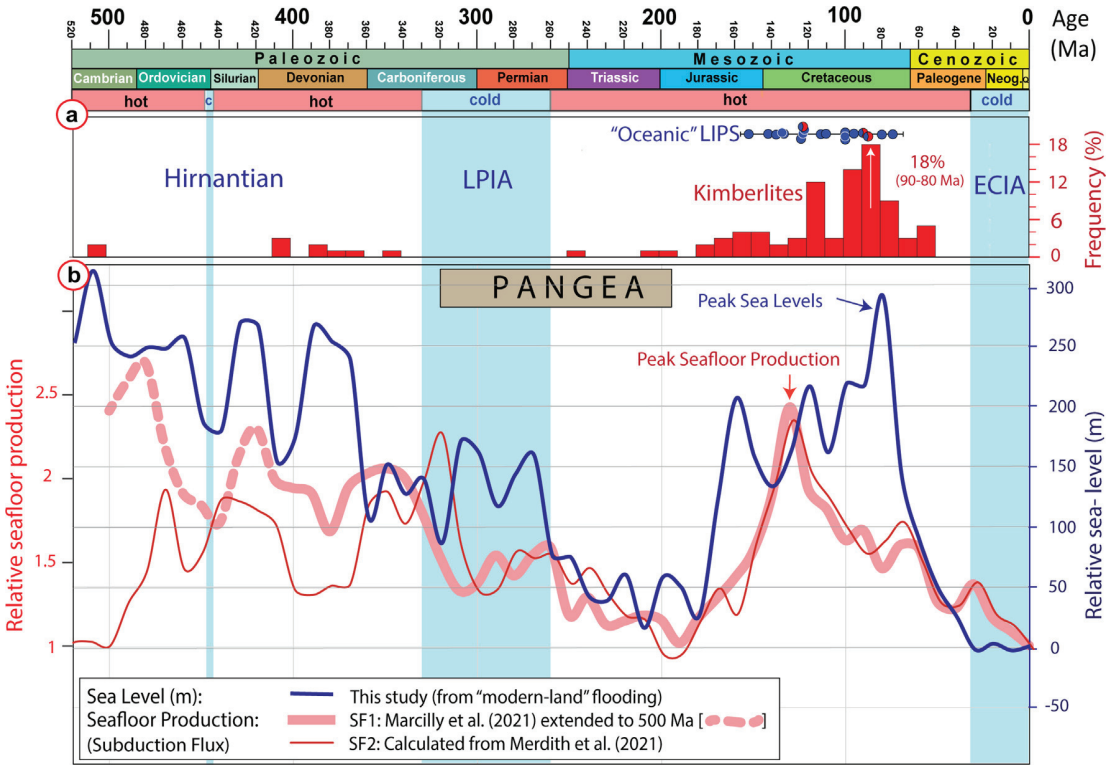

Fig. 8. **(a)** Time-scale, greenhouse (hot) vs. icehouse (cold) (See Fig. 1 caption for additional details), kimberlite frequencies for the past 520 Myrs (10 Myr bins), and preserved "oceanic" large igneous provinces (LIPs). The blue dots represent oceanic LIPs and shared blue/red dots represent continental and oceanic LIPs. **(b)** "*Modern-land*" sea level calculated from flooding maps (this study) compared to two proxies for relative seafloor production calculated from the subduction flux of full-plate models: SF1 from Marcilly et al. (2021) extended from 410 to 500 Ma.; SF2 calculated from the full-plate model of Merdith et al. (2021). (For interpretation of the references to color in this figure legend, the reader is referred to the web version of this article.)

subsidence, which would need to be globally-coherent to explain the observed changes in global flooding.

3.6. Drivers of sea level changes

3.6.1. Seafloor production

Beyond comparing to other observations of sea level change, the credibility of our flooding-based sea level reconstruction can be augmented by a comparison to predictions of sea level change based on possible driving mechanisms. Past sea level variations are dominantly linked to changes in the volume of mid-ocean ridges, which can be computed from global full-plate models (e.g., Müller et al. 2008; Karlsen et al. 2020). However, such models require reconstructions of seafloor ages for past times, and the reconstruction uncertainty, defined by the fraction of the Earth's lithosphere lost to subduction, reaches 60% by 150 Ma (Torsvik et al., 2010a). Alternatively, trends in ridge volume change, which directly impact sea level (e.g., Gaffin, 1987), can be roughly estimated from changes in seafloor production rates (e.g., Vail et al, 1977, Müller et al., 2008; Conrad, 2013). On a planet that is not shrinking or expanding, the rate of seafloor production should approximate the subduction flux. The latter can be estimated with higher confidence, as knowledge of the location of ridges in the distant past is highly limited. Therefore, we here consider subduction flux as a proxy for seafloor production rate, but subduction flux estimates should be treated with great caution prior to the assembly of Pangea.

The subduction flux curve, here named SF1, is that of Marcilly et al. (2021) but extended from 410 to 500 Ma using a full-plate global model that is largely based on two regional models detailed in Domeier (2016, 2018). For the past 300 Myrs, SF1 grossly matches subduction flux estimates from the full plate model of Meredith et al. (2021) (here named SF2), but before that time they generally show large discrepancies (Fig. 8b). SF1 and SF2 are essentially based on the same databases but with the continents, notably for the Paleozoic, located to very different longitudes. This difference leads to very different subduction flux estimates.

Although the oceanic areas of full-plate models are largely synthetic for the entire Paleozoic and parts of the Mesozoic, the SF1 curve, which is based on a full-plate model with calibrated longitudes (Torsvik et al. 2014; Marcilly et al. 2021), is characterized by a general pattern of decreasing seafloor production from 490 to 190 Ma and is grossly similar to our reconstructed sea levels (Fig. 8b). The SF1 curve shows local minima's during the Hirnantian and the LPIA, but the lowest seafloor production and sea levels are observed in the Early Mesozoic. From about 180–190 Ma, estimated sea levels and seafloor production are rising, but seafloor production rates peak at 120–130 Ma and about 40 Myrs before the sea level peak at 80 Ma. We do expect sea level rise to lag behind an increase in spreading rates, perhaps by several tens of Myr given that this is the timescale for seafloor at ridges to slowly fill the oceanic basins with shallower seafloor (Conrad, 2013). We note, however, that significant sea level rise also occurred even earlier, with a rapid rise completed by ~ 160 Ma, and thus before the major increase in seafloor production (Fig. 8b). Here we note that the emplacement of voluminous oceanic Large Igneous Provinces (LIPs) began even before the mid-late Cretaceous (e.g., the Ontong Java plateau at 125 Ma; Ernst, 2014) and may have contributed to or overprinted the sea level peak as discussed below.

3.6.2. Oceanic LIP emplacement

The oldest and youngest preserved oceanic LIPs are 155 Ma (Argo) and 73 Ma (Sierra Leone), respectively (e.g., Torsvik et al., 2021; their *Table 16.2*). In this 82 Myr period there are 22 known LIPs, including 16 oceanic, three with mixed oceanic and continental affinity, and three of continental origin (Svensen et al., 2018; Torsvik et al., 2021). Therefore, the oceanic and "mixed" LIPs represent 86% of all LIP activity from the Late Jurassic to the Late Cretaceous.

The emplacement of oceanic LIPs adds large volumes of basalt to the seafloor, leading to perturbations of global sea level. LIP emplacement may possibly explain the temporal offset between the prominent peaks in seafloor production and sea level (Fig. 8b) due to the pulse-like nature of LIP emplacement. Although the sea level impact of a LIP is challenging to assess due to volume uncertainties (Mills et al., 2014), a ~ 45 m rise between 120 and 80 Ma has been suggested from LIP emplacement models (Wright et al., 2020), while other authors have suggested larger contributions from LIP activity (e.g., Conrad, 2013). This may explain a large fraction of the ~ 70 m rise between 90 and 80 Ma (Fig. 8b), especially since our sea level peak aligns with the peak in LIP activity at ~ 85 Ma as indicated by kimberlites (Fig. 8a).

Due to subduction, there are no traces of *in-situ* oceanic LIPs prior to the Late Jurassic, but similar perturbations in nature and scale may have occurred in deeper time. Such perturbations can potentially explain mismatches and offsets between seafloor production from the plate tectonic model used here and sea level fluctuations from flooding estimates in the Paleozoic. LIPs represent catastrophic melting of the upper mantle, primarily sourced by mantle plumes from the lowermost mantle, but kimberlites (Fig. 4b) are another surface manifestation of those plumes (e.g., Torsvik et al. 2010b; Torsvik et al., 2021). Kimberlites are exclusively found on the continents and will therefore *not* contribute to global sea level changes. However, they provide essential constraints on the plume activity during Earth history. It is well known that the frequency of kimberlite volcanism was high in the Cretaceous (Torsvik et al. 2010b), in concert with LIP emplacement (Fig. 8a). In particular, a rise in kimberlite plume activity is observed from the mid-Jurassic, with a pronounced peak between 120 and 110 Ma (Fig. 8a). Still, the prominent peak, representing 15% of all known kimberlites for the past 520 Myrs, is observed between 90 and 80 Ma, and coincides with the main rise shown by most sea level curves (Fig. 8a, b). The period of intense kimberlite plume activity corresponds to the age range of major ocean LIP volcanism [i.e. the Caribbean-Colombian (90 Ma) and Madagascar events (87 Ma)], and the accumulated LIP volumes may have peaked at this time. Since the Late Cretaceous, LIP and kimberlite activity has been significantly low, with the last oceanic LIP emplaced around 82 Myrs ago (Torsvik et al., 2021). Since then, seafloor production and sea level curves show a similar decreasing pattern (Fig. 8b). Today, Earth is experiencing its lowest seafloor production and sea levels compared to the entire Phanerozoic (past 541 Myr) as also noticed by van der Meer et al. (2017) using an independent model based on strontium isotope ratios.

It is perhaps also worth noting two other periods with high kimberlite activity. First, we note that the Cretaceous peak in activity actually began in the mid-Jurassic (Fig. 8a). If LIP activity also increased in concert with the kimberlites, it may have helped to drive the mid-Jurassic sea level rise that slightly preceded the early Cretaceous increase in seafloor production (Fig. 8b). Note that LIPs emplaced during the mid-Jurassic would have been subducted by now, because the oldest seafloor is only 180 Myr old. Second, we note that the Devonian is associated with a relatively high number of kimberlites (42% of all Paleozoic occurrences) and sea levels were high between 390 and 380 Ma. Conversely, seafloor production curves show a low in this time interval (SF1 and SF2 in Fig. 8b), but seafloor production estimates must be considered with great caution for most of Paleozoic.

4. Concluding remarks

Based on global flooding maps with a constant hypsometric slope (0.0057 km/10^6km^2) we have calculated new sea level curves for the past 520 Myrs using two different definitions of flooding. However, we consider the "*modern-land*" sea level curve, which measures changes in the area of exposed land, to be more reliable and objective than the "*continental*" curve for which changes to the area of flooded continental crust cannot be expressed with high confidence.

Our two definitions of flooding only lead to an average difference of 50 m over the past 520 Ma. However, changes in the assumed value of the hypsometric slope can lead to significantly higher differences in calculated sea levels. Our hypothesis that the Pangean hypsometric slope was steeper as a result of positive dynamic topography implies significantly elevated sea level highstands. For example, a 154 m high-stand at 270 Ma grows to 333 m if we assume a steeper hypsometric slope for Pangea. However, such exercises must be treated cautiously, especially since Pangea may have assembled over elevated dynamic topography that was theoretically associated with low eustatic sea levels. Indeed, we calculate minimum sea levels at 230 Ma, in the latter part of Pangea's lifespan, and about 30 Myrs after the demise of the late Paleozoic ice age. At this time, Pangea was at its largest and centered above the TUZO LLSVP, assuming that the LLSVPs have remained semi-stable since Pangea formed.

Except for the Early Paleozoic, our sea level reconstructions are grossly similar to the stratigraphic-based Haq curves with a Pearson correlation coefficient of 0.68 ("*modern-land*" reconstruction) and 0.79 ("*continental*" reconstruction) for the past 470 Myrs. This suggests that global flooding maps, at least to first order but also probably second order, are useful for determining eustatic sea levels compared to stratigraphic methods. However, with sea level reconstructions based on tectonic models, the comparison is less favourable, especially in the distant past. One reason behind this discrepancy is that such tectonic-based reconstructions require seafloor reconstructions (full-plate models) that are increasingly uncertain in deep time.

Our sea level curve is grossly similar to proxies for temporal changes to seafloor production rates, such as the subduction flux of recent plate tectonic reconstructions, which result in similar first and second order cycles. This link between the primary mechanism for eustatic sea level change (changes in the volume of the mid-ocean ridges) and sea level change inferred from flooding estimates further strengthens the case for the reliability of the paleogeographic methods for reconstructing sea level. Because such models represent averages over large areas of the earth, they are less sensitive to regional uplift or subsidence events (e.g., from dynamic topography and local tectonics) compared to stratigraphic methods, which are usually made at specific locations. Paleogeography thus presents a useful constraint on eustatic (global) sea level change that can be used to deduce the geodynamic mechanisms that drive sea level change (e.g., ridge volume changes or LIP emplacement). Paleogeography may also prove useful for identifying regional uplift or subsidence events where local observations of sea level, such as from stratigraphy, deviate significantly from the eustatic curve.

CRediT authorship contribution statement

Chloé M. Marcilly: Conceptualization, Methodology, Software, Investigation, Formal analysis, Writing – original draft, Visualization, Data curation. **Trond H. Torsvik:** Conceptualization, Supervision, Software, Investigation, Formal analysis, Writing – review & editing, Data curation. **Clinton P. Conrad:** Investigation, Supervision, Resources, Writing – review & editing.

Declaration of Competing Interest

The authors declare that they have no known competing financial interests or personal relationships that could have appeared to influence the work reported in this paper.

Acknowledgments

We acknowledge financial support from the Research Council of Norway (RCN), through its Centres of Excellence funding scheme, project 223272 (CEED), and 288449 to CPC (MAGPIE project). We thank Michelle Kominz, Douwe van der Meer and Christian Vérard as well as one anonymous reviewer for helpful comments that improved the manuscript.

Appendix A. Supplementary data

Supplementary data to this article can be found online at https://doi.org/10.1016/j.gr.2022.05.011.

References

Algeo, T.J., Wilkinson, B.H., 1991. Modern and ancient continental hypsometries. J. Geol. Soc. Lond 148 (4), 643–653.
Algeo, T.J., Seslavinsky, K.B., 1995. The Paleozoic world; continental flooding, hypsometry, and sea level. Am. J. Sci. 295 (7), 787–822. https://doi.org/10.2475/ajs.295.7.787.
Amante, C., Eakins, B.W., (2009). ETOPO1 1 Arc-Minute Global Relief Model: Procedures, Data Sources, and Analysis. NOAA Tech. Memo. NESDIS NGDC-24. http://dx.doi.org/ 10.7289/V5C8276M.
Andersen, T.B., Jamtveit, B., Dewey, J.F., Swensson, E., 1991. Subduction and eduction of continental crust: Major mechanisms during continent-continent collision and orogenic extensional collapse, a model based on the south Norwegian Caledonides. Terra Nova 3 (3), 303–310.
Beerling, D.J., Berner, R.A., 2000. Impact of a Permo-Carboniferous high O2 event on the terrestrial carbon cycle. Proceedings of the National Academy of Sciences 97 (23), 12428–12432.
Blakey, R.C., 2008. Gondwana paleogeography from assembly to break-up—A 500 my odyssey. Geol. Soc. Am. Special Paper 441, 1–28.
Bond, G.C., 1979. Evidence of some uplifts of large magnitude in continental platforms. Tectonophysics 61, 285–305.
Boulila, S., Laskar, J., Haq, B.U., Galbrun, B., Hara, N., 2018. Long-term cyclicities in Phanerozoic sea-level sedimentary record and their potential drivers. Global and Planet. Change 165, 128–136.
Burke, K., Steinberger, B., Torsvik, T.H., Smethurst, M.A., 2008. Plume Generation Zones at the margins of Large Low Shear Velocity Provinces on the Core-Mantle Boundary. Earth Planet. Sci. 265 (1-2), 49–60.
Burgess, P.M., 2001. Modeling carbonate sequence development without relative sea-level oscillations. Geology 29 (12), 1127–1130.
Cawood, P.A., Hawkesworth, C.J., Dhuime, B., 2013. The continental record and the generation of continental crust. Bulletin 125 (1-2), 14–32.
Conrad, C.P., 2013. The solid Earth's influence on sea level. Geol. Soc. Am. Bull. 125 (7-8), 1027–1052. https://doi.org/10.1130/B30764.1.
Conrad, C.P., Husson, L., 2009. influence of dynamic topography on sea level and its rate of change. lithosphere 1 (2), 110–120. https://doi.org/10.1130/l32.1.
Domeier, M., 2016. A plate tectonic scenario for the Iapetus and Rheic Oceans. Gond. Res. 36, 275–295. https://doi.org/10.1016/j.gr.2015.08.003.
Domeier, M., 2018. Early Paleozoic tectonics of Asia: towards a full-plate model. Geosci. Front. 9 (3), 789–862. https://doi.org/10.1016/j.gsf.2017.11.012.
Doubrovine, P.V., Steinberger, B., Torsvik, T.H., 2016. A failure to reject: Testing the correlation between large igneous provinces and deep mantle structures with EDF statistics. Geochem., Geophys., Geosys. 17 (3), 1130–1163.
Ernst, R.E., 2014. Large igneous provinces. Cambridge University Press.
Fielding, C.R., Frank, T.D., Isbell, J.L. (Eds.), 2008. Resolving the Late Paleozoic ice age in time and space, Vol. 441. Geological Society of America.
Forney, G.G., 1975. Permo-Triassic Sea level change. J. Geol. 83 (6), 773–779.
Gaetani, M., Angiolini, L., Ueno, K., Nicora, A., Stephenson, M.H., Sciunnach, D., Rettori, R., Price, G.D., Sabouri, J., 2009. Pennsylvanian-Early Triassic stratigraphy in the Alborz Mountains (Iran). Geological Society, London, Special Publications 312 (1), 79–128.
Gaffin, S., 1987. Ridge volume dependence on seafloor generation rate and inversion using long term sea level change. Am. J. Sci. 287 (6), 596–611.

Garnero, E.J., Lay, T., McNamara, A., 2007. Implications of lower mantle structural heterogeneity for existence and nature of whole mantle plumes. Geol. Soc. Am. Special Paper 430, 79–102. https://doi.org/10.1130/2007. 2430(05).
Garnero, E.J., McNamara, A.K., Shim, S.-H., 2016. Continent-sized anomalous zones with low seismic velocity at the base of Earth's mantle. Nature Geosci. 9 (7), 481–489.
Golonka, J. R., Ross, M. I., & Scotese, C. R. (1994). Phanerozoic paleogeographic and paleoclimatic modeling maps.
Guillaume, B., Pochat, S., Monteux, J., Husson, L., Choblet, G., 2016. Can eustatic charts go beyond first order? Insights from the Permian-Triassic. Lithosphere 8 (5), 505–518.
Gurnis, M., 1993a. Phanerozoic marine inundation of continents driven by dynamic topography above subducting slabs. Nature 364 (6438), 589–593.
Gurnis, M., 1993b. Depressed continental hypsometry behind oceanic trenches - a clue to subduction controls on sea-level change. Geology 21 (1), 29–32. https://doi.org/10.1130/0091-7613(1993)021<0029:dchbot>2.3.co;2.
Gurnis, M., Müller, R.D., Moresi, L., 1998. Cretaceous vertical motion of Australia and the AustralianAntarctic discordance. Science 279 (5356), 1499–1504.
Hallam, A., 1984. Pre-Quaternary sea level changes. Annu. Rev. Earth Planet. Sci. 12 (1), 205–243. https://doi.org/10.1146/annurev.ea.12.050184.001225.
Hallam, A., 1992. Phanerozoic sea level changes. Columbia University Press.
Hardenbol, J., Thierry, J., Farley, M.B., Jacquin, T., de Graciansky, P.-C., Vail, P.R., 1998. Mesozoic and Cenozoic sequence stratigraphy of European basins. SEPM Spec. Publ. 60, 3–13.
Harrison, C. G. A., 1990, Long term eustasy and epeirogeny in continents, in Sea Level Change: U.S. National Research Council Geophysics study Committee (Washington D.C.), p. 141-158.
Haq, B.U., Al-Qahtani, A.M., 2005. Phanerozoic cycles of sea level change on the Arabian Platform. GeoArabia 10 (2), 127–160.
Haq, B.U., Schutter, S.R., 2008. A chronology of Paleozoic sea level changes. Science 322 (5898), 64–68.
Haq, B.U., 2014. Cretaceous eustasy revisited. Global and Planet.change 113, 44–58.
Haq, B., 2018. Triassic Eustatic Variations Reexamined. Triassic eustatic variations reexamined. Gsa Today 28 (12), 4–9.
Karlsen, K.S., Conrad, C.P., Magni, V., 2019. Deep water cycling and sea level change since the breakup of Pangea. Geochem., Geophys., Geosys. 20 (6), 2919–2935.
Karlsen, K. S., M. Domeier, C. Gaina, and C. P. Conrad (2020), A tracer-based algorithm for automatic generation of seafloor age grids from plate tectonic reconstructions, Comput. Geosci., 140, 104508, doi:https://doi.org/10.1016/j.cageo.2020.104508.
Kocsis, Á.T., Scotese, C.R., 2021. Mapping paleocoastlines and continental flooding during the Phanerozoic. Earth-Science Reviews 213, 103463. https://doi.org/10.1016/j.earscirev.2020.103463.
Kominz, M.A., Miller, K.G., Browning, J.V., Katz, M.E., Mountain, G.S., 2016. Miocene relative sea level on the New Jersey shallow continental shelf and coastal plain derived from one-dimensional backstripping: A case for both eustasy and epeirogeny. Geosphere 12 (5), 1437–1456.
Lambeck, K., Rouby, H., Purcell, A., Sun, Y., Sambridge, M., 2014. Sea level and global ice volumes from the Last Glacial Maximum to the Holocene. PNAS 111 (43), 15296–15303. https://doi.org/10.1073/pnas.1411762111.
Lithgow-Bertelloni, C., Silver, P.G., 1998. Dynamic topography, plate driving forces and the African superswell. Nature 395 (6699), 269–272.
Marcilly, C.M., Torsvik, T.H., Domeier, M., Royer, D.L., 2021. New paleogeographic and degassing parameters for long-term carbon cycle models. Gondwana Research 97, 176–203. https://doi.org/10.1016/j.gr.2021.05.016.
Merdith, A.S., Williams, S.E., Collins, A.S., Tetley, M.G., Mulder, J.A., Blades, M.L., Young, A., Armistead, S.E., Cannon, J., Zahirovic, S., Müller, R.D., 2021. Extending full-plate tectonic models into deep time: Linking the Neoproterozoic and the Phanerozoic. Earth Sci. Rev. 214. https://doi.org/10.1016/j.earscirev.2020.103477.
Miller, K.G., Kominz, M.A., Browning, J.V., Wright, J.D., Mountain, G.S., Katz, M.E., Pekar, S.F., 2005. The Phanerozoic record of global sea level change. Science 310 (5752), 1293–1298.
Mills, B., Daines, S.J., Lenton, T.M., 2014. Changing tectonic controls on the long-term carbon cycle from Mesozoic to present. Geochem., Geophys., Geosys. 15 (12), 4866–4884.
Montañez, I.P., Poulsen, C.J., 2013. The Late Paleozoic Ice Age: An Evolving Paradigm. Annu. Rev. Earth Pl. Sc. 41 (1), 629–656.
Moucha, R., Forte, A.M., Mitrovica, J.X., Rowley, D.B., Quere, S., Simmons, N.A., Grand, S.P., 2008. Dynamic topography and long-term sea level variations: There is no such thing as a stable continental platform. Earth Planet. Sci. Lett. 271 (1–4), 101–108. https://doi.org/10.1016/j.epsl.2008.03.056.
Müller, R.D., Sdrolias, M., Gaina, C., Steinberger, B., Heine, C., 2008. Long-term sea level fluctuations driven by ocean basin dynamics. Science 319 (5868), 1357–1362.
Pitman, W.C., 1978. relationship between eustacy and stratigraphic sequences of passive margins. Geol. Soc. Am. Bull. 89 (9), 1389–1403.
Rocha-Campos, A.C., dos Santos, P.R., Canuto, J.R., Fielding, C.R., 2008. Late paleozoic glacial deposits of Brazil: Paraná Basin. Resolving the late Paleozoic ice age in time and space: GSA Special Paper 441, 97–114.
Ronov, A.B., 1994. Phanerozoic transgressions and regressions on the continents; a quantitative approach based on areas flooded by the sea and areas of marine and continental deposition. Am. J. Sci. 294 (7), 777–801.
Scotese, C. R. (2016). PALEOMAP PaleoAtlas for GPlates and the PaleoData Plotter Program PALEOMAP Project (2016)(http://www.earthbyte.org/paleomap-paleoatlas-for-gplates/)
Scotese, C.R., Golonka, J., 1992. Paleogeographic atlas: Paleomap Project. Texas, Department of Geology, University of Texas at Arlington, Arlington.
Scotese, C.R., Song, H., Mills, B.J., van der Meer, D.G., 2021. Phanerozoic paleotemperatures: The earth's changing climate during the last 540 million years. Earth-Sci.Rev. 215, 103503.
Snedden, J.W., Liu, C., 2010. A Compilation of Phanerozoic Sea level Change. Coastal Onlaps and Recommended Sequence Designations. Search Discov, Artic.
Snedden, J.W., Liu, C., 2011. Recommendations for a uniform chronostratigraphic designation system for Phanerozoic depositional sequences. AAPG Bull. 95 (7), 1095–1122. https://doi.org/10.1306/01031110138.
Smith, A.G., Smith, D.G., Funnell, B.M., 2004. Atlas of Mesozoic and Cenozoic coastlines. Cambridge University Press.
Soreghan, G.S., Soreghan, M.J., Heavens, N.G., 2019. Explosive volcanism as a key driver of the late Paleozoic ice age. Geology 47 (7), 600–604.
Spasojevic, S., Liu, L., Gurnis, M., Müller, R.D., 2008. The case for dynamic subsidence of the US east coast since the Eocene. Geophysical Research Letters 35 (8), L08305. https://doi.org/10.1029/2008GL033511.
Spasojevic, S., Gurnis, M., 2012. Sea level and vertical motion of continents from dynamic earth models since the Late Cretaceous. AAPG bulletin 96 (11), 2037–2064.
Stampfli, G.M., Hochard, C., Vérard, C., Wilhem, C., vonRaumer, J., 2013. The formation of Pangea. Tectonophysics 593, 1–19.
Svensen, H.H., Torsvik, T.H., Callegaro, S., Augland, L., Heimdal, T.H., Jerram, D.A., Planke, S., Pereira, E., 2018. Gondwana Large Igneous Provinces: plate reconstructions, volcanic basins and sill volumes. Geological Society, London, Special Publications 463 (1), 17–40.
Sømme, T.O., Helland-Hansen, W., Granjeon, D., 2009. Impact of eustatic amplitude variations on shelf morphology, sediment dispersal, and sequence stratigraphic interpretation: Icehouse versus greenhouse systems. Geology 37 (7), 587–590.
Torsvik, T.H., Rousse, S., Labails, C., Smethurst, M.A., 2009. A new scheme for the opening of the South Atlantic Ocean and dissection of an Aptian Salt Basin. Geophysical Journal International 177, 1315–1333.
Torsvik, T.H., Steinberger, B., Gurnis, M., Gaina, C., 2010a. Plate tectonics and net lithosphere rotation over the past 150 My. Earth and Planet. Science Letters 291 (1-4), 106–112.
Torsvik, T.H., Burke, K., Steinberger, B., Webb, S.J., Ashwal, L.D., 2010b. Diamonds sampled by plumes from the core–mantle boundary. Nature 466 (7304), 352–355. https://doi.org/10.1038/nature09216.
Torsvik, T.H., van der Voo, R., Doubrovine, P.V., Burke, K., Steinberger, B., Ashwal, L. D., Trønnes, R.G., Webb, S.J., Bull, A.L., 2014. Deep mantle structure as a reference frame for movements in and on the Earth. PNAS 111 (24), 8735–8740.
Torsvik, T.H., Steinberger, B., Ashwal, L.D., Doubrovine, P.V., Trønnes, R.G., Polat, A., 2016. Earth Evolution and Dynamics – A tribute to Kevin Burke. Can. J. of Earth Sci. 53 (11), 1073–1087. https://doi.org/10.1139/cjes-2015-0228.
Torsvik, T.H., Cocks, L.R.M., 2017. Earth History and Palaeogeography. Cambridge University Press, p. 317 pp..
Torsvik, T. H., Svensen, H. H., Steinberger, B., Royer, D. L., Jerram, D. A., Jones, M. T., & Domeier, M. (2021). Connecting the deep Earth and the atmosphere. *In* Mantle Convection and Surface Expressions *(*Edited by Hauke Marquardt, Maxim Ballmer, Sanne Cottaar and Jasper Konter). Geophysical Monograph 263, 413-453. American Geophysical Union. DOI: 10.1002/9781119528609.ch16.
Vail, P. R., Mitchum Jr, R. M., & Thompson III, S. (1977). Seismic stratigraphy and global changes of sea level: Part 4. Global cycles of relative changes of sea level.: Section 2. Application of seismic reflection configuration to stratigraphic interpretation.
van der Meer, D.G., van den Berg van Saparoea, A.P.H., van Hinsbergen, D.J.J., van de Weg, R.M.B., Godderis, Y., Le Hir, G., Donnadieu, Y., 2017. Reconstructing first-order changes in sea level during the Phanerozoic and Neoproterozoic using strontium isotopes. Gond. Res. 44, 22–34.
Vérard, C., Hochard, C., Baumgartner, P.O., Stampfli, G.M., Liu, M., 2015. 3D palaeogeographic reconstructions of the Phanerozoic versus sea-level and Sr-ratio variations. J. Palaeogeogr. 4 (1), 64–84.
Vérard, C., 2017. Statistics of the Earth's Topography. Open Access Library Journal 04 (06), 1–50.
Veevers, J.J., 2004. Gondwanaland from 650–500 Ma assembly through 320 Ma merger in Pangea to 185–100 Ma breakup: supercontinental tectonics via stratigraphy and radiometric dating. Earth-Sci. Rev. 68 (1-2), 1–132.
Walker, L.J., Wilkinson, B.H., Ivany, L.C., 2002. Continental drift and Phanerozoic carbonate accumulation in shallow-shelf and deep-marine settings. J. Geol. 110 (1), 75–87.
Wright, N.M., Seton, M., Williams, S.E., Whittaker, J.M., Müller, R.D., 2020. Sea level fluctuations driven by changes in global ocean basin volume following supercontinent break-up. Earth Sci. Rev. 208, 103293. https://doi.org/10.1016/j.earscirev.2020.103293.
Zhang, Y., 2005. Global tectonic and climatic control of mean elevation of continents, and Phanerozoic sea level change. Earth Planet. Sci. Lett. 237 (3-4), 524–531.

Understanding the early Paleozoic carbon cycle balance and climate change from modelling

Chloé M. Marcilly, Pierre Maffre, Guillaume Le Hir, Alexandre Pohl, Frédéric Fluteau, Yves Goddéris, Yannick Donnadieu, Thea H. Heimdal, Trond H. Torsvik.

Earth and Planetary Science Letters 594 (2022)

Earth and Planetary Science Letters 594 (2022) 117717

Contents lists available at ScienceDirect

Earth and Planetary Science Letters

www.elsevier.com/locate/epsl

Understanding the early Paleozoic carbon cycle balance and climate change from modelling

Chloé M. Marcilly [a,*], Pierre Maffre [b], Guillaume Le Hir [c], Alexandre Pohl [d,e], Frédéric Fluteau [c], Yves Goddéris [f], Yannick Donnadieu [g], Thea H. Heimdal [a], Trond H. Torsvik [a,h]

[a] Centre for Earth Evolution and Dynamics (CEED), University of Oslo, 0315 Oslo, Norway
[b] Department of Earth and Planetary Science, University of California, Berkeley, CA 94720, USA
[c] Université Paris, Institut de Physique du Globe de Paris, CNRS, 1 rue Jussieu, 75005 Paris, France
[d] Biogéosciences, UMR 6282, UBFC/CNRS, Université Bourgogne Franche-Comté, 6 boulevard Gabriel, F-21000 Dijon, France
[e] Department of Earth and Planetary Sciences, University of California, Riverside, CA, USA
[f] Géosciences-Environnement Toulouse, CNRS-Université Paul Sabatier, Toulouse, France
[g] Aix-Marseille Univ, CNRS, IRD, INRA, Coll. France, CEREGE, Aix-en-Provence, France
[h] School of Geosciences, University of Witwatersrand, Johannesburg 2050, South Africa

ARTICLE INFO

Article history:
Received 11 February 2022
Received in revised form 21 June 2022
Accepted 4 July 2022
Available online 20 July 2022
Editor: B. Wing

Keywords:
Ordovician
paleoclimate
carbon modelling
paleogeography
solid Earth degassing

ABSTRACT

The Ordovician global cooling trend observed by several temperature proxies, which coincides with one of the most significant evolutionary diversifications on Earth, is yet to be fully understood. This study presents new simulations of pCO_2 and surface temperatures using a spatially resolved climate-carbon cycle Earth system model fed with refined continental reconstructions and new estimates of solid Earth degassing. First, in order to quantify the respective roles of paleogeography and degassing, the impact of continental drift alone is investigated. This is done by calculating its imprint on continental weathering rates throughout the Ordovician under a constant pCO_2, and by testing different topography inputs. Secondly, the sensitivity of the Earth's climate to paleogeography and carbon degassing changes is investigated by coupling the climate and carbon cycles in the GEOCLIM model. Based on our experiments we show that, although Early Ordovician high temperatures can be replicated within error margins, our new constraints cannot explain the intense cooling over the Mid to Late Ordovician, even if a progressive enhancement in Earth surface weatherability is taken into account. By using GEOCLIM in an inverse modelling approach, we calculate that the theoretical degassing necessary to reach proxy-derived temperatures for the Early Ordovician is three-to-five times higher compared to modern values. Further, in order to simulate the following Ordovician cooling trend, the solid Earth degassing must be reduced to modern-day values in only 30 Myrs. We conclude that, if accepting the veracity of the high Early Ordovician temperatures, alternative sources but also sinks of carbon must be considered to explain the climatic shift over the period.

1. Introduction

The Ordovician long-term global cooling trend is a key feature of the early Paleozoic climate (Trotter et al., 2008), and is also observed in recent studies (e.g. Edwards et al., 2021; Goldberg et al., 2021; Song et al., 2019). Global cooling initiated in the late Cambrian, and proceeded rapidly during the Early Ordovician, before tropical sea-surface temperatures (SSTs) reached a plateau during the Middle to Late Ordovician and subsequently stabilized at modern-like levels (Fig. 1a) (i.e., ~30 °C; Goldberg et al., 2021; Song et al., 2019; Trotter et al., 2008; Scotese et al., 2021). The striking feature of this climatic transition is its magnitude, with tropical temperatures plummeting by around 10 °C, from ~40 °C to 30 °C, excluding the short-lived end-Ordovician Hirnantian cooling (445-444 Ma) (Finnegan et al., 2011; Trotter et al., 2008) (Fig. 1a). During the Ordovician cooling phase, the global climate transitioned from a greenhouse state to the first major continental glaciation of the Phanerozoic, with continental glacial onset argued to have occurred sometime around the Darriwilian (Fig. 1a,b) (~467-458 Ma; e.g. Pohl et al., 2016; Rasmussen et al.,

* Corresponding author.
E-mail address: c.f.m.marcilly@geo.uio.no (C. M. Marcilly).

https://doi.org/10.1016/j.epsl.2022.117717

2016) or the Katian (453-445 Ma; Cocks and Torsvik, 2020; Loi et al., 2010), but peak glacial activity occurred during the short-lived Hirnantian cooling (Finnegan et al., 2011; Ghienne et al., 2014).

Recent studies suggest an intricate coupling between climate and marine biological evolution throughout the Ordovician. The Great Ordovician Biodiversification Event (GOBE) marked the radiation of the marine animal phyla that had emerged during the Cambrian Explosion (Cocks and Torsvik, 2020). Biodiversification may have been driven by cooling to more habitable temperatures alone (Trotter et al., 2008; Rasmussen et al., 2016), or in conjunction with the ensuing ocean oxygenation (Edwards et al., 2017), both being known to act synergistically on marine ectotherm habitability (Deutsch et al., 2015; Stockey et al., 2021). Ordovician cooling was not only associated with a significant increase in the number of different complex animal forms during the Mid Ordovician (~470-455 Ma; GOBE), but the later Hirnantian cooling (with SSTs averaging 22 ± 6 °C) coincided with the only known mass extinction to have occurred during icehouse conditions (Torsvik et al., 2021).

The cause(s) of the long-term Ordovician cooling trend remain(s) poorly understood due to the sparsity of data and the large spread of temperature estimates (Fig. 1a). First, temporal trends from oxygen isotope data ($\delta^{18}O$) may be distorted by diagenesis, although meticulous screening for pristine samples and trace element analyses and the use of material supposedly resistant to diagenesis (such as biogenic apatite) permit gaining confidence in reconstructed temperatures (Hearing et al., 2018). Second, the heterogeneous spatial sampling of proxy data can create an underestimation of climatic perturbations, which has been shown for the Ordovician (Jones and Eichenseer, 2021). Absolute temperature values are even more challenging to constrain compared to temporal trends, due to large error margins associated with functions used to convert isotopic values to temperature (Lécuyer et al., 2013), as well as uncertain constraints on early Paleozoic seawater isotopic compositions. Some studies suggest that the seawater isotopic composition has remained unchanged (e.g. Henkes et al., 2018) while others follow the secular trend idea of the Veizer hypothesis (Veizer and Prokoph, 2015) of a gradual enrichment of the ^{18}O isotope (e.g., Galili et al., 2019; Hodel et al., 2018; Defliese, 2020).

Several hypotheses have been proposed to explain the Ordovician long-term cooling, either by increasing the weatherability of the continents or by decreasing the amplitude of the solid Earth degassing. On the one hand, Earth's surface weatherability increases when continental drift brings continents into the warm and humid equatorial area (Nardin et al., 2011, Fig. 1b) in response to early land-plant colonization (Lenton et al., 2012; Porada et al., 2016), or, for example, through increased weathering of mafic silicate rock linked to physical erosion through changes in topography (Kump et al., 1999; Young et al., 2009; Swanson-Hysell and Macdonald, 2017; Macdonald et al., 2019). On the other hand, volcanic outgassing rates may have decreased through the early Paleozoic (McKenzie et al., 2016). The search for a unique causative mechanism for the long-term Ordovician cooling trend is elusive and these various factors may all have played a role. Unfortunately, these different hypotheses have been proposed in isolation using different methods and tools, and the importance and contribution of each of these factors remain to be quantified in an integrated numerical framework.

Here, we use the climate-carbon model GEOCLIM (Donnadieu et al., 2006-updated) to simulate the long-term Ordovician climatic trend in response to changes in paleogeography and associated silicate weathering activity as well as changes in volcanic degassing rates.

The model is fed by climatic fields that have been simulated using the atmospheric general circulation model LMDz6 (see Supplementary material) based on improved continental reconstructions (Marcilly et al., 2021). The GEOCLIM model accounts for the competing impacts of continental weathering and volcanic outgassing on the atmospheric partial pressure of CO_2 (pCO_2) and climate. This allows us to quantify the magnitude and temporal trend in global cooling, resulting from these competing mechanisms, and evaluate their relative contributions. In order to quantify the respective roles of paleogeography and degassing, we first explore the impact of continental drift alone, by calculating its imprint on continental weathering rates throughout the Ordovician under a constant pCO_2. Then, the sensitivity of the Earth's climate to paleogeography and carbon degassing variations is investigated by coupling the climate and carbon cycles in the GEOCLIM model. This study highlights the current limits of our understanding of factors driving the early Paleozoic climate and presents conceivable directions for future studies.

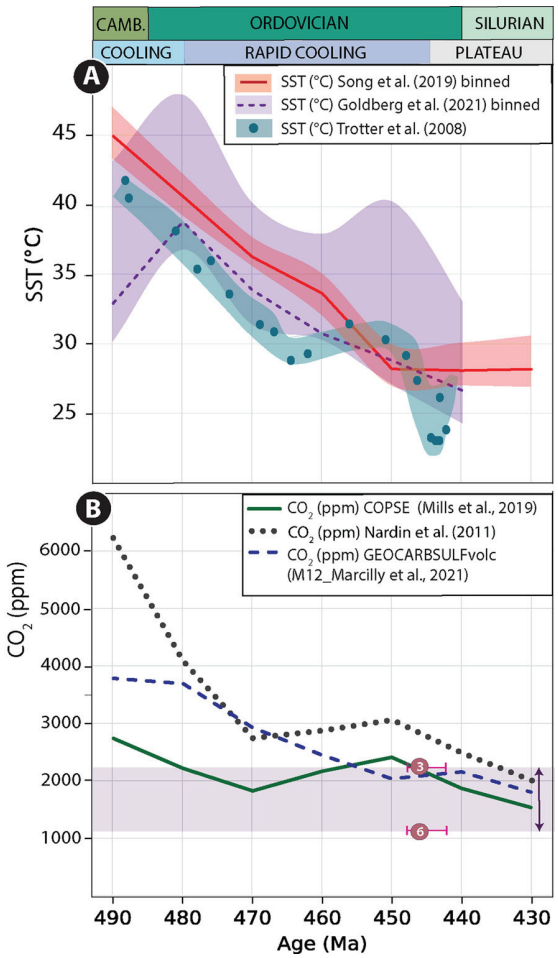

Fig. 1. **(a)** Compilation of temperature reconstructions covering the Late Cambrian to early Silurian. These datasets are from Song et al. (2019) in red, filtered to reflect only fossils found within ±30° latitude with error margins shaded. The stippled purple curve is from Goldberg et al. (2021) and represents the average of the least diagenetically altered samples. The purple shaded area represents the spread of data of the mid-to-least diagenetically altered data presented in Fig. 4 of Goldberg et al. (2021). Finally, the green dots are the temperatures reconstructed by Trotter et al. (2008) with their error band in shaded green. **(b)** Model simulations of atmospheric CO_2 levels. The green line is simulated using the forward model COPSE (Mills et al., 2019) whereas the stippled blue curve is obtained using GEOCARBSULF with updated paleogeography and degassing parameters (Marcilly et al., 2021). The dotted black curve is from Nardin et al. (2011) using GEOCLIM with the GCM FOAM. The numbers refer to the theoretical glacial inception levels with 3 and 6 °C climate sensitivity assuming 500 ppm inception level for modern times and a fainter sun in deep time (Marcilly et al., 2021). (For interpretation of the colours in the figure(s), the reader is referred to the web version of this article.)

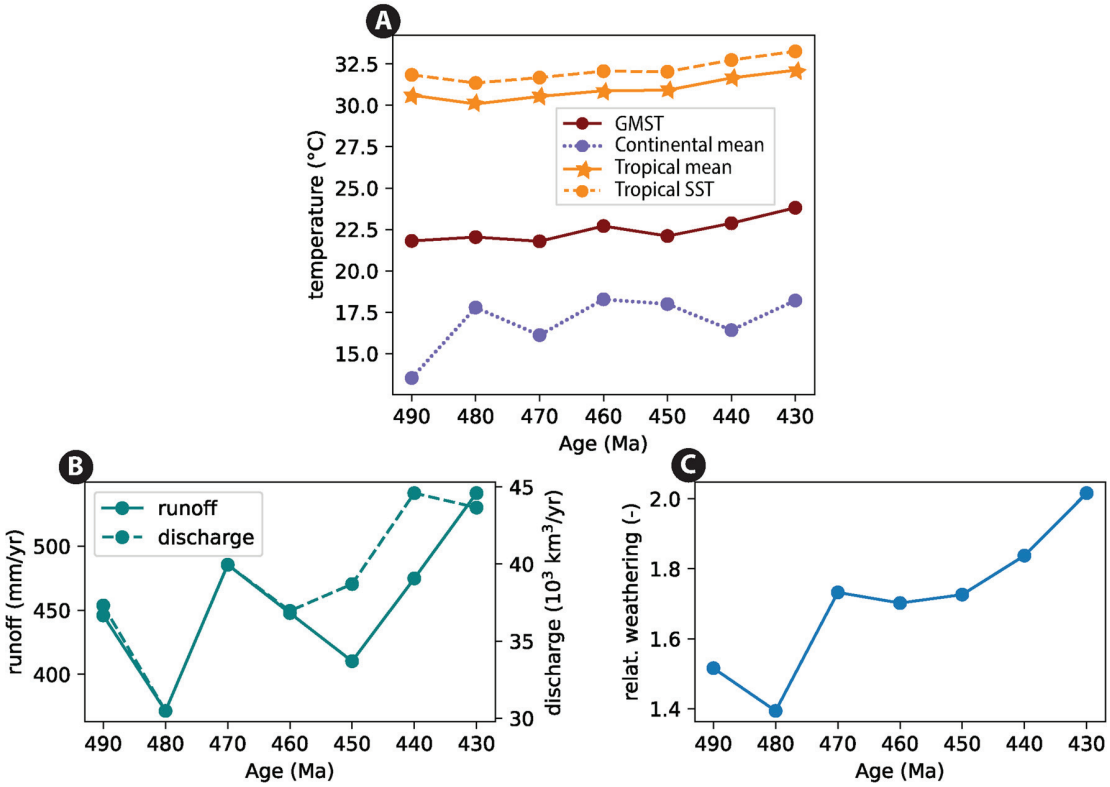

Fig. 2. **(a)** Modelled Global Mean Surface Temperatures (GMST), continental mean, tropical mean and tropical (21°N–21°S) sea-surface temperature (SST) though time. **(b)** Mean continental runoff (solid line, left axis), which corresponds to precipitation minus evaporation and globally cumulated continental discharge (dashed line, right axis) corresponding to the area-integrated runoff through time. **(c)** Total silicate weathering fluxes predicted by GEOCLIM (relative to pre-industrial control weathering flux). Climatic variables from LMDz simulations conducted at 12 PAL pCO_2 (3360 ppmv) were used to force the weathering model.

2. The paleogeographical imprint on Ordovician climate

2.1. Response of weathering to the continental configuration

To explore the interplays between Ordovician paleogeography and chemical weathering, we ran the LMDz6 climate model (see Supplementary Information) with late Cambrian to early Silurian paleogeographic maps ranging from 490 Ma to 430 Ma at 10 Myr intervals (7 time slices from Marcilly et al., 2021, see Supplementary Fig. S1). Several models for the tectonic and paleogeographic evolution exist for the Ordovician (e.g. Scotese, 2016; Blakey, 2009; Swanson-Hysell and Macdonald, 2017), but we here chose to work with the global model developed by Torsvik and collaborators (2012, 2016), which forms the basis for the exposed land maps produced in Marcilly et al. (2021; see details in supplementary section G).

In order to isolate the paleogeographical imprint, the pCO_2 in our simulations is fixed at 12 PAL (3360 ppmv) (i.e., Pre-industrial Atmospheric Level; 1 PAL = 280 ppmv) to avoid strongly non-linear climate responses associated with sea-ice feedbacks encountered at lower pCO_2 levels (Pohl et al., 2014, 2016). We vary the model solar luminosity with geological age (from ~1313 W m^{-2} at 490 Ma to ~1320 W m^{-2} at 430 Ma) according to the model of stellar evolution (Gough, 1981).

At the global scale, the global mean surface temperature (GMST) remains relatively constant at ~22.5 °C (Fig. 2a) in our simulations. However, the continental climate (i.e., temperature, runoff, and discharge) is more sensitive to paleogeographical changes (Fig. 2a, b; Fig. 3). The most important observations include significant continental warming between 490 Ma and 480 Ma (Fig. 2a), as well as local maxima of global dryness at 480 Ma and 450 Ma (Fig. 2b, Fig. S2 in SI). From 490 to 480 Ma, the global mean temperature over the continents increases by 4 °C (from 14.5 °C to 18.6 °C), followed by fluctuations between 17 °C and 19.3 °C during the rest of the investigated time period (Fig. 2a). The warmest episodes occur at 480 Ma, 460 Ma, and 430 Ma when the Gondwana continent extends less over the South Pole region.

In the tropical band (i.e., from 21°S to 21°N), the annual mean temperature increases by 2 °C (from 30.1 °C to 32.1 °C) from 480 to 430 Ma (Fig. 2a), mainly due to the solar constant increase. Despite the large fluctuations in emerged land surface, reaching a peak of ~36 × 10^6 km^2 in the tropics by 450 Ma (40% of the total land exposed, Table S1 in SI), the paleogeography has apparently little influence on the modelled terrestrial temperature in the tropics (Fig. 2a).

In the subtropics, arid zones are larger at 480 Ma and 450 Ma compared to other periods (Fig. 3, Supplementary Fig. S2), which is when the surface of the Gondwana continent located below the descending branch of the Hadley circulation is at its maximum. The increase in aridity (i.e., areas where mean precipitation minus evaporation is inferior to 0) is also favoured by the drift of smaller blocks (Southern part of South-China and Baltica) entering into the subtropics between 460 and 440 Ma (SI Figs. S1, S2).

Precipitation and runoff reach maximum values over scattered islands in the equatorial belt and equatorial Gondwana (Fig. 3). A second belt with significant runoff is shown by all model runs at mid to high latitudes (i.e., between 40°S and 80°S), reaching maximum values over the western coast of Gondwana and the western edge of mountain ranges (Fig. 3; see also Pohl et al., 2017). The slight decoupling between the mean continental runoff and globally cumulated continental discharge at 450–440 Ma is due to an increase in the total area of emerged (exposed) lands between 490

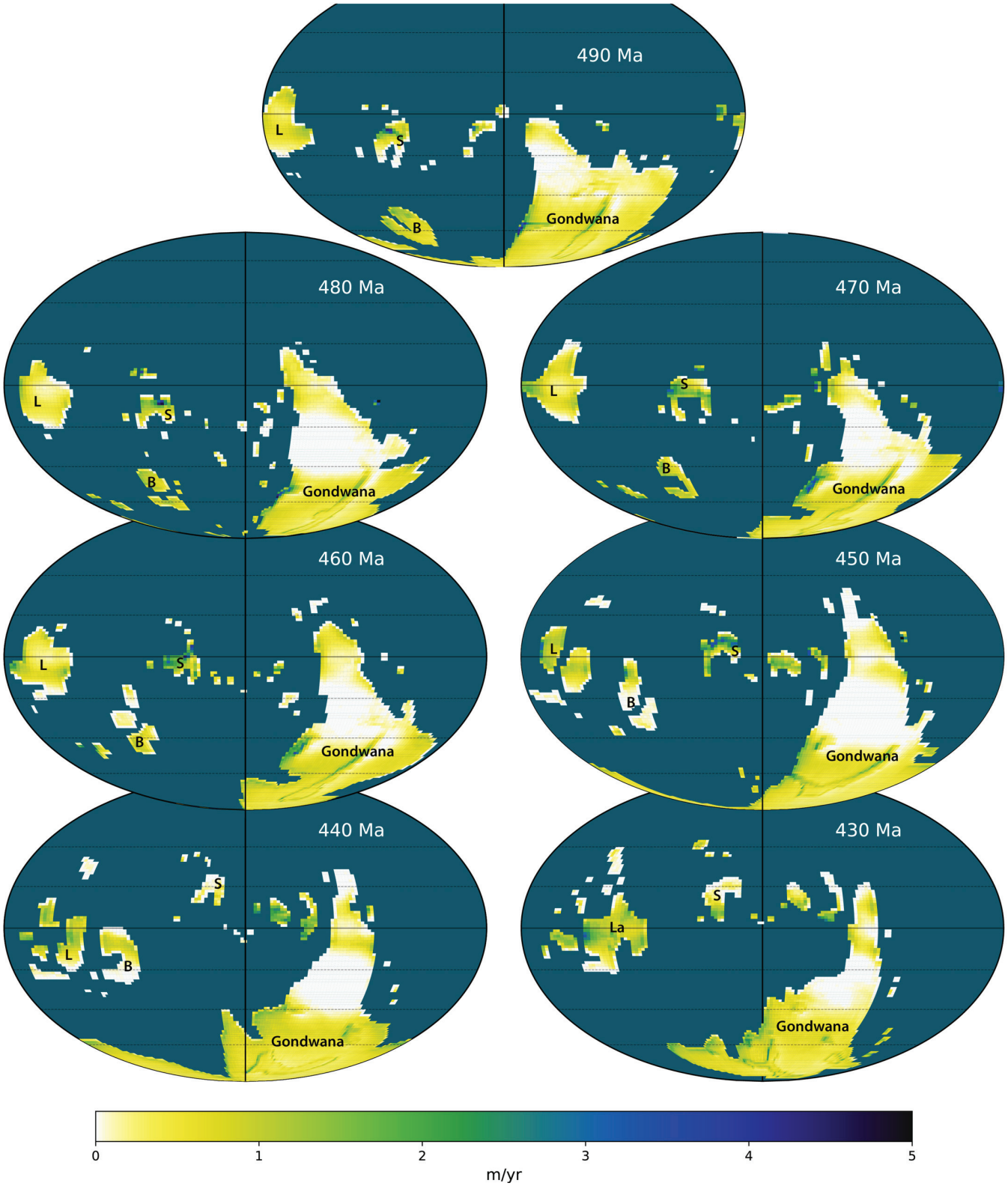

Fig. 3. Runoff patterns for each time slice at the pCO_2 of 12 PAL (3360 ppmv). Mollweide projection (equal area), parallels plotted every 20° between 60°S and 40°N. B, Baltica, L, Laurentia, S, Siberia, La, Laurussia.

and 450 Ma. This land area increase counteracts the drop in mean continental runoff. Collectively, these results explain why the Late Ordovician and early Silurian configurations (440 Ma, and mostly 430 Ma), and to a lesser extent, the 470 Ma configuration, between the two "dry intervals" (480 and 450 Ma), are associated with the highest weathering rates (Fig. 2c & Fig. 4, SI Fig. S4).

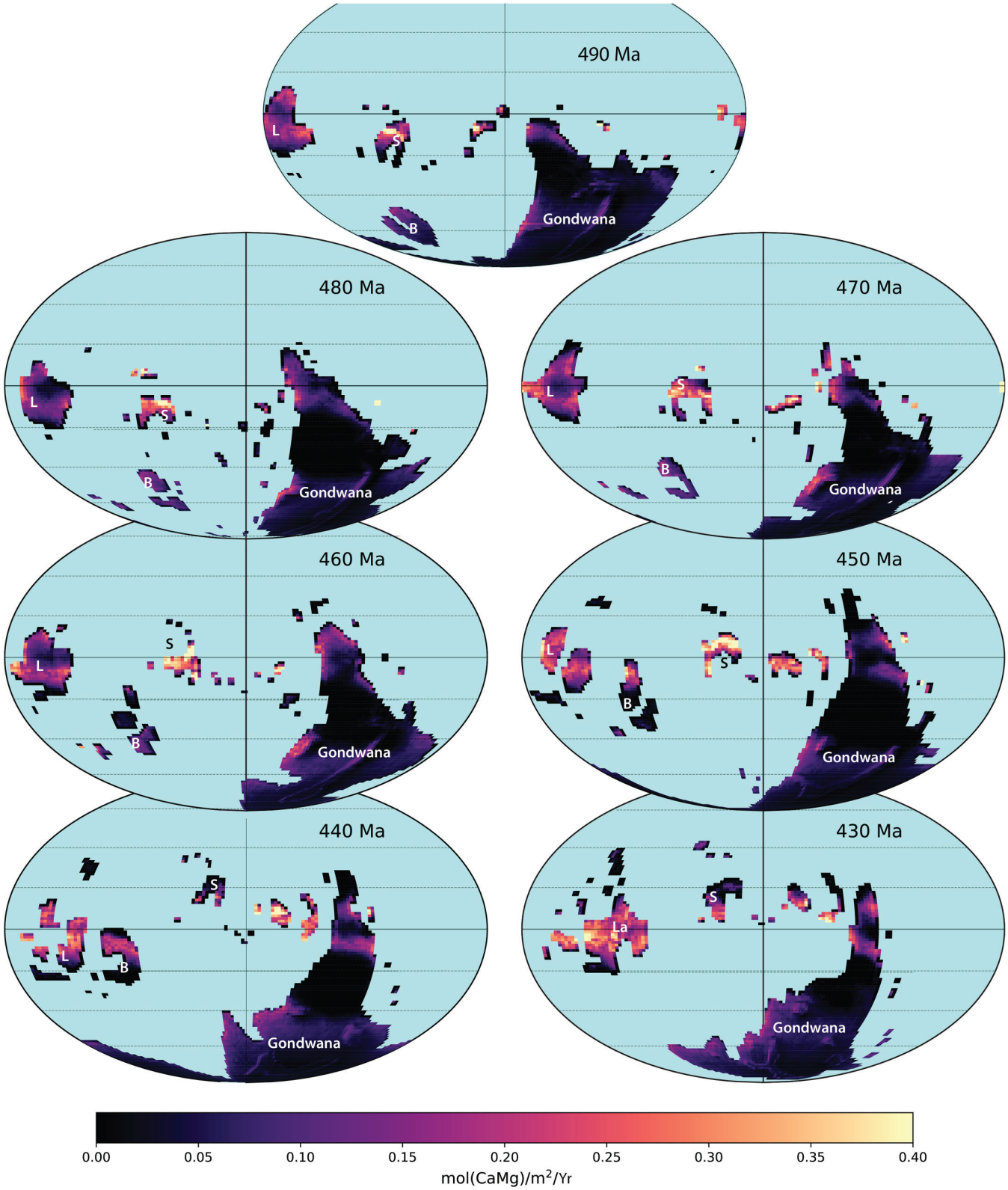

Fig. 4. Weathering patterns for each time slice with a constant pCO_2 of 12 PAL (3360 ppmv). Simulated weathering patterns are only driven by continental temperature and runoff, both depending on tectonic settings. B, Baltica, L, Laurentia, S, Siberia, La, Laurussia. Same projection and graticules as in Fig. 3.

Overall, these results demonstrate a long-term increase in continental weathering in response to continental rearrangement during the Ordovician rather than a sudden rise at the end of the Ordovician (Fig. 2c & 4). This progressive enhancement of Earth's surface weatherability (see also Marcilly et al., 2021) should lead to a pCO_2 reduction, a point explored in the following section.

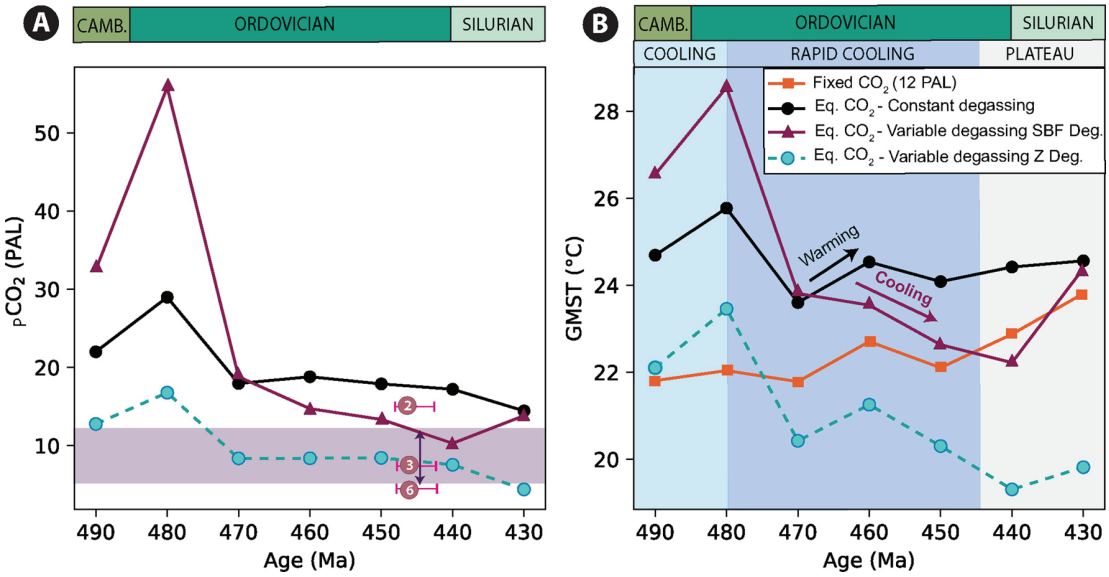

Fig. 5. a) Equilibrium pCO_2 with *constant* (black), and *variable* degassing from subduction fluxes (SBF; pink) and age-zircon distribution (Z; turquoise). The purple arrow and band display the glaciation threshold range estimated from climate models coupled with land-ice models (Herrmann et al., 2004; Lowry et al., 2014; Pohl et al., 2016). The numbers refer to the theoretical glacial inception levels with 2, 3 and 6 °C climate sensitivity assuming 500 ppm inception level from modern times and fainter sun activity in deeper time (Marcilly et al., 2021). **b)** Global mean surface temperature (GMST) of GEOCLIM, run with constant degassing (black) or variable degassing from SBF and Z (pink and turquoise). The temperature evolution at fixed CO_2 (12 PAL or 3360 ppmv) is added (orange) for comparison. Climatic trends shown with background colours in panel b are extracted from proxy compilations of different studies (Trotter et al., 2008; Song et al., 2019; Scotese et al., 2021; Goldberg et al., 2021) and simplified as follows: cooling until 480 Ma followed by rapid cooling until 450-440 Ma followed by a plateau.

2.2. Climate-carbon response to continental drift

We explore the climatic evolution over the entire Ordovician assuming a constant degassing rate of the Earth. We couple the LMDz6 climate model with a long-term carbon cycle model to compute the steady-state climate, based on the climate-carbon negative feedback (Walker et al., 1981). The resulting climate-carbon model, GEOCLIM (Donnadieu et al., 2006-updated), is described in the Supplementary Information and available online. The calculated CO_2 consumption by silicate rock weathering is calibrated on the present-day state: this means that under present-day conditions, the model predicts the silicate weathering flux of the main world rivers (Park et al., 2020). The corresponding global silicate weathering (3.3 Tmol of CO_2 consumed each year) is close to the estimate by Gaillardet et al. (1999) (2.5 Tmol/yr). This implies that the solid Earth degassing must be close to the CO_2 consumption by silicate weathering. To reach a steady state at present day, we assume that the magmatic degassing of the present day Earth is equal to 3.3 Tmol/yr of CO_2. This value is close to the CO_2 degassing estimates by Gerlach (2011) (3.4 to 5.9 Tmol CO_2/yr). Therefore, to highlight the effect of paleogeography alone, the solid Earth degassing rate for all experiments was set to 7.1 Tmol C/yr and kept constant. This value is equivalent to about 2 times that of the present-day, which corresponds to the average degassing level over the studied period from proxies for seafloor spreading (the proxies and corresponding values are presented in section 3.1). As shown in Fig. 5a (black line), the pCO_2 drops from 30 to 18 PAL (i.e., 8400-5040 ppm) between 490 and 430 Ma (Table S3 in SI), in response to the increasing surface weatherability (Fig. 2c).

The substantial drop in pCO_2 observed between 480 Ma and 470 Ma induces an important global cooling event, with GMST decreasing by 2.5 °C (Fig. 5b; black line). Between 470 Ma and 430 Ma, although pCO_2 slightly decreases (Fig. 5a), pCO_2-driven cooling is counteracted by the paleogeographical evolution accompanied by an increase in solar luminosity which, everything else unchanged, impose a warming from 470 Ma to 430 Ma (Fig. 5b, orange curve). As a result, the modelled global temperature slightly increases from 470 Ma to 430 Ma (Fig. 5b; black curve). Therefore, in our model, the paleogeographical forcing alone cannot explain the long-term Ordovician cooling trend reported based on geological data (Goldberg et al., 2021; Song et al., 2019; Trotter et al., 2008).

2.3. Climate-carbon response to enhanced topography

In order to test the effect(s) of changing topography, we ran three sets of simulations with varying topographic inputs. The first simulation (i.e., run #1, "revised topo" in Fig. 6) aimed to test the effect of higher altitudes, and so the altitudes were doubled compared to our previous simulations. Secondly, the influence of more substantial island arcs and obducted arcs were tested (Macdonald et al., 2019). To do so, new maps with increased relief areas and same doubled altitudes as in run #1 were created (i.e., run #2, "increased topo" in Fig. 6; see SI Fig. S7 for maps). The third set of simulations (i.e., run #3, "increased topo + slope" in Fig. 6) are similar to the second, but with increased slopes to accentuate the effect of increased topography on physical erosion, and hence on chemical weathering (see SI Fig. S8). All tests were first performed with constant degassing in order to isolate the topography effect (Fig. 6a).

The higher altitude simulations (run #1) led to similar temperatures compared to the previous simulations with low topography, even slightly higher between 460-440 Ma, and no intensification of the cooling can be observed (Fig. 6a). As the influence of topography is increased by taking into account larger accretion zones and island arcs (run #2), the temperature at 440 Ma is slightly lowered (Fig. 6a), but almost negligible as showing only a −0.18 °C difference. Even with steepened slopes (run #3), the difference only reached −0.51 °C (Fig. 6a). Contrarily to our first simulations with constant degassing and lower topography (Section 2.2), which suggest a warming from 450 Ma, all the simulations with enhanced topography suggest cooling from 460 Ma and lasting until 440 Ma.

These results show that changing topography does not have a large influence on the simulated Ordovician climatic trend. Taking

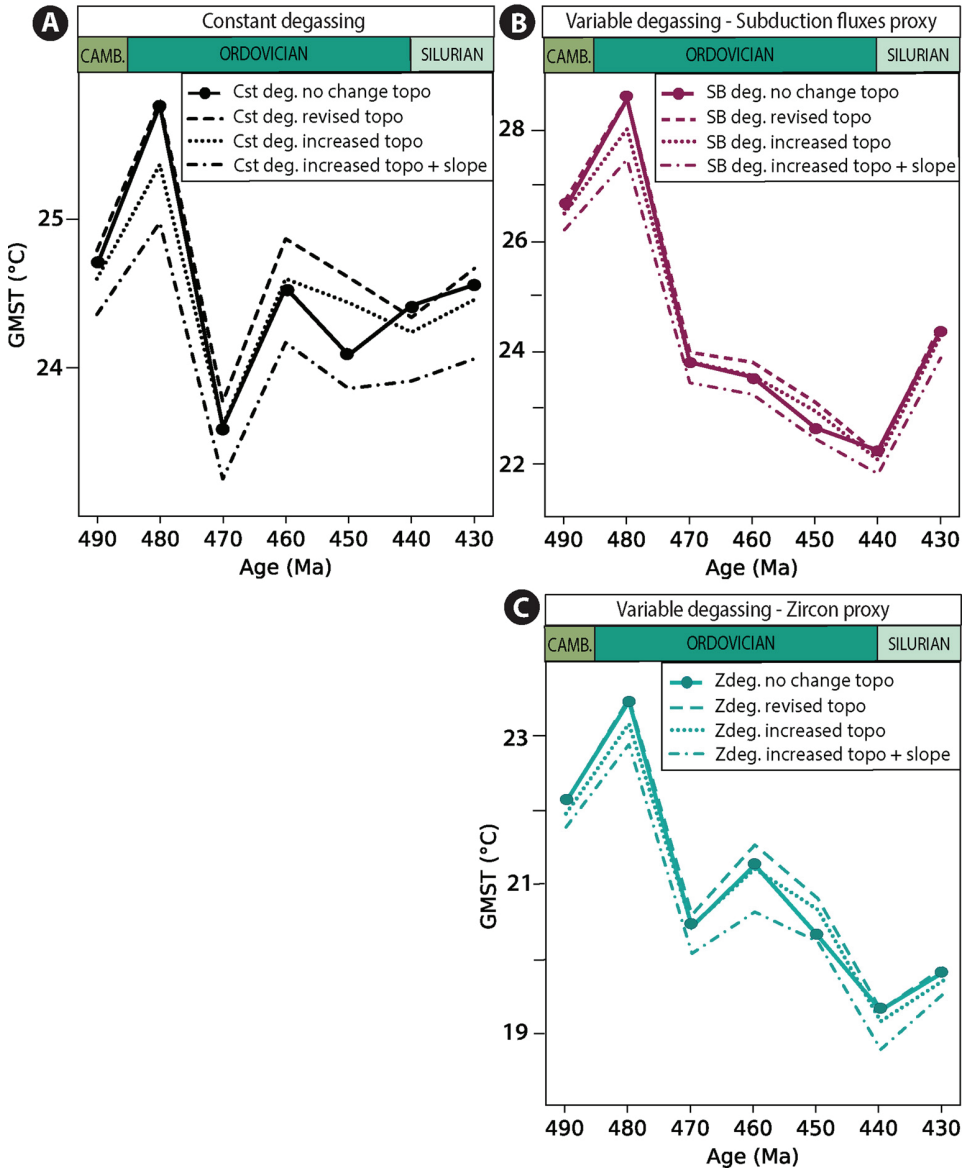

Fig. 6. Global mean average surface temperature (GMST) simulated in GEOCLIM. Simulations with **a)** constant degassing, **b)** variable degassing from subduction fluxes, and **c)** variable degassing from zircon proxy. Each panel includes 4 simulations with varying topography. The solid line is the topography used in our primary set of maps, the dashed line with doubled relief altitude, the dotted line with doubled relief altitude and increased topography from Macdonald et al. (2019) and finally the dash-dotted line is the same as the dotted line but with increased slopes.

into account larger topography and steeper slope does make the Earth slightly cooler (by ~1 °C compared to the revised but not increased topography), but quasi uniformly on the whole period, since there is no significant temporal variation of global topography (growth nor decay) over the studied period. Therefore, the climatic trend is virtually unchanged, except for a slight prolonged cooling at 450-430 Ma in the increased topography and slope simulation. However, it is important to note that only modest changes in topography have been tested, as this parameter is poorly constrained through time.

3. Transition from a warm climate state to the ice age

3.1. Testing a variable degassing throughout the Ordovician

The Ordovician long-term cooling trend could potentially be attributed to fluctuations in the major long-term carbon sources. However, as direct measurements for solid Earth degassing in the Ordovician do not exist, we must rely on proxies. The long-term solid Earth degassing mainly occurs at spreading ridges, volcanic arcs and continental rifts (Kelemen and Manning, 2015). Reconstructions of degassing fluctuations through time have traditionally been based on the past activity of seafloor spreading, and such estimates are commonly used in long-term carbon cycle models (Berner, 2006; Goddéris and Donnadieu, 2019; Mills et al., 2019; Pohl et al., 2020).

Here we use two proxies for seafloor production rate, which in turn act as a proxy for solid Earth degassing (Fig. 7). The first is based on estimates of subduction fluxes from the full-plate model of Domeier and Torsvik (2014) extended back to the early Paleozoic (Marcilly et al., 2022) (see SI for more information). Note that the early Paleozoic estimates have large uncertainties since all the oceanic lithosphere prior to the Jurassic has been subducted and absolute longitudes in the Paleozoic are strongly debated. We here estimate uncertainties associated with the subduction flux based

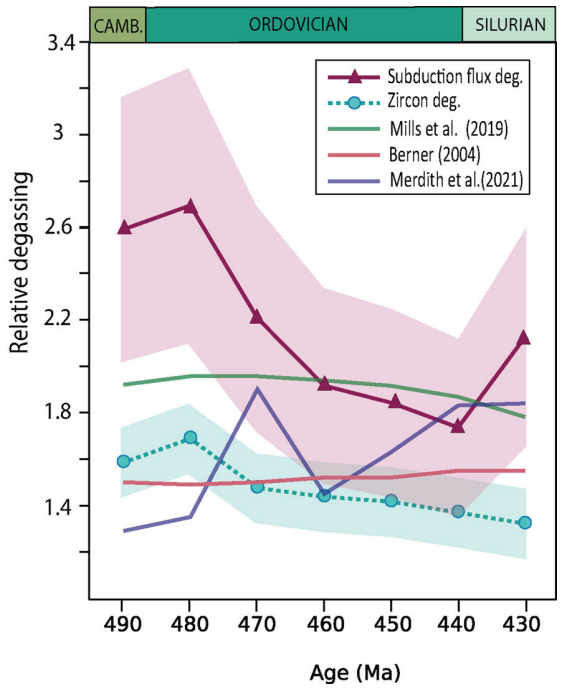

Fig. 7. Degassing relative to present-day flux derived from subduction fluxes ("subduction flux deg.") from a full-plate model (pink solid line) and age zircon distribution ("Zircon deg.") (turquoise dashed line). The proxies are plotted with their estimated error range. For comparison purposes, other estimations are plotted: Mills et al. (2019) based on hybrid subduction and rift lengths, Berner (2004) using sea-level inversion and calculated subduction flux from the Merdith et al. (2021) full plate model.

on previous versions of our subduction flux estimates (Fig. 7). The second proxy is the age distribution of zircon presented in Marcilly et al. (2021). Considering the increasing uncertainty of subduction flux estimates with deeper time, the age-frequency relationship of detrital zircons, mimicking variations in the subduction flux, both regionally and globally has been suggested as a more objective proxy for seafloor production (Domeier et al., 2018; McKenzie et al., 2016; Marcilly et al., 2021). Uncertainties for this proxy are based on its difference with subduction flux estimates in more recent time (Fig. 7). This zircon-based proxy suggests solid Earth degassing values in the same order of magnitude compared to other proxies commonly used in long-term carbon cycle modelling (e.g., Berner, 2006; Mills et al., 2019; Goddéris and Donnadieu, 2019; Merdith et al., 2021; Fig. 7), although it suggests lower estimates towards the end-Ordovician and a slight decrease between 480 Ma and 430 Ma. In contrast, the subduction-flux-based proxy we use here suggests higher values, especially between 490 and 470 Ma.

By introducing an up-to-date variable degassing reconstruction from subduction fluxes in the GEOCLIM simulations, the GMST temporal trend is amplified (Fig. 5b; purple curve) compared to simulations performed with a solid degassing held constant (Fig. 5b; black curve). While the Early Ordovician becomes warmer compared to the constant degassing scenario (T_{max} of 28.5 °C *vs.* 26 °C at 480 Ma; Fig. 5b), the model now predicts a cooler Late Ordovician climate (22 °C *vs.* 24.5 °C at 440 Ma; Fig. 5b). However, even by combining paleogeographical evolution and solid Earth degassing variations, our model fails to reproduce the full extent of the observed tropical SST drop derived from proxy data (Song et al., 2019; Goldberg et al., 2021; Fig. 8). The lower degassing scenario derived from the zircon-based proxy produces simulations generally more in line with proxy temperatures (Fig. 8c). However, the high temperatures of the Early Ordovician are well out of reach, with a maximum SST modelled at 32.5 °C at 480 Ma against ~40 °C from proxies (Fig. 8c). In summary, the simulation based on the subduction flux degassing matches more closely the proxy data between 490-480 Ma while the zircon proxy degassing curve is a better match from 470 Ma and onwards (Fig. 8b, & 8c), even if the total cooling intensity is only ~2.5 °C (Fig. 8c).

Increasing the topography with varying degassing does not lead to a more pronounced global cooling (Fig. 6b,c), and contrarily to simulations with constant degassing, this trend is not changed nor intensified between 460 and 440 Ma. Here as well, the change in values at 440 Ma is negligible with a maximum change of only −0.42 °C with subduction flux degassing (Fig. 6b) and −0.53 °C with zircon degassing (Fig. 6c).

Overall, our simulations match the Early Ordovician cooling trend, but cannot explain why the cooling continues after the Middle Ordovician (~460 Ma) and lasted for more than 40 Myrs (Fig. 8). It should be noted that, although various models and temperature reconstructions point towards a Mid-Ordovician cooling (Trotter et al., 2008; Rasmussen et al., 2016) there are no known Mid-Ordovician glacial deposits that can confirm this (Cocks and Torsvik, 2020). Furthermore, while the proxies suggest a total cooling of more than 10 °C (Fig. 8), our results show that the tectonic settings (from subduction fluxes) can drive a cooling close to 4 °C. This is in agreement with regional $\delta^{18}O$ data from Baltica, suggesting a drop of 4-5 °C during the Middle Ordovician (Rasmussen et al., 2016).

3.2. Linking the $\delta^{18}O$ record, paleogeography, and degassing

Regarding the conundrum of the Mid-Late Ordovician cooling, we complete our study by permitting the model parameters to reconcile modelled and proxy-derived SSTs. For that purpose, we adopt an inverse modelling approach by prescribing a tropical SST from the proxy reconstructions as a target in our model and calculating the degassing rate required to reproduce this Ordovician SST trend. We consider two alternative SST targets: after Goldberg et al. (2021) or after Song et al. (2019), both here averaged over 10 Myrs to fit our reconstruction intervals (see Fig. 1a & 8). The latter estimates have been checked to reflect only tropical temperatures (Marcilly et al., 2021). Further, Late Cambrian to early Silurian SSTs are almost exclusively derived from (apatite) conodonts that once lived from 12°N to 23°S (mean paleolatitude = 13± 5°N/S). These SSTs should therefore reflect a reasonably well constrained cooling trend over the Ordovician with respect to the underestimation from biased geographical sampling described by Jones and Eichenseer (2021).

The two sets of temperature estimates differ mostly during the Late Cambrian-Early Ordovician, but following this time period, their trend and absolute values are similar and within error margins of each other (Figs. 1a, 8). While the estimates by Song et al. (2019) are based on phosphatic fossils (conodonts), the ones from Goldberg et al. (2021) are from bulk rock isotopes. The scarcity of estimates in both studies may represent a limitation mostly for 490 Ma where only a few points are analyzed. In particular, the spread of the estimates is the largest for the Ordovician between 490-480 Ma in Goldberg et al. (2021), and therefore might represent the least constrained interval of their study as all data for this age is extracted from the same location (i.e., Newfoundland at the equator at the time). Similarly, the data reported in Song et al. (2019) become depleted of data coverage for 490 Ma after filtering and therefore reflect only an extrapolation of the continuity between the late Cambrian and 480 Ma. Therefore, we cannot rule out a local anomaly such as a temperature low as reconstructed in Goldberg et al. (2021).

The degassing rate scenarios obtained using the inverse approach differ significantly compared to those previously used in this study (Fig. 9a). For example, the inverse approach suggests

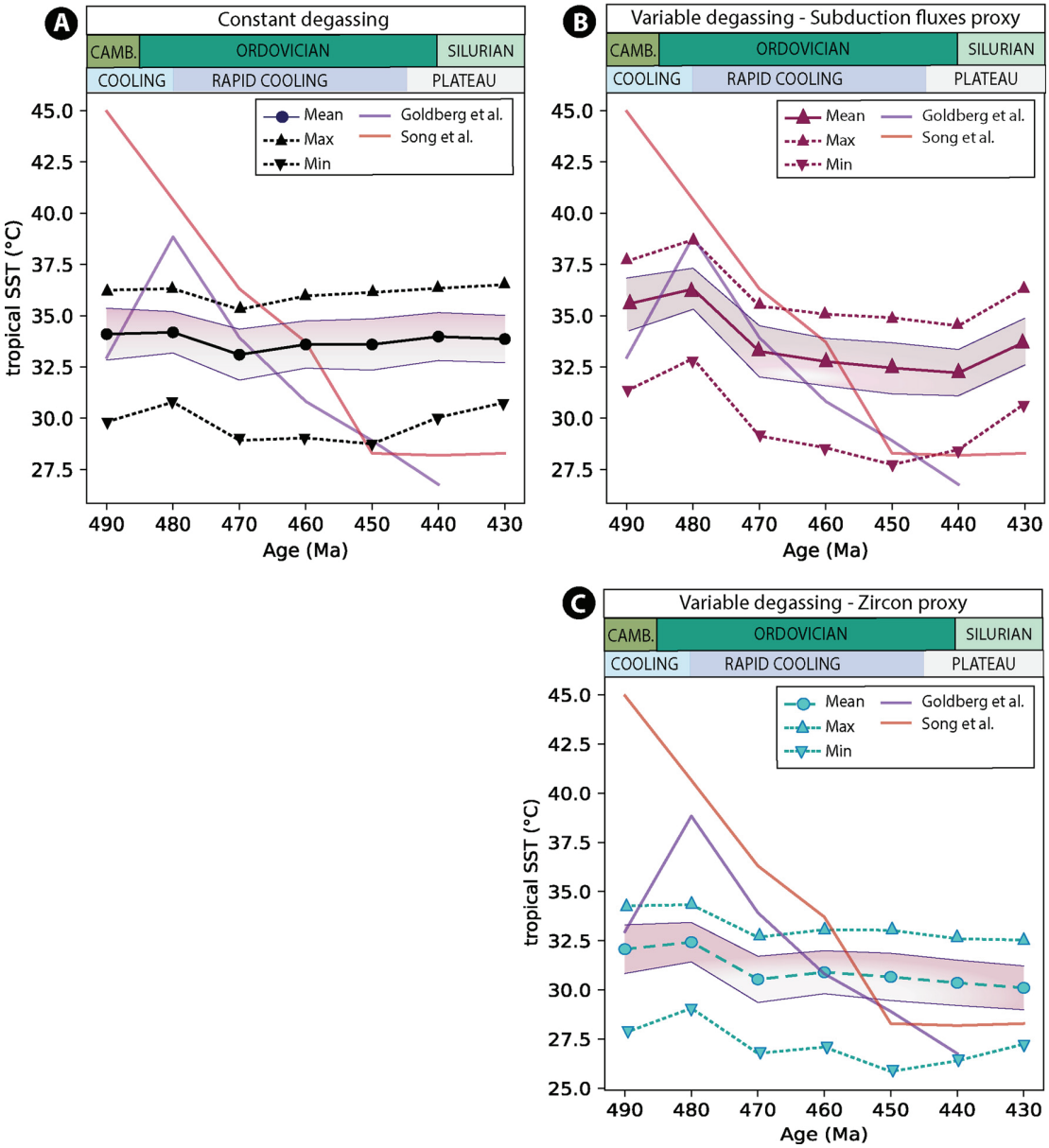

Fig. 8. Equilibrium tropical sea-surface temperature (SST) simulated in GEOCLIM. Simulations with **a)** constant degassing, **b)** variable degassing from subduction fluxes, and **c)** variable degassing from zircon proxy. Shaded pink areas represent standard deviation. Purple and red solid lines represent mean tropical SST estimates from Goldberg et al. (2021) and Song et al. (2019), respectively.

that 10.7 to 11.8 Tmol C/yr would be required in order to match the observed mean tropical SST at 480 Ma (i.e., 38-41 °C; Song et al., 2019; Goldberg et al., 2021), which is significantly higher compared to the solid Earth degassing rate set in our previous experiments (averaging to 7.1 Tmol C/yr; see section 2.2). On the other hand, to simulate temperatures cooler than 30 °C at 450 Ma, the solid Earth degassing must be reduced to modern-day values (Fig. 9a).

4. Discussion

The existence of extremely high temperatures in the Late Cambrian-Early Ordovician remains uncertain as interpretations of observed $\delta^{18}O$ data are debated. Two models for the early Paleozoic temperature exist; the "hot" and "cool" models (Scotese et al., 2021). Studies supporting the "cool" model suggest that the long-term trend in seawater $\delta^{18}O$ is due to an enrichment of the heavier oxygen isotope (^{18}O) through geological time and does therefore not reflect change of the water temperature. This model, often referred as the "Veizer hypothesis" (Veizer and Prokoph, 2015), argues that early Paleozoic seawater was enriched in the light oxygen isotope (^{16}O) because of this evolution and that the high temperatures of the early Paleozoic are not accurate (Fig. 10). The main obstacle to this hypothesis is the lack of a primary mechanism that could trigger such a change, but also that other records that do not show the same feature. Those records support the "hot" model, which builds on the fact that the isotopic composition of seawater has remained constant so that the lighter $\delta^{18}O$ values accurately reflect warmer paleo-temperatures during the early Paleozoic (e.g. Henkes et al., 2018; Bergmann et al., 2018) (Fig. 10a,b). Moreover, the peak in SST during this interval followed by a sharp cooling is well in agreement with the Cambrian radiation and mostly the GOBE demonstrating a strong (negative) correlation between biodiversity expansion and temperature (Cocks and Torsvik, 2020).

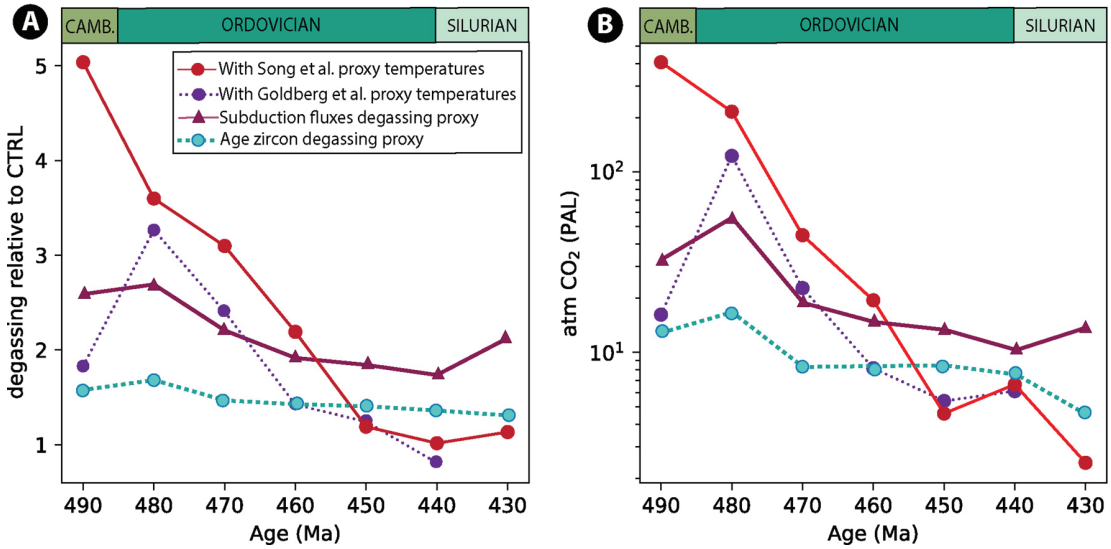

Fig. 9. a) CO_2 degassing rate required by GEOCLIM to match the observed tropical sea-surface temperature (SST) of Goldberg et al. (2021) (purple), Song et al. (2019) (red line) and for comparison degassing from subduction fluxes proxy (pink line) and zircon proxy (turquoise line). **b)** pCO_2 of the corresponding GEOCLIM runs as in **a**.

If the "hot" model is correct, the state of the carbon mass balance during the Early Ordovician must have been largely different from the modern one. Indeed, the SST reconstructed from sedimentary $\delta^{18}O$ records considering the "hot" hypothesis are critically high for the Early Ordovician and difficult to reproduce with a 3D-climate model. Tropical temperatures above 40 °C require very high atmospheric CO_2. Those levels will necessarily depend on the sensitivity of the climate model to atmospheric CO_2 (SI Fig. S5). But regardless of what this sensitivity was in the deep past, which has been estimated to be ~3 °C per CO_2 doubling during ice-free periods (greenhouse climates) and ~6 °C per CO_2 doubling in the presence of land ice (Royer, 2016), or fluctuating from 2 to 5 °C (IPCC working group 1: Solomon et al., 2007), simulating temperatures above 40 °C in the tropical ocean will necessarily require very high levels of CO_2. To generate a very warm tropical ocean, CO_2 levels as high as 300 times the present-day partial pressure are required in our models. By comparison, such levels are close to the post-snowball glaciation levels (Le Hir et al., 2008). We consider such CO_2 levels to be unrealistically high for the early Ordovician, however, they cannot be ruled out, because no reliable CO_2 proxies are extended further in the past than the Late Ordovician.

By targeting the proxy-based temperatures in our model, we have shown that the high CO_2 values prevailing in the early Ordovician would require a release flux of carbon into the ocean-atmosphere system of about 3 to 5 times that of the present-day volcanic outgassing (Fig. 9a). A factor of 3 to 5 decreasing to only 1 over 30 Myrs (Fig. 9a) would require drastic, and perhaps unrealistic, changes in the geodynamic settings since the largest reduction in degassing reconstructed from proxies is by a factor of 2.2 (observed over the past 120 Myrs; Marcilly et al., 2021).

If we consider the proxy record as being biased (such as in the Veizer hypothesis; Fig. 10), then the calculated temperatures become significantly lower for the Ordovician. If our models with both degassing scenarios fit this "cool" model until 470 Ma, the simulated temperatures plot well above the data of Veizer following this time period (Fig. 10b). In order to simulate such temperatures, an even sharper decrease in degassing needs to be invoked, which seems unrealistic considering the tectonic activity of the time period and that the zircon degassing proxy already suggests the lowest estimates among different reconstruction methods.

Reconstructing actual CO_2 outgassing levels of the early Paleozoic is challenging. Considering the tectonic settings of the early Ordovician (490-480 Ma), with the initial rifting of the Rheic Ocean between Gondwana and Avalonia, a high rate of seafloor spreading is plausible. A change in volcanic outgassing has previously been argued to represent the principal driver for Ordovician climate change (McKenzie et al., 2016). However, no full-plate models, nor other methods to assess seafloor spreading (e.g., age-zircon distribution, sea level inversion, subduction zone lengths, continental rift lengths, or combinations of these) have ever suggested such high rates during the Phanerozoic or even the Neoproterozoic (Goddéris and Donnadieu, 2019; Marcilly et al., 2021; Mills et al., 2019).

Adding fluxes from continental rifts (Brune et al., 2017) and explicitly considering the intersection of continental magmatic arcs with carbonate-filled basins (e.g., Lee and Lackey, 2015) could certainly increase solid Earth degassing during the early Ordovician, but an additional release of carbon required to sustain high temperatures may come from other sources than solid Earth degassing. Imbalances in the organic carbon cycle may theoretically release CO_2 into the ocean and atmosphere if the oxidation of reduced sediments exposed on the continents exceeds the burial of organic carbon. The overall increase in the carbonate $\delta^{13}C$ from the base of the Ordovician to the Upper Ordovician sections suggests a progressive predominance of burial versus oxidation (Veizer et al., 1999; Edwards and Saltzman, 2016; Hu et al., 2021) which is compatible with a decreasing carbon release from the Early to the Late Ordovician. However, the amplitude of the decrease needed to explain the Ordovician cooling is extremely large. If we assume that the "missing" Early Ordovician carbon source originates from the organic carbon sub-cycle instead of the outgassing flux, then the early Paleozoic must have been characterized by a very low organic carbon burial rate, or by significant oxidation of reduced sediments on the continents. Simple mass balance calculations show that if this were the case, the $\delta^{13}C$ of seawater would be as low as −20‰ PDB in the Early Ordovician, far below the observed value of about −2‰ PDB. Finally, another process able to release carbon into the ocean-atmosphere system is the oxidative weathering of sedimentary pyrite exposed in the uplifted regions. This process generates sulfuric acid, which dissolves carbonate rocks, releasing carbon in the rivers and ultimately in the ocean (Torres et al., 2014). However, it has been shown that this carbon source is only transitory and cannot drive the long-term evolution of the carbon cycle (Maffre et al., 2020).

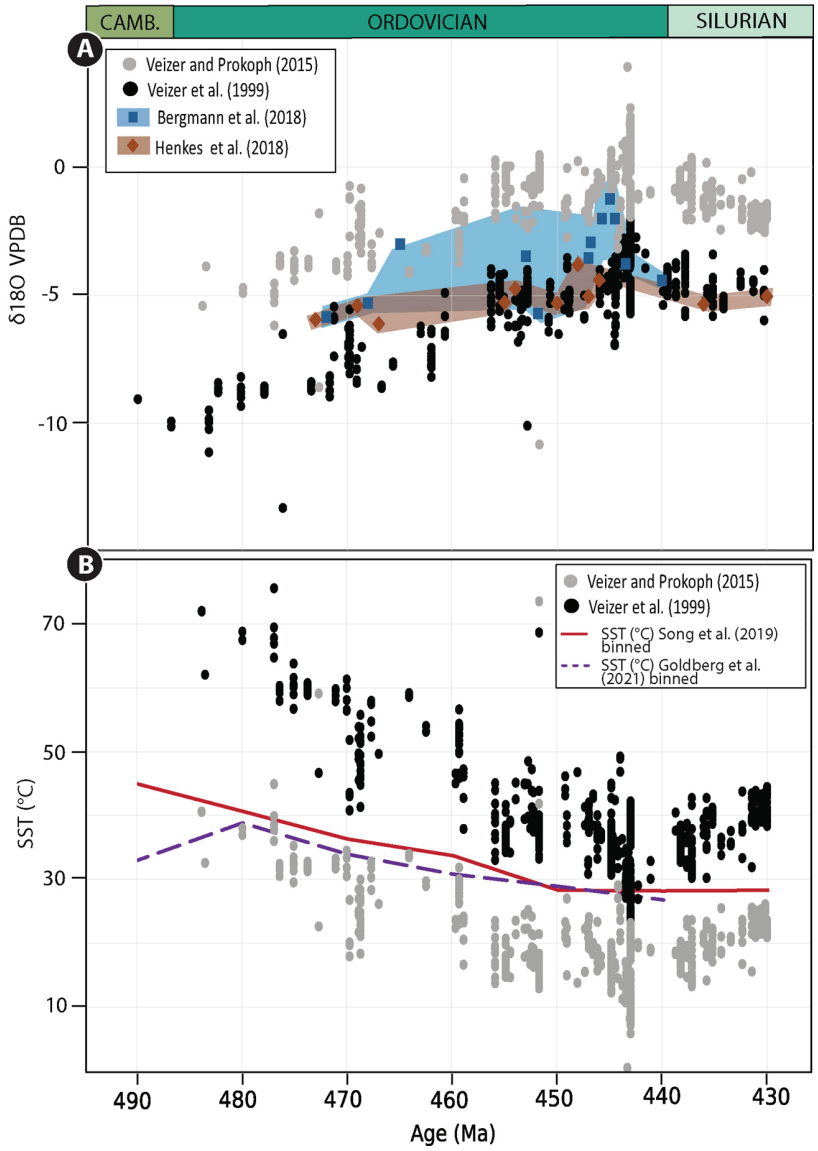

Fig. 10. **(a)** Oxygen isotope data from Veizer et al. (1999) in black. Changes following the secular trend from Veizer and Prokoph (2015) are indicated in grey. The dataset of the "warm" models from Bergmann et al. (2018) and Henkes et al. (2018) are represented with their error margins in shaded corresponding colours.**(b)** Reconstructed paleotemperatures from phosphatic fossils from Song et al. (2019), Bulk-rock $\delta^{18}O$ from Goldberg et al. (2021) and carbonate fossil database of Veizer et al. (1999). The grey data points represent the calculated temperature of the Veizer dataset following changes due to secular trend as suggested by the Veizer hypothesis.

Similar to the high temperatures of the Early Ordovician, our simulations do not replicate the cooling trend reconstructed based on proxy data (Figs. 1 & 8b,c). However, it should be noted that only the mean tropical SST has been considered, while proxy data have been collected at various geographical locations. Accounting for the spread of simulated SSTs at various longitudes within the tropical band reduces the model-data discrepancy (Fig. 8b,c). However, the corresponding $\pm 1\ \sigma$ SST envelope, more representative of common SST conditions found in the simulated climatic states, remains far from capturing the proxy-derived temperatures (Fig. 8b,c). Moreover, when invoking changing degassing, the correlation between our models and the latest temperature reconstructions (i.e., Song et al., 2019; Scotese et al., 2021 & Goldberg et al., 2021) is reasonable with an average Pearson correlation coefficient of 0.85 for both scenarios (Table 1).

Our simulations reveal that the paleogeographical evolution on its own cannot explain observed Ordovician cooling, and if no change in solid Earth degassing is accounted for, the continental drift and masses distribution imposes a warming from 470 Ma onward (Fig. 5b). This is highlighted by the very low Pearson coefficient correlation between the latest temperature reconstructions and our model (0.2; Table 1). This observation differs slightly from the findings of Nardin et al. (2011), even if, globally, both studies show a similar flat trend in temperature (i.e., maximum variation of $\sim 3\,^{\circ}C$). However, these authors used the GEOCLIM model with a fixed degassing, as well as a simpler representation of continental weathering. Their climatic fields were derived from a previous generation of the model, based on a lower spatial resolution (FOAM) of different continental reconstructions (Nardin et al., 2011). Further, the temporal resolution of this study was also lower compared to our study, with one GEOCLIM simulation every 20 Myrs (vs. 10 Myrs). Discrepancies between Nardin et al. (2011) and the results presented here reflect therefore differences in the continental reconstructions, the climate model, and the representation of continental weathering (Park et al., 2020). The major difference between these two GEOCLIM studies is that the model

Table 1
Pearson correlation coefficients for our GEOCLIM simulations with different degassing scenarios compared to two proxy reconstructions of sea surface temperatures Song et al. (2019) and Goldberg et al. (2021).

PEARSON	GEOCLIM no degassing	GEOCLIM zircon degassing	GEOCLIM subduction flux degassing
Song et al. (2019)	0.24	0.89	0.83
Scotese et al. (2021)	0.19	0.84	0.87
Goldberg et al. (2021)	0.17	0.82	0.86
Average	0.20	0.85	0.85

of Nardin et al. (2011) is able to create a cooler climate by the end of the Ordovician, whereas the update provided here, benefiting from new constraints on paleogeography, does not support global cooling triggered by changes in land distribution.

Constraining pCO_2 thresholds for the glacial onset during the Ordovician has been the topic of a range of studies, going back to Crowley and Baum (1991). Some of these studies coupled climate models to land-ice models, which effectively simulate ice-sheet nucleation (Herrmann et al., 2004; Lowry et al., 2014; Pohl et al., 2016). Due to differences in the models and boundary conditions, values reported by these studies are widespread (1120 ppm to 3360 ppm; Herrmann et al., 2004; Lowry et al., 2014; Pohl et al., 2016). Pohl et al. (2016) used a similar climate modelling setup as our study (LMDz6 forced with FOAM-derived SSTs, see Supplementary Information), so these results might be the most comparable. The simulations presented here yield CO_2 levels below the 3360 ppm threshold as suggested by Pohl et al. (2016) by 440 Ma, at the end of a 40-Myr cooling (Fig. 5a). Therefore, we demonstrate that CO_2 levels for the Ordovician are compatible with the onset of a glaciation such as the short-lived Hirnantian glaciation (445-444 Ma), even though the intense global cooling as shown by proxies cannot be replicated. For comparison, other carbon cycle models, such as GEOCARBSULFvolc, estimate CO_2 levels almost similar to the simulations presented here when applying the same degassing parametrization (variable age-zircon distribution degassing; Marcilly et al., 2021). This study estimated theoretical glacial inception levels at 1035 ppm and 2142 ppm, based on climate sensitivities of 6 °C and 3 °C. Assuming an even lower climatic sensitivity (2 °C) yields a threshold as high as 4434 ppm (Fig. 5a).

Model-data disagreement in our simulations may come, at least in part, from the limitations of our models. Regarding the climatic component, results are necessarily model-dependent. More particularly, the double intertropical convergence zone, which represents a very general bias of ocean-atmosphere general circulation models, and is amplified in our simulations by the continental configuration featuring vast ocean basins at low latitudes, reduces precipitation rates over tropical emerged lands (Figs. 2, 3). This bias alters the climate-weathering relationship. In addition, due to the large number of simulations required to force the carbon cycle component, we did not run the ocean-atmosphere version of our CMIP6-class model. Instead, the atmospheric component (LMDz6) was forced with SSTs derived from an ocean-atmosphere model of a previous generation run under identical boundary conditions (FOAM see Supplementary Information). Such setup, used in previous work (Ladant et al., 2014; Licht et al., 2014; Pohl et al., 2016), may also lead to bias in our results, although this impact remains difficult to quantify. Importantly, we emphasize that uncertainty in the model climatic sensitivity would only alter the simulated pCO_2 and not affect simulated temperatures, which constitute our focus. Another source of uncertainty could come from the computation of weathering rates. The recent developments embedded in the version of GEOCLIM used here (Park et al., 2020) largely rely on continental topography, which is used to derive local slope and physical erosion rates (see Supplementary Information). Therefore, uncertainties in topography on land, inherent in every deep-time study due to the lack of robust and widespread proxies for paleoelevation, constitute a limitation in our work.

The inability of our climate-carbon cycle model to simulate the long-term Ordovician cooling trend may also reflect missing mechanisms. In particular, including the impact of land plant colonization on weathering could help reconcile models and proxies (Porada et al., 2016; Lenton et al., 2012). However, the impact of non-vascular land plants on weathering is debated (Edwards et al., 2015; Porada et al., 2016). In addition, recent studies pinpoint the impact of the colonization scenario on weathering rates (Maffre et al., 2022), and this colonization remains poorly documented in the Ordovician. Consequently, the impact of non-vascular plants on Ordovician climate evolution remains elusive.

Another possible mechanism to explain the intensification of climate change during the Ordovician could reside in the weathering of obducted volcanic arcs as recently demonstrated by Conwell et al. (2022). Indeed, this study argues, using $^{87}Sr/^{86}Sr$ seawater records, that a shift in the weathering source lithology is synchronous with the Ordovician cooling, and this can be linked to enhanced weathering of uplifted mafic oceanic crust associated with the Taconic orogeny. This hypothesis has also been suggested by several authors (i.e., Swanson-Hysell and Macdonald, 2017); Macdonald et al., 2019). Macdonald et al. (2019) placed Laurentia about 10° more northward between 480 and 444 Ma (Fig. 11a) compared with our reconstructions (see SI Fig S6), motivated by exhuming mafic and ultramafic lithologies during arc-continent collisions within the warm and wet tropical latitudes (±10°). Swanson-Hysell and Macdonald (2017) argued that a Taconic-related increase in silicate weatherability contributed to long-term Ordovician cooling, but this was not quantified in their study. One way of estimating changes in silicate weatherability is to examine the amount of exposed land where chemical weathering is assumed to be the most intense. Exposed land within ± 10° was steadily increasing during the Ordovician (SI Table S1), peaking at around 450 Ma with ∼22 × 10^6 km^2 or ∼24% of total land exposed between 10°S and 10°N. In the Late Ordovician, we estimate about 3000 km globally of ophiolite-bearing sutures in our paleogeographic model or ∼5500 km in the Swanson-Hysell and Macdonald (2017) model. These estimates are based on Macdonald et al. (2019) but here revised since no Ordovician ophiolites are known in Greenland and all Ordovician ophiolites in Baltica (Fig. 11a) were obducted in the Silurian (e.g., Andersen and Andresen, 1994; Jakob et al., 2022). Fig. 1 in Macdonald et al. (2019) at 445 Ma, therefore, requires a major revision in suture lengths. In order to compare suture lengths with exposed land we (generously) assume an obduction width of 100 km, and as a simple theoretical exercise we multiply the resulting area by a factor of 10 to account for potentially higher weatherability of mafic/ultramafic rocks and elevated topography (Dessert et al., 2003; West et al., 2005). Note, however, that hydrothermal basaltic alteration and ultramafic serpentinization would have lowered their weathering efficiency compared to direct weathering of juvenile volcanics. This exercise shows that the potentially added weathering effect of obducted rocks in the tropics (compared to the amount of exposed land, mostly 'granitic') amounts to 27% at most, and as low as 3% considering the Scotese (2016) reconstructions (Fig. 11).

Adding the potential effect of obduction and increased weathering using the GEOCARBSULF model (e.g., increasing the f_{Aw}/f_A parameter, i.e. "fraction of land area undergoing chemical weath-

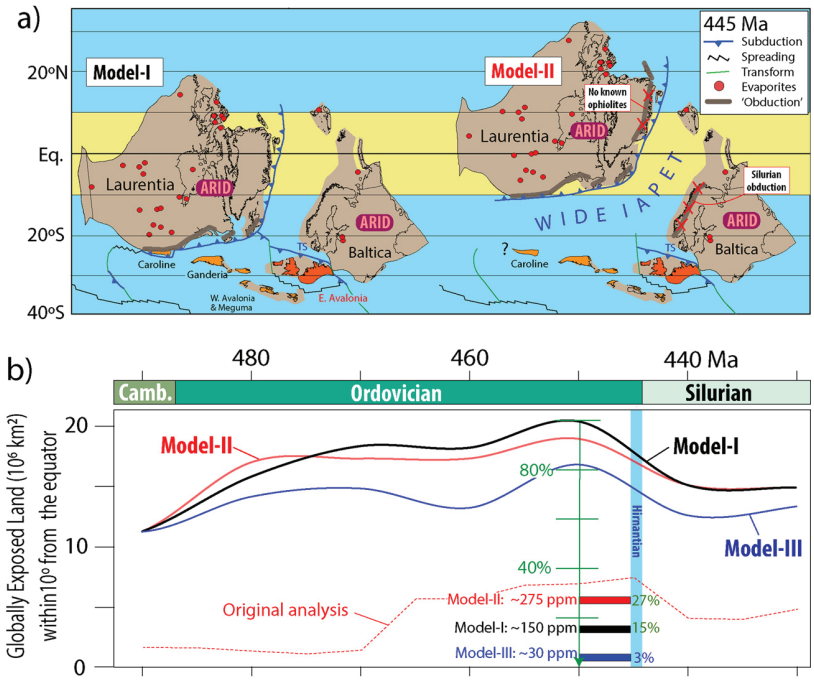

Fig. 11. a) Late Ordovician reconstruction of the Iapetus bordering continents. We place the southern margin of Laurentia at ~20°S (Model-I, Torsvik et al., 2012) whilst Swanson-Hysell and Macdonald (2017; *see* their figure DR1 at 445 Ma) place Laurentia ~10° more northward (Model-II, *see* supplementary section G). Thick dark brown lines in Model-II reconstruction were named 'ophiolite-bearing sutures' in Macdonald et al. (2019; *see* their Fig. 1 at 445 Ma) but there are no known ophiolites in Greenland and ophiolites in western Baltica were all obducted in the Silurian. This has been accounted for in Model-I reconstruction where no ophiolites in the Iapetus realm were obducted within 10° from the equator (yellow band). Globally, reconstruction in Swanson-Hysell and Macdonald (2017) and Macdonald et al. (2019) are identical to those of Torsvik & Cocks (2016), except for locating Laurentia 10° more northward during the Ordovician (Supplementary Fig. G). This result in a much wider Iapetus Ocean at 445 Ma, the Caroline Terrane has yet not collided with Laurentia and the Model-II requires fast latitudinal plate velocities (18 cm yr^{-1}) to close the Iapetus at around 430 Ma. **(b)** Exposed land globally within 10° from the equator based on our Model I, Model-II (as Model-I except modified Laurentia) and Scotese (2016; Model III). All models are based on exposed land mapped out in 10 Myrs intervals in Marcilly et al. (2021) and peaks in exposed land in all models occur at 450 Ma. Swanson-Hysell and Macdonald (2017) argued for a peak in obducted arc *lengths* in the Late Ordovician but did not attempt to quantify the effect in terms of atmospheric CO_2 drawdown. As a simple back-of-the-envelope calculation, we estimate the effect of increased weathering by considering an obduction width of 100 km, which have been multiplied by 10 in order to account for a higher theoretical weathering efficiency (mafic versus felsic rocks) and elevated topography. Compared with the total exposed land (10°S-10°N) the added weathering potential can be (generously) estimated to 27% (Model-I), 15% (Model-II) and 3% (Model II). In terms of CO_2 drawdown that amounts to 275 ppm (Model-I), 150 ppm (Model-II) and 30 ppm (Model-III) in the GEOCARBsulf model. The red stippled line is based on the original estimates in Macdonald et al. (2019).

ering") results in a theoretical CO_2 reduction of 150 ppm in our preferred paleogeographic model (Fig. 11b). This exercise however, assumes that the climate gradients during the Ordovician were similar to modern times, but the occurrences of evaporites in Laurentia at low latitudes suggest a dry climate, rather than warm and wet tropics (e.g., Boucot et al., 2013; Torsvik & Cocks 2016; Torsvik et al., 2021).

When integrating island arcs and increased topography linked to obducted arcs as suggested by Macdonald et al. (2019) (Fig. 6, SI Fig. S6 and SI Fig. S7), our simulations did not yield any large effect linked to topography. Moreover, considering the trend in cooling enhancement seen in the simulations with a shift from low to moderate topography, only a considerable change towards very high relief can trigger large fluctuations.

5. Conclusion

By using a spatially resolved climate-carbon cycle Earth system model fed with updated continental reconstructions and new estimates of volcanic degassing, we show that the Early Ordovician high temperatures can be modelled within error margins of the proxy data. However, our new constraints cannot explain the intense cooling over the Mid to Late Ordovician even if revealing a progressive enhancement in Earth's surface weatherability. The calculated, theoretical degassing scenario necessary to reproduce the proxy-derived Ordovician long-term cooling trend features degassing rates reaching 3 to 5 times that of the current value, which is not supported by geodynamical models nor geological proxies. Therefore, we interpret the inability of our up-to-date climate-carbon cycle model to reproduce Ordovician cooling as the existence of a missing parameter or a faulty influence of a present one. Accepting the veracity of the high Early Ordovician temperatures, alternative sources but also sinks of carbon must be considered. The contribution of the organic carbon sub-cycle and oxidative weathering of pyrite is currently not supported by proxy data. The impact of the colonization of land surfaces by non-vascular plants may help bring models and data into a closer agreement, but the overall impact of vegetation on climate remains difficult to quantify. Our simulations with increased topography did not intensify the Ordovician cooling, but note that the model used here holds large limitations considering the integration of relief and slopes. A more detailed analysis on this subject is necessary to draw any firm conclusions.

CRediT authorship contribution statement

Chloé M. Marcilly: Conceptualization, Data curation, Formal analysis, Investigation, Methodology, Software, Visualization, Writing – original draft. **Pierre Maffre:** Conceptualization, Data curation, Formal analysis, Investigation, Methodology, Resources, Software, Visualization, Writing – review & editing. **Guillaume Le Hir:** Conceptualization, Formal analysis, Investigation, Resources, Visualization, Writing – review & editing. **Alexandre Pohl:** Conceptualization, Data curation, Formal analysis, Investigation, Method-

ology, Resources, Software, Writing – review & editing. **Frédéric Fluteau:** Conceptualization, Data curation, Formal analysis, Investigation, Methodology, Resources, Software, Visualization, Writing – review & editing. **Yves Goddéris:** Conceptualization, Data curation, Formal analysis, Investigation, Resources, Software, Supervision, Writing – review & editing. **Yannick Donnadieu:** Conceptualization, Data curation, Formal analysis, Investigation, Resources, Software, Writing – review & editing. **Thea H. Heimdal:** Supervision, Writing – review & editing. **Trond H. Torsvik:** Methodology, Resources, Supervision, Writing – review & editing.

Declaration of competing interest

The authors declare that they have no known competing financial interests or personal relationships that could have appeared to influence the work reported in this paper.

Acknowledgements

Calculations were performed using HPC resources from DNUM CCUB (Centre de Calcul de l'Université de Bourgogne). This work was granted access to the HPC resources of TGCC under the allocations 2019-A0070107601 and 2020-A0090107601 made by GENCI. This project has received funding from the European Union's Horizon 2020 research and innovation program under the Marie Sklodowska-Curie grant agreement No. 838373, and the Research Council of Norway (RCN), through its Centres of The Excellence funding scheme, project number 223272 (CEED). This is a contribution to UNESCO project IGCP 735 "Rocks and the Rise of Ordovician Life" (Rocks n' ROL).

Appendix A. Supplementary material

Supplementary material related to this article can be found online at https://doi.org/10.1016/j.epsl.2022.117717.

References

Andersen, T.B., Andresen, A., 1994. Stratigraphy, tectonostratigraphy and the accretion of outboard terranes in the Caledonides of Sunnhordland, W. Norway. Tectonophysics 231, 71–84.

Bergmann, K.D., Finnegan, S., Creel, R., Eiler, J.M., Hughes, N.C., Popov, L.E., Fischer, W.W., 2018. A paired apatite and calcite clumped isotope thermometry approach to estimating Cambro-Ordovician seawater temperatures and isotopic composition. Geochim. Cosmochim. Acta 224, 18–41. https://doi.org/10.1016/j.gca.2017.11.015.

Berner, R.A., 2004. The Phanerozoic carbon cycle: CO_2 and O_2. Oxford University Press on Demand.

Berner, R.A., 2006. GEOCARBSULF: a combined model for Phanerozoic atmospheric O2 and CO2. Geochim. Cosmochim. Acta 70 (23), 5653–5664. https://doi.org/10.1016/j.gca.2005.11.032.

Blakey, R.C., 2009. Gondwana paleogeography from assembly to break-up—a 500 my odyssey. Spec. Pap., Geol. Soc. Am. 441, 1–28.

Boucot, A.J., Xu, C., Scotese, C.R., 2013. Phanerozoic paleoclimate: an atlas of lithologic indicators of climate. In: SEPM Concepts in Sedimentology and Paleontology, p. 11.

Brune, S., Williams, S.E., Müller, R.D., 2017. Potential links between continental rifting, CO2 degassing and climate change through time. Nat. Geosci. 10, 941–946. https://doi.org/10.1038/s41561-017-0003-6.

Cocks, L.R.M., Torsvik, T.H., 2020. Ordovician palaeogeography and climate change. Gondwana Res. 100, 53–72. https://doi.org/10.1016/j.gr.2020.09.008.

Conwell, C.T., Saltzman, M.R., Edwards, C.T., Griffith, E.M., Adiatma, Y.D., 2022. Nd isotopic evidence for enhanced mafic weathering leading to Ordovician cooling. Geology.

Crowley, T.J., Baum, S.K., 1991. Toward reconciliation of Late Ordovician (440 Ma) glaciation with very high CO_2 levels. J. Geophys. Res., Atmos. 96, 22597–22610. https://doi.org/10.1029/91JD02449.

Defliese, W.F., 2020. The impact of Snowball Earth glaciation on ocean water δ18O values. Earth Planet. Sci. Lett. 554, 116661. https://doi.org/10.1016/j.epsl.2020.116661.

Dessert, C., Dupré, B., Gaillardet, J., François, L.M., Allegre, C.J., 2003. Basalt weathering laws and the impact of basalt weathering on the global carbon cycle. Chem. Geol. 202 (3–4), 257–273.

Deutsch, C., Ferrel, A., Seibel, B., Pörtner, H.O., Huey, R.B., 2015. Climate change tightens a metabolic constraint on marine habitats. Science 348 (6239), 1132–1135. https://doi.org/10.1126/science.aaa1605.

Donnadieu, Y., Goddéris, Y., Pierrehumbert, R., Dromart, G., Fluteau, F., Jacob, R., 2006. A GEOCLIM simulation of climatic and biogeochemical consequences of Pangea breakup. Geochem. Geophys. Geosyst. 7 (11), Q11019. http://doi.wiley.com/10.1029/2006GC001278.

Domeier, M., Torsvik, T.H., 2014. Focus review paper: plate kinematics of the Late Paleozoic. Geosci. Front. 5, 303–350. https://doi.org/10.1016/j.gsf.2014.01.002.

Domeier, M., Magni, V., Hounslow, M.W., Torsvik, T.H., 2018. Episodic zircon age spectra mimic fluctuations in subduction. Sci. Rep. 8, 1747. https://doi.org/10.1038/s41598-018-35040-z.

Edwards, D., Cherns, L., Raven, J.A., 2015. Could land-based early photosynthesizing ecosystems have bioengineered the planet in mid-Palaeozoic times? Palaeontology 58, 803–837. https://doi.org/10.1111/pala.12187.

Edwards, C.T., Saltzman, M.R., 2016. Paired carbon isotopic analysis of Ordovician bulk carbonate (δ13Ccarb) and organic matter (δ13Corg) spanning the Great Ordovician Biodiversification Event. Palaeogeogr. Palaeoclimatol. Palaeoecol. 458, 102–117. https://doi.org/10.1016/j.palaeo.2015.08.005.

Edwards, C.T., Saltzman, M.R., Royer, D.L., Fike, D.A., 2017. Oxygenation as a driver of the Great Ordovician Biodiversification Event. Nat. Geosci. 10, 925–929. https://doi.org/10.1038/s41561-017-0006-3.

Edwards, C.T., Jones, C.M., Quinton, P.C., Fike, D.A., Sciences, P., Louis, S., 2021. Oxygen isotope (18 O) trends measured from Ordovician conodont apatite using secondary ion mass spectrometry (SIMS): implications for paleo-thermometry studies. GSA Bull. 1, 1–14. https://doi.org/10.1130/B35891.1/5294555/b35891.pdf.

Finnegan, S., Bergmann, K., Eiler, J.M., Jones, D.S., Fike, D.A., Eisen- man, I., Hughes, N.C., Tripati, A.K., Fischer, W.W., 2011. The magnitude and duration of late Ordovician-early Silurian glaciation. Science 331 (6019), 903–906. https://doi.org/10.1126/science.1200803.

Gaillardet, J., Dupré, B., Louvat, P., Allegre, C.J., 1999. Global silicate weathering and CO2 consumption rates deduced from the chemistry of large rivers. Chem. Geol. 159 (1–4), 3–30. https://doi.org/10.1016/S0009-2541(99)00031-5.

Galili, N., Shemesh, A., Yam, R., Brailovsky, I., Sela-Adler, M., Schuster, E.M., Halevy, I., 2019. The geologic history of seawater oxygen isotopes from marine iron oxides. Science 365 (6452), 469–473. https://doi.org/10.1126/science.aaw9247.

Gerlach, T., 2011. Volcanic versus anthropogenic carbon dioxide. Eos Trans. AGU 92 (24), 201–202. https://doi.org/10.1029/2011EO240001.

Ghienne, J.F., Desrochers, A., Vandenbroucke, T., et al., 2014. A Cenozoic-style scenario for the end-Ordovician glaciation. Nat. Commun. 5, 4485. https://doi.org/10.1038/ncomms5485.

Goddéris, Y., Donnadieu, Y., 2019. A sink-or a source-driven carbon cycle at the geological timescale? Relative importance of palaeogeography versus solid Earth degassing rate in the Phanerozoic climatic evolution. Geol. Mag. 156 (2), 355–365. https://doi.org/10.1017/S0016756817001054.

Goldberg, S.L., Present, T.M., Finnegan, S., Bergmann, K.D., 2021. A high-resolution record of early Paleozoic climate. Proc. Natl. Acad. Sci. 118 (6), e2013083118. https://doi.org/10.1073/pnas.2013083118.

Gough, D.O., 1981. Solar interior structure and luminosity variations. Sol. Phys. 74 (13), 21–34. https://doi.org/10.1007/BF00151270.

Hearing, T.W., Harvey, T.H.P., Williams, M., Leng, M.J., Lamb, A.L., Wilby, P.R., Gabbott, S.E., Pohl, A., Donnadieu, Y., 2018. An early Cambrian greenhouse climate. Sci. Adv. 4 (5), eaar5690. https://doi.org/10.1126/sciadv.aar5690.

Henkes, G.A., Passey, B.H., Grossman, E.L., Shenton, B.J., Yancey, T.E., Pérez-Huerta, A., 2018. Temperature evolution and the oxygen isotope composition of Phanerozoic oceans from carbonate clumped isotope thermometry. Earth Planet. Sci. Lett. 490, 40–50. https://doi.org/10.1016/j.epsl.2018.02.001.

Herrmann, A.D., Patzkowsky, M.E., Pollard, D., 2004. The impact of paleogeography, pCO_2, poleward ocean heat transport and sea level change on global cooling during the Late Ordovician. Palaeogeogr. Palaeoclimatol. Palaeoecol. 206 (1), 59–74. https://doi.org/10.1016/j.palaeo.2003.12.019.

Hodel, F., Macouin, M., Trindade, R.I.F., Triantafyllou, A., Ganne, J., Chavagnac, V., Agrinier, P., 2018. Fossil black smoker yields oxygen isotopic composition of Neoproterozoic seawater. Nat. Commun. 9 (1), 1–7. https://doi.org/10.1038/s41467-018-03890-w.

Hu, D., Zhang, X., Li, M., Xu, Y., Shen, Y., 2021. Carbon isotope (δ13Ccarb) stratigraphy of the Lower-Upper Ordovician of the Yangtze Platform, South China: Implications for global correlation and the Great Ordovician Biodiversification Event (GOBE). Glob. Planet. Change, 103546. https://doi.org/10.1016/j.gloplacha.2021.103546.

Jakob, J., Andersen, T.B., Mohn, G., Kjøll, H.J., Beyssac, O., 2022. A revised tectonostratigraphic scheme for the Scandinavian Caledonides and its implications for our understanding of the Scandian orogeny. Spec. Pap., Geol. Soc. Am. In New Developments in the Appalachian-Caledonian-Variscan Orogen.

Jones, L.A., Eichenseer, K., 2021. Uneven spatial sampling distorts reconstructions of Phanerozoic seawater temperature. Geology. https://doi.org/10.1130/G49132.1.

Kelemen, P.B., Manning, C.E., 2015. Reevaluating carbon fluxes in subduction zones, what goes down, mostly comes up. Proc. Natl. Acad. Sci. 112 (30), E3997–E4006.

Kump, L.R., Arthur, M.A., Patzkowsky, M.E., Gibbs, M.T., Pinkus, D.S., Sheehan, P.M., 1999. A weathering hypothesis for glaciation at high atmospheric pCO2 during the Late Ordovician. Palaeogeogr. Palaeoclimatol. Palaeoecol. 152 (1–2), 173–187.

Ladant, J.B., Donnadieu, Y., Lefebvre, V., Dumas, C., 2014. The respective role of atmospheric carbon dioxide and orbital parameters on ice sheet evolution at the Eocene-Oligocene transition. Paleoceanography 29, 810–823. https://doi.org/10.1002/2013PA002593.

Le Hir, G., Donnadieu, Y., Goddéris, Y., Pierrehumbert, R.T., Halverson, G.P., Macouin, M., Ramstein, G., 2008. The snowball Earth aftermath: exploring the limits of continental weathering processes. Earth Planet. Sci. Lett. 277 (3–4), 453–463. https://doi.org/10.1016/j.epsl.2008.11.010.

Lécuyer, C., Amiot, R., Touzeau, A., Trotter, J., 2013. Calibration of the phosphate δ18O thermometer with carbonate-water oxygen isotope fractionation equations. Chem. Geol. 347, 217–226. https://doi.org/10.1016/j.chemgeo.2013.03.008.

Lee, C.T.A., Lackey, J.S., 2015. Global continental arc flare-ups and their relation to long-term greenhouse conditions. Elements 11 (2), 125–130. https://doi.org/10.2113/gselements.11.2.125.

Lenton, T., Crouch, M., Johnson, M., et al., 2012. First plants cooled the Ordovician. Nat. Geosci. 5, 86–89. https://doi.org/10.1038/ngeo1390.

Licht, A., van Cappelle, M., Abels, H.A., Ladant, J.B., Trabucho-Alexandre, J., France-Lanord, C., Donnadieu, Y., Vandenberghe, J., Rigaudier, T., Lécuyer, C., Terry, D. Jr, Adriaens, R., Boura, A., Guo, Z., Soe, A.N., Quade, J., Dupont-Nivet, G., Jaeger, J.J., 2014. Asian monsoons in a late Eocene greenhouse world. Nature 513, 501–506. https://doi.org/10.1038/nature13704.

Loi, A., Ghienne, J.-F., Dabard, M.P., Paris, F., Botquelen, A., Christ, N., Elaouad-Debbaj, Z., Gorini, A., Vidal, M., Videt, B., Destombes, J., 2010. The Late Ordovician glacio-eustatic record from a high-latitude storm-dominated shelf succession: The Bou Ingarf section (Anti-Atlas, Southern Morocco). Palaeogeogr. Palaeoclimatol. Palaeoecol. 296, 332–358. https://doi.org/10.1016/j.palaeo.2010.01.018.

Lowry, D.P., Poulsen, C.J., Horton, D.E., Torsvik, T.H., Pollard, D., 2014. Thresholds for Paleozoic ice sheet initiation. Geology 42, 627–630. https://doi.org/10.1130/G35615.1.

Macdonald, F.A., Swanson-Hysell, N.L., Park, Y., Lisiecki, L., Jagoutz, O., 2019. Arc-continent collisions in the tropics set Earth's climate state. Science 364 (6436), 181–184.

Maffre, P., Swanson-Hysell, N.L., Goddéris, Y., 2020. Limited carbon cycle response to increased sulfide weathering due to oxygen feedback. Geophys. Res. Lett. 48 (19), e2021GL094589. https://doi.org/10.1029/2021GL094589.

Maffre, P., Goddéris, Y., Pohl, A., Donnadieu, Y., Carretier, S., Le Hir, G., 2022. The complex response of continental silicate rock weathering to the colonization of the continents by vascular plants in the Devonian. Am. J. Sci. 322 (3), 461–492.

Marcilly, C.M., Torsvik, T.H., Domeier, M., Royer, D.L., 2021. New paleogeographic and degassing parameters for long-term carbon cycle models. Gondwana Res. https://doi.org/10.1016/j.gr.2021.05.016.

Marcilly, C.M., Torsvik, T.H., Conrad, C.P., 2022. Global Phanerozoic sea levels from paleogeographic flooding maps. Gondwana Res.

Merdith, A.S., Williams, S.E., Collins, A.S., Tetley, M.G., Mulder, J.A., Blades, M.L., Müller, R.D., 2021. Extending full-plate tectonic models into deep time: linking the Neoproterozoic and the Phanerozoic. Earth-Sci. Rev. 214, 103477. https://doi.org/10.1016/j.earscirev.2020.103477.

McKenzie, N.R., Horton, B.K., Loomis, S.E., Stockli, D.F., Planavsky, N.J., Lee, C.-T.A., 2016. Continental arc volcanism as the principal driver of icehouse-greenhouse variability. Science 352 (6284), 444–447. https://doi.org/10.1126/science.aad5787.

Mills, B.J., Krause, A.J., Scotese, C.R., Hill, D.J., Shields, G.A., Lenton, T.M., 2019. Modelling the long-term carbon cycle, atmospheric CO2, and Earth surface temperature from late Neoproterozoic to present day. Gondwana Res. 67, 172–186. https://doi.org/10.1016/j.gr.2018.12.001.

Nardin, E., Goddéris, Y., Donnadieu, Y., Le Hir, G., Blakey, R.C., Pucéat, E., Aretz, M., 2011. Modeling the early Paleozoic long-term climatic trend. Bull. Geol. Soc. Am. 123 (5), 1181–1192. https://doi.org/10.1130/B30364.1.

Park, Y., Maffre, P., Goddéris, Y., Macdonald, F.A., Anttila, E.S.C., Swanson-Hysell, N.L., 2020. Emergence of the Southeast Asian islands as a driver for Neogene cooling. Proc. Natl. Acad. Sci. 117 (41), 25319–25326. https://doi.org/10.1073/pnas.2011033117.

Pohl, A., Donnadieu, Y., Le Hir, G., Buoncristiani, J.F., Vennin, E., 2014. Effect of the Ordovician paleogeography on the (in)stability of the climate. Clim. Past 10 (6), 2053–2066. https://doi.org/10.5194/cp-10-2053-2014.

Pohl, A., Donnadieu, Y., Le Hir, G., Ladant, J.B., Dumas, C., Alvarez-Solas, J., Vandenbroucke, T.R.A., 2016. Glacial onset predated Late Ordovician climate cooling. Paleoceanography 31, 800–821. https://doi.org/10.1002/2016PA002928.

Pohl, A., Donnadieu, Y., Le Hir, G., Ferreira, D., 2017. The climatic significance of Late Ordovician-early Silurian black shales. Paleoceanography 32, 397–423. https://doi.org/10.1002/2016PA003064.

Pohl, A., Donnadieu, Y., Godderis, Y., Lanteaume, C., Hairabian, A., Frau, C., Michel, J., Laugié, M., Reijmer, J.J.G., Scotese, C.R., Jean, B., 2020. Carbonate platform production during the Cretaceous. GSA Bull. 132, 2606–2610. https://doi.org/10.1130/B35680.1.

Porada, P., Lenton, T.M., Pohl, A., Weber, B., Mander, L., Donnadieu, Y., Beer, C., Pöschl, U., Kleidon, A., 2016. High potential for weathering and climate effects of non-vascular vegetation in the Late Ordovician. Nat. Commun. 7, 12113. https://doi.org/10.1038/ncomms12113.

Rasmussen, C.M. Ø, Ullmann, C.V., Jakobsen, K.G., Lindskog, A., Hansen, J., Hansen, T., Eriksson, M.E., Dronov, A., Frei, R., Korte, C., Nielsen, A.T., Harper, D.A.T., 2016. Onset of main Phanerozoic marine radiation sparked by emerging Mid Ordovician icehouse. Sci. Rep. 6, 18884. https://doi.org/10.1038/srep18884.

Royer, D.L., 2016. Climate sensitivity in the geologic past. Annu. Rev. Earth Planet. Sci. 44. https://doi.org/10.1146/annurev-earth-100815-024150.

Scotese, C.R., 2016. PALEOMAP PaleoAtlas for GPlates and the PaleoData plotter program. Abstr. Program – Geol. Soc. Am. 48 (5). http://www.scotese.com/newpage1.htm.

Scotese, C.R., Song, H., Mills, B.J., van der Meer, D.G., 2021. Phanerozoic paleotemperatures: the Earth's changing climate during the last 540 million years. Earth-Sci. Rev. 103503. https://doi.org/10.1016/j.earscirev.2021.103503.

Solomon, S., Manning, M., Marquis, M., Qin, D., 2007. Climate change 2007-the physical science basis: Working group I contribution to the fourth assessment report of the IPCC (Vol. 4). Cambridge University Press.

Song, H., Wignall, P.B., Song, H., Dai, X., Chu, D., 2019. Seawater temperature and dissolved oxygen over the past 500 million years. J. Earth Sci. 30 (2), 236–243. https://doi.org/10.1007/s12583-018-1002-2.

Stockey, R., Pohl, A., Ridgwell, A., Finnegan, S., Sperling, E.A., 2021. Decreasing Phanerozoic extinction intensity is a predictable consequence of Earth surface oxygenation and metazoan ecophysiology. Proc. Natl. Acad. Sci. 118, e2101900118. https://doi.org/10.1073/pnas.2101900118.

Swanson-Hysell, N.L., Macdonald, F.A., 2017. Tropical weathering of the Taconic orogeny as a driver for Ordovician cooling. Geology, G38985.1. http://geology.gsapubs.org/lookup/doi/10.1130/G38985.1.

Torres, M.A., West, A.J., Li, G., 2014. Sulphide oxidation and carbonate dissolution as a source of CO 2 over geological timescales. Nature 507 (7492), 346–349. https://doi.org/10.1038/nature13030.

Torsvik, T.H., Van der Voo, R., Preeden, U., Mac Niocaill, C., Steinberger, B., Doubrovine, P.V., Cocks, L.R.M., 2012. Phanerozoic polar wander, palaeogeography and dynamics. Earth-Sci. Rev. 114 (3–4), 325–368. https://doi.org/10.1016/j.earscirev.2012.06.007.

Torsvik, T.H., Svensen, H.H., Steinberger, B., Royer, D.L., Jerram, D.A., Jones, M.T., Domeier, M., 2021. Connecting the deep Earth and the atmosphere. In: Marquardt, H., Ballmer, M., Cottaar, S., Konter, J. (Eds.), Mantle Convection and Surface Expressions. In: Geophysical Monograph, vol. 263. American Geophysical, Union, pp. 413–453.

Trotter, J.A., Williams, I.S., Barnes, C.R., Lécuyer, C., Nicoll, R.S., 2008. Did cooling oceans trigger Ordovician biodiversification? Evidence from conodont thermometry. Science 321 (5888), 550–554. https://doi.org/10.1126/science.1155814.

Veizer, J., Ala, D., Azmy, K., Bruckschen, P., Buhl, D., Bruhn, F., Strauss, H., 1999. 87Sr/86Sr, δ13C and δ18O evolution of Phanerozoic seawater. Chem. Geol. 161 (1–3), 59–88. https://doi.org/10.1016/S0009-2541(99)00081-9.

Veizer, J., Prokoph, A., 2015. Temperatures and oxygen isotopic composition of Phanerozoic oceans. Earth-Sci. Rev. 146, 92–104. https://doi.org/10.1016/j.earscirev.2015.03.008.

Walker, J.C., Hays, P.B., Kasting, J.F., 1981. A negative feedback mechanism for the long-term stabilization of Earth's surface temperature. J. Geophys. Res., Oceans 86 (C10), 9776–9782. https://doi.org/10.1029/JC086iC10p09776.

West, A.J., Galy, A., Bickle, M., 2005. Tectonic and climatic controls on silicate weathering. Earth Planet. Sci. Lett. 235 (1–2), 211–228.

Young, S.A., Saltzman, M.R., Foland, K.A., Linder, J.S., Kump, L.R., 2009. A major drop in seawater 87Sr/86Sr during the Middle Ordovician (Darriwilian): links to volcanism and climate? Geology 37 (10), 951–954.

Appendices

➢ **Appendix 1:** Composite maps of exposed land reconstructions

Composite maps of exposed land reconstructions with identified major continents and oceans through time.

All maps follow the same legend, as displayed below:

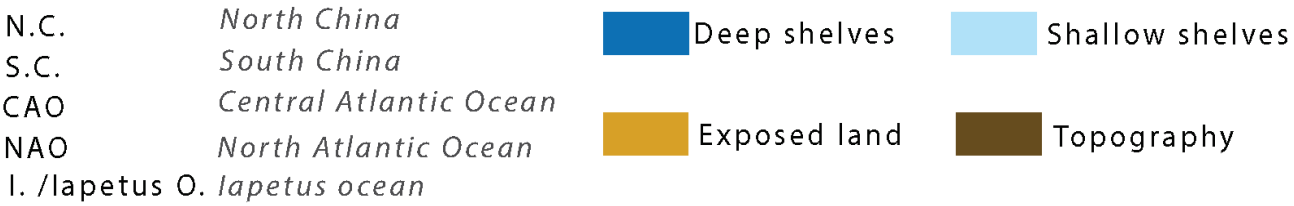

The maps from 60 -10 Ma are based on the model of Heine et al. (2015)* corrected for updated fossil distribution and therefore do not include an assessment of topography.

<u>The maps are separated in 18 plates:</u>

- **Plate 1**: 540-530-520 Ma
- **Plate 2**: 510-500-490 Ma
- **Plate 3:** 480-470-460 Ma
- **Plate 4**: 450-440-430 Ma
- **Plate 5**: 420-410-400 Ma
- **Plate 6**: 390-380-370 Ma
- **Plate 7**: 360-350-340 Ma
- **Plate 8**: 330-320-310 Ma
- **Plate 9**: 300-290-280 Ma
- **Plate 10**: 270-260-250 Ma
- **Plate 11**: 240-230-220 Ma
- **Plate 12**: 210-200-190 Ma
- **Plate 13**: 180-170-160 Ma
- **Plate 14**: 150-140-130 Ma
- **Plate 15**: 120-110-100 Ma
- **Plate 16**: 90-80-70 Ma
- **Plate 17**: 60-50-40 Ma
- **Plate 18**: 30-20-10 Ma

*Heine, C., Yeo, L. G., & Müller, R. D. (2015). Evaluating global paleoshoreline models for the Cretaceous and Cenozoic. *Australian Journal of Earth Sciences*, *62*(3), 275-287.

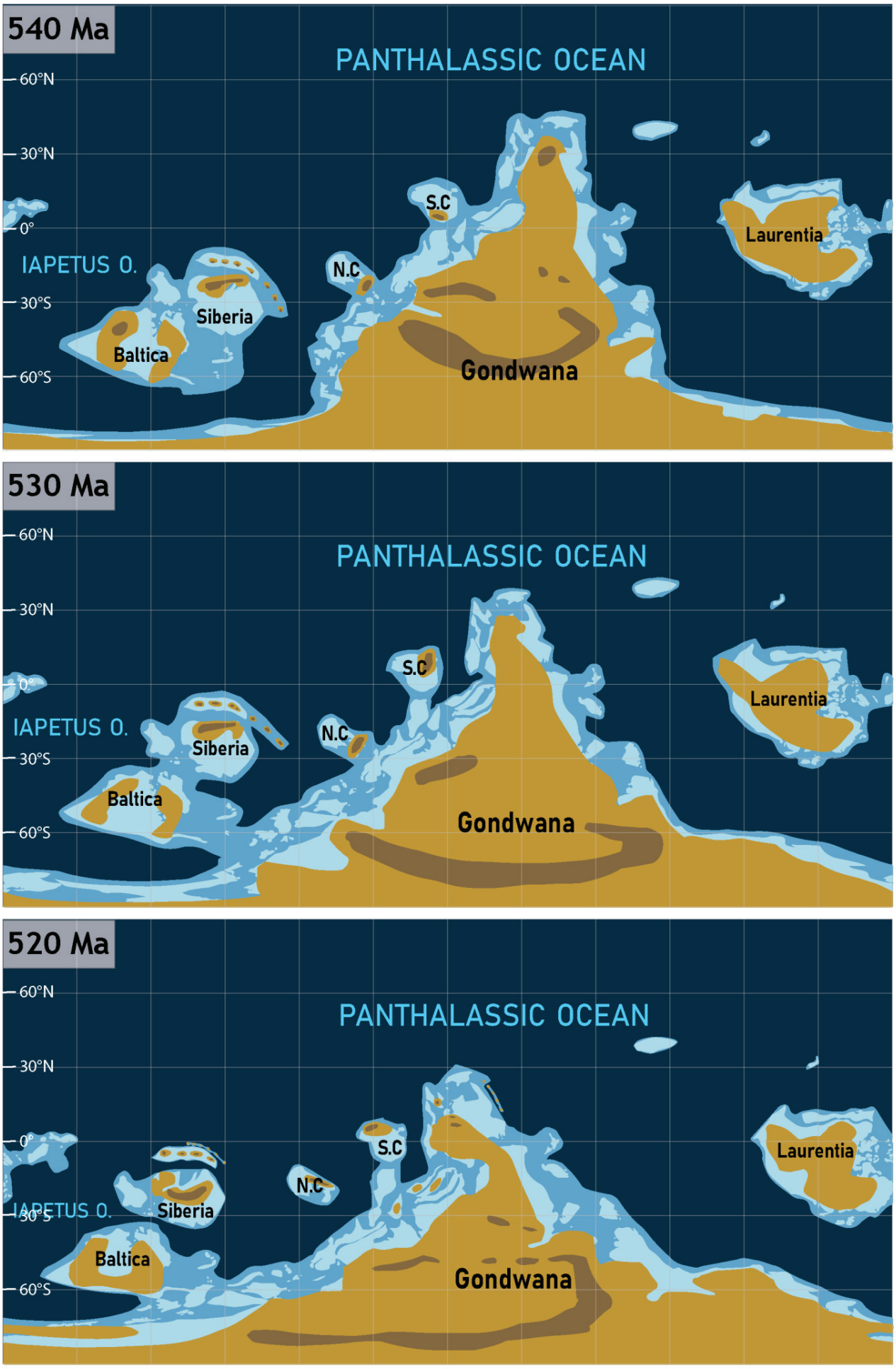
540 Ma
PANTHALASSIC OCEAN
60°N
30°N
0°
30°S
60°S
IAPETUS O.
Siberia
Baltica
N.C
S.C
Laurentia
Gondwana
530 Ma
PANTHALASSIC OCEAN
60°N
30°N
0°
30°S
60°S
IAPETUS O.
Siberia
Baltica
N.C
S.C
Laurentia
Gondwana
520 Ma
PANTHALASSIC OCEAN
60°N
30°N
0°
30°S
60°S
IAPETUS O.
Siberia
Baltica
N.C
S.C
Laurentia
Gondwana

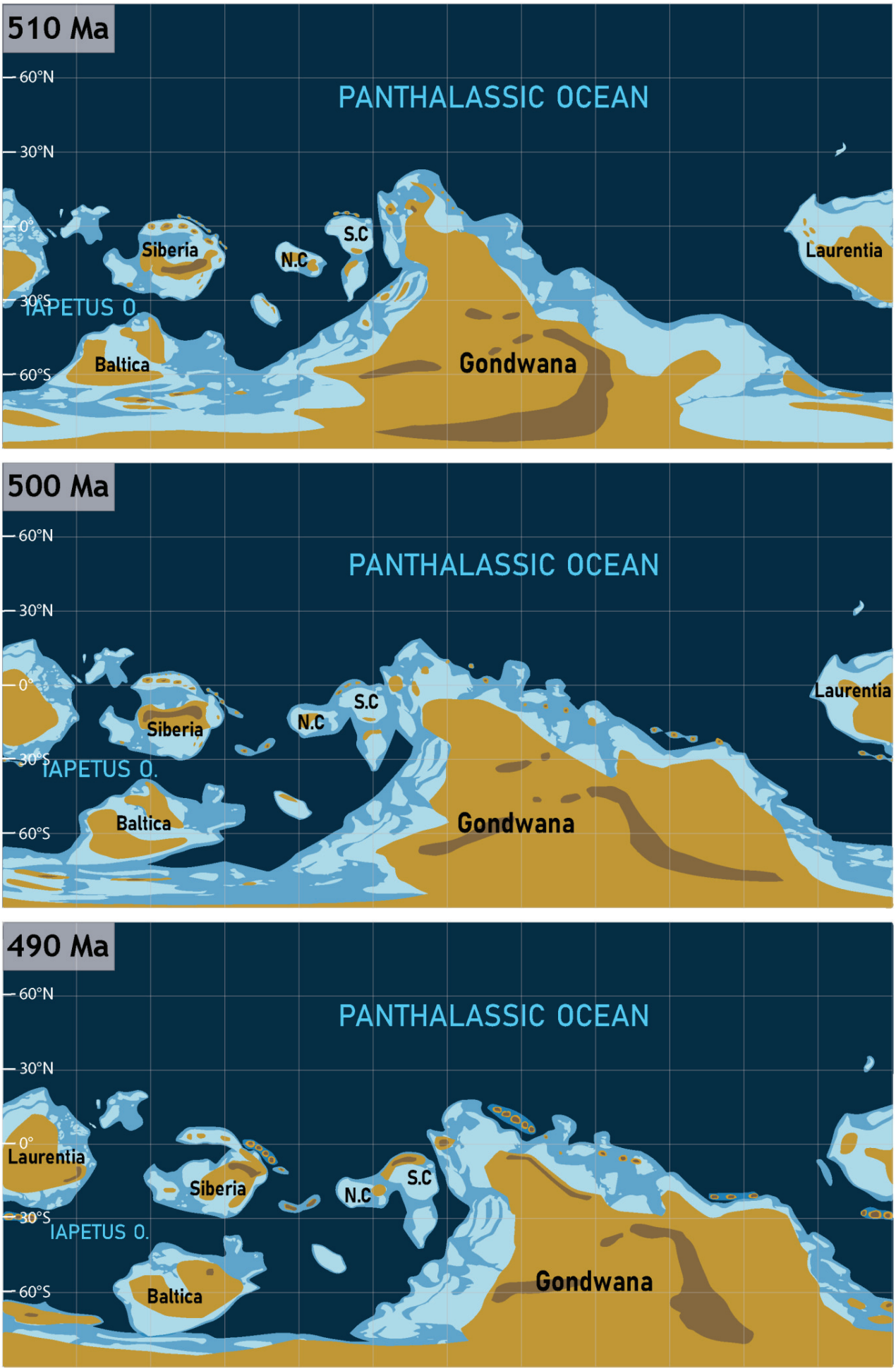
510 Ma
60°N
30°N
0°
30°S
60°S
PANTHALASSIC OCEAN
Siberia
N.C
S.C
Laurentia
IAPETUS O
Baltica
Gondwana
500 Ma
60°N
30°N
0°
30°S
60°S
PANTHALASSIC OCEAN
Laurentia
S.C
N.C
Siberia
IAPETUS O.
Baltica
Gondwana
490 Ma
60°N
30°N
0°
30°S
60°S
PANTHALASSIC OCEAN
Laurentia
Siberia
N.C
S.C
IAPETUS O.
Baltica
Gondwana

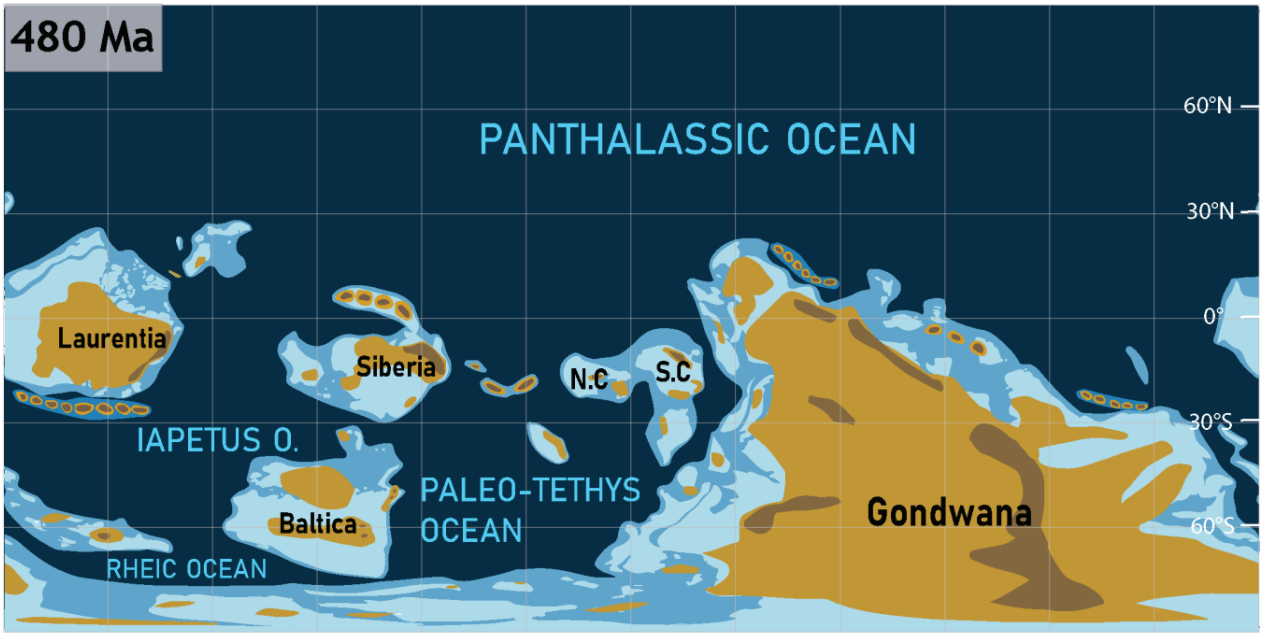
480 Ma
PANTHALASSIC OCEAN
60°N
30°N
0°
30°S
60°S
Laurentia
Siberia
N.C
S.C
IAPETUS O.
PALEO-TETHYS
OCEAN
Baltica
Gondwana
RHEIC OCEAN

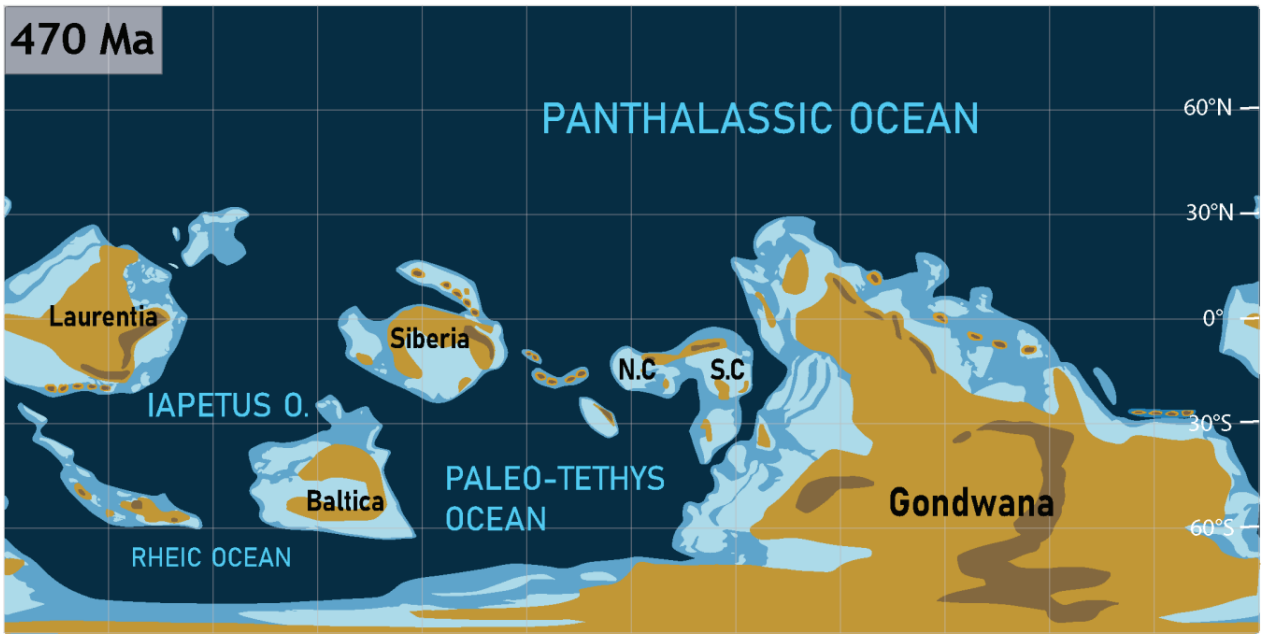
470 Ma
PANTHALASSIC OCEAN
60°N
30°N
0°
30°S
60°S
Laurentia
Siberia
N.C
S.C
IAPETUS O.
PALEO-TETHYS
OCEAN
Baltica
Gondwana
RHEIC OCEAN

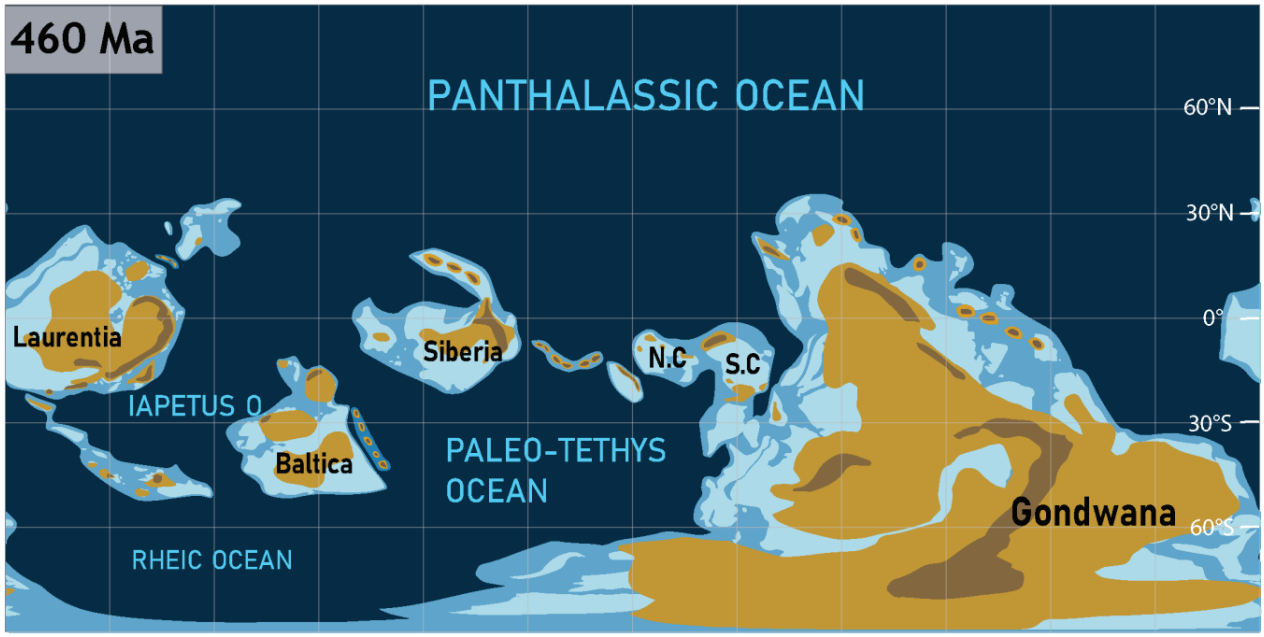
460 Ma
PANTHALASSIC OCEAN
60°N
30°N
0°
30°S
60°S
Laurentia
Siberia
N.C
S.C
IAPETUS O
PALEO-TETHYS
OCEAN
Baltica
Gondwana
RHEIC OCEAN

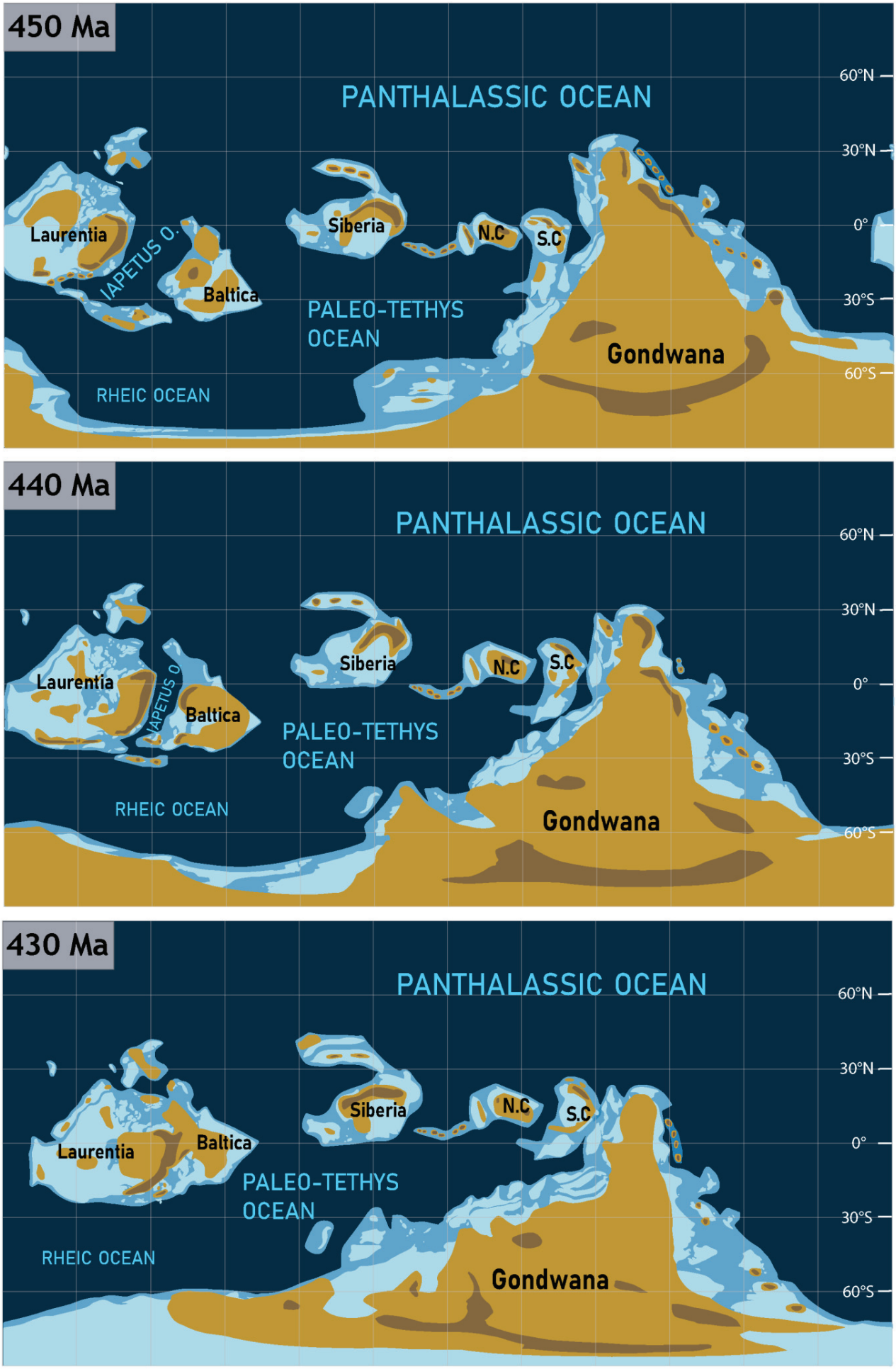
450 Ma
PANTHALASSIC OCEAN
60°N
30°N
0°
30°S
60°S
Laurentia
IAPETUS O.
Baltica
Siberia
N.C
S.C
PALEO-TETHYS
OCEAN
Gondwana
RHEIC OCEAN
440 Ma
PANTHALASSIC OCEAN
60°N
30°N
0°
30°S
60°S
Laurentia
IAPETUS O.
Baltica
Siberia
N.C
S.C
PALEO-TETHYS
OCEAN
RHEIC OCEAN
Gondwana
430 Ma
PANTHALASSIC OCEAN
60°N
30°N
0°
30°S
60°S
Laurentia
Baltica
Siberia
N.C
S.C
PALEO-TETHYS
OCEAN
RHEIC OCEAN
Gondwana

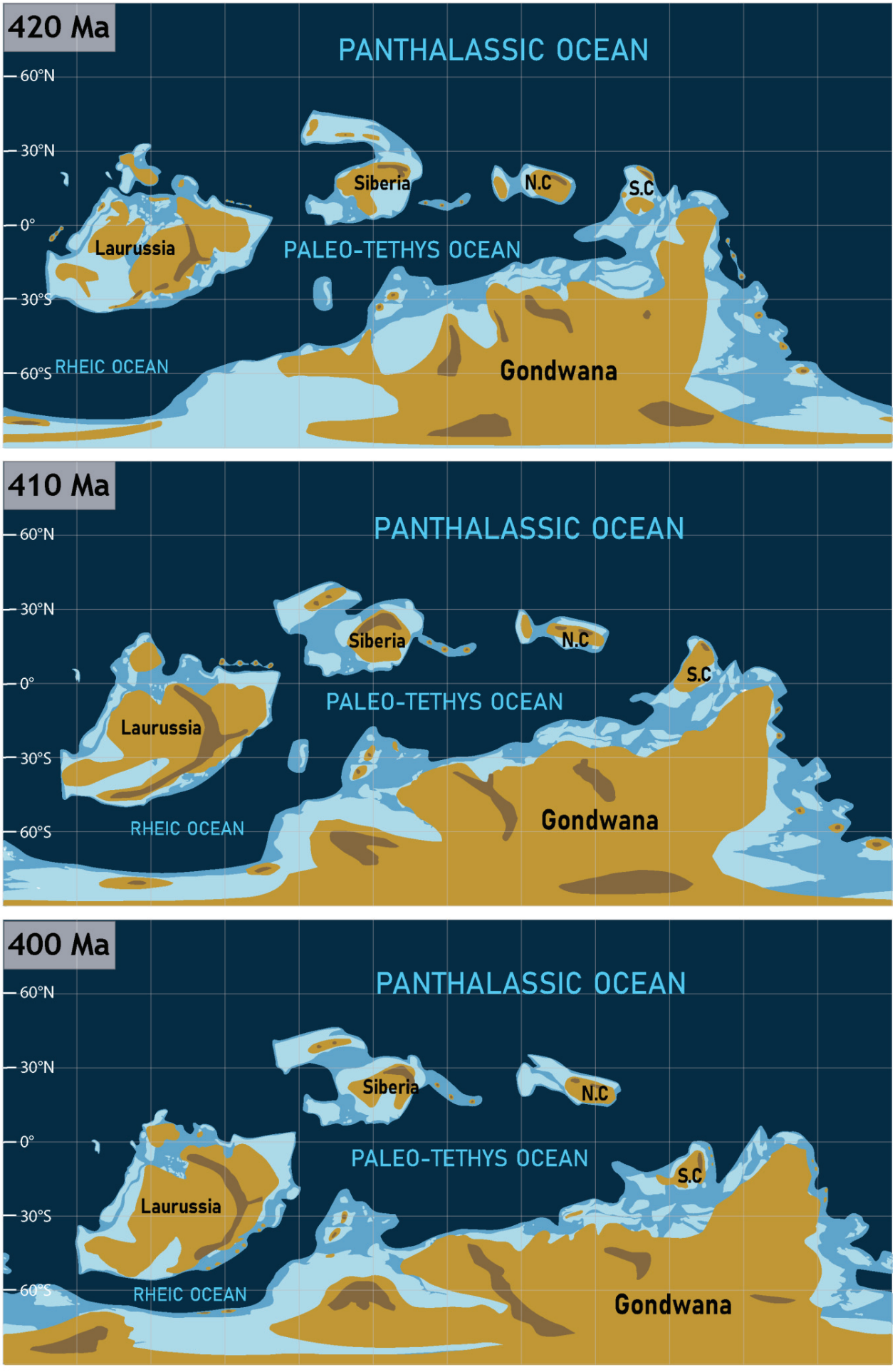
420 Ma
PANTHALASSIC OCEAN
60°N
30°N
0°
30°S
60°S
Siberia
N.C
S.C
Laurussia
PALEO-TETHYS OCEAN
RHEIC OCEAN
Gondwana
410 Ma
PANTHALASSIC OCEAN
60°N
30°N
0°
30°S
60°S
Siberia
N.C
S.C
Laurussia
PALEO-TETHYS OCEAN
RHEIC OCEAN
Gondwana
400 Ma
PANTHALASSIC OCEAN
60°N
30°N
0°
30°S
60°S
Siberia
N.C
S.C
Laurussia
PALEO-TETHYS OCEAN
RHEIC OCEAN
Gondwana

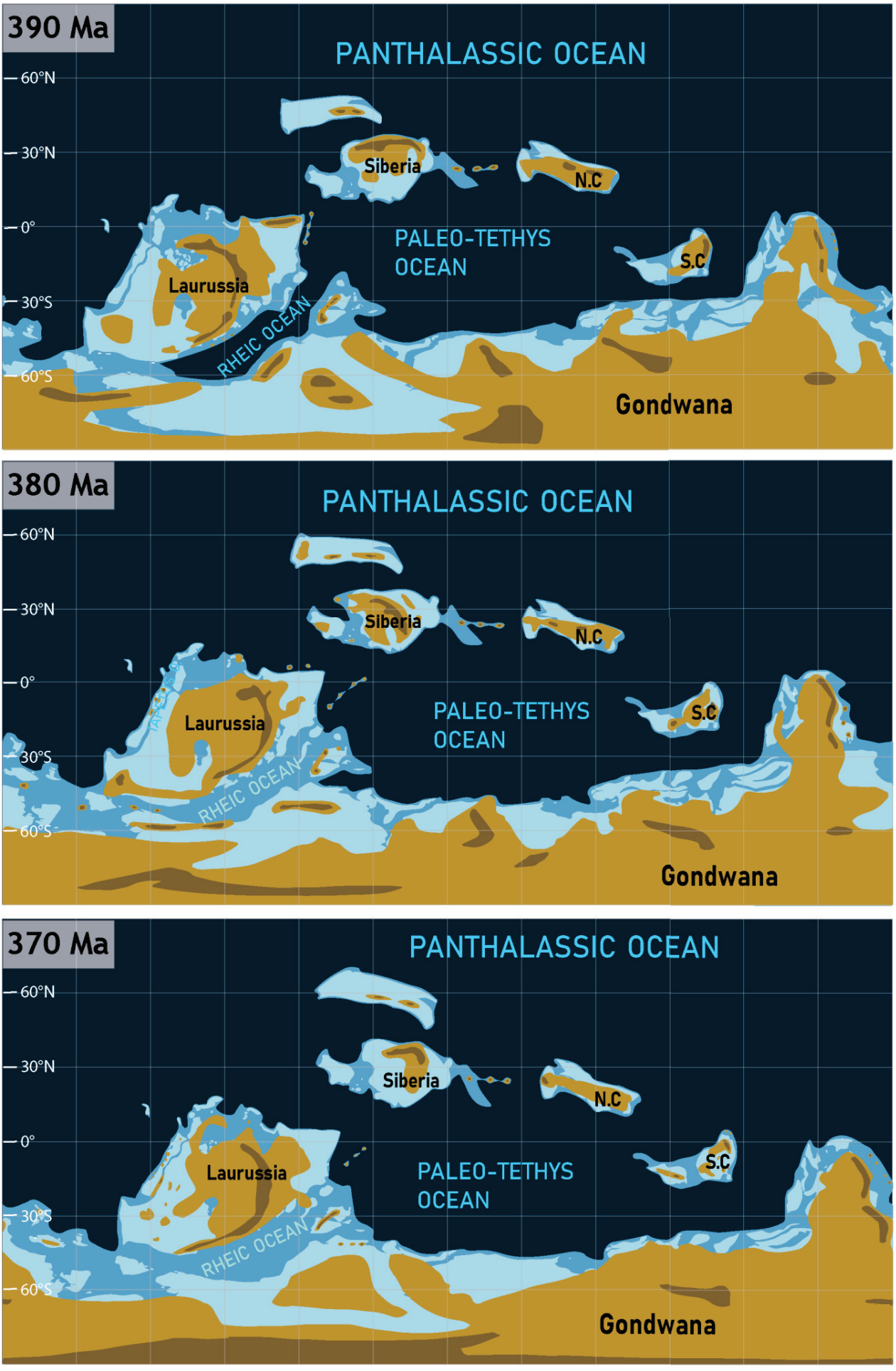
390 Ma
PANTHALASSIC OCEAN
60°N
30°N
0°
30°S
60°S
Siberia
N.C
PALEO-TETHYS
OCEAN
S.C
Laurussia
RHEIC OCEAN
Gondwana
380 Ma
PANTHALASSIC OCEAN
60°N
30°N
0°
30°S
60°S
Siberia
N.C
Laurussia
PALEO-TETHYS
OCEAN
S.C
RHEIC OCEAN
Gondwana
370 Ma
PANTHALASSIC OCEAN
60°N
30°N
0°
30°S
60°S
Siberia
N.C
Laurussia
PALEO-TETHYS
OCEAN
S.C
RHEIC OCEAN
Gondwana

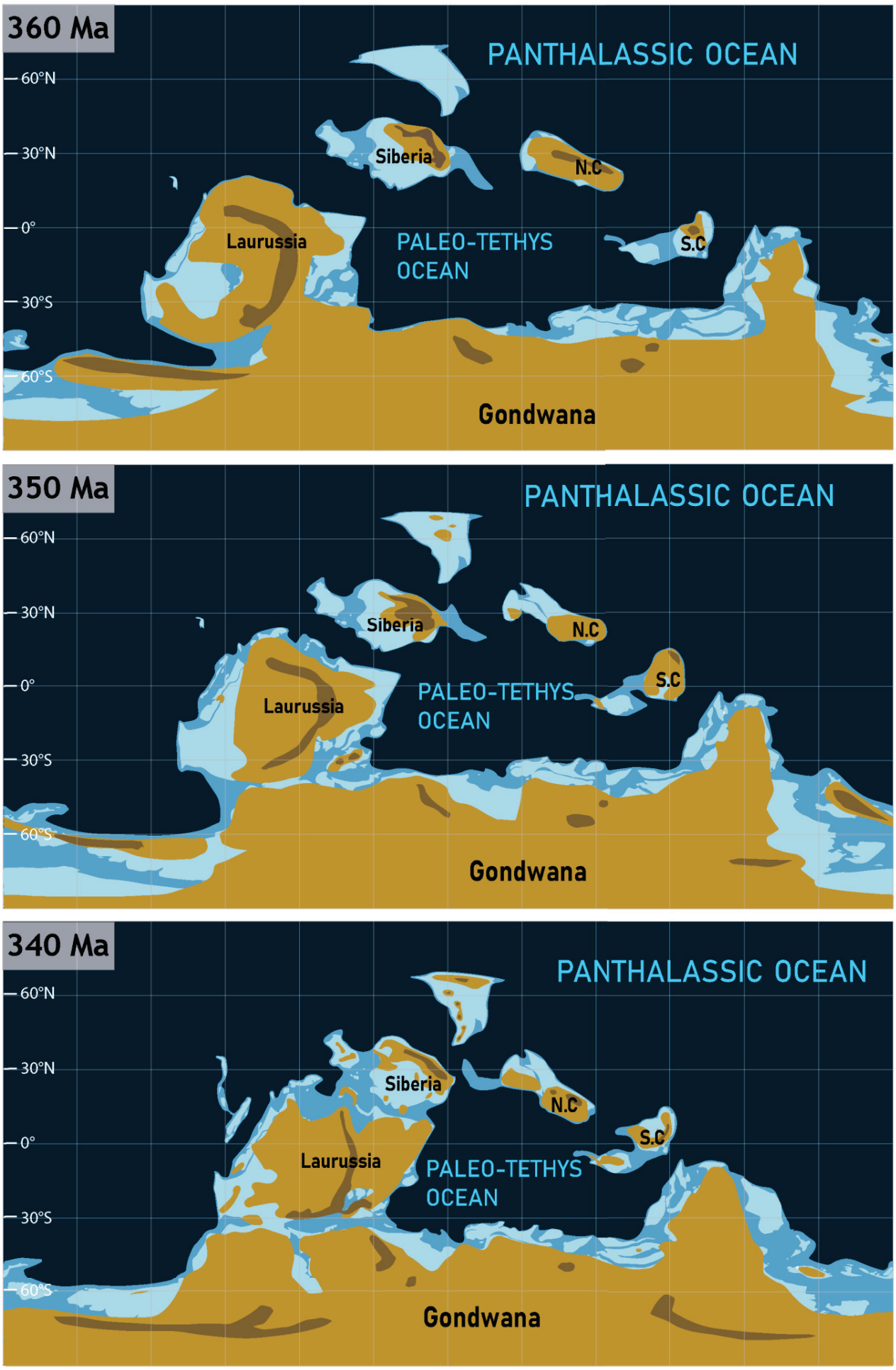
360 Ma
PANTHALASSIC OCEAN
60°N
30°N
0°
30°S
60°S
Siberia
N.C
Laurussia
PALEO-TETHYS
OCEAN
S.C
Gondwana
350 Ma
PANTHALASSIC OCEAN
60°N
30°N
0°
30°S
60°S
Siberia
N.C
S.C
Laurussia
PALEO-TETHYS
OCEAN
Gondwana
340 Ma
PANTHALASSIC OCEAN
60°N
30°N
0°
30°S
60°S
Siberia
N.C
S.C
Laurussia
PALEO-TETHYS
OCEAN
Gondwana

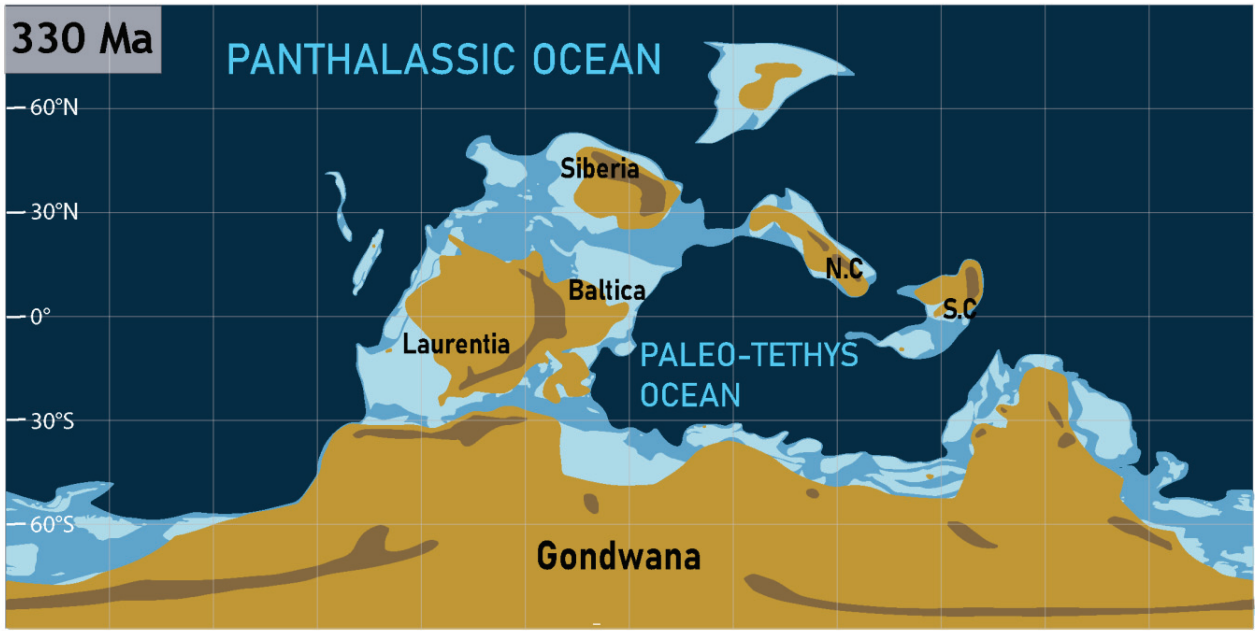
330 Ma
PANTHALASSIC OCEAN
60°N
30°N
0°
30°S
60°S
Siberia
N.C
Baltica
S.C
Laurentia
PALEO-TETHYS
OCEAN
Gondwana


320 Ma
PANTHALASSIC OCEAN
60°N
30°N
0°
30°S
60°S
Siberia
N.C
S.C
Baltica
Laurentia
PALEO-TETHYS
OCEAN
Gondwana


310 Ma
PANTHALASSIC OCEAN
60°N
30°N
0°
30°S
60°S
Siberia
Baltica
N.C
Laurentia
S.C
PALEO-TETHYS
OCEAN
Gondwana

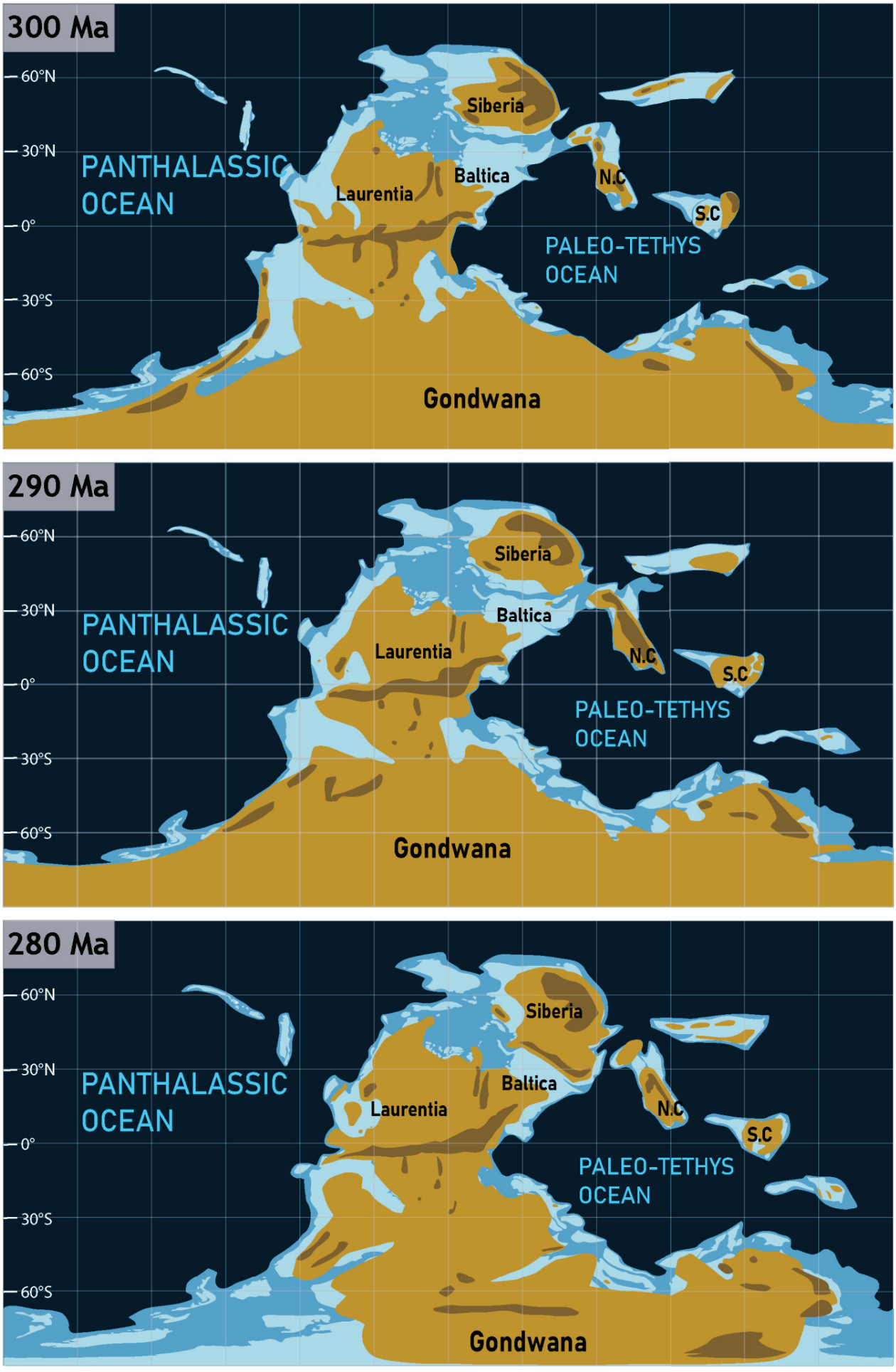
300 Ma
60°N
30°N
0°
30°S
60°S
PANTHALASSIC OCEAN
Siberia
Baltica
Laurentia
N.C
S.C
PALEO-TETHYS OCEAN
Gondwana
290 Ma
60°N
30°N
0°
30°S
60°S
PANTHALASSIC OCEAN
Siberia
Baltica
Laurentia
N.C
S.C
PALEO-TETHYS OCEAN
Gondwana
280 Ma
60°N
30°N
0°
30°S
60°S
PANTHALASSIC OCEAN
Siberia
Baltica
Laurentia
N.C
S.C
PALEO-TETHYS OCEAN
Gondwana

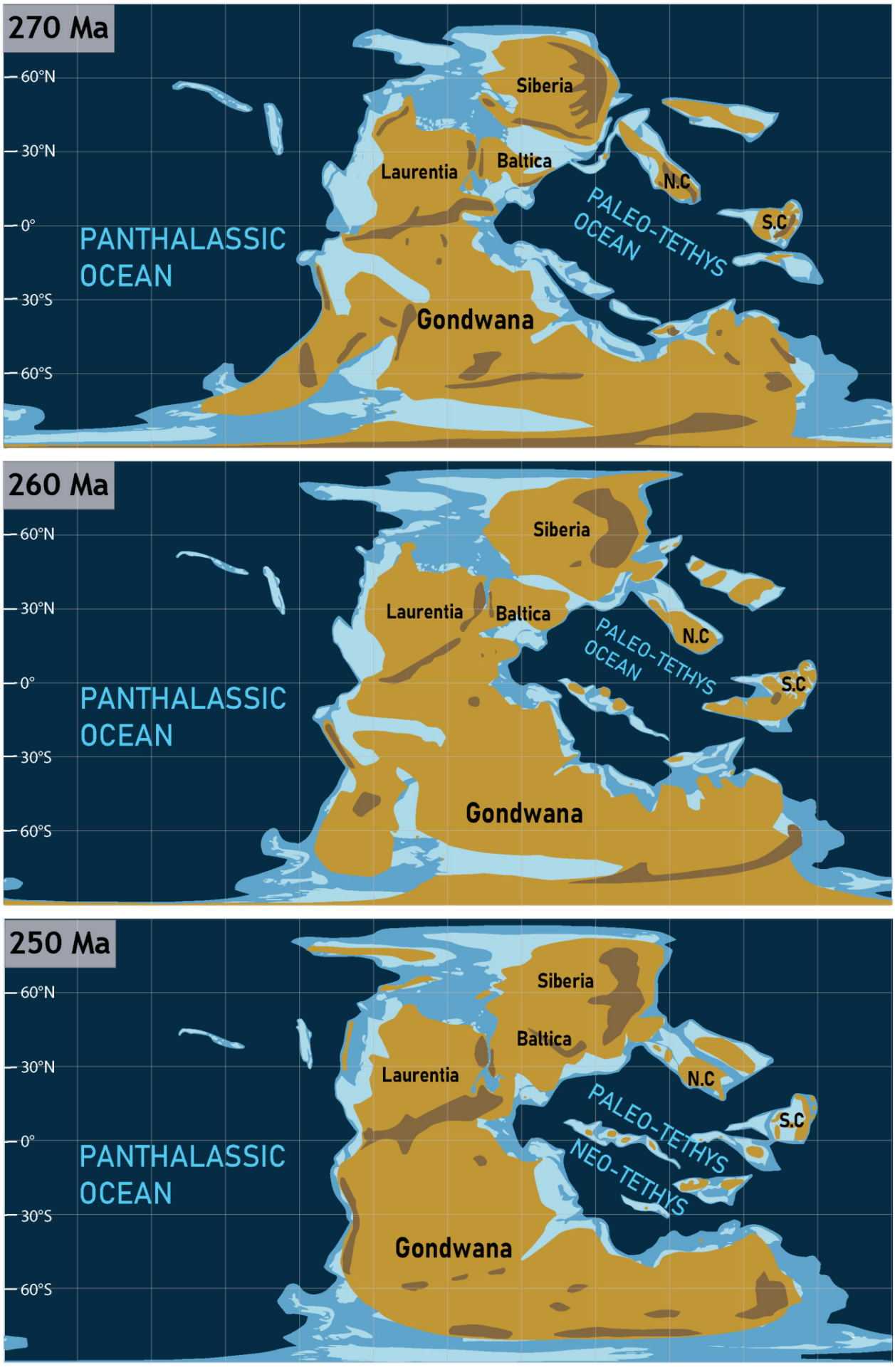
270 Ma
60°N
30°N
0°
30°S
60°S
Siberia
Laurentia
Baltica
N.C
S.C
PALEO-TETHYS OCEAN
PANTHALASSIC OCEAN
Gondwana
260 Ma
60°N
30°N
0°
30°S
60°S
Siberia
Laurentia
Baltica
N.C
PALEO-TETHYS OCEAN
S.C
PANTHALASSIC OCEAN
Gondwana
250 Ma
60°N
30°N
0°
30°S
60°S
Siberia
Baltica
Laurentia
N.C
S.C
PALEO-TETHYS
NEO-TETHYS
PANTHALASSIC OCEAN
Gondwana

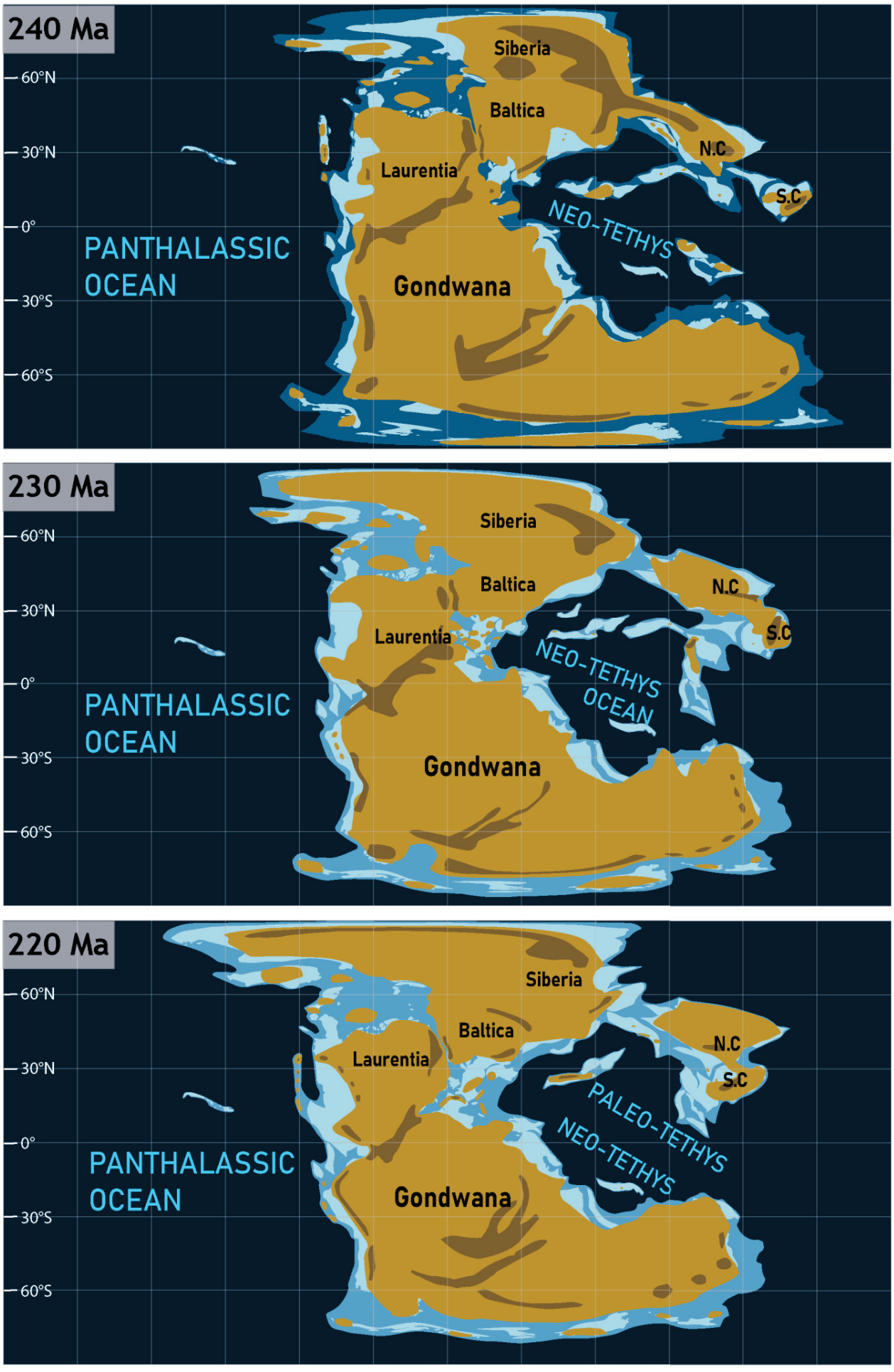
240 Ma
60°N
30°N
0°
30°S
60°S
Siberia
Baltica
Laurentia
N.C
S.C
NEO-TETHYS
PANTHALASSIC
OCEAN
Gondwana
230 Ma
60°N
30°N
0°
30°S
60°S
Siberia
Baltica
Laurentia
N.C
S.C
NEO-TETHYS
OCEAN
PANTHALASSIC
OCEAN
Gondwana
220 Ma
60°N
30°N
0°
30°S
60°S
Siberia
Baltica
Laurentia
N.C
S.C
PALEO-TETHYS
NEO-TETHYS
PANTHALASSIC
OCEAN
Gondwana

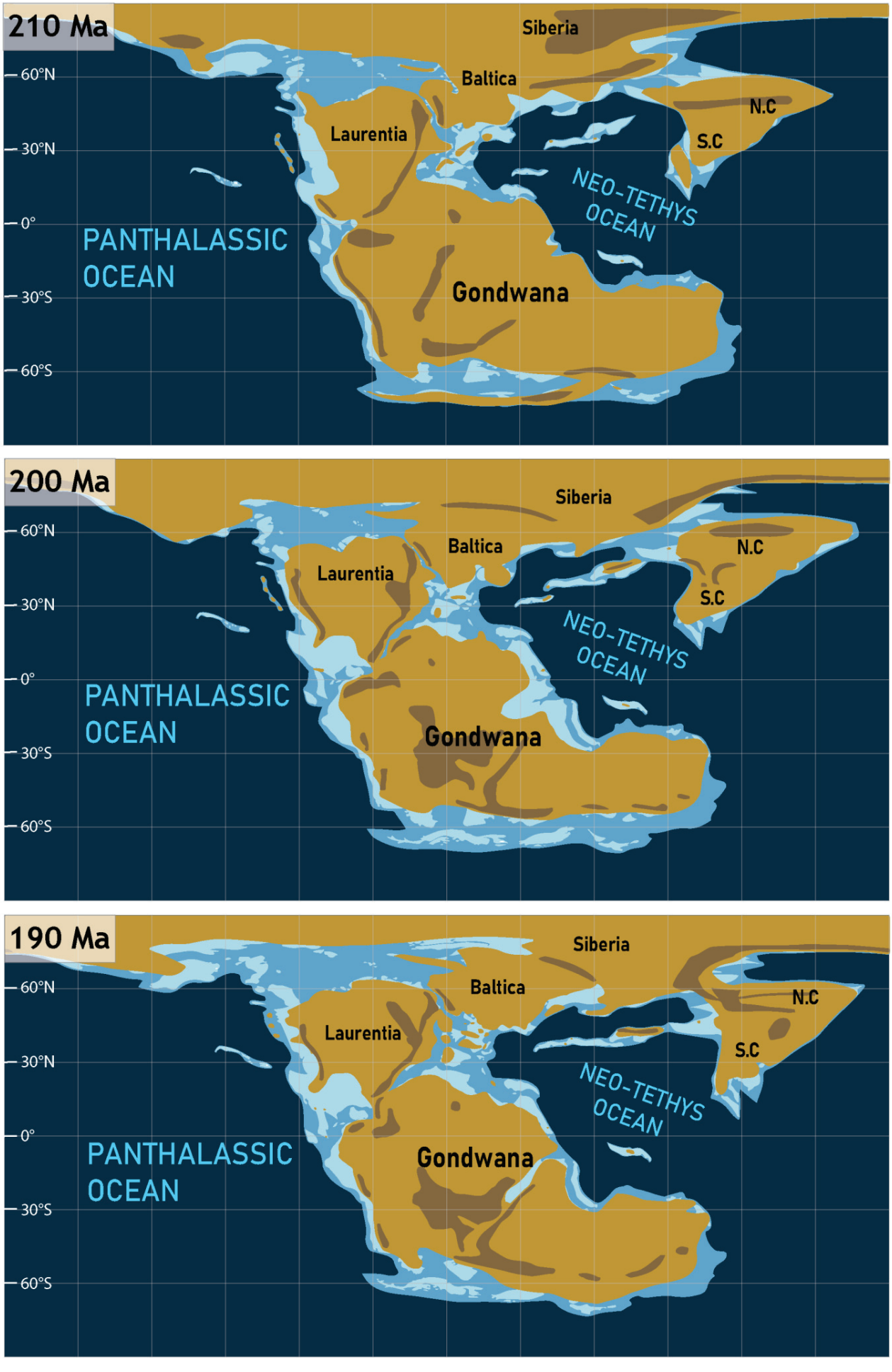
210 Ma
60°N
30°N
0°
30°S
60°S
Siberia
Baltica
Laurentia
N.C
S.C
NEO-TETHYS OCEAN
PANTHALASSIC OCEAN
Gondwana
200 Ma
60°N
30°N
0°
30°S
60°S
Siberia
Baltica
Laurentia
N.C
S.C
NEO-TETHYS OCEAN
PANTHALASSIC OCEAN
Gondwana
190 Ma
60°N
30°N
0°
30°S
60°S
Siberia
Baltica
Laurentia
N.C
S.C
NEO-TETHYS OCEAN
PANTHALASSIC OCEAN
Gondwana


180 Ma
60°N
30°N
0°
30°S
60°S
Siberia
Laurentia
Baltica
N.C
S.C
PANTHALASSIC
OCEAN
NEO-TETHYS
OCEAN
Gondwana


170 Ma
60°N
30°N
0°
30°S
60°S
Siberia
Laurentia
Baltica
N.C
S.C
PANTHALASSIC
OCEAN
NEO-TETHYS
OCEAN
Gondwana


160 Ma
60°N
30°N
0°
30°S
60°S
Siberia
Laurentia
Baltica
N.C
S.C
PANTHALASSIC
OCEAN
NEO-TETHYS
OCEAN
Gondwana

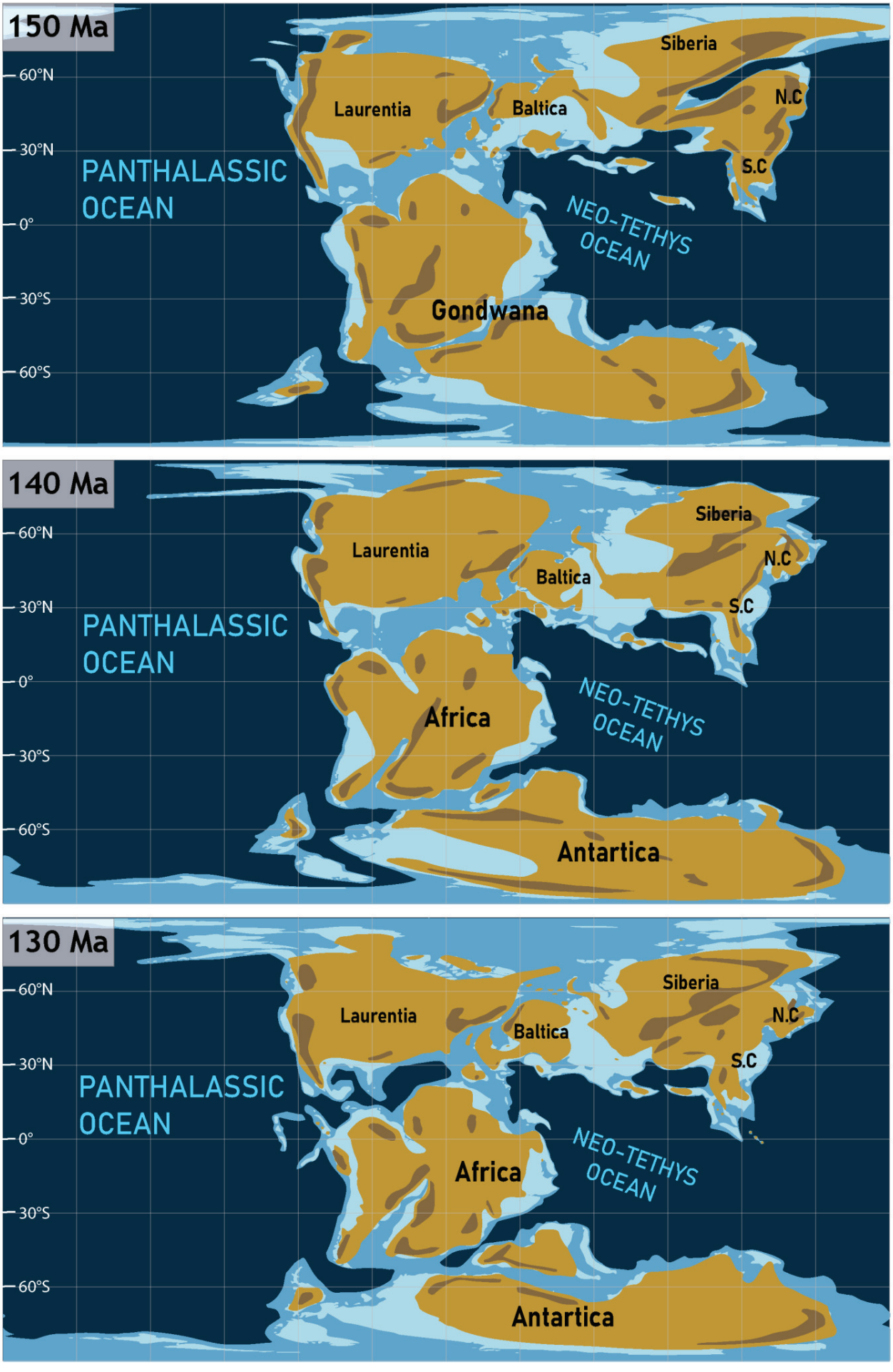
150 Ma
60°N
30°N
0°
30°S
60°S
PANTHALASSIC OCEAN
Laurentia
Baltica
Siberia
N.C
S.C
NEO-TETHYS OCEAN
Gondwana
140 Ma
60°N
30°N
0°
30°S
60°S
PANTHALASSIC OCEAN
Laurentia
Baltica
Siberia
N.C
S.C
Africa
NEO-TETHYS OCEAN
Antartica
130 Ma
60°N
30°N
0°
30°S
60°S
PANTHALASSIC OCEAN
Laurentia
Baltica
Siberia
N.C
S.C
Africa
NEO-TETHYS OCEAN
Antartica

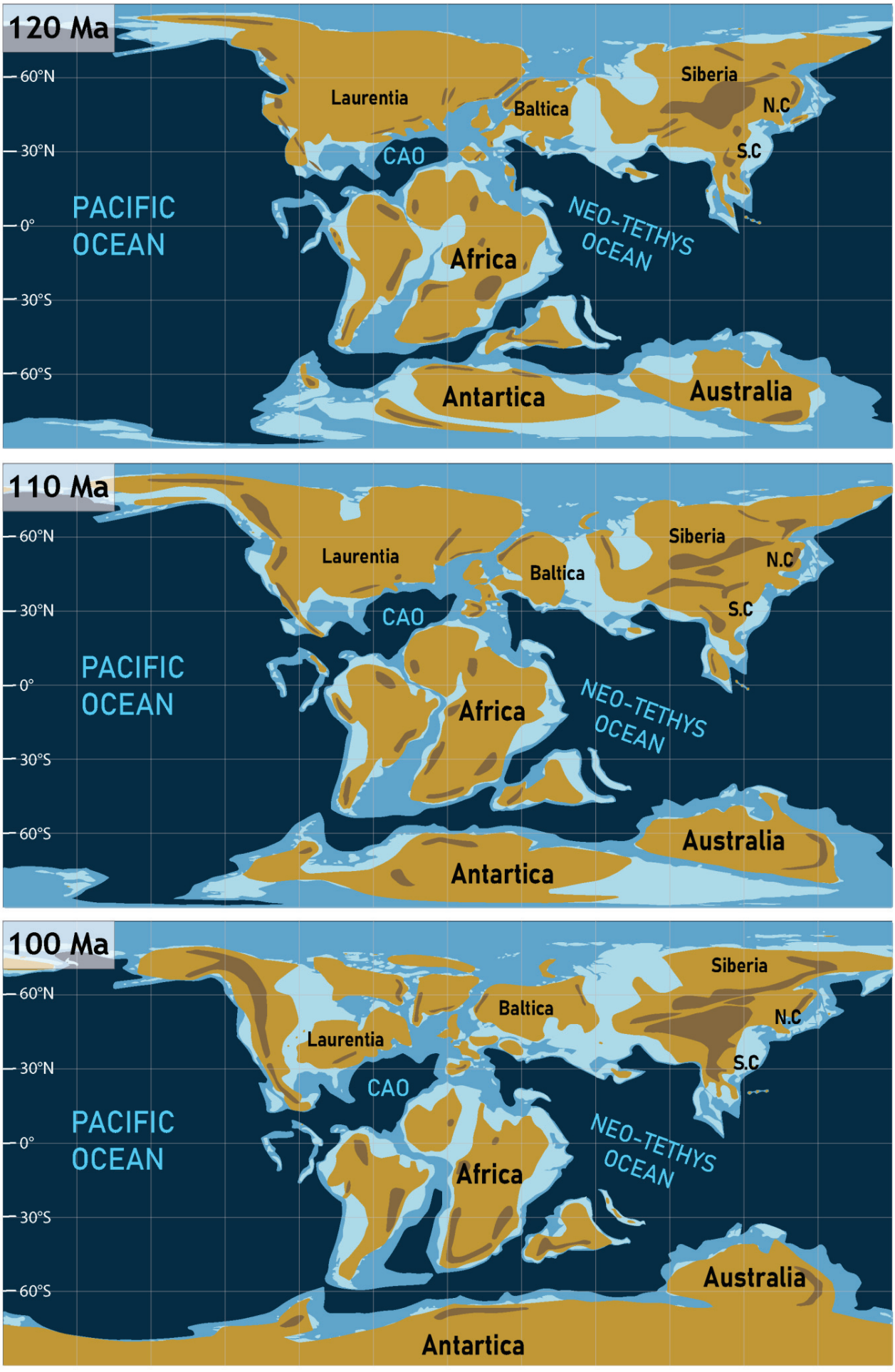
120 Ma
60°N
30°N
0°
30°S
60°S
Laurentia
Baltica
Siberia
N.C
S.C
CAO
PACIFIC
OCEAN
NEO-TETHYS
OCEAN
Africa
Antartica
Australia
110 Ma
60°N
30°N
0°
30°S
60°S
Laurentia
Baltica
Siberia
N.C
S.C
CAO
PACIFIC
OCEAN
NEO-TETHYS
OCEAN
Africa
Australia
Antartica
100 Ma
60°N
30°N
0°
30°S
60°S
Siberia
Baltica
N.C
Laurentia
S.C
CAO
PACIFIC
OCEAN
NEO-TETHYS
OCEAN
Africa
Australia
Antartica

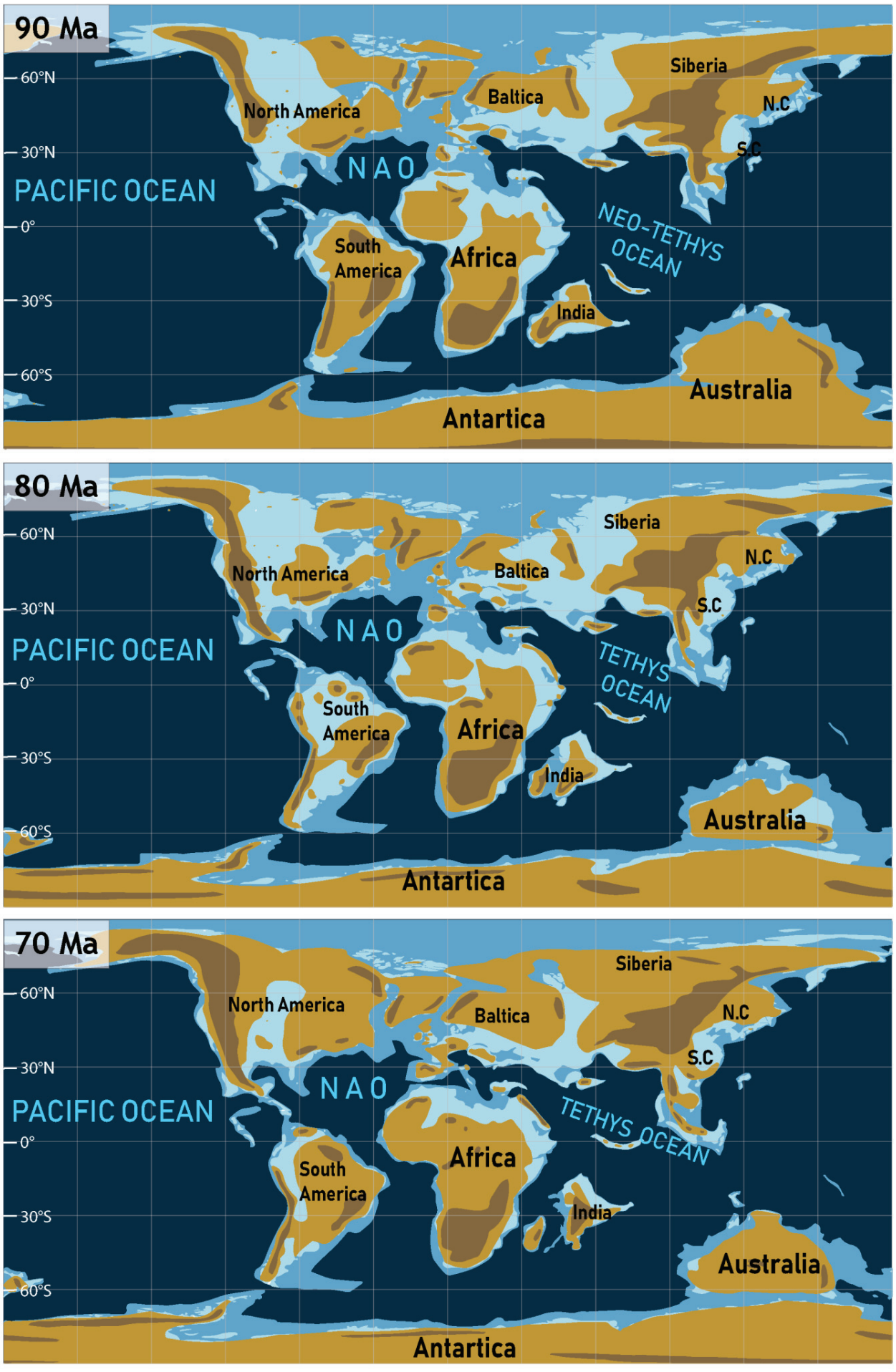
90 Ma
60°N
30°N
0°
30°S
60°S
PACIFIC OCEAN
North America
Baltica
Siberia
N.C
S.C
NAO
NEO-TETHYS OCEAN
South America
Africa
India
Australia
Antartica
80 Ma
60°N
30°N
0°
30°S
60°S
PACIFIC OCEAN
North America
Baltica
Siberia
N.C
S.C
NAO
TETHYS OCEAN
South America
Africa
India
Australia
Antartica
70 Ma
60°N
30°N
0°
30°S
60°S
PACIFIC OCEAN
North America
Baltica
Siberia
N.C
S.C
NAO
TETHYS OCEAN
South America
Africa
India
Australia
Antartica


60 Ma
60°N
30°N
0°
30°S
60°S
PACIFIC OCEAN
North America
Baltica
Siberia
N.C
S.C
NAO
TETHYS OCEAN
South America
Africa
India
Australia
Antartica


50 Ma
60°N
30°N
0°
30°S
60°S
PACIFIC OCEAN
North America
Baltica
Siberia
N.C
S.C
NAO
TETHYS OCEAN
India
Africa
South America
SOUTH ATLANTIC OCEAN
Australia
Antartica


40 Ma
60°N
30°N
0°
30°S
60°S
PACIFIC OCEAN
North America
Baltica
Siberia
N.C
S.C
NAO
India
Africa
South America
SOUTH ATLANTIC OCEAN
Australia
Antartica


30 Ma
60°N
30°N
0°
30°S
60°S
PACIFIC OCEAN
North America
Siberia
Baltica
N.C
S.C
India
Africa
ATLANTIC OCEAN
South America
Australia
Antartica


20 Ma
60°N
30°N
0°
30°S
60°S
PACIFIC OCEAN
North America
Siberia
Baltica
N.C
S.C
India
Africa
ATLANTIC OCEAN
South America
Australia
Antartica

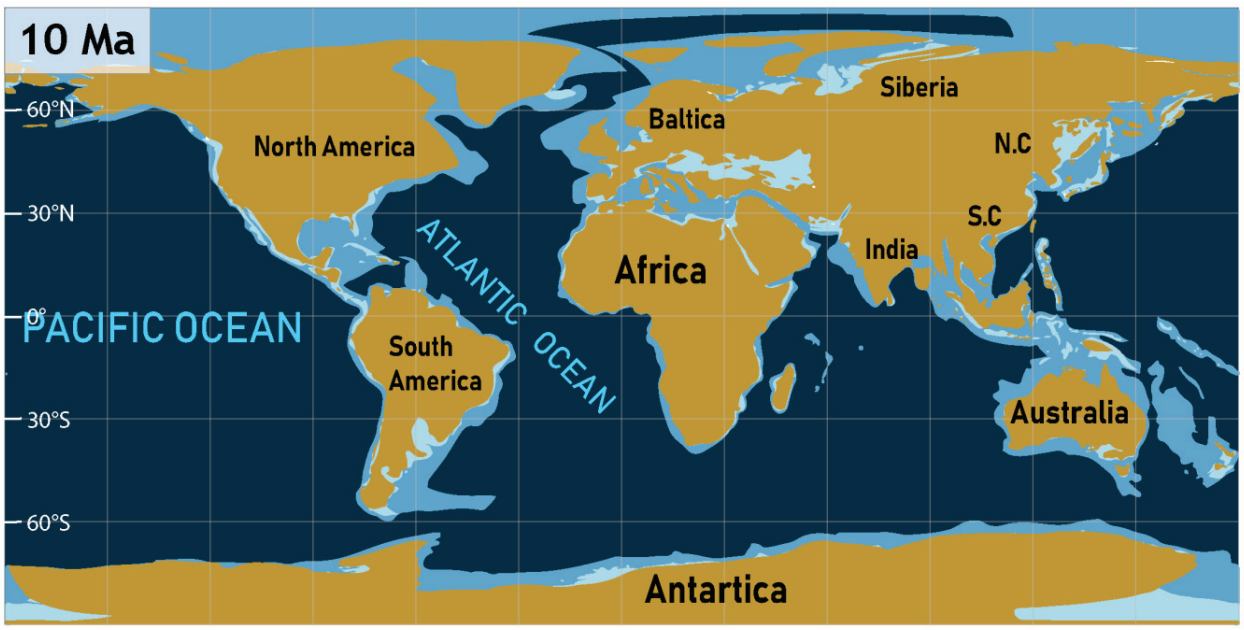
10 Ma
60°N
30°N
0°
30°S
60°S
PACIFIC OCEAN
North America
Siberia
Baltica
N.C
S.C
India
Africa
ATLANTIC OCEAN
South America
Australia
Antartica

Appendix 2 : Land data used for articles 1 and 2. *Note that reviews on maps have updated values for exposed land between 520-430 Ma between the publication of article 1 and article 2.*

Age	Total land (ceed land)	Exposed land	Exposed land 10°	Total 40-50° n/s	Modern-land flooding	Modern land sea level
(MA)	10^6km^2	10^6km^2	10^6km^2	10^6km^2	10^6km^2	m
540	116.65	86.79	16.91	12.19	29.87	169.04
530	117.00	80.47	14.54	10.90	36.53	206.77
520	116.26	75.61	12.41	10.38	43.42	245.74
510	117.93	66.95	7.98	9.42	53.74	304.20
500	118.98	78.29	9.41	13.11	43.45	245.93
490	119.10	80.37	11.28	11.86	41.50	234.88
480	118.89	78.86	15.81	11.40	42.79	242.22
470	119.17	79.29	18.34	13.12	42.63	241.32
460	118.99	77.69	18.20	12.17	44.06	249.39
450	119.07	89.80	20.39	10.59	32.03	181.30
440	119.08	90.86	15.13	10.64	30.98	175.37
430	119.26	75.77	14.91	8.98	46.25	261.81
420	120.37	77.37	14.82	9.80	45.76	259.03
410	120.50	96.75	10.30	15.42	26.51	150.06
400	122.67	95.50	6.74	19.19	29.93	169.41
390	123.10	80.10	6.41	10.49	45.76	259.04
380	123.06	82.21	8.65	8.19	43.62	246.88
370	123.26	85.04	8.29	10.32	40.98	231.97
360	123.13	107.55	14.73	17.37	18.35	103.85
350	123.16	99.92	15.20	17.51	26.01	147.21
340	125.52	106.48	17.85	16.35	21.81	123.44
330	126.26	105.10	15.90	16.34	23.93	135.44
320	129.46	117.44	16.10	18.16	14.78	83.67
310	132.04	105.51	16.47	17.17	29.30	165.82
300	135.67	110.77	16.55	16.74	27.66	156.56
290	136.08	118.78	17.12	17.38	20.06	113.52
280	136.35	114.45	17.64	16.68	24.67	139.63
270	136.49	111.91	14.33	20.27	27.34	154.74
260	136.99	126.82	18.71	21.77	12.93	73.19
250	138.57	128.62	16.29	22.84	12.72	72.00
240	138.61	134.29	18.53	26.01	7.08	40.08
230	138.61	134.84	16.37	25.36	6.54	37.01
220	138.62	131.18	16.66	25.96	10.20	57.72
210	138.52	138.69	21.76	25.19	2.59	14.65

200	139.12	132.04	17.56	24.75	9.84	55.72
190	138.96	133.28	20.67	23.98	8.44	47.79
180	139.12	137.46	19.97	27.38	4.42	24.99
170	139.65	121.50	16.62	29.47	20.91	118.36
160	140.12	107.39	17.07	24.49	35.49	200.87
150	139.64	115.35	16.94	23.89	27.05	153.13
140	141.62	119.88	18.90	21.51	22.88	129.51
130	142.07	115.04	16.73	22.30	27.97	158.33
120	142.88	106.04	16.75	20.43	37.22	210.69
110	142.98	115.77	18.40	20.62	27.75	157.05
100	144.84	106.18	12.94	18.69	37.59	212.74
90	144.59	106.57	12.93	18.92	37.44	211.92
80	145.47	94.19	11.95	17.96	50.07	283.41
70	146.12	119.99	16.82	21.04	24.52	138.79
60	146.00	129.82	17.11	23.20	14.95	84.60
50	147.10	137.04	20.92	22.52	8.22	46.55
40	147.69	141.67	19.31	20.78	4.20	23.80
30	148.00	146.64	19.70	20.87	-0.51	-2.87
20	149.28	147.05	18.15	18.35	0.34	1.94
10	149.86	148.57	21.01	17.71	-0.64	-3.62
0	150.88	149.00	21.54	19.10	0.00	0.00

Appendix 3 : Revised parameters for long-term carbon cycle models used for articles 1 and 3. The blue highlighted values correspond to the newly developed degassing estimates from subduction fluxes used in article 3.

Age (Ma)	f_A	$f_{AW}\_f_A$	$f_{AW}\_f_A$ **adjusted for aridity**	$f_{AW10}\_f_A$	$f_{AW10}\_f_A$ **adjusted for aridity**	f_{SR} **sub.flux** (subduction fluxes:	f_{SR} **Zircon** (V11+QF+AF+ARC filtered and de-trended)
540	0.58	1.27	1.27	1.34	1.34		1.67
530	0.54	1.19	1.19	1.25	1.25		1.77
520	0.5	1.12	1.12	1.13	1.13		1.8
510	0.45	0.96	0.96	0.82	0.82		1.78
500	0.53	1.07	1.07	0.83	1.83	1.83	1.72
490	0.54	1.07	1.07	0.97	2.04	2.04	1.58
480	0.53	1.28	1.28	1.38	2.4	2.4	1.69
470	0.53	1.47	1.47	1.59	1.68	1.68	1.48
460	0.52	1.45	1.45	1.62	1.4	1.4	1.44
450	0.6	1.28	1.28	1.57	1.62	1.62	1.42
440	0.61	1.05	1.05	1.15	1.54	1.54	1.37
430	0.51	1.17	1.1 7	1.36	1.75	1.75	1.32
420	0.52	1.18	1.18	1.32	1.95	1.95	1.3
410	0.65	0.98	0.98	0.73	2	2	1.3
400	0.64	1.01	1.01	0.49	1.94	1.94	1.3
390	0.54	0.78	0.78	0.55	1.92	1.92	1.32
380	0.55	0.76	0.76	0.73	1.68	1.68	1.39
370	0.57	0.81	0.81	0.67	1.95	1.95	1.62
360	0.72	1.11	1.11	0.94	2.03	2.03	1.9
350	0.67	1.21	1.21	1.05	2.06	2.06	2.06
340	0.71	1.19	1.19	1.16	2.01	2.01	1.79
330	0.71	1.14	1.14	1.04	1.8	1.8	1.62
320	0.79	1.08	1.08	0.95	1.53	1.53	1.37
310	0.71	1.18	1.18	1.08	1.33	1.33	1.33
300	0.74	1.11	1.11	1.03	1.37	1.37	1.3
290	0.8	1.08	1.08	0.99	1.54	1.54	1.32
280	0.77	1.11	1.11	1.06	1.42	1.42	1.44
270	0.75	1.14	1.14	0.88	1.54	1.54	1.48
260	0.85	1.18	0.86	1.02	1.59	1.59	1.58
250	0.86	1.13	0.88	0.87	1.18	1.18	1.58
240	0.9	1.23	0.99	0.95	1.29	1.29	1.45
230	0.9	1.15	1.15	0.84	1.13	1.13	1.39

220	0.88	1.2	0.94	0.88	1.15	1.15	1.34
210	0.93	1.25	0.89	1.08	1.18	1.18	1.35
200	0.89	1.19	0.83	0.92	1.15	1.15	1.35
190	0.89	1.24	0.86	1.07	1.01	1.01	1.47
180	0.92	1.28	0.93	1	1.16	1.16	1.66
170	0.82	1.4	1.06	0.94	1.28	1.28	2
160	0.72	1.43	1.03	1.1	1.4	1.4	2.07
150	0.77	1.31	0.97	1.01	1.57	1.57	1.99
140	0.8	1.25	0.88	1.09	1.89	1.89	1.77
130	0.77	1.26	0.91	1	2.43	2.43	1.71
120	0.71	1.3	0.91	1.09	1.94	1.94	2.43
110	0.78	1.25	0.88	1.1	1.82	1.82	1.94
100	0.71	1.1	1.1	0.84	1.63	1.63	1.76
90	0.72	1.11	1.11	0.84	1.69	1.69	1.39
80	0.63	1.18	1.18	0.87	1.46	1.46	1.27
70	0.81	1.17	1.17	0.97	1.6	1.6	1.21
60	0.87	1.15	1.15	0.91	1.58	1.58	1.28
50	0.92	1.17	1.17	1.05	1.26	1.26	1.1
40	0.95	1.05	1.05	0.94	1.22	1.22	1.05
30	0.98	1.02	1.02	0.93	1.37	1.37	1.08
20	0.99	0.92	0.92	0.85	1.17	1.17	1.07
10	1	0.97	0.97	0.98	1.09	1.09	1
0	1	1	1	1	1	1	1

Appendix 4 : additional information for article 3

➢

a. Paleogeography description - 7 time slices

Paleogeographic reconstructions with definitions of exposed land, shallow and deep shelves (Fig. S1) follow Marcilly et al. (2021) and are mostly based on reconstructions from Torsvik and Cocks (2016) and Cocks and Torsvik (2020). Particular attention was paid to the location and extent of microcontinents, terranes, and island arcs throughout the Ordovician. The time-uncertainty for each map is in the order of ± 5 Myrs.

In the late Cambrian and Early Ordovician, almost all the continents were located in the Southern hemisphere with Gondwana, the largest unit, stretching from the South Pole to the equator. Baltica and some smaller Asian units such as North China drifted northwards during the Ordovician, Avalonia (including southern England) also rifted of the Gondwanan margin, and as a result, a large amount of landmasses is found in the tropics by the Late Ordovician. Avalonia and Baltica docked in the Late Ordovician and by the early Silurian (430 Ma) Laurussia formed from the collision of Laurentia with the combined Baltica/Avalonia, and effectively closing the Iapetus gateway. The distribution of topography is primarily based on Scotese (2016) except for 490 and 430 Ma where Golonka (2002), Golonka et al. (1994), and Scotese (2016) are used and adapted to our reconstructions. We attributed an altitude to each grid point following four arbitrary classes: 1) deep continental shelves: -200 m, 2) shallow continental shelves: -100 m, 3) land: 200-500 m, and 4) highs: 1000-1500 m, as a first step in testing the effect of topography. We kept elevation below 1500 m as more than 95% of the land elevation in the present day is under this value (Vérard, 2017). This creates a limitation in simulating the climatic response, as runoff is particularly sensitive to topography, and might be underestimated due to the low altitudes implemented here. We chose to only integrate four classes in this study as a primary step to address the problem, as the topography location and orogenic history for the Ordovician are not well known. However, the program we developed to make those maps allows up to nine classes of altitudes and opens possibilities for future research enhancement.

The maps were produced in GPlates, which served as the base to extract land parameters, and a special *in-house* land tool allows us to directly calculate the latitudinal distribution of land areas in km^2 and % of total land as presented in Table S1 for the studied period.

Table S1: Latitudinal distribution of tropical land area from paleogeographic maps from Marcilly et al. (2021)

Age (Ma)	±10°		Tropics ±23.5°	
	× 10^6 km^2	% of total land	× 10^6 km^2	% of total land
490	12.3	15.2	22.4	27.6
480	17.1	21.5	30.2	37.9
470	19.1	23.9	28.5	35.6
460	19.3	24.5	29.9	38
450	21.7	23.8	36.5	40.1
440	16.2	17.7	31.7	34.5
430	15.4	20.2	27	35.4

b. Solid Earth degassing from full-plate model

Full-plate models not only track the motion of the continents but also the oceanic lithosphere and the evolution of plate boundaries, and therefore the evolution of tectonic plates themselves (Gurnis et al., 2012). As the Paleozoic oceanic lithosphere has been subducted, full plate models of the Paleozoic depend strongly on indirect inferences drawn from the records preserved on continents (Domeier & Torsvik, 2019; Domeier, 2018). A full description of the model used and extended here is presented in Domeier & Torsvik (2014). This model is constrained in latitude using paleomagnetic data and in longitude using the distribution of large igneous provinces, kimberlites but also lithofacies and provincial faunas. The model is expressed in the paleomagnetic frame. As full-plate models reconstruct the full evolving configuration of tectonic plates and plate boundaries, they allow us to calculate directly the subduction fluxes linked to their motion and the corresponding seafloor spreading, considered as a proxy for solid Earth degassing (Marcilly et al., 2021). We here used an extension of the full-plate model of Domeier and Torsvik (2014) and Torsvik et al. (2019) after 250 Ma, presented in Marcilly et al. (2021), back to 490 Ma in Marcilly et al (2022).. This model is the base of both paleogeographic maps of exposed land and the calculation of subduction fluxes.

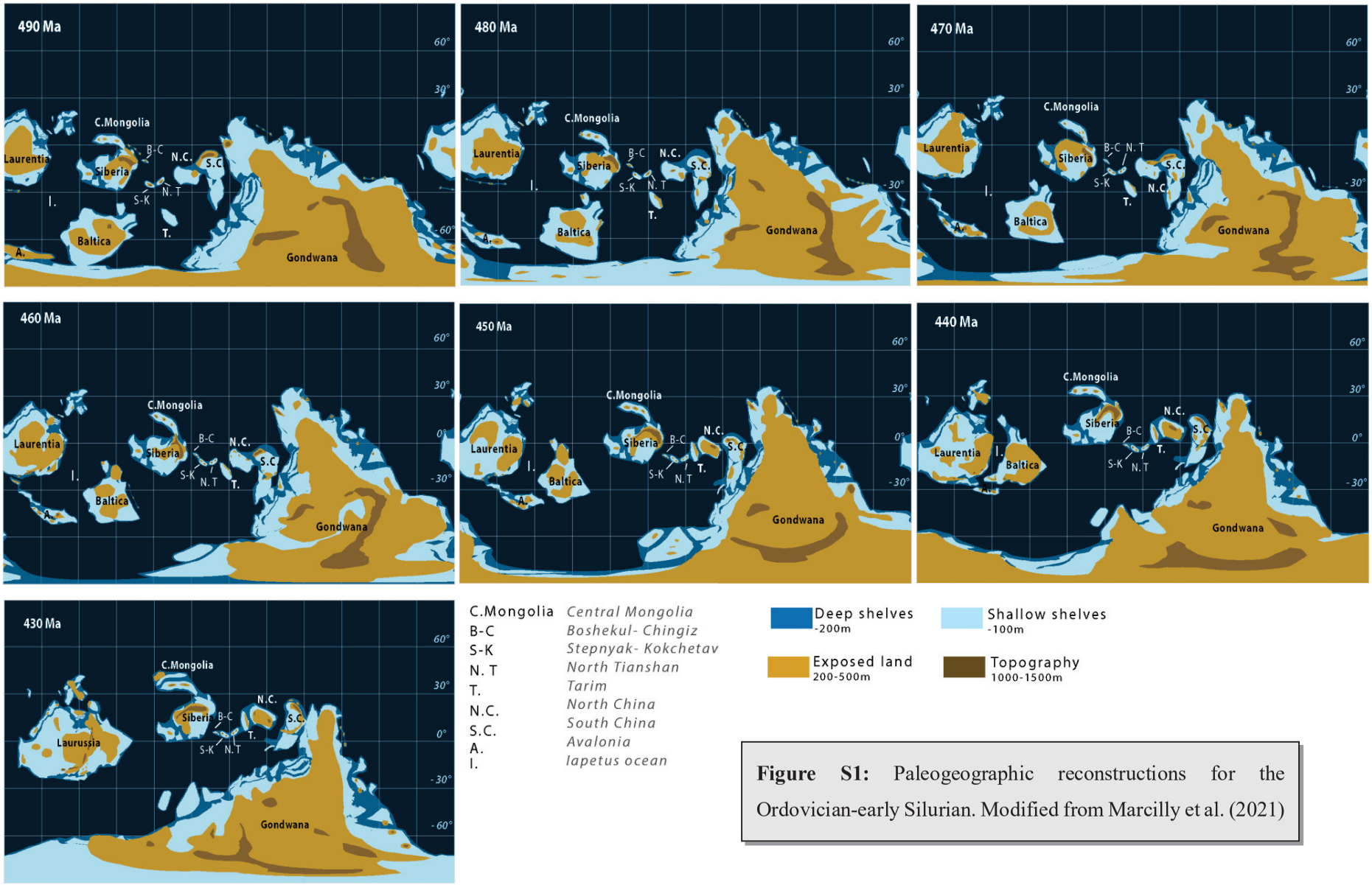

Figure S1: Paleogeographic reconstructions for the Ordovician-early Silurian. Modified from Marcilly et al. (2021)

c. Climate models description

FOAM (Fast Ocean-Atmosphere Model) version 1.5 is a fully coupled mixed-resolution ocean-atmosphere general circulation model with no flux corrections (Jacob, 1997). Its quick turnaround time allows for long millennium-scale integrations. FOAM is consequently well designed for paleoclimate studies, for which purpose it has been routinely used in the past, including for the Ordovician (Nardin et al., 2011; Pohl et al., 2014, 2016). The atmospheric component of the model is the National Center for Atmospheric Research's (NCAR) Community Climate Model version 2 (CCM2) benefitting from the upgraded radiative and hydrologic physics from CCM3 version 3.2. It is run at an R15 spectral resolution (4.5 × 7.5) with 18 vertical levels (14 in the troposphere). The ocean module is the Ocean Model version 3 (OM3). It is a finite difference, 24-level z coordinate ocean general circulation model providing a higher resolution than the atmospheric module (1.4 × 2.8) on a rectangular grid. Sea ice is simulated using the thermodynamics of the NCAR's Climate System Model 1.4 sea ice module, which is based on the Semtner (1976) three-layer thermodynamic snow/ice model.

The LMDz model is an IPCC-class (Intergovernmental Panel on Climate Change) atmospheric general circulation model benefiting, as the atmospheric component of the state-of-the-art IPSL (Institut Pierre-Simon Laplace) Earth system model, from the latest physical and dynamical refinements (Boucher et al., 2020). A mid-resolution version of the model is used here, providing a resolution of 1.9 × 3.75 with 79 vertical levels on a rectangular grid.

d. Coupling between climate models

We couple the ocean-atmosphere climate model FOAM with the atmospheric climate model LMDz (Laboratoire de Météorologie Dynamique Zoom, Boucher et al., 2020), following a procedure previously developed to simulate deep-time climate, including the Late Ordovician glaciation (Ladant et al., 2014; Licht et al., 2014; Pohl et al., 2016). FOAM computes the climate steady-state under a range of pCO_2 values representative of the Ordovician from 1120 ppm (4 PAL) to 6720 ppm (24 PAL) (Table S2). Then, for the same pCO_2 levels, LMDz is forced by FOAM sea-surface temperatures to specifically refine the atmospheric component. This coupling has been adopted because LMDz finer resolution grid (144x142x79) offers greater precision as well as greater accuracy for the hydrological cycle for continental climates. Experiments have been run for 30 years. Results of the last 10 years of each LMDz simulation (land temperature and runoff—estimated as the difference Precipitation minus Evaporation) are averaged and gathered in a matrix of pCO_2-dependend climatic conditions (Fig. S2).

Table S2: Range of PCO_2 values foe the Ordovician for FOAM simulations.

	490 Ma	480 Ma	470 Ma	460 Ma	450 Ma	440 Ma	430 Ma
Solar constant (W m^2)	1313.24	1314.31	1315.38	1316.46	1317.54	1318.62	1319.70
6720 ppm	X	X	X				
3360 ppm	X	X	X	X	X	X	X
2800 ppm	X	X	X	X	X	X	
2240 ppm	X	X	X	X	X	X	
1680 ppm	X	X	X	X	unstable	X	X
1400 ppm							X
1120 ppm							X

e. Climate simulations and boundary conditions

The maps were originally produced in GPlates with a resolution of 1 x 1° and then converted in GEOCARBNET to the grid size used in GEOCLIM [1.40625 (latitude) x 2.8125 (longitude)] (Fig. S3) We then attributed an altitude to each grid point following the four arbitrary classes defined in section a. In the absence of abundant land plants, a rocky desert is imposed on every continental grid point (soil albedo is set to 0.24 in the visible band). Simulations were conducted using a solar constant evolving through time from 1313.24 W m^{-2} (at 490 Ma) to 1319.7 W m^{-2} (at 430 Ma) (Gough, 1981). Regarding uncertainties about atmospheric carbon dioxide concentrations, we tested from 3 to 5 values for each time slice for covering the spectrum of possibilities. The purpose of this study being to investigate long-term climatic responses, orbital parameters were kept fixed with present-day obliquity (23.441°) and eccentricity set to zero (circular orbit). We did not prescribe an ice sheet in all runs. However, we accounted for seasonal sea-ice calculated by the model FOAM.

1

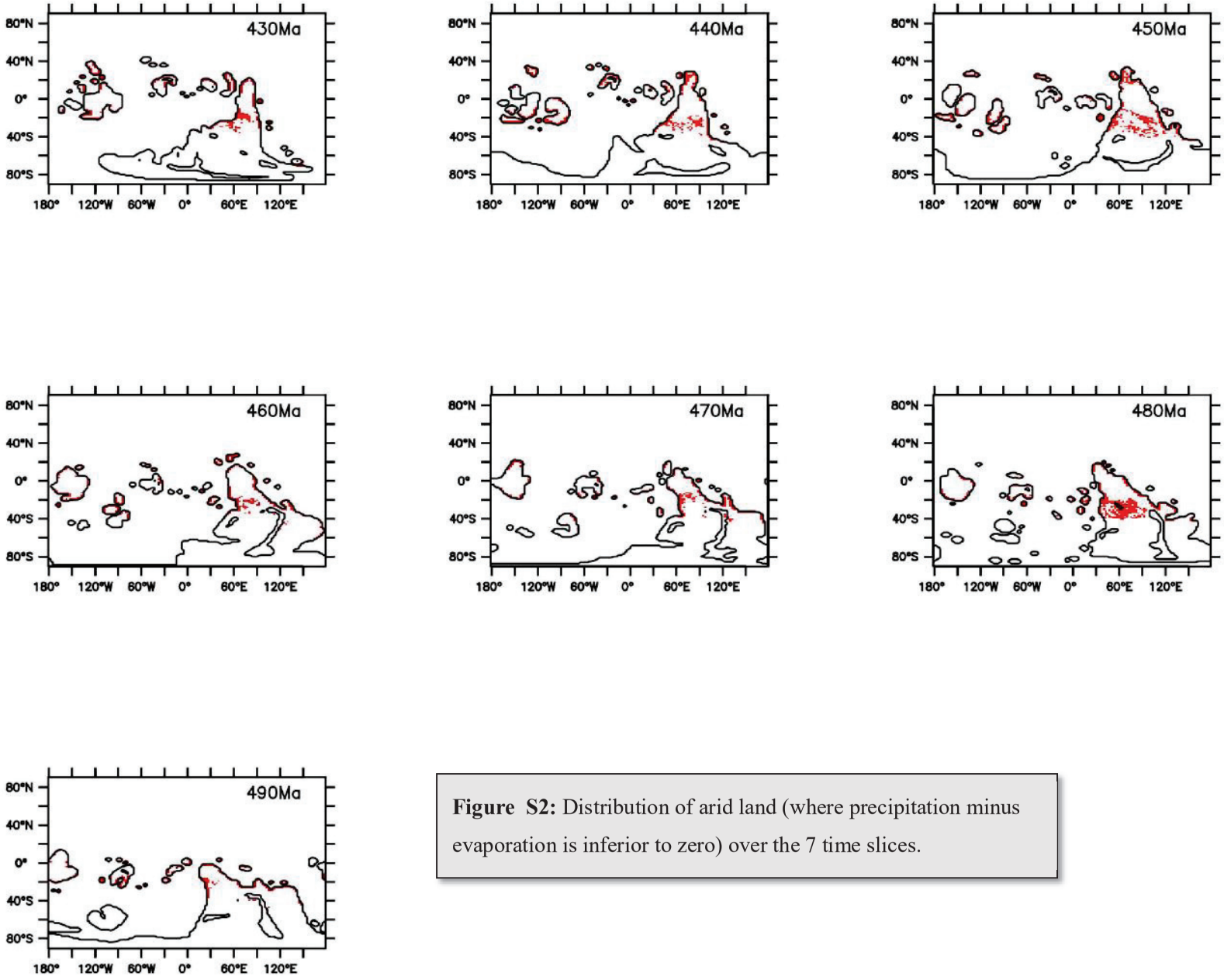

Figure S2: Distribution of arid land (where precipitation minus evaporation is inferior to zero) over the 7 time slices.

2

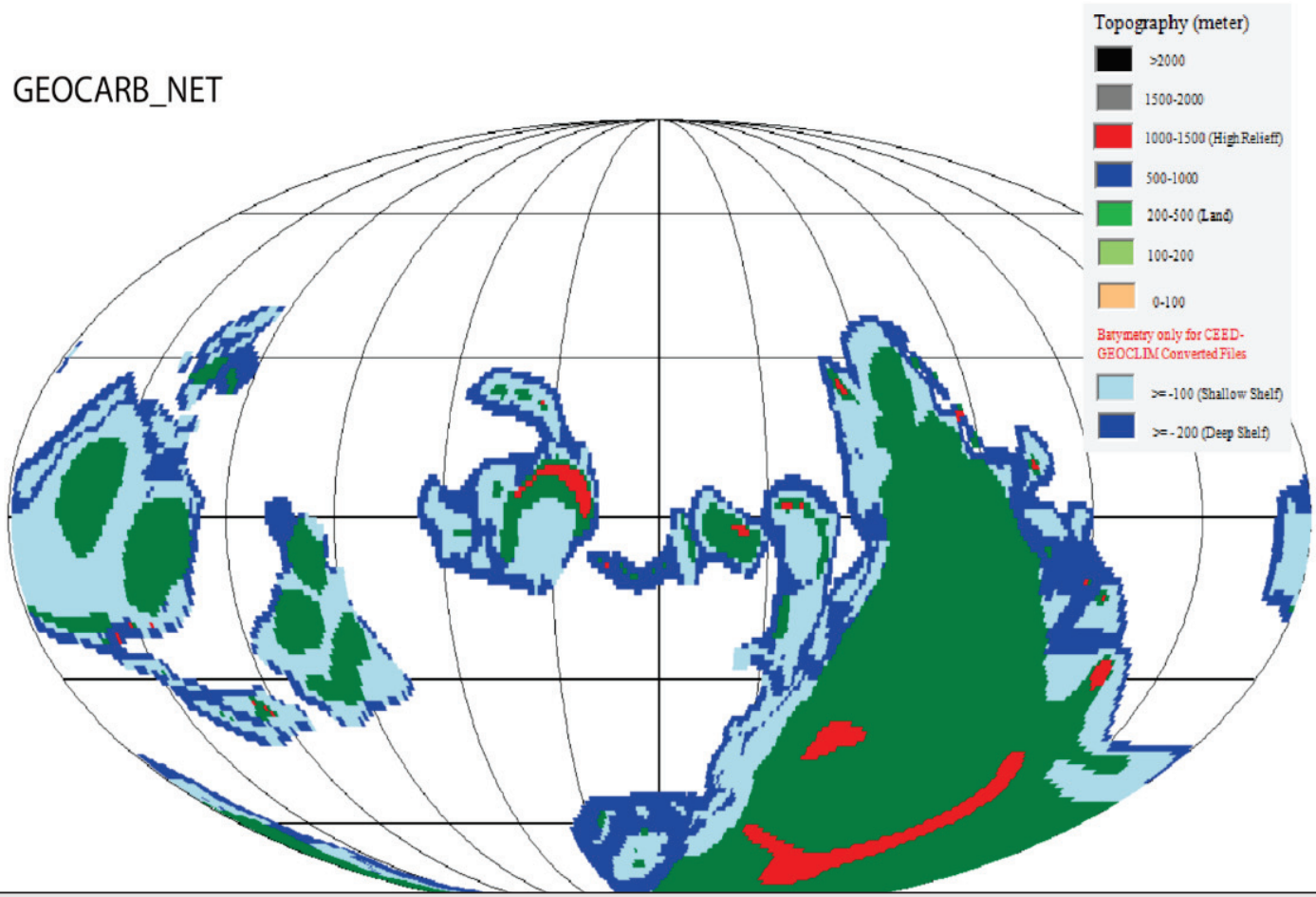

Figure S3: View of the in-house software GEOCARBNET here used to translate the GPlates reconstructions into maps to run in GEOCLIM. The topography selection holds nine classes from which we only used four.

Weathering computation

The silicate weathering (Fig S4) computation uses recent improvements of GEOCLIM (Park et al., 2020). Weathering rate depends on erosion rate, runoff, temperature, and lithology. Only three lithological classes have been kept for this study: carbonates (not contributing to silicate weathering), basalts, and ”other silicate rocks” (merged in a single class). The proportions of outcrops were kept identical to modern ones (respectively, 9%, 5%, and 86% of the continental area). Those values have been applied uniformly on Ordovician emerged lands (i.e., same value for each model ”pixel”), given the absence of a lithological map reconstruction. We used the single best-fit parameters combination of Park et al. (2020), with ”mafic” Ca-Mg content for our current ”basalt” lithology and area-weighted average of the other lithological classes for our ”merged” class. In addition, we increased the constant k_d, representing the kinetics efficiency of weathering (Park et al., 2020), for the ”basalts” class, from 5. 10^{-4} to 1. 10^{-3}, so that basalts contribute to 30% of the total weathering flux in the pre-industrial control simulation. This parameterization yields a total weathering flux of 3.275 Tmol(C) yr^{-1}. The erosion rate is computed with the same model as Park et al. (2020). The slope field has been reconstructed from the paleo-topography, using a slope-elevation relationship.

f. Climate-carbon simulations

The GEOCLIM model couples the 3D atmospheric general circulation model to the model of the biogeochemical cycles of carbon and alkalinity COMBINE (the coupled model of biogeochemical cycles and climate model, Goddéris and Joachimski, 2004; Donnadieu et al., 2006; Goddéris et al., 2008). A full description of the GEOCLIM model was published by Donnadieu et al. (2006) and recent enhancements made from previous versions are described in Godderis et al. (2014).

We conducted two sets of simulations with fixed solid degassing and variable degassing (Table S3). Fixed degassing simulations were conducted by fixing the CO_2 emissions from solid Earth degassing; a numerical loop between LMDz and COMBINE is generated until the sink equilibrates with the given degassing. Therefore, for each time slice and continental configuration, the model reached a steady-state atmospheric CO_2 concentration. Seven time slices were simulated every 10 Myrs from 490 to 430 Ma. For each time slice, the paleogeography and degassing were reconstructed. The results are summarized in Table S3 below.

Table S3: Simulations values of CO_2 in PAL and ppm units as well as GMST following the different degassing scenarios used in the study: Constant degassing (constant deg.), variable degassing from subduction fluxes proxy (var. deg. SBF) and age zircon distribution (var.deg.Z).

	CO_2 (PAL/ppm)			GMST (°C)			
Age (Ma)	Constant deg.	Var.deg. SBF	Var.deg.Z	Constant deg.	Var.deg. SBF	Var.deg. Z	Fixed deg.
490	22.1 / 6188	32.5 / 9100	12.8 / 3584	24.7	26.6	21.47	21.8
480	29.1 / 8148	55.8 /15 625	16.7 / 4676	25.8	28.6	23.4	22
470	18 / 5040	18.8/ 5265	8.3 / 2324	23.6	23.8	20.4	21.8
460	18.9 / 5292	14.7 / 4125	8.4 / 2352	24.6	23.6	21.2	22.7
450	18.1 / 5068	13.3 / 3739	8.45 / 2366	24.1	22.7	20.2	22.1
440	14.4 / 4872	10.3 / 2884	7.54 / 2111	24.4	22.2	19.3	22.9
430	14.6 / 4088	13.8 / 3875	4.48 / 1254	24.6	24.4	19.8	23.8

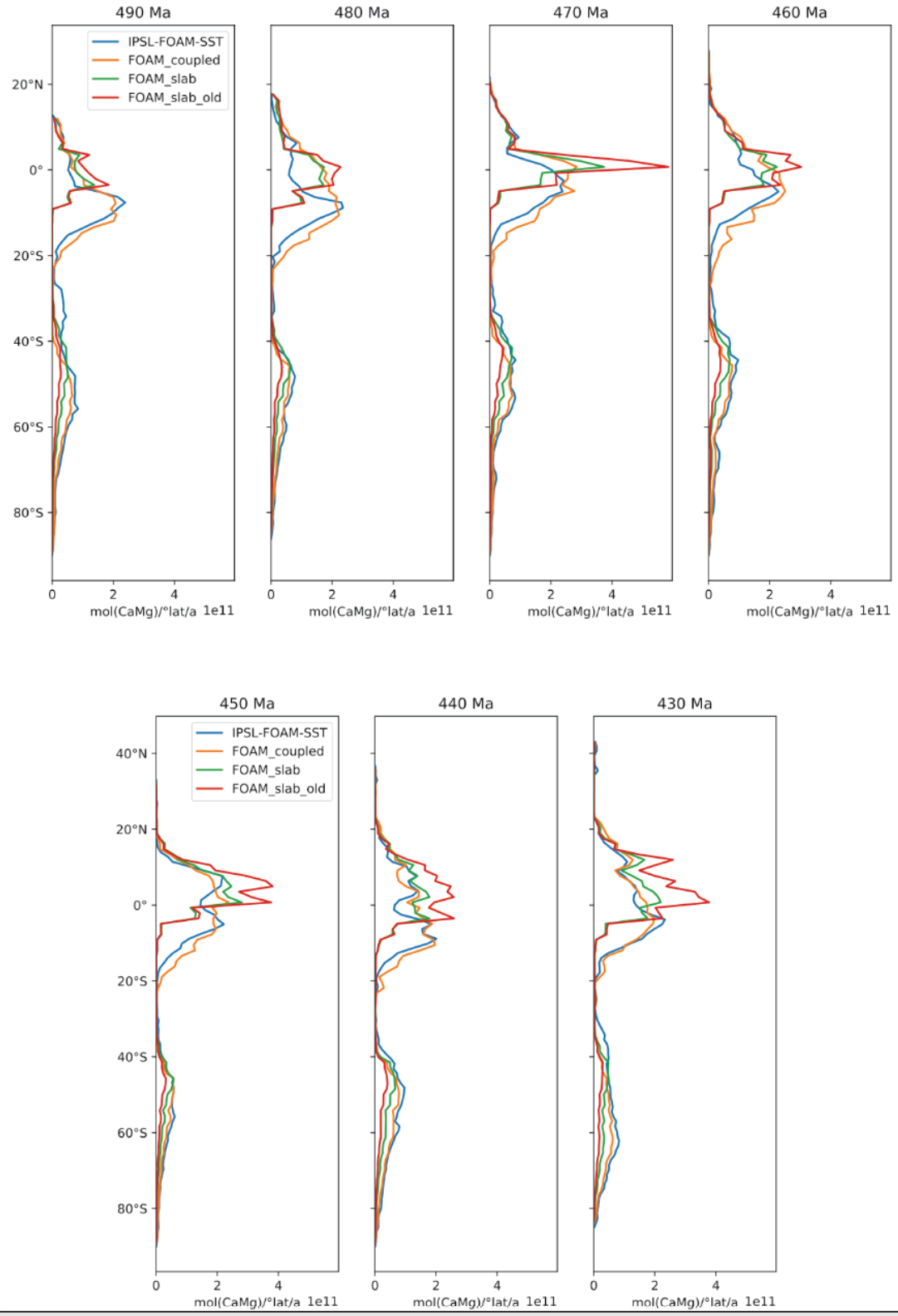

Figure S4: Latitudinal weathering profile for each time slice. With a constant pCO_2 (12 PAL or 3360 ppmv) obtained with same boundary conditions with different climate models: mixed-layer (FOAMslab, FOAM-Nardin) or fully coupled models (FOAMcoupled, FOAM-LMDz)

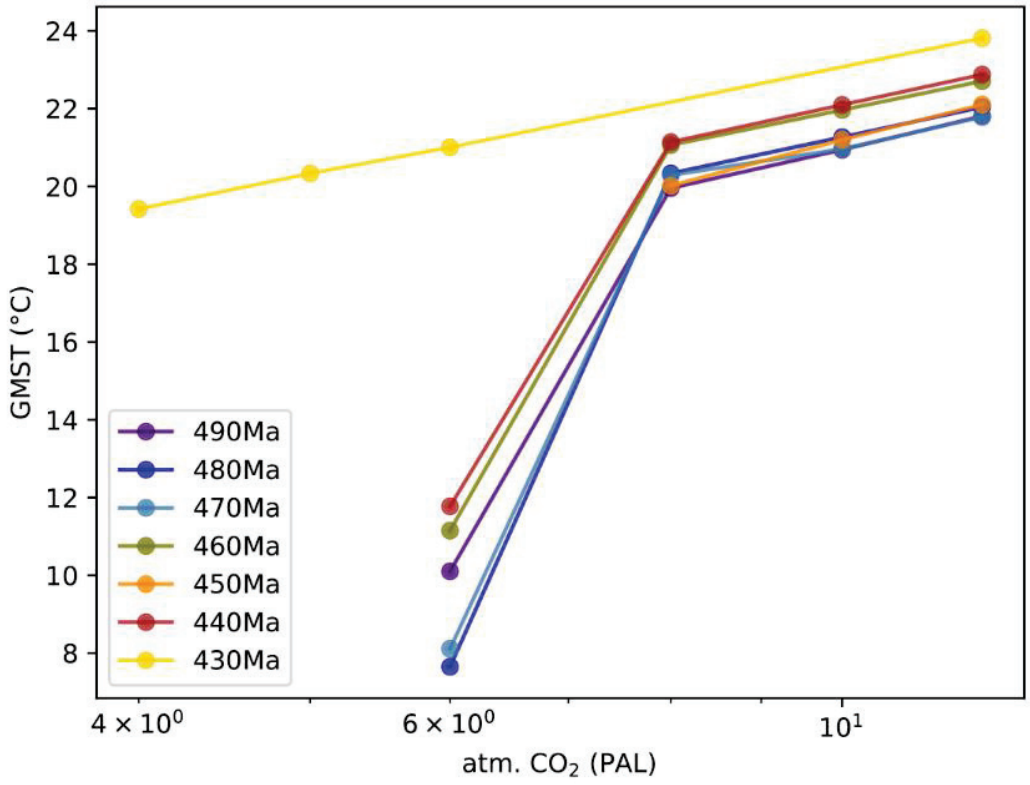

Figure S5: GMST for each time slice for a wide range of *p*CO2 values illustrating the climate sensitivity as a function of the paleogeographical configuration. The sudden cooling simulated below 8 PAL in most time slices, and associated increase in climatic sensitivity, is due to the expansion of sea ice in the Northern Hemisphere. The reader is referred to Pohl et al. (2014) for an analysis of the underlying climatic mechanisms. In short, the continental configuration during the Ordovician, with an oceanic Northern Hemisphere, induces a specific structure of the oceanic heat transport (with a minimum at the mid latitudes) that allows sea ice to suddenly expand from the North Pole to ~45°N, which in turns leads to global cooling. The northward drift of Siberia during the Ordovician, by favoring the deflection of zonal ocean currents, induces an increase in the oceanic heat transport. As a result, sea ice expands at lower pCO2 levels at 430 Ma. Pohl et al. (2014) obtained similar results using another Ordovician continental reconstruction, which demonstrates that this climatic behavior is not overly dependent on the continental reconstruction.

g. On the Ordovician latitudinal location of Laurentia

Our plate reconstructions are based on paleomagnetic data (when available) but no new Ordovician data have emerged from North America or northern Scotland (part of Laurentia) over the past three decades. Thus, our latitudinal position of North America is similar to that of (e.g.) Van der Voo (1990), which places the southern margin of Laurentia at about 20°S during the Ordovician. Ordovician reconstructions provided by Chris Scotese (www.scotese.com) have also not changed much over the past three decades (e.g., McKerrow & Scotese 1990; Golonka et al. 1994; Blakey 2009; Scotese, 2016), but these reconstructions, for some unknown reasons, place Laurentia at higher southerly latitudes during the Late Cambrian and most of the Ordovician (Fig. S6b).

Our positioning of Laurentia is based on a smooth apparent polar wander path (dark thick line in SI Fig. 6a) published in Torsvik et al. (2012). For North America, there are only two Ordovician poles, both located is an expected location between Late Cambrian and Silurian poles, but a primary signature of both these poles (poles T and St in SI Fig. S6) was questioned in Swanson-Hysell and Macdonald (2017). Both poles, however, pass a positive fold test, remagnetization must therefore be older than the Caledonian (Silurian) event at ~430 Ma. They may well represent Late Ordovician (Taconic) overprints, but irrespectively, these poles (primary or secondary) place the southern margin of North America at around 20°S during the Ordovician.

Paleomagnetic data of variable reliability from some Ordovician (Taconic) *allochthonous* terranes (ophiolites) yield lower latitudes that those of cratonic North America, but they are mostly within error of the cratonic data (Fig. S7b), and inferred to have formed in volcanic arcs close to the Laurentian margin (e.g., Van der Pluijm et al. 1996; Mac Niocaill et al. 1997; Van Staal et al. 1998; Domeier, 2015; Torsvik & Cocks, 2016). By excluding the only Ordovician poles from North America, Swanson-Hysell and Macdonald (2017) moved Laurentia 10° northward so that the paleolatitudes from most of the Taconic Terranes were located well to the south of the Laurentian margin before they were obducted. Their model, however, further implies that Laurentia first moved 10°N after 480 Ma and then 10°S after 444 Ma. Only adjusting Laurentia in the global model of Torsvik & Cocks (2016) leads to a much wider Iapetus by the end of the Ordovician (Fig. 11 in article), and would require very high plate speeds (>18 cm yr^{-1}) to close the Iapetus at around 430 Ma. It is also unclear what mechanisms caused Laurentia to first move northward (after 480 Ma) and then southward again after 444 Ma.

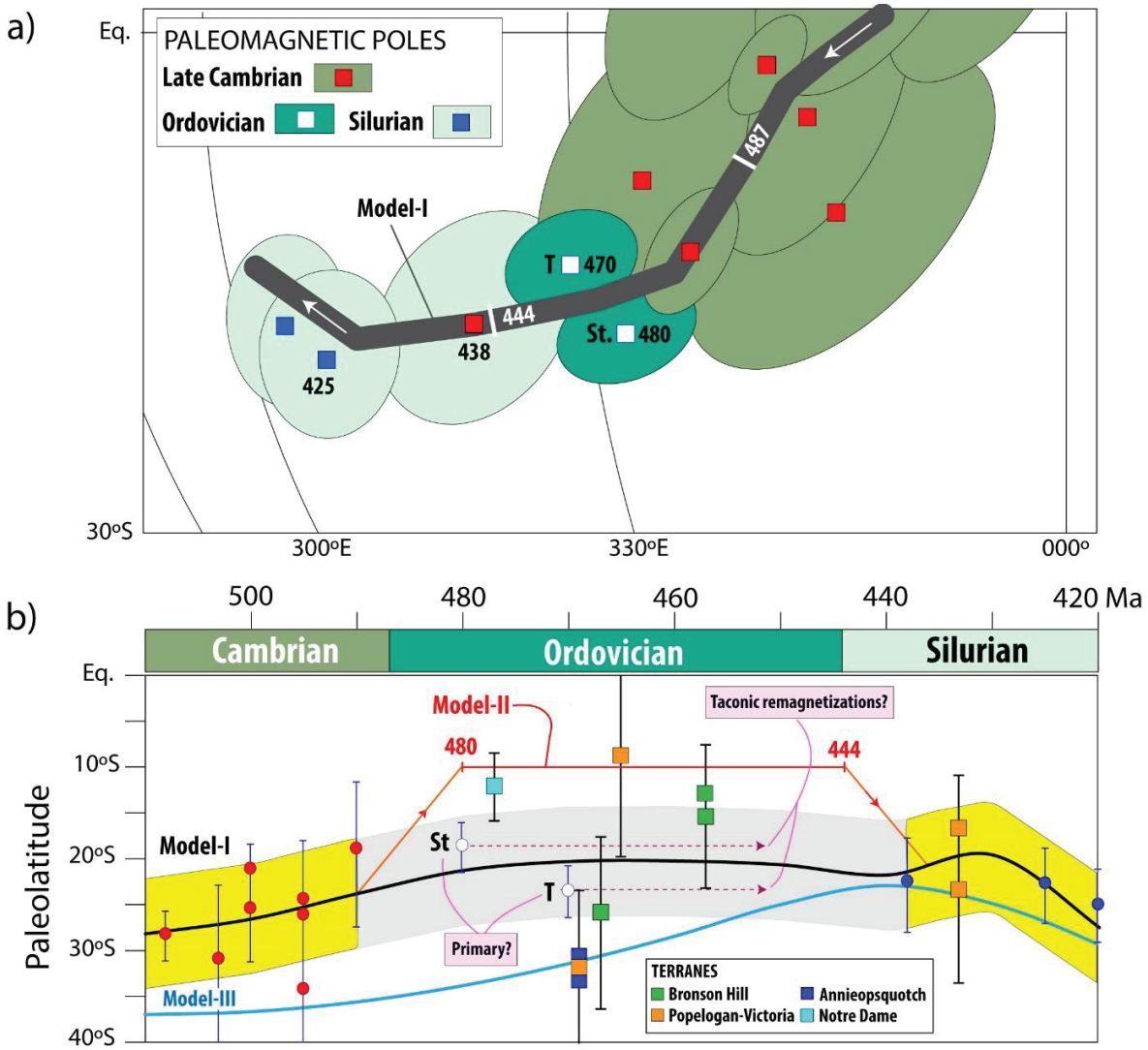

Figure S6. (a) Late Cambrian-Silurian paleomagnetic poles from cratonic North America (Laurentia) with 95% confidence ovals, and a fitted spherical spline path with input poles weighted by their Q-factor (Torsvik et al. 2012). The only Ordovician poles (from Newfoundland) are marked St (St. George Group) and T (Tablehead Group). The primary nature of these poles has been questioned (e.g., Swanson-Hysell and Macdonald 2017). **(b)** Predicted latitude for the spline path in panel a (Model-I which is from Torsvik & Cocks, 2016) and the hypothetical model of Swanson-Hysell and Macdonald (2017) (Model II) that pushes the southern margin of Laurentia equatorward to ~10°S between 470 and 444 Ma. We also show the predicted latitudes from the Scotese (2016) model and the paleolatitude of some selected allochthonous Taconic Terranes (see Table DR1 in Swanson-Hysell and Macdonald 2017). All latitudes re-calculated to a common latitude (48°N) and Model-I is plotted with an error-band of ± 6°. The latitude of the two Ordovician poles (St and T) may not be primary and could potentially reflect a Taconic remagnetization (indicated by stippled line and arrows) since they must be older than the Silurian (pre-fold magnetizations). Model III is the one of Scotese (2016).

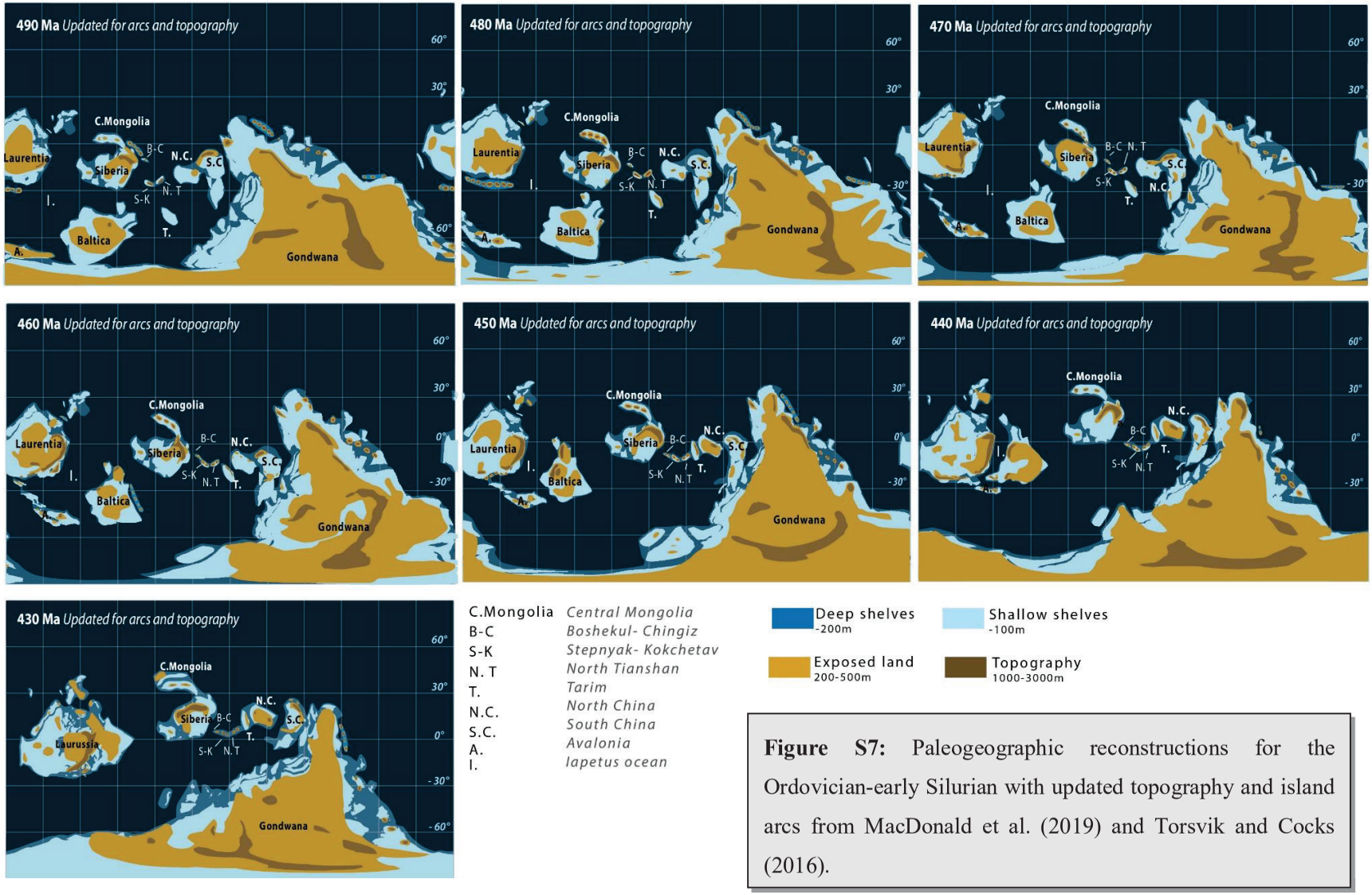

Figure S7: Paleogeographic reconstructions for the Ordovician-early Silurian with updated topography and island arcs from MacDonald et al. (2019) and Torsvik and Cocks (2016).

h. Topographic enhancements

Figure S8 shows the slope associated with the updated topography, at the resolution of the climate model LMDz (1.90° × 3.75°), for the ages 480Ma and 430Ma, illustrating the modifications that were made. The slope reconstruction for the updated topography (Fig. S8 c-d) and the enlarged uddated topography (Fig. S8 e-f) was conducted in the same way as for the original topography. An additional test was conducted were we merged the bins "1000m–3000m" and ">3000m". Because the updated topography peaks at 3000m, and never falls in the ">3000m" bin, this results in enhanced slope on all the orogens (Fig. S8 g-h).

This modification of topography generated slight differences in the land-sea mask. In other words, some pixels that were fully oceanic with the initial topography became —at least partially— continental. To assign a runoff value on these "new" continental pixels, we longitudinally interpolated the "existing" runoff field (i.e., continental point of the original topography), similarly to Park et al. (2020) when dealing with Greenland and the Sunda shelf. On each latitude band of pixels:

- If a group of "new" continental pixels is surrounded (East and West) by existing continental pixels, we linearly interpolated runoff between the East and West bound.
- If a group of "new" continental pixels is only adjacent to one existing continental pixel, we set that single value to the entire group
- If a group of "new" continental pixels is isolated, we set the mean runoff value of the entire current latitude band to the entire group.

For the temperature on the "new" continental pixels, we simply kept the ocean surface temperature (similarly to Park et al. 2020).

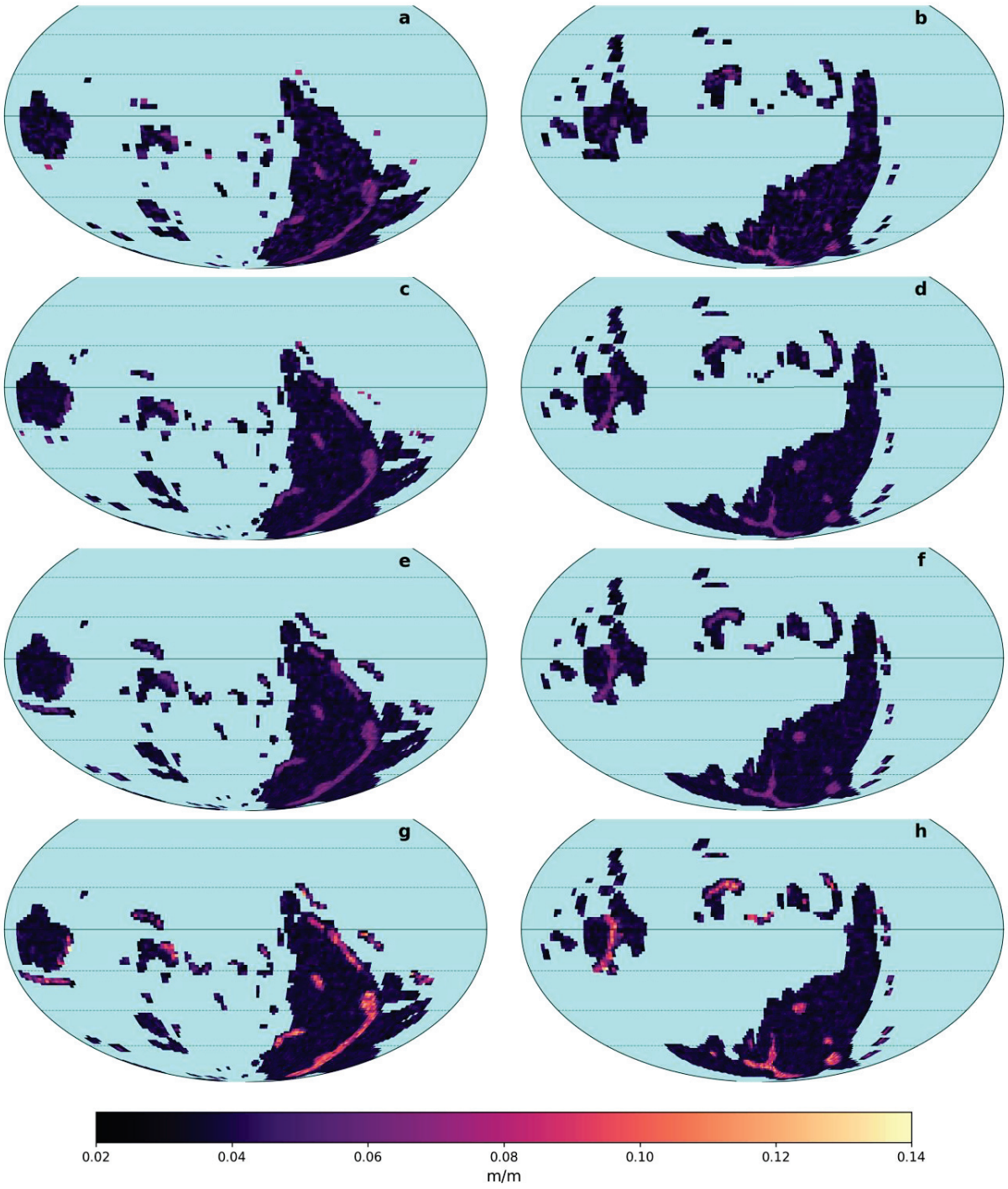

Figure S8: Slope field at the ages 480 Ma (left column: a, c, e, g) and 430 Ma (right column: b, d, f, h), at the resolution of LMDz. a-b: original topography, c-d: updated topography, e-f: enlarged updated topography, g-h: enlarged updated topography with enhanced slope. Mollweide projection, parallels are drawn every 20° from 60°S to 60°N).

References:

Blakey, R. C. (2009). Gondwana paleogeography from assembly to break-up—A 500 my odyssey. Geol. Soc. Am. Special Paper, 441, 1-28.

Boucher, O., Servonnat, J., Albright, A. L., Aumont, O., Balkanski, Y., Bastrikov, V., Bekki S., et al. (2020). Presentation and evaluation of the IPSL-CM6A-LR climate model. Journal of Advances in Modeling Earth Systems, 12(7), doi.org/10.1029/2019MS002010.

Cocks, L. R. M. and Torsvik, T. H. (2020). Ordovician palaeogeography and climate change, Gondwana Res., (November), doi:10.1016/j.gr.2020.09.008.

Domeier, M. (2015). A tectonic scenario for the Iapetus and Rheic Oceans. Gondwana Res. https://doi.org/10.1016/j.gr.2015.08.003.

Domeier, M., Torsvik, T. H. (2019). Full-plate modelling in pre-Jurassic time. Geological Magazine, 156(2), 261-280, doi:10.1017/S0016756817001005

Domeier, M. (2018). Early Paleozoic tectonics of Asia: Towards a full-plate model. Geoscience Frontiers, 9(3), 789-862, doi.org/10.1016/j.gsf.2017.11.012

Domeier, M. & Torsvik, T.H. (2014). Focus Review Paper: Plate kinematics of the Late Paleozoic. *Geoscience Frontiers* **5**, 303-350, doi.org/10.1016/j.gsf.2014.01.002.

Donnadieu, Y., Goddéris, Y., Pierrehumbert, R., Dromart, G., Fluteau, F. and Jacob, R. (2006). A GEOCLIM simulation of climatic and biogeochemical consequences of Pangea breakup, Geochemistry, Geophys. Geosystems, 7(11),Q11019 [online] Available from http://doi.wiley.com/10.1029/2006GC001278.

Goddéris, Y., Donnadieu, Y., Le Hir, G., Lefebvre, V., & Nardin, E. (2014). The role of paleogeography in the Phanerozoic history of atmospheric CO_2 and climate. Earth-Science Reviews*, 128*, 122-138. doi:10.1016/j.earscirev.2013.11.004

Goddéris, Y., Donnadieu, Y., Tombozafy, M., & Dessert, C. (2008). Shield effect on continental weathering: implication for climatic evolution of the Earth at the geological timescale. Geoderma, 145(3-4), 439-448, doi.org/10.1016/j.geoderma.2008.01.020.

Goddéris, Y., & Joachimski, M. M. (2004). Global change in the Late Devonian: modelling the Frasnian–Famennian short-term carbon isotope excursions. Palaeogeography, Palaeoclimatology, Palaeoecology, 202(3-4), 309-329, doi.org/10.1016/S0031-0182(03)00641-2.

Golonka, J. (2002). Plate-tectonic maps of the Phanerozoic.

Golonka, J. R., Ross, M. I., & Scotese, C. R. (1994). Phanerozoic paleogeographic and paleoclimatic modeling maps.

Gough, D. O. (1981). Solar interior structure and luminosity variations, Sol. Phys., 74(13), 21–34, doi:10.1007/BF00151270.

Gurnis, M., Turner, M., Zahirovic, S., DiCaprio, L., Spasojevic, S., Müller, R. D; Boyden, J; Seton, M.; Manea, V.C. & Bower, D. J. (2012). Plate tectonic reconstructions with continuously closing plates. Computers & Geosciences, 38(1), 35-42, doi.org/10.1016/j.cageo.2011.04.014.

Jacob, R. L. (1997). Low frequency variability in a simulated atmosphere-ocean system. The University of Wisconsin-Madison.

Ladant, J. B., Donnadieu, Y., Lefebvre, V., Dumas, C. (2014). The respective role of atmospheric carbon dioxide and orbital parameters on ice sheet evolution at the Eocene-Oligocene transition, Paleoceanography, 29, 810–823, doi:10.1002/2013PA002593

Licht, A., van Cappelle, M., Abels, H. et al. Asian monsoons in a late Eocene greenhouse world. Nature 513, 501–506 (2014). https://doi.org/10.1038/nature13704Maher, K., & Chamberlain, C. P. (2014). Hydrologic regulation of chemical weathering and the geologic carbon cycle. science, 343(6178), 1502-1504.

Marcilly, C. M., Torsvik, T. H., Domeier, M. and Royer, D. L. (2021) New paleogeographic and degassing parameters for long-term carbon cycle models, Gondwana Res., doi:10.1016/j.gr.2021.05.016.

Mac Niocaill, van der Pluijm, B.A., Van der Voo, R. (1997). Ordovician paleogeography and the evolution of the Iapetus ocean. Geology, 25, 2, 159–162.

McKerrow, W.S. & Scotese, C.R. (1990). *Palaeozoic Palaeogeography and Biogeography* (eds). Geological Society Memoir 12.

Nardin, E., Goddéris, Y., Donnadieu, Y., Le Hir, G., Blakey, R. C., Pucéat, E. and Aretz, M. (2011): Modeling the early Paleozoic long-term climatic trend, Bull. Geol. Soc. Am., 123(5), 1181–1192, doi:10.1130/B30364.1, 2011.

Park, Y., Maffre, P., Goddéris, Y., Macdonald, F.A., Anttila, E.S.C., Swanson-Hysell, N.L (2020). Emergence of the Southeast Asian islands as a driver for Neogene cooling, PNAS, 117(41) 25319–25326, doi: 10.1073/pnas.2011033117, 2020

Pohl, A., Donnadieu, Y., Le Hir, G., Ladant, J. B., Dumas, C., Alvarez- Solas, J. and Vandenbroucke, T. R. A.: (2016) Glacial onset predated Late Ordovician climate cooling, Paleoceanography, 31, 800–821, doi.org/10.1002/2016PA002928.

Pohl, A., Donnadieu, Y., Le Hir, G., Buoncristiani, J. F., & Vennin, E. (2014). Effect of the Ordovician paleogeography on the (in)stability of the climate. Climate of the Past, 10(6), 2053-2066, doi.org/10.5194/cp-10-2053-2014.

Scotese, C. R. (2016). PALEOMAP PaleoAtlas for GPlates and the PaleoData plotter program. In Geological Society of America Abstracts with Programs (Vol. 48, No. 5). http://www.scotese.com/newpage1.htm

Semtner, A.J. (1976). A Model for the Thermodynamic Growth of Sea Ice in Numerical Investigations of Climate. J. Phys. Oceanogr. https://doi.org/10.1175/1520-0485(1976)006<0379:amfttg>2.0.co;2

Swanson-Hysell, N. L. and Macdonald, F. A. (2017). Tropical weathering of the Taconic orogeny as a driver for Ordovician cooling, Geology, G38985.1 [online] Available from: http://geology.gsapubs.org/lookup/doi/10.1130/G38985.1 .

Torsvik, T.H., Cocks, L.R.M. (2016). Earth History and Palaeogeography. Cambridge University Press. 317 pp.

Torsvik, T.H. Smethurst, M.A., Bride, J.C. & Sturt, B.A. (1990). A review of Palaeozoic palaeomagnetic data from Europe and their palaeogeographical implications. In McKerrow, W.S. & Scotese, C.R. (eds) *Palaeozoic Palaeogeography and Biogeography.* Geological Society Memoir 12, 25-41.

Torsvik, T.H. Van der Voo, R., Preeden, U., Mac Niocaill, C., Steinberger, B., Doubrovine, P.V., van Hinsbergen, D.J.J., Domeier, M., Gaina, C., Tovher, E., Meert, J.G., McCausland, P.J. & Cocks, L.R.M (2012). Phanerozoic polar wander, paleogeography and dynamics. *Earth Science Reviews* 114, 325-368.

Torsvik, T. H., Steinberger, B., Shephard, G. E., Doubrovine, P. V., Gaina, C., Domeier, M., Conrad, C.P. & Sager, W. W. (2019). Pacific-Panthalassic reconstructions: Overview, errata and the way forward. Geochemistry, Geophysics, Geosystems, 20(7), 3659-3689, doi.org/10.1029/2019GC008402

Van der Pluijm, B.A., Van der Voo, R. & Torsvik, T.H. (1996). Convergence and subduction at the Ordovician margin of Laurentia. In: CURRENT PERSPECTIVES IN THE APPALACHIAN-CALEDONIAN OROGEN. Edited by Hibbard, J.P., van Staal, C.R., and Cawood, P.A. Geol. Ass. Can. Spec.Paper, 41, 127-136.

Van der Voo, R. (1990). The reliability of paleomagnetic data. Tectonophysics, 184(1), 1-9.

Van Staal, C.R., Dewey, J.E, Mac Niocaill, C. & McKerrow, W.S. (1998). The Cambrian-Silurian tectonic evolution of the northern Appalachians and British Caledonides: history of a complex, west and southwest Pacific-type segment of Iapetus. *In:* BLUNDELL, D. J. & SCOTT, A. C. (eds) *Lyell: the Past is the Key to the Present.* Geological Society, London, Special Publications, 143, 199-242.